AFWAL-TR-83-4141

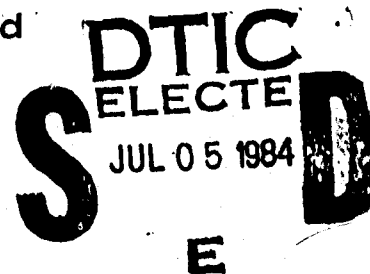# PROPERTY SCREENING AND EVALUATION OF CERAMIC TURBINE MATERIALS

D. C. Larsen and J. W. Adams

IIT Research Institute
Materials Technology
Nonmetallic Materials and Composites
Chicago, Illinois 60616

April 1984

Final Technical Report
For Period July 1979 - July 1983

DTIC
ELECTE
JUL 0 5 1984
S   D
E

MATERIALS LABORATORY
AIR FORCE WRIGHT AERONAUTICAL LABORATORIES
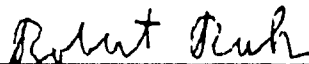AIR FORCE SYSTEMS COMMAND
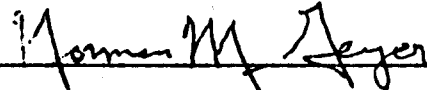WRIGHT - PATTERSON AFB, OHIO 45433

84 · 07 02 022

ROBERT RUH
Project Engineer

FOR THE COMMANDER

NORMAN M. GEYER
Technical Manager
Processing & High Temperature
  Materials Branch
Metals & Ceramics Division

HENRY C. GRAHAM, Chief
Processing & High Temperature
  Materials Branch
Metals & Ceramics Division

REPORT DOCUMENTATION PAGE		READ INSTRUCTIONS BEFORE COMPLETING FORM
1. REPORT NUMBER AFWAL-TR-83-4141	2. GOVT ACCESSION NO AD-A142 739	3. RECIPIENT'S CATALOG NUMBER
4. TITLE (and Subtitle) PROPERTY SCREENING AND EVALUATION OF CERAMIC TURBINE MATERIALS		5. TYPE OF REPORT & PERIOD COVERED Final Report 1 July 1979-30 July 1983
		6. PERFORMING ORG. REPORT NUMBER M06054-48
7. AUTHOR(s) D. C. Larsen and J. W. Adams		8. CONTRACT OR GRANT NUMBER(s) F33615-79-C-5100
9. PERFORMING ORGANIZATION NAME AND ADDRESS IIT Research Institute 10 West 35 Street Chicago, IL 60616		10. PROGRAM ELEMENT, PROJECT, TASK AREA & WORK UNIT NUMBERS P.E.62102F 2420-01-14
11. CONTROLLING OFFICE NAME AND ADDRESS AFWAL/MLLM AFSC Wright-Patterson AFB, OH 45433		12. REPORT DATE April 1984
		13. NUMBER OF PAGES 331
14. MONITORING AGENCY NAME & ADDRESS(If different from Controlling Office)		15. SECURITY CLASS. (of this report) Unclassified
		15a. DECLASSIFICATION/DOWNGRADING SCHEDULE

16. DISTRIBUTION STATEMENT (of this Report)

Approved for Public Release; Distribution Unlimited.

17. DISTRIBUTION STATEMENT (of the abstract entered in Block 20, if different from Report)

18. SUPPLEMENTARY NOTES

19. KEY WORDS (Continue on reverse side if necessary and identify by block number)

Silicon Nitride
Silicon Carbide
Transformation-Toughened Zirconia
Mechanical Properties

High Temperature Properties
Silicon Ceramics
Structural Ceramics
Gas Turbine Ceramics

20. ABSTRACT (Continue on reverse side if necessary and identify by block number)

State-of-the-art technical ceramics, mainly silicon carbide and silicon nitride, that have potential as structural components in advanced gas turbine engines, were evaluated. Thermal and mechanical property data were generated on candidate materials, and the results were interpreted with respect to microstructure, purity, secondary phases, environmental effects, and processing methods. Measured properties were related to microstructure. Failure modes and the nature of the critical strength-controlling

flaws were determined by optical and SEM fracture surface analysis. Structure-property relations were developed, and generated data were compared to literature data. To date, over sixty materials have been extensively characterized. Properties measured include: flexure strength, elastic modulus, stress-strain, fracture toughness, creep, oxidation, thermal expansion, thermal diffusivity, thermal shock, and stress rupture. Emphasis was placed on defining the limiting aspects of each material, such as the time-dependent strength relating to the existence of operable subcritical crack growth mechanisms. Property measurements were made up to 1500°C in air atmosphere.

FOREWORD

This is the Final Report on AFWAL Contract F33615-79-C-5100, "Property Screening and Evaluation of Ceramic Turbine Materials", covering the period 1 July 1979 - 30 July 1983.

Data obtained for each material have been integrated with data previously reported on AFML Contract F33615-75-C-5196. Thus, results to date on all materials and test parameters are summarized and interpreted herein.

Zirconia materials that have potential use in diesel engines were also evaluated on this program. These results are also reported here.

A corrosion-erosion study also formed part of this program. This DOE/METC-sponsored program entailed the corrosion-erosion of various carbide, nitride, and oxide ceramics in a high temperature coal-gas environment. This work, "Evaluation of Corrosion/Erosion Behavior of Various Ceramic Materials" will be issued as a separate AFWAL Technical Report in 1984.

IITRI personnel who have contributed to this program include J. L. Sievert, B. N. Norikane, G. T. Jeka, W. R. Logan, H. H. Nakamura, and J. Berlanga. The many discussions on the subject of the properties and microstructure of technical ceramics with S. A. Bortz, Y. Harada, and R. F. Firestone, are acknowledged.

Thanks are due the organizations that have contributed test samples to this program. The various personnel in the organizations that have contributed more than sixty materials to this program are listed in the accompanying table. Their contributions and cooperation are greatly appreciated.

We are indebted to Dr. H. Priest and Mr. F. Burns at USAMMRC for supplying oxygen content data. Also, thanks to Mr. J. Muntz of AFWAL for supplying cation impurity analyses performed by spectrographic and atomic absorption techniques. Additionally,

i

Accession For	
NTIS GRA&I	☒
DTIC TAB	☐
Unannounced	☐
Justification	
By	
Distribution/	
Availability Codes	
Dist	Avail and/or Special
A-1	

ii

PRINCIPAL VENDOR CONTACTS

Organization	Contacts
AiResearch	K. H. Styhr
Annawerk	E. Gugel
Associated Engineering Development	J. C. Moore
Battelle	R. R. Wills
Carborundum	G. W. Weber
Ceradyne	J. Rubin
Chemetal/SFL	J. J. Stiglich
Coors	D. Roy, K. Green, B. Seegmiller
Cummins Engine	R. Kamo
ESK	K. A. Schwetz
Fiber Materials	P. F. Jahn
Ford	A. F. McLean
General Electric	C. A. Johnson, W. A. Nelson
Georgia Tech	J. N. Harris
GTE	C. L. Quackenbush
Harbison-Walker	D. Petrak
Indussa/Nippon Denko	N. Ramesh
Kawecki-Berylco	R. J. Longenecker
Kyocera	W. Everitt
NASA-Lewis	S. N. Dutta
Naval Research Laboratory	R. W. Rice
Norton	R. Bart, M. L. Torti
Raytheon	J. S. Waugh
Rocketdyne	G. Schnittgrund
Toshiba	T. Ochiai
UKAEA	W. A. McLaughlan
U.S. Bureau of Mines	H. Heystek
Westinghouse	R. Bratton

TABLE OF CONTENTS

TABLE OF CONTENTS (cont.)

TABLE OF CONTENTS (cont.)

LIST OF FIGURES

LIST OF FIGURES (cont.)

LIST OF FIGURES (cont.)

LIST OF FIGURES (cont.)

LIST OF FIGURES (cont.)

LIST OF FIGURES (cont.)

LIST OF FIGURES (cont.)

LIST OF TABLES

LIST OF TABLES (cont.)

LIST OF TABLES (cont.)

1. INTRODUCTION

Silicon-base ceramics, silicon nitride and silicon carbide, and zirconia ceramics have potential structural application in advanced heat engines such as gas turbines and diesel engines. Components include rotor blades, stator vanes, combustion chambers, piston caps, and cylinder liners. Such utilization of ceramics offers several potential advantages, including higher temperature operation leading to increased thermal efficiency and decreased specific fuel consumption, decreased weight and thus lower stresses in rotating components, greater thrust-to-weight ratio, lower potential life cycle cost, decreased complexity through the use of noncooled components, and reduced dependency on the use of strategic materials (e.g., cobalt and chromium) that are used in metallic superalloys.

Over the past decade the various forms of Si_3N_4 and SiC have been the most promising materials for advanced heat engine application. These materials are high strength, oxidation-resistant, and thermal shock resistant. Improved versions of SiC and Si_3N_4 are currently being developed within the ceramics industry. These materials have enjoyed some success, although limited, as structural components in the hot section of prototype and demonstration engines. For ceramics to become a reality in the intended application, various requirements must be met including: the development of overall life prediction methodology; employment of realistic design methodology; and demonstration of fabrication process feasibility for the required ceramic component configurations. What is currently lacking for structural ceramics is uniformity, reproducibility, and reliability. Much work is being performed to develop an overall life prediction methodology for various ceramic component designs. The biggest challenges facing designers in the use of structural ceramics include: the statistical strength distribution; low fracture toughness and surface sensitivity; the existence of

1

time-dependent effects such as subcritical crack growth and associated strength degradation; the lack of data regarding the combined environmental effects of oxidation, corrosion, erosion, and deposition from the fuel combustion products; batch-to-batch variability resulting from inadequate process control; and lack of an NDE technology capable of detecting critical strength-limiting flaws.

These challenges are compounded by the fact that new candidate materials for advanced heat engine applications are continually emerging, and their properties are strongly dependent on microstructure, purity, and processing history. Therefore, this program was established with the purpose of supporting various current component design efforts through the comprehensive screening characterization of a wide variety of silicon-base ceramics that have potential use as components in high-temperature gas turbines, radome structures, and other high performance/severe environment applications. There is clearly a need to continue property generation and microstructural studies of these materials that are in a continual stage of improvement.

In this program, thermal and mechanical property data were measured on candidate materials, and the results interpreted with respect to microstructure, purity, secondary phases, environmental effects, and processing methods. Measured properties were related to microstructure. Failure modes and the nature of the critical strength-controlling flaws were determined by optical and SEM fracture surface analysis. Structure-property relations were developed, and generated data were compared to literature data. To date, over sixty materials have been extensively characterized. Properties measured include: flexure strength, elastic modulus, stress-strain, fracture toughness, creep, oxidation, thermal expansion, thermal diffusivity, thermal shock, and stress rupture. Emphasis is placed on defining the limiting aspects of each material, such as the time-dependent strength relating to the existence of operable subcritical crack growth mechanisms. Property measurements were made up to 1500°C in air atmosphere.

2

This program has the same objective and scope as its predecessor, AFWAL Contract No. F33615-75-C-5196. That program was summarized in AFML-TR-79-4188.[1] This report summarizes and overviews the pertinent properties obtained on over sixty (60) silicon-base and zirconia ceramics that are candidates for advanced heat engine applications. Emphasis is placed on predominant behavioral trends for each material type to aid in materials selection. Details of this work may be found in the widely distributed semiannual interim technical reports issued on this program.[2-6] Additionally, various papers have been presented and published that deal with specific aspects of this program.[7-18]

It is noted that zirconia materials were included on this program. These materials in transformation-toughened forms are currently receiving much attention for potential use in diesel engines.

This program involved much more SEM microscopy and microstructural analysis than its predecessor. Reflected light microstructural analysis reveals grain size and porosity distribution. These aspects of microstructure are directly correlated with the strength of ceramics. We cannot overemphasize the importance of SEM examination of fracture surfaces to reveal fracture mode and fracture origins.

This properties screening and evaluation work is a continuing effort in this laboratory. A follow-on program with similar objectives and scope has been initiated (AFWAL Contract F33615-82-C-5101). In the continuing work, the major emphasis is on ceramic-matrix composites, however.

This report is organized as follows. The first two sections that follow list the specific materials studied on this program and the test plan. The chemical composition and phase assemblage of the materials are then presented in Section 4. Section 5 contains the details of the test methodology used on this program. Photographs of specific test equipment are included. Section 6 presents the room-temperature strength and elastic properties of

3

the SiC and Si_3N_4 materials, as correlated to the nature of their microstructure (grain size and porosity). Typical fracture origins for each material are discussed. Elevated temperature strength behavior is presented in Section 7. Here we correlate the high temperature strength and deformation behavior with the fracture mode and the existence of oxide intergranular phases, leading to subcritical crack growth or other forms of static fatigue. Sections 8-11 contain information on (1) creep, (2) thermal expansion, (3) thermal shock, and (4) oxidation behavior. Finally, Section 12 presents our evaluation of various foreign and domestic technical zirconia ceramics.

2. MATERIALS

A wide variety of silicon-base ceramics have emerged during recent years that have potential application as components in high temperature gas turbines and other advanced heat engines. Silicon nitride and silicon carbide, in hot-pressed, reaction bonded, and pressureless sintered forms are currently the most promising materials for this application. These materials range from commercially available (which in most cases are in a continual state of development) to highly developmental. Also, certain materials have been specifically developed for lower cost, less stringent applications. Thus, the intended ap·lication and the processing maturity must be considered when comparing materials performance.

Available Si_3N_4 and SiC bodies represent a large family of materials with wide property variation and broad response characteristics during interaction with severe environments. Even though some are termed commercially available, they are in a continual state of development and change. In general, property differences between materials of a given type are directly related to: (1) existence of secondary phases, (2) purity, (3) microstructural aspects such as pore size and distribution, grain size, etc., (4) phase stability, (5) microstructural stability, (6) existence of subcritical crack growth, and (7) the nature of the critical strength-controlling flaws (e.g., contaminant inclusions, pores/pore agglomerates, large grains, unreacted particles, impurity particles, etc.) and how the critical flaws change with time, temperature, and environmental exposure.

Table 1 contains a listing of all materials evaluated on this program (and its predecessor) arranged according to material type (excluding various developmental AFWAL materials). All materials, with the exception of the Norton materials investigated early on Contract F33615-75-C-5196 (Norton NC-132, NC-435,

TABLE 1. MATERIALS EVALUATED TO DATE

A. Hot-Pressed Si_3N_4

- Norton NC-132 HP-Si_3N_4 (1% MgO)
- Norton NCX-34 HP-Si_3N_4 (8% Y_2O_3)
- Harbison-Walker HP-Si_3N_4 (10% CeO_2)
- Kyocera SN-3 HP-Si_3N_4 (4% MgO, 5% Al_2O_3)
- Naval Research Laboratory HP-Si_3N_4 (4-16 wt% ZrO_2)
- AFML Developmental HP-Si_3N_4 (CeO_2 and BN Additives)
- Ceradyne Ceralloy 147A, HP-Si_3N_4 (1% MgO)
- Ceradyne Ceralloy 147Y, HP-Si_3N_4 (15% Y_2O_3)
- Ceradyne Ceralloy 147Y-1, HP-Si_3N_4 (8% Y_2O_3)
- Fiber Materials HP-Si_3N_4 (4% MgO)
- Toshiba HP-Si_3N_4 (4% Y_2O_3, 3% Al_2O_3)
- Toshiba HP-Si_3N_4 (3% Y_2O_3, 4% Al_2O_3, SiO_2)
- Westinghouse HP-Si_3N_4 (4% Y_2O_3, SiO_2)
- NASA/AVCO/Norton HP-Si_3N_4 (10% ZrO_2)

B. Hot Isostatic Pressed Si_3N_4

- Battelle HIP-Si_3N_4 (5% Y_2O_3)

C. Sintered Si_3N_4

- Kyocera SN-205 Sintered Si_3N_4 (5% MgO, 9% Al_2O_3)
- Kyocera SN-201 Sintered Si_3N_4 (4% MgO, 7% Al_2O_3)
- GTE Sintered Si_3N_4 (6% Y_2O_3)
- AiResearch Sintered Si_3N_4 (8% Y_2O_3, 4% Al_2O_3)
- Rocketdyne SN-50 Sintered Si_3N_4 (6% Y_2O_3, 4% Al_2O_3)
- Rocketdyne SN-104 and SN-46 Sintered Si_3N_4 (14% Y_2O_3, 7% SiO_2)

D. Reaction Sintered Si_3N_4

- 1976 Norton NC-350 RS-Si_3N_4
- Kawecki-Berylco RS-Si_3N_4

6

TABLE 1 (cont.)

D. Reaction Sintered Si_3N_4 (cont.)

- Ford Injection Molded $RS-Si_3N_4$
- AiResearch Slip Cast $RS-Si_3N_4$ (Airceram RBN-101)
- Raytheon Isopressed $RS-Si_3N_4$
- Indussa/Nippon Denko $RS-Si_3N_4$
- AiResearch Injection Molded $RS-Si_3N_4$ (Airceram RBN-122)
- 1979 Norton NC-350 $RS-Si_3N_4$
- Annawerk Ceranox NR-115H $RS-Si_3N_4$
- Associated Engineering Developments (AED) Nitrasil $RS-Si_3N_4$
- Georgia Tech $RS-Si_3N_4$
- AME $RS-Si_3N_4$
- AiResearch RBN-104 $RS-Si_3N_4$

E. Hot-Pressed SiC

- Norton NC-203 HP-SiC ($\sim 2\%$ Al_2O_3)
- Ceradyne Ceralloy 146A, HP-SiC (2% Al_2O_3)
- Ceradyne Ceralloy 146I, HP-SiC (2% B_4C)

F. Sintered SiC

- General Electric Sintered β-SiC
- Carborundum Sintered α-SiC (1977 vintage)
- Kyocera SC-201, Sintered α-SiC (1980 vintage)
- Carborundum 1981 SASC (Hexoloy SX-05)
- ESK Sintered α-SiC

G. Silicon-Densified SiC (Siliconized)

- Norton NC-435 Si/SiC
- UKAEA/BNF Refel Si/SiC (diamond-ground and as-processed)
- Norton NC-430 Si/SiC
- Coors Si/SiC (1979, SC-1)
- Coors Si/SiC (1981 and 1982, SC-2)
- General Electric Silcomp Si/SiC (Grade CC)

TABLE 1 (concluded)

H. SiC Coatings
    - Chemetal/SFL CNTD-SiC Coating/Graphite Substrate

I. SiAlON Materials

    - AFML/General Electric GE-129 SiAlON
    - AFML/General Electric GE-130 SiAlON
    - BuMines $ZrSiO_4$-doped Sintered SiAlON (3 compositions)
    - BuMines Y_2O_3-doped Sintered SiAlON

J. Oxide Materials

    - Corning Glass Pyroceram 9606 Glass-Ceramic
    - AFML Zyttrite ZrO_2 (YSZ)
    - Zirconia Ceramics from Australian, German, Japanese, and Domestic Sources
    - Ceres/NRL Single-Crystal Zirconia

and NC-350*), were supplied without charge by the respective manufacturers. In cases where material billets rather than as-sintered or machined test samples were supplied, AFWAL arranged for machining under a separate contract.

Table 2 contains density and machining information on all materials, as well as the date each material was received. The date received is important since several materials are termed commercially available but are actually still being developed. Some materials have undergone various processing modifications recently which have resulted in improved properties. The indication of the date received thus permits an assessment of the performance of the material as determined in this program, with respect to its maturity level. Some suppliers have made significant improvements in processing technology over the duration of this program, and have supplied new upgraded versions of their materials. It is expected that this will continue with various manufacturers as improved processing techniques yield upgraded materials.

---

*Early on the previous program (Contract F33615-75-C-5196), the work scope allowed for test samples to be purchased. On the present program, however, funding was not available for this.

TABLE 2. ADDITIONAL MATERIALS INFORMATION

	Material	Sample ID Code, 1st letter	Bulk Density, $g\ cm^{-3}$	Surface Finish, $\mu in.$ rms	Comments[a]	Date Received
1	Norton NC-132 HP-Si_3N_4 (1% MgO)	1	3.18	12	Diamond ground at Norton	11/75
2	Norton NCX-34 HP-Si_3N_4 (8% Y_2O_3)	5	3.37	15	Diamond ground at Bomas	8/77
3	Harbison-Walker HP-Si_3N_4 (10% CeO_2)	H	3.34	5	Supplied diamond ground	7/77
4	Kyocera SN-3 HP-Si_3N_4	A	3.06	8	Supplied diamond ground	2/77
5	Norton NC-435 Si/SiC	4	2.96	5	Diamond ground at Norton	1/76
6	Carborundum Sintered α-SiC	8	3.16	10	Supplied diamond ground	3/77
7	General Electric Sintered SiC	G	3.04	12	Supplied diamond ground	2/77
8	UKAEA/BNF Refel Si/SiC	U	3.11	8	Supplied diamond ground (designated batch 1 in material ID notation)	5/77
9	Kyocera SN-201 Sintered Si_3N_4	B	3.00	15	Supplied diamond ground	2/77
10	Kyocera SN-205 Sintered Si_3N_4	2	2.81	20	Supplied diamond ground	2/77
11	Norton NC-350 RS-Si_3N_4	3	2.41-2.55	6	Diamond ground at Norton	1/76

TABLE 2 (cont.)

Material	Sample ID Code, 1st letter	Bulk Density, g cm⁻³	Surface Finish, µin. rms	Comments[a]	Date Received
12 Kawecki-Berylco RS-Si$_3$N$_4$	K	2.35-2.53	20-60	Supplied as-fabricated, diamond ground as reqd. to meet dimension spec.	6/76
13 AiResearch (slip-cast) RS-Si$_3$N$_4$ (RBN-101)	7	2.85	16	Diamond ground at Bomas	8/77
14 Ford (injection molded) RS-Si$_3$N$_4$	F	2.75	29	Supplied as-sintered	8/77
15 Raytheon (isopressed) RS-Si$_3$N$_4$	6	2.43	10-30	Supplied rough ground; ultrasonic machined at Bullen; finish diamond ground at IITRI.	3/77
16 Indussa/Nippon Denko RS-Si$_3$N$_4$	N	2.08	110	Diamond ground at AFML (very porous material)	7/77
17 Naval Res. Lab. HP-Si$_3$N$_4$ + 4-16 w/o ZrO$_2$	R	3.1-3.4	8	Supplied diamond ground	3/77
18 Ceradyne Ceralloy 147A HP-Si$_3$N$_4$ (1% MgO)	X	3.22	20	Diamond ground at Bomas	11/77
19 Ceradyne Ceralloy 147Y HP-Si$_3$N$_4$ (15% Y$_2$O$_3$)	Z	3.37	18	Diamond ground at Bomas	11/77
20 Ceradyne Ceralloy 147Y-1 HP-Si$_3$N$_4$ (8% Y$_2$O$_3$)	Y	3.29	15	Diamond ground at Bomas	11/77
21 GTE Sylvania Sintered Si$_3$N$_4$ (6% Y$_2$O$_3$)	C	3.23	12	Supplied diamond ground	6/78
22 AiResearch (injection molded) RS-Si$_3$N$_4$ (RBN-122)	9	2.66	50-80	Supplied as processed	11/77

TABLE 2 (cont.)

	Material	Sample ID Code, 1st letter	Bulk Density, g cm^{-3}	Surface Finish, μin. rms	Comments[a]	Date Received
23	Norton NC-350 RS-Si$_3$N$_4$	3	2.38	22	As-nitrided (designated batch 6 in IITRI sample ID notation)	6/77
24	UKAEA/BNF Refel Si/SiC (as-processed)	U	3.09	40-70	Supplied as-processed (designated batch 2)	11/77
25	Ceradyne Ceralloy 146 HP-SiC (2% Al$_2$O$_3$)	V	3.22	18	Diamond ground at Bomas	11/77
26	Ceradyne Ceralloy 146I HP-SiC (2% B$_4$C)	W	3.21	15	Diamond ground at Bomas	11/77
27	Norton NC-203 HP-SiC (2% Al$_2$O$_3$)	E	3.32	10	Diamond ground at Bomas	9/78
28	Annawerk Ceranox NR-115 H RS-Si$_3$N$_4$	I	2.44-2.68	50-100	As-nitrided	10/78
29	Fiber Materials, Inc. HP-Si$_3$N$_4$ (4% MgO)	J	3.16-3.2	15	Diamond ground at Bomas	10/78
30	Associated Engineering Developments Nitrasil RS-Si$_3$N$_4$	P	2.5-2.6 2.6	25, 100 15	Supplied diamond ground and as-nitrided, 4 batches; batch 5, diamond-ground at Bomas	10/78 10/80
31	Norton NC-350 RS-Si$_3$N$_4$	3	2.4	9	Supplied diamond ground (designated batch 9)	2/79
32	Harbison-Walker HP-Si$_3$N$_4$ (10% CeO$_2$)	H	3.38	16	Supplied diamond ground (designated batch 2)	2/79
33	Norton NC-430 Siliconized SiC	O	3.1	5	Diamond ground at Bomas	3/79

TABLE 2 (cont.)

	Material	Sample ID Code, 1st letter	Bulk Density, g cm^{-3}	Surface Finish, μin. rms	Comments[a]	Date Received
34	AiResearch Sintered Si$_3$N$_4$ (8% Y$_2$O$_3$, 4% Al$_2$O$_3$)	L	3.1	30-50	Injection molded. Tested as-nitrided	7/79
35	Rocketdyne SN-50 Sintered Si$_3$N$_4$ (Y$_2$O$_3$, Al$_2$O$_3$)	RC	3.25	35	Injection molded. Tested as-nitrided	11/79
36	Rocketdyne SN-46, SN-104 Sintered Si$_3$N$_4$ (Y$_2$O$_3$, SiO$_2$)	RC	3.4	40	Injection molded. Tested as-nitrided	11/79, 5/80
37	Coors Si/SiC (SC-1)	CG	3.0	10	Supplied diamond-ground	10/79
38	Chemetal CNTD SiC Coating on Graphite Substrate	CS1 CS2 CS3, CS4 CS5,6,7	-- -- -- --	40-100 30-50 -- --	UT-22 graphite (Batch 1) SIC-6 graphite (Batch 2) SIC-6 graphite (Batch 3,4) SIC-6 graphite (Batch 5,6,7)	9/79 2/80 9/80 1/81
39	Toshiba HP-Si$_3$N$_4$	TO	3.24	10	Supplied diamond-ground	2/80
40	Toshiba HP-Si$_3$N$_4$	TR	3.20	15	Samples diamond-ground from hot-pressed cylinder liner. Most samples contained bonded joint region	4/80
41	Georgia Tech RS-Si$_3$N$_4$	GT	2.5-2.6	10	Diamond-ground at Bomas	4/80
42	CSIRO Transformation-Toughened ZrO$_2$	ZT	5.7	20	Supplied diamond-ground	7/80
43	Westinghouse HP-Si$_3$N$_4$	WB	3.2-3.3	10	Diamond-ground at Bomas	9/80
44	Kyocera SC-201 Sintered SiC	KK	3.14	30	Supplied diamond-ground	9/80

13

TABLE 2 (cont.)

	Material	Sample ID Code, 1st letter	Bulk Density, $g\ cm^{-3}$	Surface Finish, $\mu in.$ rms	Comments[a]	Date Received
45	AME RS-Si$_3$N$_4$	BI1	2.1	130	Supplied diamond-ground	10/80
46	AiResearch RBN-104 RS-Si$_3$N$_4$	BI2	2.8	60	Supplied diamond-ground	10/80
47	Battelle HIP-Si$_3$N$_4$	BW	3.24	14	Supplied diamond-ground	1/80
48	NASA/AVCO/Norton HP-Si$_3$N$_4$ (10% ZrO$_2$)	NA	3.36	17	Diamond-ground at Bomas	6/81
49	Carborundum SASC (Hexolov SX-05)	8H2	3.1	70	Injection molded, as-fired	8/81
50	Coors Si/SiC (SC-2)	CG2	3.1	30	Supplied diamond-ground	10/81
51	Coors Si/SiC (SC-2)	CG3	3.1	-	Supplied diamond-ground	12/82
52	General Electric Silcomp Si/SiC (Grade CC)	GS1	2.9	12	Diamond-ground at Bomas	4/82
53	ESK Sintered α-SiC	FS1	3.1	12	Supplied diamond-ground	9/82
54	BuMines Sintered SiAlON (Y$_2$O$_3$)	UH1	3.04	~10	Diamond-ground at Bomas	10/82
55	BuMines Sintered SiAlON (ZrSiO$_4$)	UH2	2.64	~20	Diamond-ground at Bomas	10/82
56	BuMines Sintered SiAlON (ZrSiO$_4$)	UH3	2.63	~60	Diamond-ground at Bomas	5/83
57	BuMines Sintered SiAlON (ZrSiO$_4$)	UH4	2.90	~20	Diamond-ground at Bomas	2/83

[a] All diamond-machined specimens were longitudinally ground (i.e., parallel to the tensile axis of the test bar). Norton refers to Norton Company, Worcester, MA. Bomas refers to Bomas Machine Specialties, Inc., Boston, MA. Bullen refers to Bullen Ultrasonics Company, Eaton, OH.

3. TEST PLAN

Tables 3 through 5 present the various pre-test and post-test characterization parameters, as well as the general test plan for this program. For any given material, the specific tests that are conducted are a function of number of test samples available, expected properties (determines specific test temperatures), and intended use of the material. In general, tests are conducted at room temper... to establish a baseline, and in the appropriate elevated temperature range where the properties (e.g., strength) are expected to begin to change rapidly (i.e., T >1000°C). All testing is being performed in air. The maximum test temperature is 1500°C. For strength behavior, it is important to recognize this as a screening effort where the typical test sample population is five to ten for any given test temperature. Therefore, only rough estimates of Weibull moduli can be made.

TABLE 3.   PRE-TEST CHARACTERIZATION PARAMETERS

● Density-Porosity Characterization

● Microstructural Analysis

● Impurity Content
    ● Cations - spectrographic (AFWAL)
    ● Oxygen - neutron activation analysis (AMMRC)

● Phase Identification - XRD (AFWAL)

● X-radiographic Inspection (AFWAL)

TABLE 4.   POST-TEST ANALYSIS

● Correlation of Properties

● Comparison with Literature Data

● Establish Structure-Property Relations

● Interpretation of Mechanisms

● Failure Mode Analysis, Identification of Critical
  Flaws by Fractographic Techniques. Performed on
  virgin and exposed flexural test bars broken at
  25°C and at elevated temperatures.

TABLE 5. SCREENING TESTS CONDUCTED[a]

- Flexural Strength-Modulus (4 point), Stress-Strain (25°C, 1000°-1500°C)

- Fracture Toughness
    - Controlled Flaw (25°C, 1000°-1500°C)

- Creep (stepwise) (1300°-1500°C); rate, stress-dependence

- Long Term Oxidation Exposure (100 and 1000 hr at ∿1400°C) Residual Strength at 25°C, fracture origins, weight changes, surface scale morphology (optical and SEM), scale products (XRD, XRF)

- Thermal Expansion (25°-1500°C)

- Thermal Diffusivity (25°C, 800°-1500°C)

- Thermal Shock
    - Water Quench/Internal Friction/Residual Strength
    - Analytical Thermal Stress Resistance Parameters

- Dynamic Young's Modulus (room temperature)

- Slow Crack Growth Evaluated on Selected Materials Using Differential Strain Rate Tests

- Stress Rupture

---

[a] Tests conducted in air atmosphere.

4. MATERIALS CHARACTERIZATION

Materials characterization parameters include X-ray phase
identification and spectrographic metallic impurity analysis
(both performed by AFWAL). Table 6 lists the phases present in
the materials studied to date, as determined by X-ray diffrac-
tion. Spectrographic impurity analysis results are presented in
Table 7. Elements present in quantity <0.2% were detected by
emission spectrographic analysis. For elements present in quan-
tities >0.2%, an emission spectrographic technique was used
wherein unknown samples were fused, dissolved into solution, and
appropriate standard references established. The dilute unknowns
were then submitted for standard spectrographic analysis to de-
termine the cation impurity levels. Oxygen analysis of supplied
test materials was conducted at USAMMRC, Watertown, Mass. Re-
sults obtained to date are presented in Table 8.

TABLE 6. X-RAY DIFFRACTION ANALYSIS RESULTS

Material	Phases Present	
	Major	Minor
Hot-Pressed Si_3N_4		
Norton NC-132 (1% MgO)	β-Si_3N_4	Si_2N_4O
Norton NCX-34 (8% Y_2O)	β-Si_3N_4	$Y_2O_3 \cdot Si_3N_4$
Harbison-Walker (10% CeO_2)	β-Si_3N_4	α-Si_3N_4
Kyocera SN-3 (MgO, Al_2O_3)	β-Si_3N_4	α-Si_3N_4, Si_2N_2O
Ceradyne 147A (1% MgO)	β-Si_3N_4	
Ceradyne 147Y-1 (8% Y_2O_3)	β-Si_3N_4	
Ceradyne 147Y (15% Y_2O_3)	β-Si_3N_4	$YSiO_2N$
Fiber Materials (4% MgO)	β-Si_3N_4	
Toshiba	β-Si_3N_4	
Toshiba (cylinder liner)	β-Si_3N_4	
Westinghouse	β-Si_3N_4	$Y_2Si_2O_7$, α-$Y_2Si_2O_7$, trace $Y_4Si_3O_{12}$
NASA/AVCO/Norton (10% ZrO_2)	β-Si_3N_4	
Battelle HIP-Si_3N_4 (5% Y_2O_3)	β-Si_3N_4	$Y_5(SiO_4)_3N$
Reaction Sintered Si_3N_4		
Norton NC-350 (1976)	α-Si_3N_4	β-Si_3N_4
KBI	a	a
KBI	α-Si_3N_4	β-Si_3N_4
Ford (IM)	α-Si_3N_4	β-Si_3N_4
AiResearch (SC)	a	a
Raytheon (IP)	α-Si_3N_4	β-Si_3N_4
Indussa/Nippon Denko	α-Si_3N_4	β-Si_3N_4
AiResearch (IM)	α-Si_3N_4	β-Si_3N_4
Norton NC-350 (1977)	α-Si_3N_4	β-Si_3N_4
Norton NC-350 (1979)	α-Si_3N_4	β-Si_3N_4
Annawerk Ceranox	α-Si_3N_4	β-Si_3N_4
AED Nitrasil		
Batch 1	α-Si_3N_4	β-Si_3N_4
Batch 2	α-Si_3N_4	β-Si_3N_4
Batch 3	α-Si_3N_4	β-Si_3N_4
Batch 4	a	a
Batch 5	α-Si_3N_4	β-Si_3N_4
Georgia Tech	a	a
AME	α-Si_3N_4	β-Si_3N_4
AiResearch RBN-104	α-Si_3N_4	β-Si_3N_4

TABLE 6 (cont.)

| Material | Phases Present | |
	Major	Minor

Sintered Si_3N_4

Kyocera SN-205 (MgO, Al_2O_3)	β-Si_3N_4	α-Si_3N_4
Kyocera SN-201 (MgO, Al_2O_3)	β-Si_3N_4	
GTE (6% Y_2O_3)	β-Si_3N_4	
Rocketdyne SN-50 (Y_2O_3, Al_2O_3)	β-Si_3N_4	
Rocketdyne SN-104 (Y_2O_3, SiO_2)	β-Si_3N_4	

SiC Materials

Carborundum SSC (1977)	α-SiC (4H, 15R, and/or 21R)	
General Electric SSC (B1)	β-SiC (3C)	
General Electric SSC (B2)	β-SiC (3C)	Trace α-SiC (15R?)
Norton NC-435 Si/SiC	α-SiC	Si
UKAEA BNF Refel Si/SiC	α-SiC (4H, 15R, and/or 21R)	Si
Norton NC-430 Si/SiC	α-SiC (6H, 15R)	Si
Coors Si/SiC (1979)	α-SiC (2H, 4H, 6H, 15R)	β-SiC (3C), Si
Ceradyne 146A HPSC (2% Al_2O_3)	α-SiC (4H, 15R, and/or 21R)	
Ceradyne 146I HPSC (2% B_4C)	α-SiC (4H, 15R, and/or 21R)	
Norton NC-203 HPSC (2% Al_2O_3)	α-SiC (6H, 33R, 51R)	β-SiC (3C)
Chemetal CNTD SiC Coating		
Batch 1	β-SiC (3C)	Trace α-SiC
Batch 2	β-SiC (3C)	Si; trace α-SiC
Kyocera SC-201 SSC	α-SiC (6H, 15R, 21R?)	
Coors Si/SiC (1981)	α-SiC (6H, 4H, 15R, 2H)	β-SiC (3C)
Carborundum SSC (1981)	α-SiC (6H, 4H, 15R)	
G. E. Silcomp Si/SiC	β-SiC (3C)	Si, trace α-SiC
Coors Si/SiC (1982)	α-SiC (6H,4H,2H)	Si, trace α-SiC, 21R
ESK SSC	α-SiC (6H,4H,2H)	Trace α-SiC (21R)

[a]Approximately equal amounts of α-Si_3N_4 and β-Si_3N_4.

TABLE 7. METALLIC IMPURITY ANALYSIS[a]

Material	Weight Percent Element[b]									Total Wt% Metallic Impurities incl. Trace Elements
	Al	Fe	Mn	Cr	Ca	Mg	B	W	Others	
Hot-Pressed Si_3N_4										
Norton NCX-34 (8% Y_2O_3)	0.3	0.5	0.05	0.02	0.05			2.25	0.15Co	3.6% + 5.8% Y
Harbison-Walker (10% CeO_2)	0.53	0.6			0.1	0.005		0.1		1.3% + 7% Ce
Norton NC-132 (1% MgO)	0.17	0.55	0.05	0.02	0.04	0.84		2.1	0.20Co	4%
Kyocera SN-3	2.6	1.4–1.9	0.04	0.1	0.2–0.33	1.9–2.3			0.1Na, 0.23K	7%
Ceradyne (1% MgO)	0.5	0.77	0.014		0.22	0.7		0.31		2.5 – 4.6%
Ceradyne (8% Y_2O_3)	1.0	1.4	0.03		0.17	0.1				2.6% + 6% Y
Ceradyne (15% Y_2O_3)	1.0	1.1	0.024		0.18					2.3% + 12.4% Y
Harbison-Walker (10% CeO_2) Batch 2	0.37	0.81			0.11					1.4% + 5.1% Ce (6.2% CeO_2)
Fiber Materials (4% MgO)	0.18–0.23	0.25			0.12–0.18	2.1–2.9				2.7 – 3.6%
Toshiba	1.6	0.04								1.7% + 2.95% Y
Toshiba (cylinder liner)	2.3	0.03								2.4% + 2.35% Y
Westinghouse	0.05	0.71	0.06		0.02			3.6	0.04Ti, 0.25Co	4.78% + 3.1% Y
NASA/AVCO/Norton (10% ZrO_2)	0.10	0.21	0.05		0.1			1.6	0.09Co	2.2% + 1.7% Y + 5.2% Zr
Battelle HIP (5% Y_2O_3)	0.06	0.07								0.2% + 3.15% Y (4% Y_2O_3)
Hot-Pressed SiC										
Ceradyne (2% Al_2O_3)	1.0	0.44			<0.1		0.1	0.43	0.06Co	2.1 – 3.9%
Ceradyne (2% B_4C)	1.5	0.1					0.92			2.5 – 3.3%
Norton NC-203 (2% Al_2O_3) Batch 1	1.5	0.03		0.19				3.8		5.6%
Norton NC-203 (2% Al_2O_3) Batch 2	1.7	0.55		0.13				3.8		6.3%

21

TABLE 7 (cont.)

Material	Al	Fe	Mn	Cr	Ca	Mg	B	W	Others	Total Wt% Metallic Impurities incl. Trace Elements
SiC Coatings										
Chemetal CNTD SiC, Batch 1										0.057
Chemetal CNTD SiC, Batch 2										0.097
Si/SiC										
UKAEA/BNF Refel (diamond ground)		0.27								0.3 + Si
UKAEA/BNF Refel (as-processed)	0.1	0.58								0.6 – 0.7% + Si
Norton NC-435	0.14	0.4	0.05		0.02	0.02		<0.02		0.65% + Si
Norton NC-430	0.4	0.1								0.55% + Si
Coors Si/SiC (1979)	0.11	0.12								0.35% + Si
Coors Si/SiC (1981)	0.09	0.11								0.33% + Si
Coors Si/SiC (1982 SC-2)	0.16	0.12					0.14		0.05Zr	0.57% + Si
GE Silcomp Si/SiC (CC)	0.36	0.17					0.15		0.06Ti	0.80% + Si
Sintered SiC										
Carborundum (α-SiC) (1977)	0.06–0.09	0.18–0.27					0.41	0.07		0.6%
General Electric (β-SiC) (Batch 1)	0.1	0.19–0.29					0.42–0.47	1.1–1.2	0.075Co	1.9 – 2.5%
General Electric (β-SiC) (Batch 2)	0.04	0.27					0.36	2.0		2.4%
Kyocera SC-201		0.11					0.5	<0.02	0.04Ti	0.73%
Carborundum (1981)	0.09	0.03					0.36		0.07Ti	0.25%
ESK (α-SiC)	0.57	0.03					0.08			0.75%

Weight Percent Element[b]

22

TABLE 7 (cont.)

Material	Weight Percent Element[b]									Total Wt% Metallic Impurities incl. Trace Elements
	Al	Fe	Mn	Cr	Ca	Mg	B	W	Others	
Sintered Si_3N_4										
Kyocera SN-201	3.5-3.8	1.3-1.8	0.03	0.1	0.25-0.39	2.1-2.6				6-8.6%
Kyocera SN-205	4.9-5.0	1.4-2.3	0.04	0.1	0.25-0.45	2.4-3.2				5-11%
GTE Sylvania	0.04	0.12							.1Mo	0.4% + 5.6% Y (7.1% Y_2O_3)
AiResearch (8% Y_2O_3, 4% Al_2O_3)	1.2	0.62							.15Mo	2.1% + 6.4% Y (8.1% Y_2O_3)
Rocketdyne SN-50 (Y_2O_3, Al_2O_3)	2.0	0.05						.02	.15Mo	2.3% + 4.5% Y
Rocketdyne SN-104 (Y_2O_3, SiO_2)	0.16	0.04						1.5	0.08Ti 0.10Co	1.9% +10.6% Y
Reaction Sintered Si_3N_4										
Norton NC-350 (original batch 1)	0.14	0.4	0.05	0.02	0.04	0.01		<0.02		0.7%
KBI	0.15-0.2	0.41-0.61	0.02	<0.1	0.13-0.17	0.02		0.02		0.8-2%
AiResearch (SC)	0.25	1.1								1.4%
Ford (IM)	0.1	1.0	0.1							1.2%
Raytheon (IP)	0.95	1.3								2.3%
Indussa/Nippon Denko	0.43	0.4		0.1	0.25					1.2%
AiResearch (IM)	0.54	1.1	0.016		0.029					1.4-1.7%
Annawerk Ceranox NR-115 H	0.3	0.52	0.06	0.1	0.04					1.1%

TABLE 7 (cont.)

Material	Weight Percent Element[b]									Total Wt% Metallic Impurities incl. Trace Elements
	Al	Fe	Mn	Cr	Ca	Mg	B	W	Others	
	Reaction Sintered Si_3N_4 (cont.)									
Norton NC-350 (Batch 6)	0.16	0.32								0.6%
Norton NC-350 (Batch 9)	0.16	0.27								0.5%
AED Nitrasil (Batch 1)	0.75	0.64			0.26					1.8%
AED Nitrasil (Batch 2)	0.72	0.58			0.27					1.75%
AED Nitrasil (Batch 3)	0.22	0.34								0.7%
AED Nitrasil (Batch 4)	0.24	0.44								0.8%
Georgia Tech	0.24	0.28								0.7%
AED Nitrasil (Batch 5)	0.49	0.37	0.02		0.21			<0.02	0.04Ti	1.2%
AME	0.72	0.44			0.18			<0.02	0.04Na, 0.06Ti, 0.02V	1.6%
AiResearch RBN-104	0.17	1.3						<0.02	0.02Ni, 0.04Ti, 0.04Mo, 0.04V	1.7%

[a] Emission spectrographic analysis for elements present in quantity <0.2%; quantitative wet chemical analysis for elements >0.2%. Does not include oxygen and unreacted silicon impurities.

[b] Elements present in amount <0.1 wt% usually not recorded, but appear as trace elements in the summed total of metallic impurities.

TABLE 8.   OXYGEN CONTENT OF CERAMIC TEST MATERIALS

Material	Oxygen, wt%[a]
A. Hot Pressed Si_3N_4	
• Norton NC-132 HP Si_3N_4 (1% MgO)	3.33
• Norton NCX-34 HP-Si_3N_4 (8% Y_2O_3)	3.33
• Harbison-Walker HP-Si_3N_4 (10% CeO_2)	2.81-2.95
• Kyocera SN-3 HP-Si_3N_4 (4% MgO, 5% Al_2O_3)	9.97
• Ceradyne Ceralloy 147A, HP-Si_3N_4 (1% MgO)	1.72
• Ceradyne Ceralloy 147Y, HP-Si_3N_4 (15% Y_2O_3)	5.16
• Ceradyne Ceralloy 147Y-1, HP-Si_3N_4 (8% Y_2O_3)	4.43
• Fiber Materials, Inc. HP-Si_3N_4 (4% MgO)	2.51
• Toshiba (4% Y_2O_3, 3% Al_2O_3)	2.26
• Toshiba (3% Y_2O_3, 4% Al_2O_3, SiO_2)	4.29
• Westinghouse (4% Y_2O_3, SiO_2)	3.16
B. Sintered Si_3N_4	
• Kyocera SN-205 Sintered Si_3N_4 (5% MgO, 9% Al_2O_3)	8.94
• Kyocera SN-201 Sintered Si_3N_4 (4% MgO, 7% Al_2O_3)	6.20
• GTE Sylvania Sintered Si_3N_4 (6% Y_2O_3)	3.04
• AiResearch (IM) Sintered Si_3N_4 (8% Y_2O_3, 4% Al_2O_3)	5.57
• Rocketdyne SN-50 (6% Y_2O_3, 4% Al_2O_3)	4.81
• Rocketdyne (14% Y_2O_3, 7% SiO_2)	7.42
C. Reaction Sintered Si_3N_4	
• Norton NC-350 RS-Si_3N_4 (1976)	0.84
• Kawecki-Berylco RS-Si_3N_4	1.14
• Ford Injection Molded RS-Si_3N_4	1.39
• AiResearch Slip-Cast RS-Si_3N_4 (Airceram RBN-101)	1.26
• Raytheon Isopressed RS-Si_3N_4	1.65

TABLE 8 (cont.)

Material	Oxygen, wt%[a]
C. Reaction Sintered Si$_3$N$_4$ (cont.)	
• Indussa/Nippon Denko RS-Si$_3$N$_4$	0.85
• AiResearch Injection Molded RS-Si$_3$N$_4$ (Airceram RBN-122)	1.75
• Norton NC-350 RS-Si$_3$N$_4$ (1977 As-fired)	1.02
• Norton NC-350 RS-Si$_3$N$_4$ (1979 Vintage)	0.89
• Annawerk Ceranox NR-115H RS-Si$_3$N$_4$	2.29
• Associated Engineering Development, Ltd. Nitrasil RS-Si$_3$N$_4$	1.15
• Georgia Tech RS-Si$_3$N$_4$	1.74
• AME RS-Si$_3$N$_4$	2.66
• AiResearch RBN-104 RS-Si$_3$N$_4$	1.48
D. SiC Materials	
• Norton NC-435 Siliconized SiC	0.34
• General Electric Boron-Doped Sintered β-SiC	0.02-0.10
• Carborundum Sintered α-SiC	0.01
• UKAEA/British Nuclear Fuels Refel Si/SiC (siliconized)(diamond ground and as-processed)	0.01-0.02
• Ceradyne Ceralloy 146A, HP-SiC (2% Al$_2$O$_3$)	0.49
• Ceradyne Ceralloy 146I, HP-SiC (2% B$_4$C)	1.28
• Norton NC-203 HP-SiC (∿2% Al$_2$O$_3$)	1.27-1.31
• Norton NC-430 Si/SiC	0[b]
• Coors Siliconized SiC	0.03
• Chemetal CNTD SiC Coating	0.05
• Kyocera Sintered α-SiC	0.05
• ESK Sintered α-SiC	0.05
• GE Silcomp Si/SiC Composite	c
• Coors 1982 SC-2 Si/SiC	c

[a]Measured at USAMMRC by neutron activation analysis.

[b]Below limit of detection.

[c]Submitted to AMMRC for measurement.

5. TEST METHODOLOGY

The test methodology employed on this program follows standard methods and procedures that are used widely throughout the technical ceramic industry.

5.1 REFLECTED LIGHT MICROSCOPY

The goal of microstructural analysis is to reveal the grain size and shape, the amount and distribution of any porosity, and the existence of any highly reflective metal inclusions (impurity particles). This is done by reflected light examination of as-received samples that have been polished and etched to reveal the microstructural features.

Samples of the SiC and Si_3N_4 materials were prepared for optical microscopy by rough grinding through 220, 360, and 600 grit diamond-bonded metal disks using water as a lubricant.[a] They were ultrasonically cleaned between every stage of preparation. Rough polishing was done on chemotextile lap coverings through 9, 6, and 1 μm diamond pastes using a water-base extender. In general, a 0.25 μm diamond micropolishing stage concluded the preparation. However, a final polishing with 0.3 μm α-Al_2O_3 instead of the diamond paste was found to be useful for some of the silicon-densified forms of SiC. The various etching procedures used for the hot-pressed, sintered, and siliconized forms of SiC are summarized in Table 9. The various etching procedures used for the hot-pressed and sintered silicon nitride materials are summarized in Table 10. Etched samples were cleaned and examined with a Leitz MM-5px metallograph.

---

[a] Procedures for the zirconia materials are discussed in Section 12.

TABLE 9.   SUMMARY OF MICROSTRUCTURAL ANALYSIS ETCHING PROCEDURES
FOR HOT-PRESSED, SINTERED, AND SILICONIZED SiC

Material	Etching Procedure
Hot-Pressed and Sintered α-SiC	Boiling Murikami's reagent (60 g KOH + 60 g $K_3Fe(CN)_6$ + 120 ml H_2O) 3 to 10 min to preferentially reveal α-α and α-β grain boundaries.[19]
Sintered β-SiC	A fused salt mixture of 90 wt% KOH + 10 wt% KNO_3 at 450°C, 30 sec to 1.5 min to reveal β-β grain boundaries.[19] May be used in conjunction with the Murikami's reagent etch.
Siliconized SiC	An electrolytic etch of 20% KOH in distilled water using direct current, 6 V at 1 amp for 2 to 4 min.[20]

TABLE 10.   SUMMARY OF MICROSTRUCTURAL ANALYSIS ETCHING PROCEDURE
FOR HOT-PRESSED AND SINTERED Si_3N_4

a)   A chemical etch of 7:2:2 concentrated H_2SO_4:HF:NH_4F solution in a Pt container at 300°C for times from 0.5 to 11 min.[21]

b)   HCl swabbed onto surface at room temperature for normally 20 to 60 sec (up to 5 min for some materials).[22]

c)   Boling phosphoric/sulfuric acid (3:1) for 6 hr.[23]

d)   A solution of 100 ml H_2O + 8 ml HF + 8 g $NaHF_2$ + 1 ml H_2O_2 at 80°C for 1 to 1.5 min.[24]

5.2 FLEXURAL STRENGTH AND ELASTIC MODULUS

Flexure strength was determined in the quarter 4-point configuration on test samples that were of nominal dimensions 1/8 x 1/4 x 2 1/4 inch. Test samples were usually supplied diamond ground or as-nitrided by the manufacturer (refer to Table 2). All samples were corner chamfered. All machined samples were diamond ground in the longitudinal direction, i.e., parallel to the tensile axis of the bend bar.

Unless otherwise indicated, the upper and lower spans were 0.875 and 1.750 in., respectively.[*] For room-temperature tests, a stainless steel fixture was used. The upper pins were independently free to adjust for any taper across the sample width. The entire upper carrier was free to adjust for any taper along the sample length. Loads were applied in an Instron Universal test machine at a crosshead rate of 0.02 in/min. Elastic modulus was obtained using a 120 Ω foil strain gage applied at the center of the specimen on the tension side. Prior to load application, the alignment was checked visually by inspecting for any light gap between specimen surface and pin. Alignment is also checked by attempting to move the upper pin carriers with gentle pressure of the hand. If the pin is squarely on the specimen surface, movement is not possible.

The outer fiber tensile stress was computed from simple elastic beam theory. Using the nomenclature shown in Figure 1, the lower span is L, the upper span is L/2, and the load applied is P. The outer fiber tensile stress for the bar in bending is

$$\sigma = \frac{Mc}{I} \qquad (1)$$

---

[*]A few samples tested were only 1.25 in. long. The upper and lower spans in these cases were 0.500 and 1.000 inch, respectively.
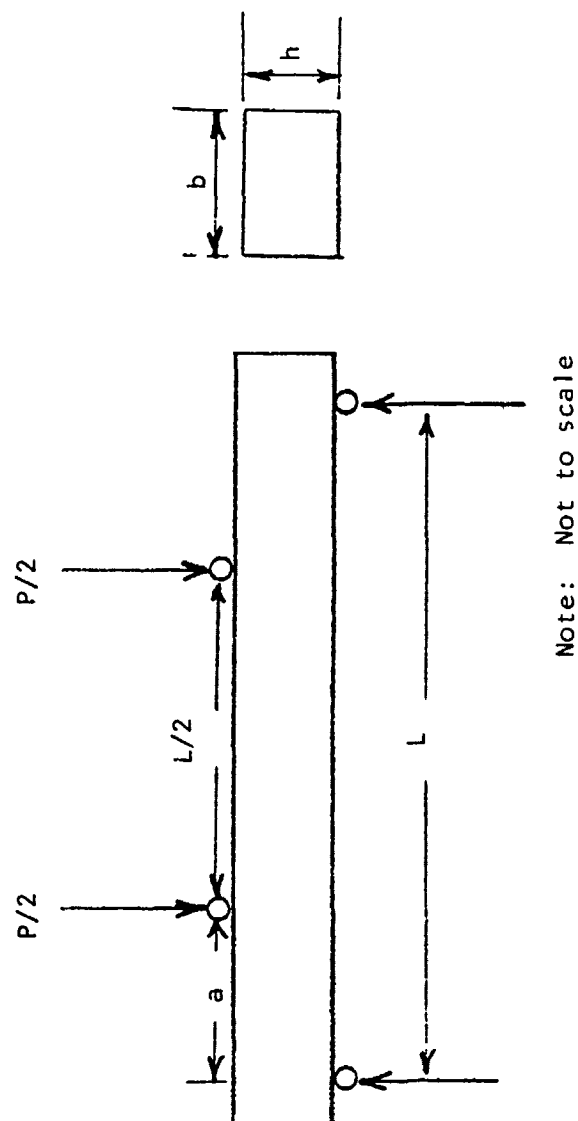
Figure 1. Quarter 4-point flexure configuration.

Note: Not to scale

where σ = outer fiber tensile stress (flexure stress)

M = bending moment = $Pa/2$

a = $L/4$ for the quarter 4-point configuration

c = distance from the specimen neutral axis to the outer tensile fiber = $h/2$

I = moment of inertia of the specimen cross-section about the neutral axis = $bh^3/12$

Substituting:

$$\sigma = \frac{3Pa}{bh^2} \tag{2}$$

High temperature flexure tests were conducted in an IITRI designed and constructed SiC-element furnace which was rolled in and out of an Instron load frame. The furnace was equipped with a shuttle to move specimens into test position while the furnace was at temperature, and with several access ports to permit manipulation of the specimen and fixtures. The fixturing is unique in that it provides for some degree of self-alignment at temperatures up to 1500°C. The system is shown schematically in Figure 2. Photographs of various parts of the fixturing are shown in Figure 3. Silicon carbide pins are fixed to the saddle fixture (refer to Figure 2). The specimen is pushed onto the saddle fixture using the Al_2O_3 alignment pins to center the specimen. The top load rod/upper load fixture assembly is then lowered into position with the aid of the Al_2O_3 alignment pins. The upper load fixture (upper span) allows alignment in two directions through the use of the key/side plate method of attachment to the top loading rod (see Figure 3). The top loading rod applies a line contact load to the upper fixture load pin. Outside the furnace, alignment is further attained through the use of hemispherical load platens located between the loading rod and the Instron movable crosshead. Fixtures are made with a combination of materials, mostly various commercially available forms of silicon carbide.

31
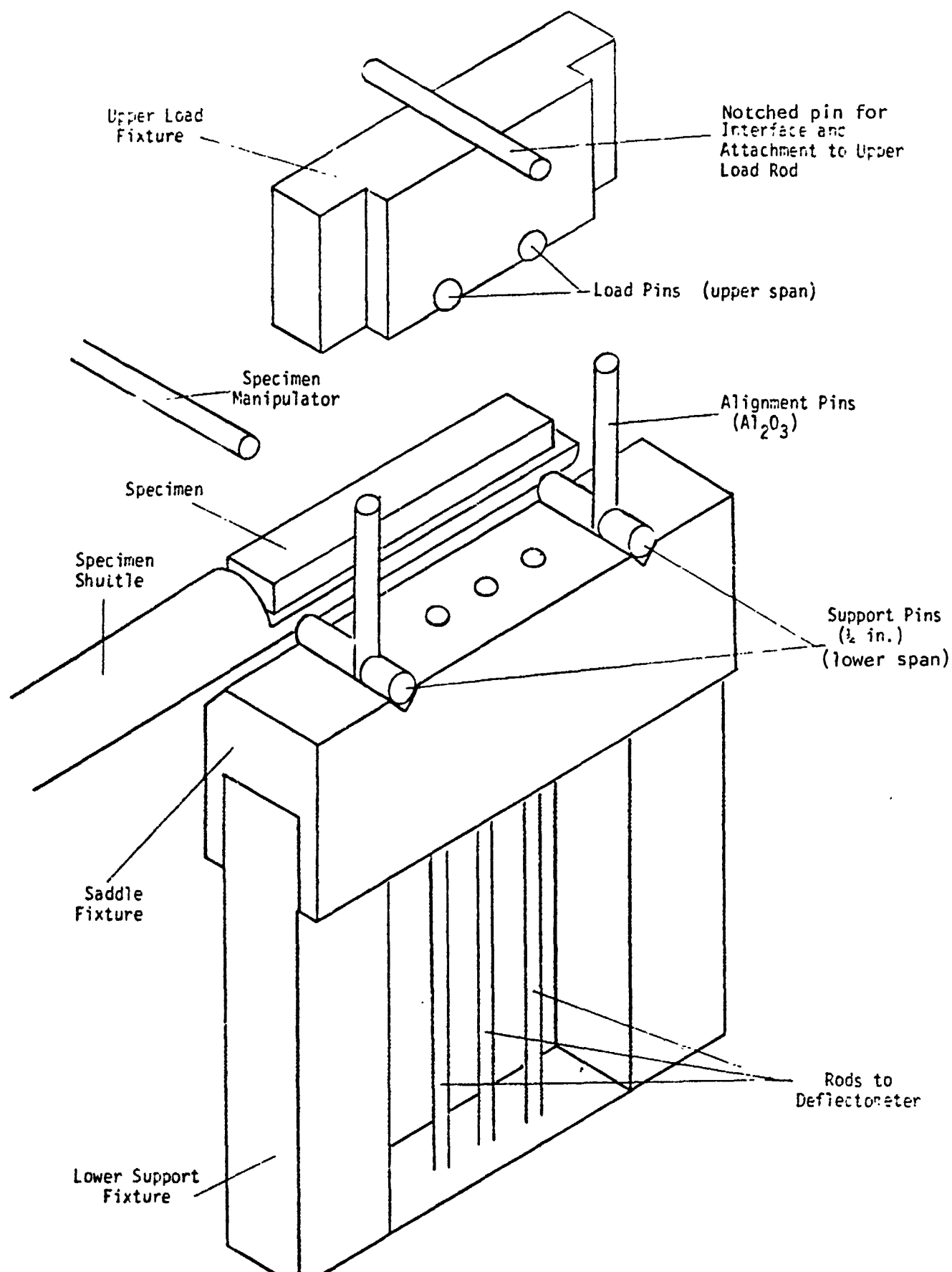
Figure 2. Schematic of high-temperature flexure apparatus.
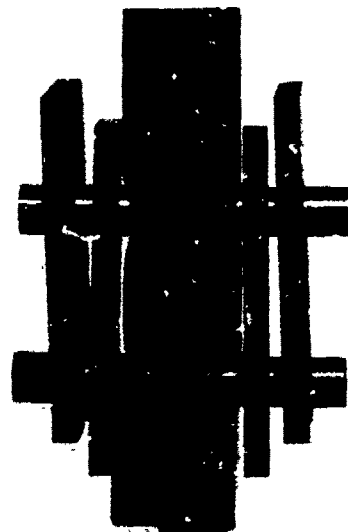
(a)   (b)

Front and side views of upper load fixture and loading rod. Load is applied
to pin at top of upper load fixture. Keys and side plates allow alignment
in two directions while providing attachment to load rod.
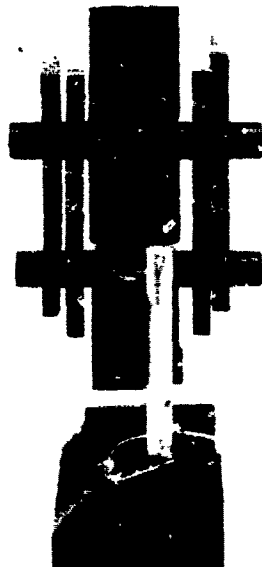
(c)   (d)

Front and side views of top load rod/upper load fixture assembly being
lowered onto saddle fixture.

Figure 3.   Various views of silicon carbide flexure fixturing.

33

Elevated temperature flexural deformation was recorded continuously using the IITRI-designed and built 3-point electromechanical deflectometer shown in Figure 4. The three deflectometer rods (KT-SiC, Al_2O_3, or sapphire) contact the tensile surface of the bend bar within the region of pure bending. Accounting for test fixture deformation is not necessary, since the test sample deformation is measured directly from the relative movement of the center rod with respect to the mean position of the two outer rods, giving $\Delta\delta$, the beam deflection, which is related to the outer fiber tensile strain. From simple beam theory,[25] with reference to Figure 4, the maximum deflection at the center of the beam, δ_{max}, is

$$\delta_{max} = \frac{Pa}{48EI} (3L^2 - 4a^2) \tag{3}$$

The deflection at the outer deflectometer rod, δ_x is

$$\delta_x = \frac{Pa}{12EI} [3Lx - 3x^2 - a^2] \tag{4}$$

The sample deformation $\Delta\delta = \delta_{max} - \delta_x$ is the difference in these two deflections

$$\Delta\delta = \frac{Pa}{4EI} [\frac{1}{4}L^2 - Lx + x^2] \tag{5}$$

The heart of this deflectometer is a DC-DC displacement transducer* having 10^{-5} in. resolution. This device is an integrated package consisting of a precision linear variable differential transformer, a solid state oscillator and a phase-sensitive demodulator. The output of this high linearity, high resolution, high sensitivity transducer is a DC voltage proportional to the displacement of the axial core (center deflectometer rod) within a coil assembly (attached to outer two

---

*Trans-Tek Series 240.

34
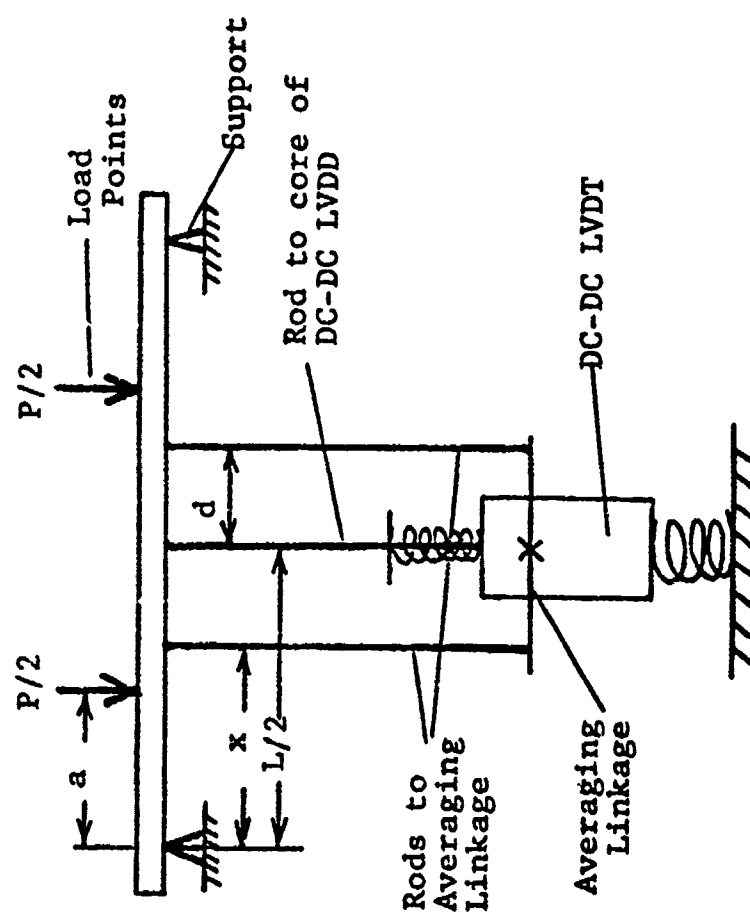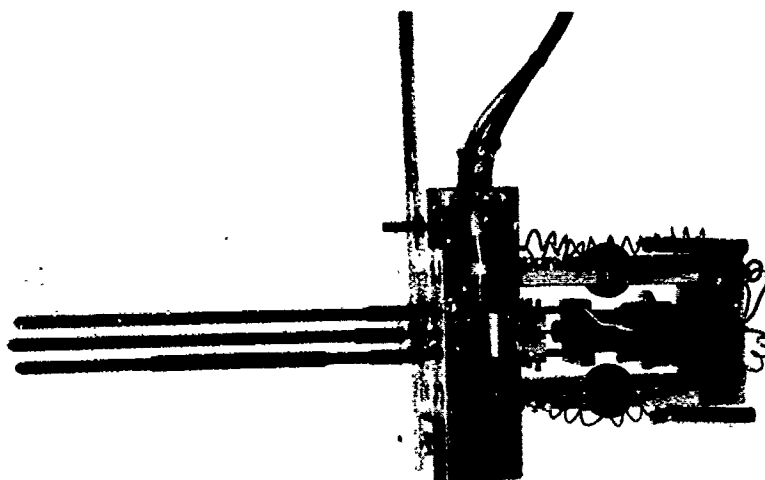
Figure 4. Electromechanical deflectometer for direct measurement of flexural specimen strain.

35

deflectometer rods). The entire deflectometer was calibrated with a high-precision micrometer head with resolution to 10^{-5} in. Use of this deflectometer system in conjunction with the Instron load cell permits recording of continuous load-deflection curves, which are then used to construct stress-strain curves.

5.3 CREEP AND STRESS RUPTURE

Creep rates were measured in 4-point bending at temperatures up to 1500°C in air. The stepwise method was used, with deformation continuously recorded using the 3-point electromechanical deflectometer described above. Samples were tested at various incremental stress levels, with enough time spent at any given level to obtain stage 2 (secondary) creep (maximum of 24 hr at any stress level). Deadweight loading was employed. Testing continued for 3-4 stress steps per sample. Testing of approximately three samples in this manner permitted the steady-state stress dependence of the creep rate to be assessed for each material studied. The interior of the creep test rig, showing the SiC fixturing, is presented in Figure 5.

Static fatigue tests were conducted on a stress rupture apparatus with deadweight loading. A photograph is provided in Figure 6. The sample was loaded at constant stress, and the time to failure was recorded.

Dynamic fatigue testing has also been used on this program. These tests are often referred to as differential strain rate flexure tests, and are conducted on an Instron universal test machine. The stressing rate (i.e., crosshead speed) was varied to give a range of sample failure times. The resulting strength-time curve is analyzed like a static fatigue or stress rupture curve, i.e., by linear least-squares curve fitting analysis.

5.4 DYNAMIC ELASTIC MODULI

A flexural sonic resonance technique was used to measure the dynamic Young's elastic modulus. The apparatus conforms to that

36
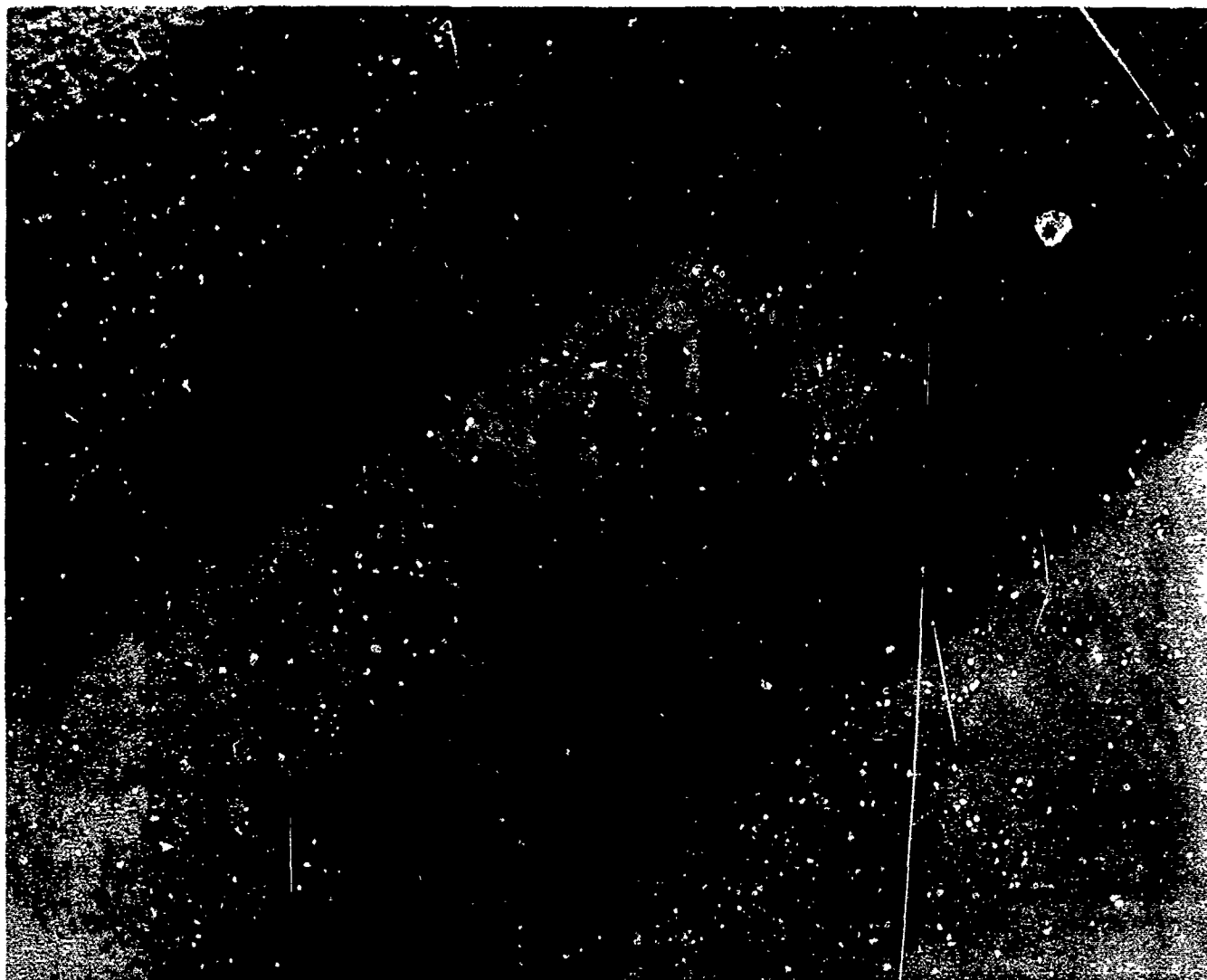
Figure 5.   SiC flexural creep deflection fixturing for use
at 1500°C in air.
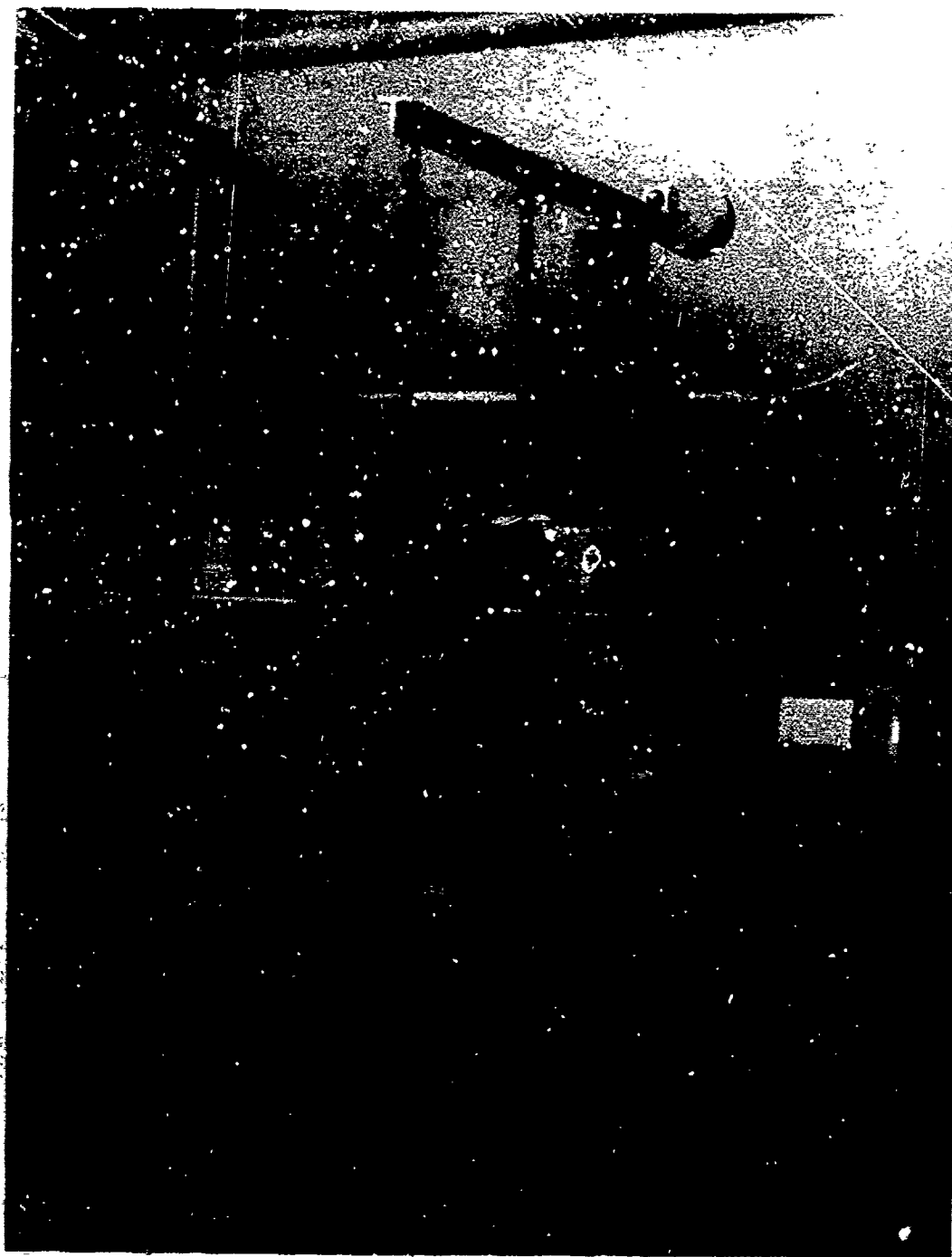
Figure 6.   Stress-rupture furnaces for use
at 1500°C in air.

described by Spinner and Tefft,[26] which is the accepted standard of the industry. An oscillator (sonic frequency) signal was fed to a power amplifier, which energized a piezoelectric driver. The driver frequency was measured with a frequency counter. The mechanical vibration was transmitted to and from the sample by suspending it from the driver and pickup transducers. Cotton thread worked well at room temperature while platinum/rhodium wire may be used at elevated temperature. The pickup signal was amplified and detected on a meter and/or as a maximum in the Lissajou pattern on an oscilloscope.

Suspending a flexure bar of nominal dimensions 0.090 x 0.250 x 2.500 in. from points just adjacent to the flexural nodal points permitted detection of the flexural resonant frequency, and subsequent computation of the dynamic Young's moduli from the relation[26]

$$E = \frac{0.94642}{386.09} \quad \frac{\rho L^4 f^2 T}{t^2} \tag{6}$$

where E = Young's elastic modulus for flexural resonance of a prism of rectangular cross-section, psi

ρ = density, lb in.$^{-3}$

L = sample length, in.

f = flexural resonant frequency (fundamental mode), Hz

t = sample thickness, in.

T = correction and shape factors given by Spinner and Tefft.[26]

Similarity, if a wider sample is used, e.g., .090 x 1.000 x 2.500 in., the sample can be suspended from opposite corners, and torsional as well as flexural vibrations induced.[26] This is mentioned because it is a relatively easy way to obtain Poisson's ratio for ceramics. The shear modulus is given by the relation

$$G = \frac{4f^2 \rho R L^2}{386.09} \tag{7}$$

39

where   G = shear modulus for torsional resonance

         f = torsional fundamental resonant frequency

         R = shape factor[26]

Poisson's ratio, μ, is computed from the Young's and shear moduli using the relation:

$$\mu = \frac{E}{2G} - 1 \tag{8}$$

5.5 THERMAL SHOCK/INTERNAL FRICTION

Thermal shock resistance was determined on this program by the water quench method, with the initiation of thermal shock damage being detected by internal friction measurement. This technique was chosen not in an attempt to simulate in-service engine conditions, but rather as a relative ranking of candidate materials in severe thermal down-shock. In conducting this test, internal friction was measured before and after water quench from successively higher temperatures using the flexural resonant frequency Zener bandwidth method. A marked change in internal friction (specific damping capacity) indicated the onset of thermal shock damage (i.e., thermal stress-induced crack initiation). This defined the critical quench temperature difference, ΔT_c, which was compared to analytical thermal stress resistance parameters.

Zener[27] and others[28-30] have provided excellent reviews of internal friction. Hookean elastic theory implies a direct and instantaneous linear relation between low level force application and resultant deformation. However, as the rate of loading and unloading is increased, there appears a phase lag between stress and strain which results in the absorption of energy. This time-dependent elastic behavior is termed anelasticity. Internal friction may be defined as the amount of energy absorbed during deformation compared to the maximum amount of energy applied initially. As the number and extent of flaws in a body

40

increases, the amount of energy absorbed through flaw surface friction, plastic zone dislocation motion, etc., also increases. Thus, the internal friction is an integrated effect, the measurement of the total flaw spectrum in a material.

On the present program, test samples were suspended from piezoelectric drive and pickup transducers as described above for dynamic elastic modulus measurement. Using a Hewlett-Packard spectrum analyzer,[*] the frequency range just adjacent (above and below) the fundamental resonant frequency was scanned. The Zener bandwidth[27] method involves computing the internal friction, Q^{-1}, from the measured peak width at half maximum amplitude:

$$Q^{-1} = \frac{\Delta f}{\sqrt{3}\ f} \tag{9}$$

where Q^{-1} = internal friction

   f = resonant frequency

   Δf = peak width at half amplitude

The concept is illustrated in Figure 7. This method is useful for measuring the range of internal friction normally found in ceramic materials (10^{-2} to 10^{-6}).

5.6 THERMAL EXPANSION

Thermal expansion was measured from ambient room temperature to 1500°C using a NETZSCH automatic recording single pushrod dilatometer. Samples of nominal dimensions 1/4 x 1/8 x 2 in. were temperature cycled in air at 1°C/min from 25° to ~200°C, and at 5°C/min from 200° to 1500°C. The cooling rate was approximately 5°C/min. Sample length changes were continuously recorded during both heating and cooling cycles with a precision LVDT system exhibiting 1 micron resolution. The apparatus is illustrated in

---

[*]Model No. 3580A.

41

Internal Friction
for Thermal Shock Analysis

	f, Hz	Δf, Hz	Q^{-1}
Unshocked	6176.4	1.63	1.52×10^{-4}
Thermal shocked	6011.9	9.62	9.24×10^{-4}

$\rightarrow$ 1 Hz $\leftarrow$

Amplitude

Unshocked

Thermal Shocked
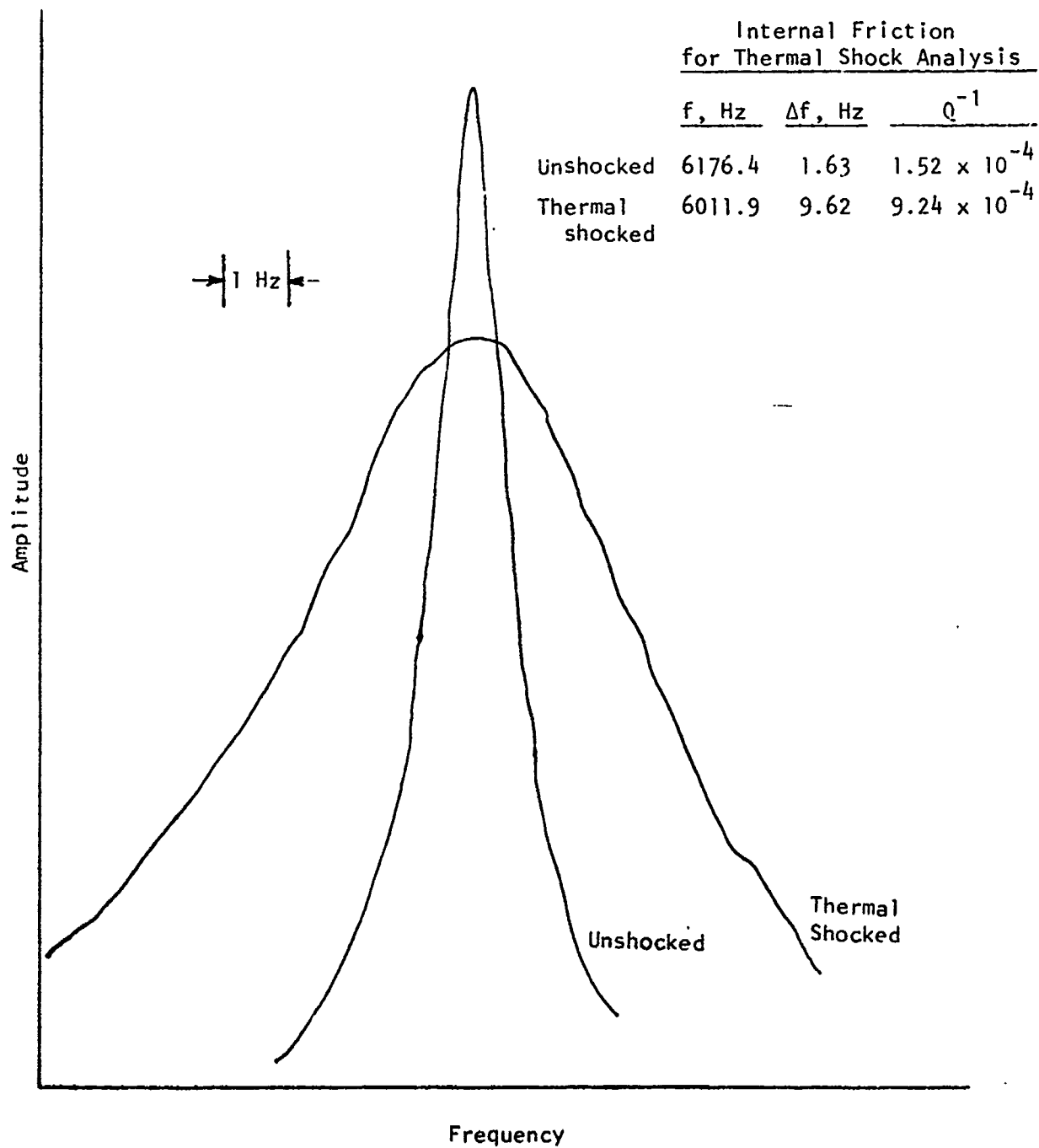
Frequency

Figure 7. Typical amplitude-frequency curves of unshocked and thermal shocked ceramics for internal friction measurement.

Figure 8. A tungsten standard reference material[*] was used to calibrate the system. The data were reported as percent linear expansion vs. temperature. From these data, any average or instantaneous coefficient of expansion can be computed.

5.7 THERMAL DIFFUSIVITY

Thermal diffusivity is defined as the ratio of the thermal conductivity to the density-specific heat product. The thermal diffusivity was measured in air at 25°C, and at various temperatures from 1000° to 1500°C. The sample was contained in an IITRI-built molybdenum wire-wound zirconia tube furnace with a porous zirconia sample holder. The laser pulse method[31] was employed. The front face of the disk-shaped sample (9/16 in. dia. x 0.050 in. thick) was irradiated with a single pulse of laser energy (25 joule pulse at 6943 Å, 500 μsec pulse duration),[§] and the resulting sample back face temperature transient recorded. A liquid nitrogen-cooled indium antimonide detector[**] was used to detect the temperature response at 25°C, and a biased silicon photodiode[§§] was used at elevated temperatures. The general apparatus is shown in Figures 9 and 10, and a typical rear face temperature response is shown in Figure 11. Initial time, t_o, for the measurement was determined when lasing occurred through the use of an auxiliary photodiode system monitoring the ruby laser performance.

Thermal diffusivity, α, was computed from the expression:

$$\alpha = \frac{0.1388 \; L^2}{t_{1/2}} \tag{10}$$

---

[*]NBS SRM NO. 737.

[§]Korad pulsed ruby laser, Model K1.

[**]Texas Instruments, ISV 3105

[§§]EGG SGD-100-A.

43
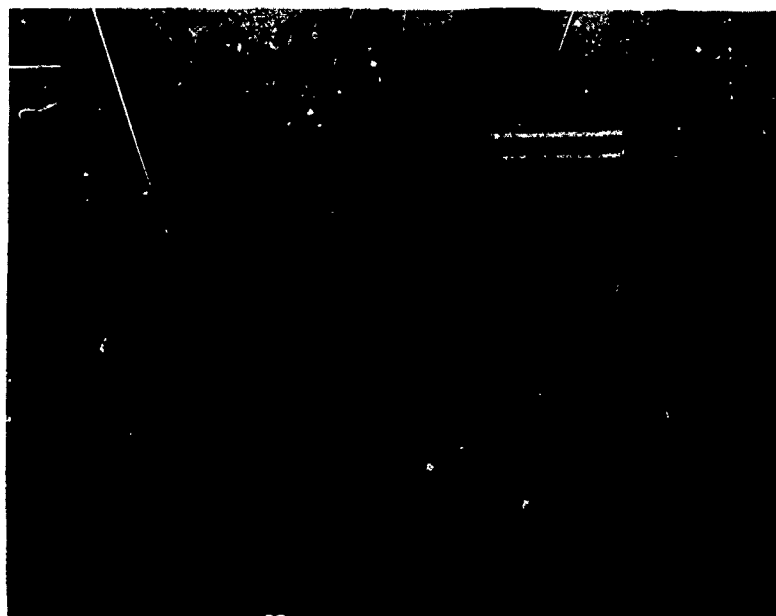
Figure 8. Thermal expansion apparatus.
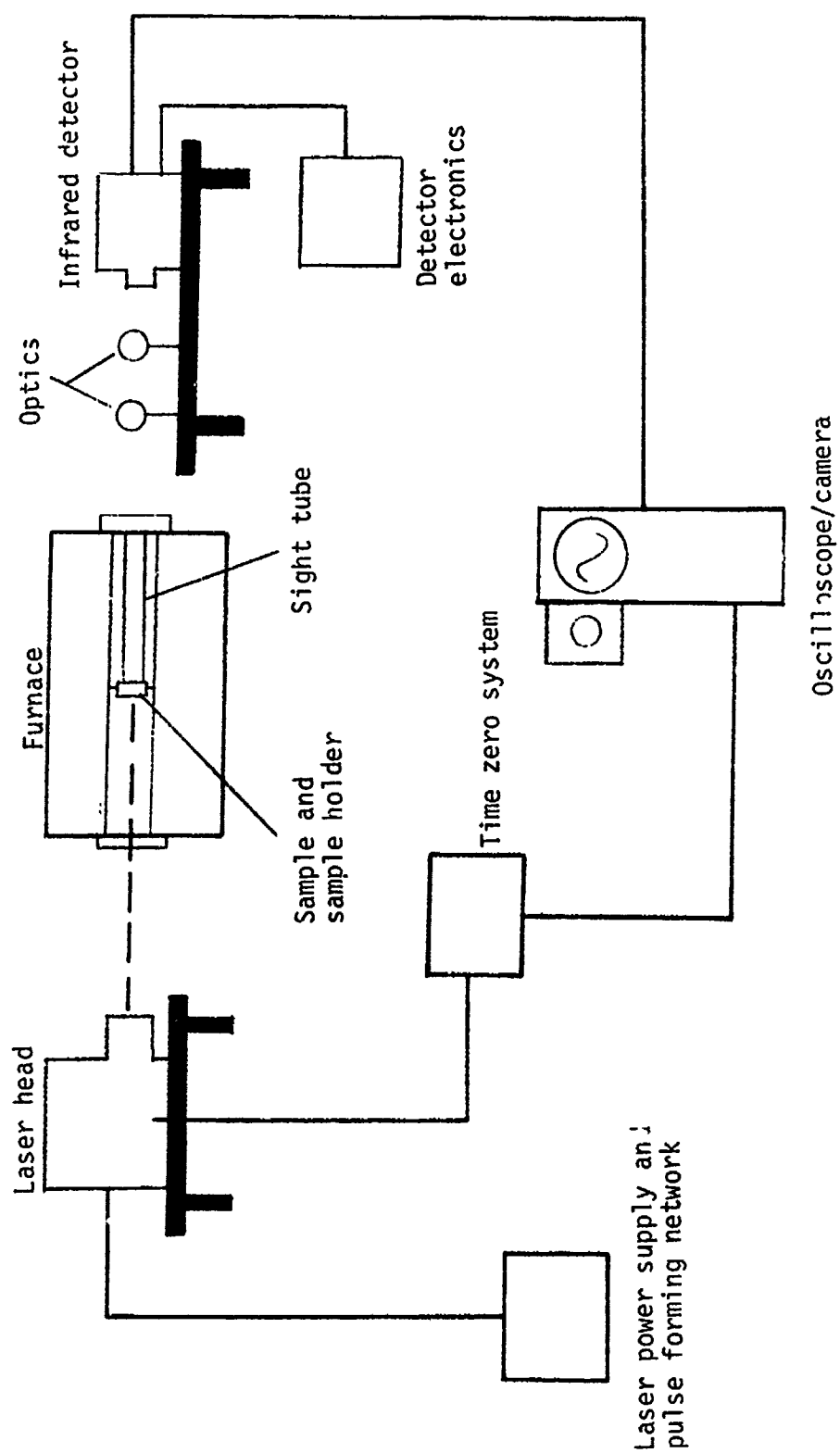
Figure 9. Schematic of laser flash thermal diffusivity method.
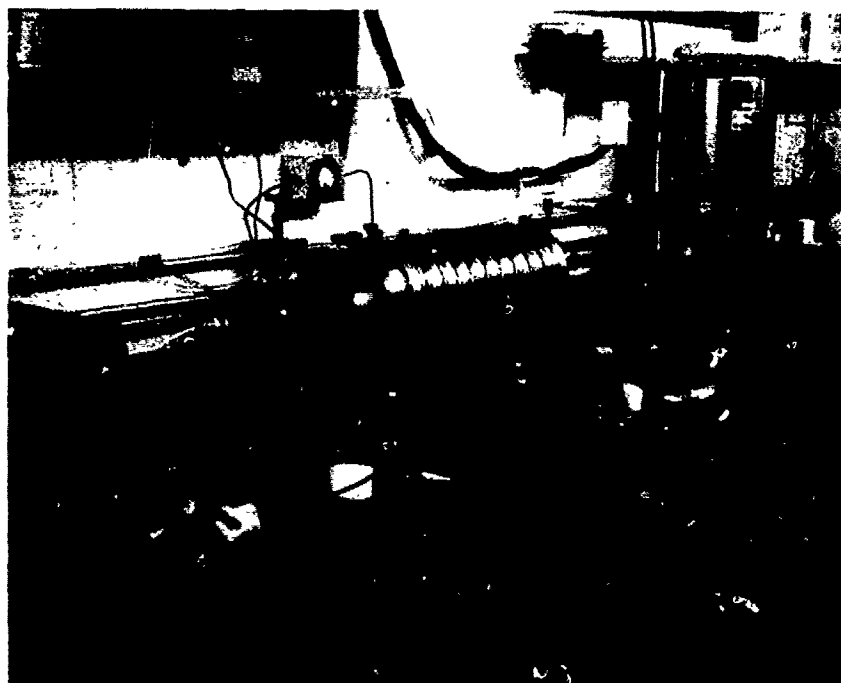
Figure 10.   Thermal diffusivity apparatus.
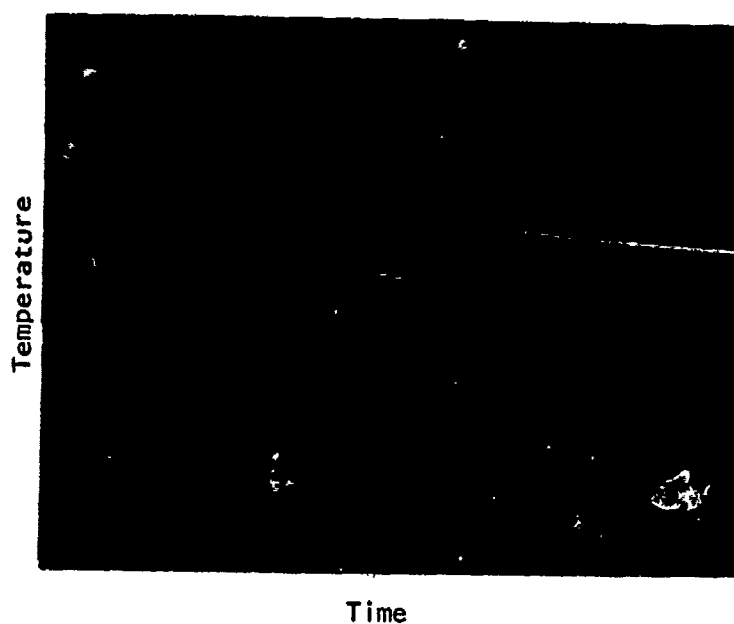
Time

Figure 11.   Temperature transient for
thermal diffusivity measurements.

where   L = sample thickness, cm

$t_{1/2}$ = time for rear face temperature to reach
half its maximum value.

If the laser pulse width is not small compared to the characteristic transit time through the sample, a correction must be applied to account for the resulting finite pulse time effect. This usually occurred for high density, high thermal diffusivity silicon carbide tested at low temperature. In that case the finite pulse time correction[32-34] was applied to the data using the relation:

$$\alpha = \frac{(0.3155)L^2}{(2.273)t_{1/2} - \tau} \qquad (11)$$

The term τ is the pulse width, and this relationship applies for $t_{1/2}/t_c < 1.8$, t_c being the sample characteristic rise time:

$$t_c = \frac{L^2}{\alpha \pi^2} \qquad (12)$$

One of the boundary conditions employed to obtain the ideal analytical solution to this experiment is that there are no heat losses from the specimen surfaces that would alter the shape of the temperature transient. This boundary condition is often violated by radiation losses at high temperatures. Taylor[34] discusses a convenient correction for this effect based on Cowan's original work.[35] This correction involves comparison of the shape of the experimentally obtained temperature transient at times out to ~$10t_{1/2}$ to the shape of the ideal rear face temperature transient obtained from the ideal analytical solution (the general shape of the rear face temperature transient is independent of sample thermal diffusivity). The correction was applied to all data generated on this program above 800°C.

6. MICROSTRUCTURE, ROOM-TEMPERATURE STRENGTH, AND ELASTIC PROPERTIES

The room temperature strength and fracture mode of silicon-base ceramics are determined by the microstructural features of grain size and shape, the size and distribution of porosity, and the nature of the particular processing defects (or machining flaws) that cause fracture (i.e., the type of defect, and its size and shape). The elastic properties are determined by the nature of the atomic bonding in the basic system.

6.1 Si_3N_4 MATERIALS

Silicon nitride materials are processed by hot-pressing, sintering, and reaction sintering. The highest strengths are achieved with HP-Si_3N_4, the use of pressure-assisted consolidation and oxide additives (MgO, Y_2O_3, CeO_2, ZrO_2) resulting in nearly fully dense materials. Pressureless sintering also involves the use of oxide densification aids. Densities and strengths are somewhat lower than for hot-pressed forms. Reaction sintered Si_3N_4 is processed by nitridation of precompacted silicon powder. This process results in a relatively porous body (up to 20% porosity), with correspondingly lower strength.

6.1.1 Microstructural Features

The microstructures of the various hot-pressed Si_3N_4 materials evaluated on this program are presented in Figure 12. These micrographs were generally obtained from polished/etched sections viewed in reflected light. The micrographs for the various sintered Si_3N_4 materials are presented in Figure 13.[*]

---

[*]The results for the highly developmental sintered SiAlON materials from the U.S. Bureau of Mines are presented in Reference 36.

48

(a) Norton NC-132 (1% MgO) etched 6 min.

(b) Replica TEM micrograph of Norton
NC-132 (1% MgO). Courtesy of
K. S. Mazdiyasni, AFWAL.

Figure 12. SEM micrographs of polished and
etched hot-pressed silicon nitride mate-
rials (Etchant: 7:2:2 H_2SO_4/HF/NH_4F
etchant shown in Table 10).

(c) Norton NCX-34 (8% Y_2O_3) etched 6 min.
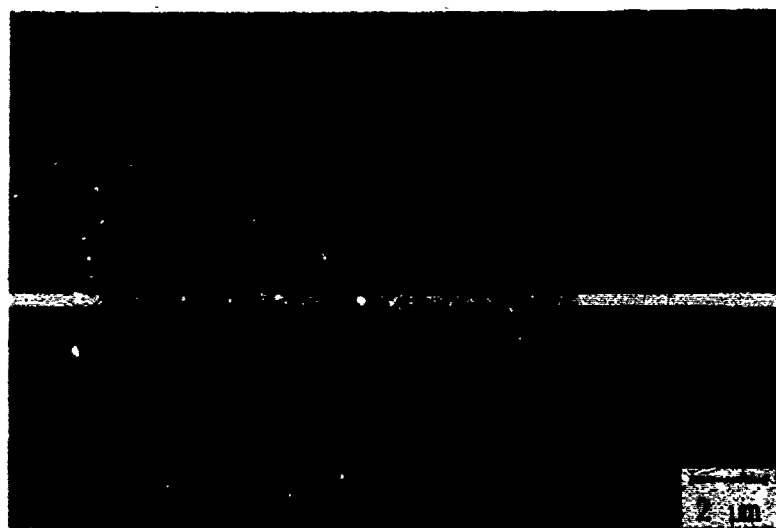
(d) Harbison-Walker (10% CeO_2) etched 3.5 min.

Figure 12 (cont.)

(e) Kyocera SN-3 (4% MgO, 5% Al$_2$O$_3$) etched
15 sec at room temperature.
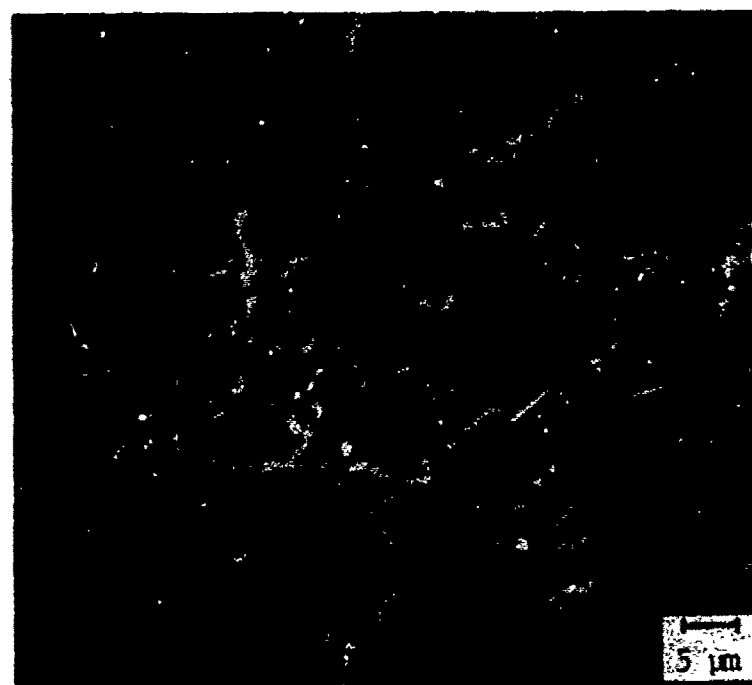
(f) Ceradyne Ceralloy 147A (1% MgO) etched
10 min.

Figure 12 (cont.)

(g) Ceradyne Ceralloy 147Y (15% Y_2O_3) etched 6 min

(h) Ceradyne Ceralloy 147Y-1 (8% Y_2O_3) etched 7 min

Figure 12 (cont.)

52
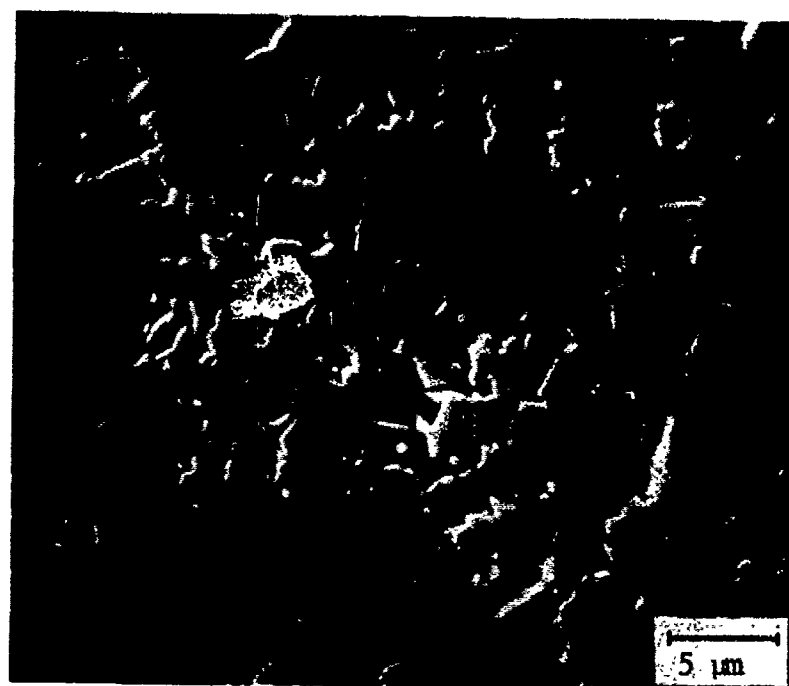
(i) Fiber Materials, Inc., (4% MgO)
etched 11 min

(j) Westinghouse (4% Y_2O_3, SiO_2)
etched 5 min

Figure 12 (cont.)

53
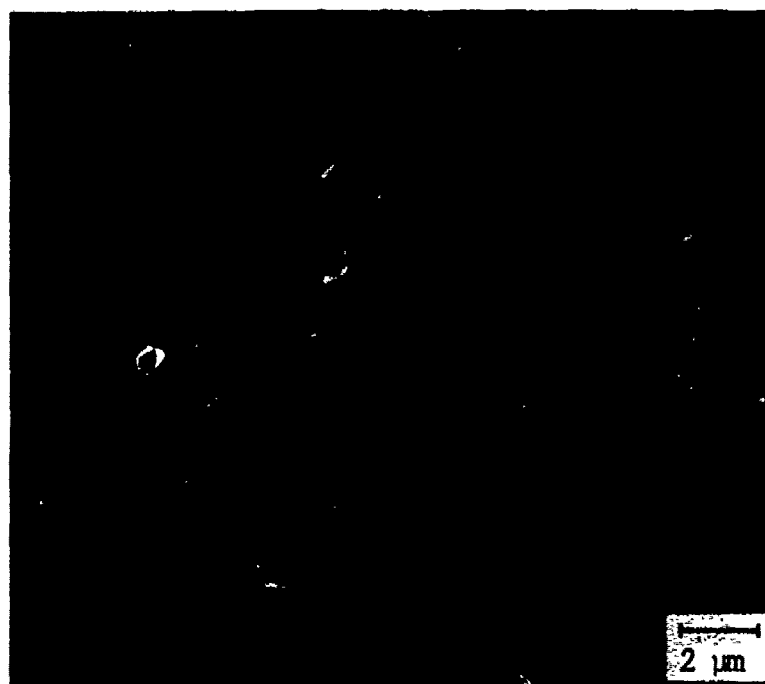
(k) Toshiba (4% Y_2O_3, 3% Al_2O_3)
    etched 0.5 min
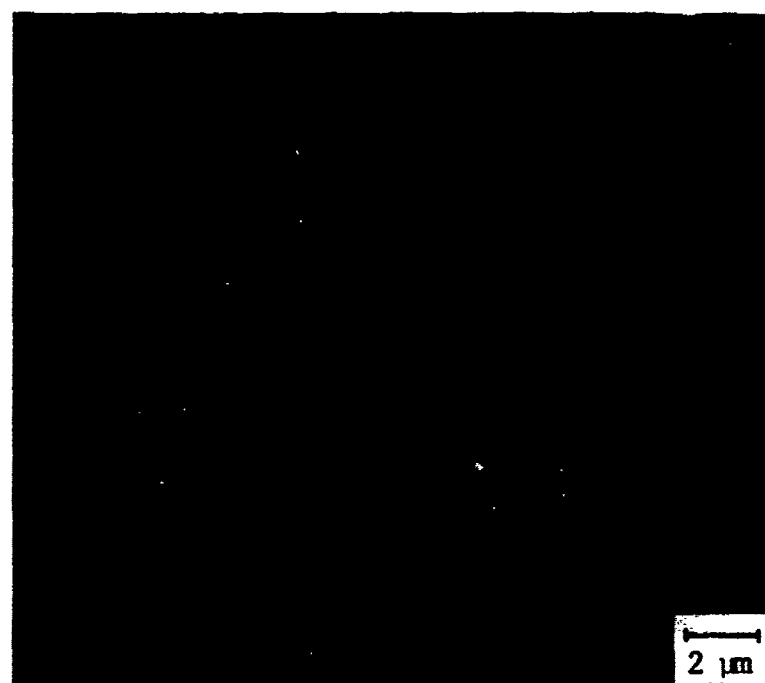
(1) Toshiba (3% Y_2O_3, 4% Al_2O_3, SiO_2)
    etched 0.75 min

Figure 12 (cont.)

54

(m) NASA/AVCO/Norton (10% ZrO_2)
etched 2.5 min

(n) Battelle HIP-Si_3N_4 (5% Y_2O_3) etched
2.5 min

Figure 12 (cont.)
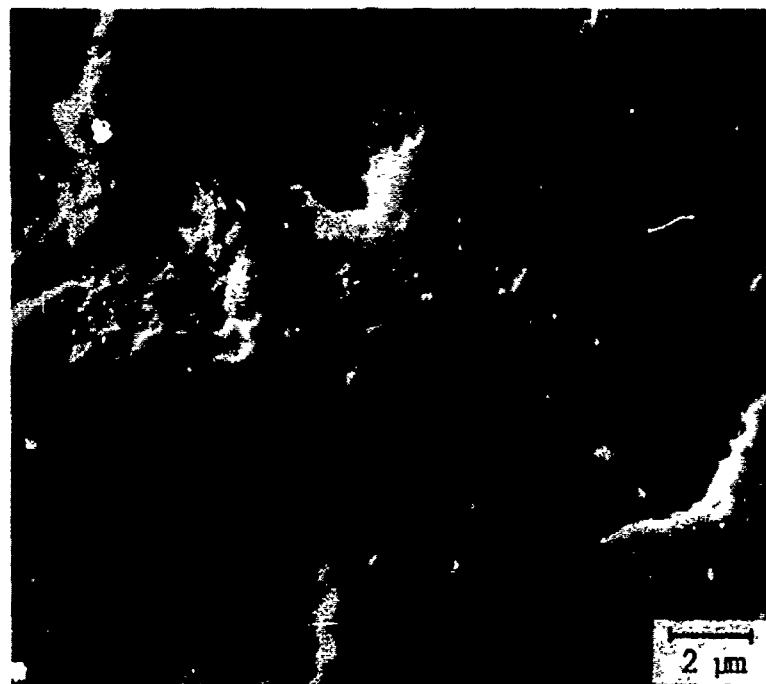
(a) Kyocera SN-205 (5% MgO, 9% Al$_2$O$_3$)
etched 55 sec[a]
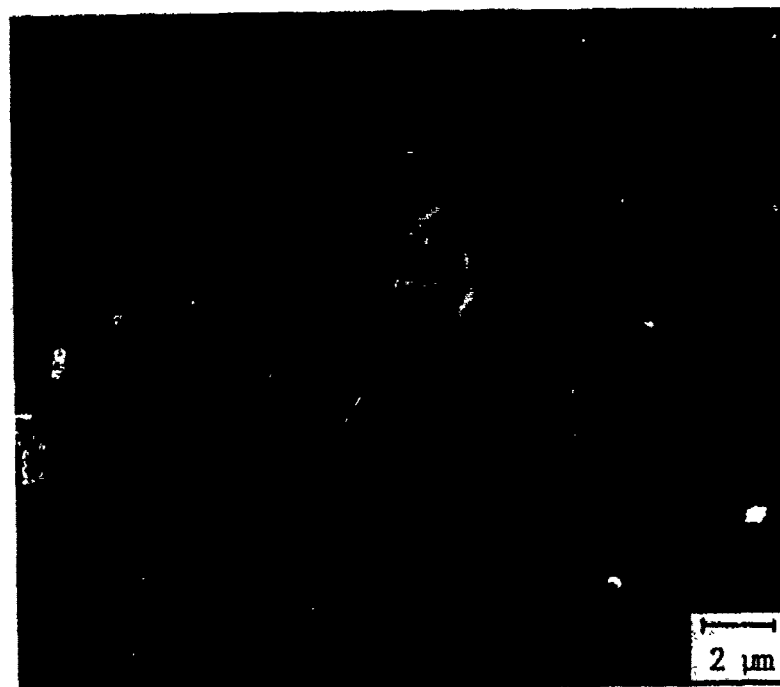
(b) Kyocera SN-201 (4% MgO, 7% Al$_2$O$_3$)
etched 35 sec[a]

Figure 13.   SEM micrographs of etched sintered
silicon nitride materials.
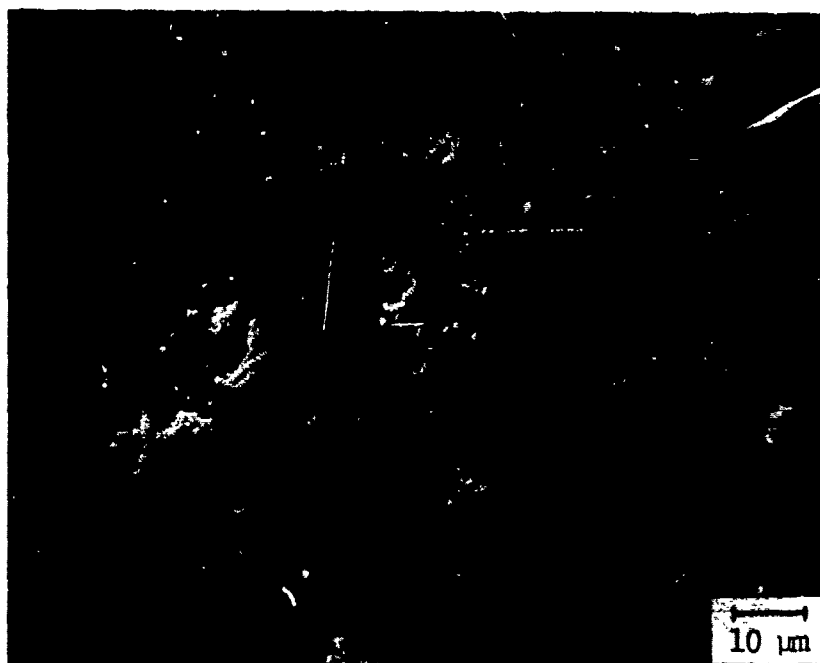
(c) GTE Sylvania (6% Y_2O_3) etched 6 hr[b]

(d) AiResearch (8% Y_2O_3, 4% Al_2O_3)
etched 5 min[c]

Figure 13 (cont.)

(e) Rocketdyne SN-50 (6% Y_2O_3, 4% Al_2O_3) etched 9.5 min[c]

(f) Rocketdyne SN-104 (14% Y_2O_3, 7% SiO_2) etched 6 min[c]

Figure 13 (cont.)

[a] $H_2SO_4/HF/NH_4F$ shown in Table 10.
[b] HCl etch shown in Table 10.
[c] 3:1 Phosphoric/sulfuric acid etch shown in Table 10.
[d] $H_2O/HF/NaHF_2/H_2O_2$ etch shown in Table 10.

These micrographs reveal grain size and shape, as well as the location of any porosity. The microstructure of reaction-sintered Si_3N_4 materials was evaluated by slightly different means. There is no significant intergranular phase in RS-Si_3N_4 that can be readily etched to reveal grain size and shape. Thus, the major features observed in the microstructural analysis of RS-Si_3N_4 materials are the size and distribution of porosity and the existence of any free silicon metal. Pores and pore agglomerates are often identified as the fracture origins in RS-Si_3N_4. Accordingly, polished sections were prepared of all RS-Si_3N_4 materials evaluated on this program. Both reflected light (optical) microscopy and scanning electron microscopy were used to view and record the nature of the microstructure of these materials. The photographic results are compiled in Appendix A.

The results of microstructural analysis for the hot-pressed, sintered, and reaction sintered Si_3N_4 materials (as well as sintered SiAlON materials) are summarized in Table 11. In this tabulation, we include density, mean room-temperature fracture strength, and the average and maximum grain size. The approximate grain size determination was made by an overall visual inspection of the micrographs, and not quantitatively determined by lineal analysis or other statistical techniques. The comments in Table 11 regarding fracture origins were made from the fracture surface analysis of bend bars broken at room temperature.

It is observed that for fully dense HP-Si_3N_4, the average grain size typically ranged from 0.5-2 µm. In some materials, occasional grains as large as 17 µm were observed. For sintered Si_3N_4, with usually slightly lower density, the grain size was also typically 0.5-2 µm. The size range of the largest grains observed in these materials was 5-10 µm. These HP- and sintered-Si_3N_4 materials generally exhibit grains that are slightly elongated and randomly oriented. This leads to an interlocking type structure that generally results in higher fracture toughness than in other types of ceramics where the grains are equiaxed.

59

TABLE 17. MICROSTRUCTURAL ANALYSIS SUMMARY FOR Si_3N_4 MATERIALS

Material	Bulk Density, g cm⁻³	Mean 25°C Bend Strength, psi	Grain size, [a] μm		Room Temperature Fracture Origins
			Average	Maximum	
Hot-Pressed Si_3N_4					
Norton NC-132 (1% MgO)	3.18	103,100	0.5-1.0	3.0	Primarily machining flaws, other processing defects.
Norton NCX-34 (8% Y₂O₃)	3.37	126,730	0.5-1.8	8.0	Machining flaws and processing defects.
Harbison-Walker (10% Ceria)	3.33	76,780	---	--	Primarily inclusions.
Kyocera SN-3 (4% MgO, 5% Al₂O₃)	3.07	74,860	0.5-2.5	--	Primarily inclusions.
Ceradyne Ceralloy 147A (1% MgO)	3.22	87,090	1.0-5.0	12-17	Primarily inclusions.
Ceradyne Ceralloy 147Y (15% Y₂O₃)	3.37	87,850	0.5-3.0	14	Undetermined.
Ceradyne Ceralloy 147Y-1 (8% Y₂O₃)	3.29	83,250	1.0-3.0	10-12	Machining flaws and processing defects.
Fiber Materials, Inc. (4% MgO)	3.17	66,840	0.5-1.8	5-7	Dark inclusions.
Tosniba (4% Y₂O₃, 3% Al₂O₃)	3.25	105,700	---	--	Dark, shiny inclusions.
Toshiba (3% Y₂O₃, 3% Al₂O₃, SiO₂)	3.20	33,600	---	--	Inclusions.
Westinghouse (4% Y₂O₃, SiO₂)	3.25	90,980	0.5-2.0	--	Dark, shiny inclusions.
NASA/AVCO/Norton (10% ZrO₂)	3.37	91,190	---	--	Dark, shiny inclusions, other processing defects.
Battelle HIP (5% Y₂O₃)	3.25	,000[c]	---	--	See footnote c .
Sintered Si_3N_4					
Kyocera SN-205 (5% MgO, 9% Al₂O₃)	2.81	37,770	0.5-1.0	--	Inclusions and porosity.
Kyocera SN-201 (4% MgO, 7% Al₂O₃)	3.00	49,610	0.5-2.0	4.0	Primarily inclusions, some pores.
GTE Sylvania (6% Y₂O₃)	3.23	78,?00	0.5-3.0	5-8	Inclusions, pores and pore/inclusions.
AiResearch (8% Y₂O₃, 4% Al₂O₃)	3.15	79,450	0.5-2.0	6.0	Surface and subsurface porosity.
Rocketdyne SN-50 (6% Y₂O₃, 4% Al₂O₃)	3.25	51,600	0.5-2.0	8-9	Porosity open to tensile surface.
Rocketdyne SN-104, SN-46 (14% Y₂O₃, 7% SiO₂)	3.40	51,600	0.5-1.5	5-6	Porosity open to tensile surface.

60

TABLE 11 (cont.)

Reaction Sintered Si_3N_4

Material	Bulk Density, g cm^{-3}	Mean 25°C Bend Strength, psi	Approximate Pore Size, μm^{a,b} Average	Maximum	Nature of Porosity	Room Temperature Fracture Origins
1976 Norton NC-350	2.41-2.55	29,450	0.5-3.0	12	Even distribution of pores and pore clusters.	Primarily undetermined, some processing flaws
Kawecki-Berylco (Batch 2, 1976)	2.35-2.53	19,940	10-15	70	Even distribution of porosity. Fine, evenly distributed free Si	Particles, pores, some undetermined.
Kawecki-Berylco (Batch 3, 1976)	2.35-2.53	19,940	5-15	30-70	Some large interconnected pores 100 μm. Uneven distribution of free Si.	Particles, pores, some undetermined.
Ford Injection-Molded	2.75	38,180	2-8	100	Avg. clusters 10-20 μm w/large clusters 80-100 μm. Some free Si.	Processing defects, inclusions and pores.
AiResearch Airceram RBN-101 (SC)	2.85	37,920	2-5	35	Angular pores. Avg. clusters 12-25 μm. Some free Si evenly distributed.	Primarily inclusions.
Raytheon (isopressed)	2.43	21,550	0.5-5.0	25	Even porosity Avg. cluster 5-10 μm.	Processing defects and undetermined
Indussa/Nippon Denko	2.08	10,580	20-40	180	Much large, interconnected porosity.	Some pores, some undetermined.
AiResearch Airceram RBN-122 (IM)	2.66	32,580	0.5-3.0	20	Avg. cluster size 5-15 μm. Some free Si unevenly distributed	Inclusions, some with pores.
1979 Norton NC-350	2.60	37,560	0.5-5.0	20	Large pores 5-10 μm with clusters 15-22 μm. No obvious free Si visible	Primarily inclusions.
AiResearch Ceramco NR-115H	2.44-2.68	28,870	2-10	60	Many large pores and clusters 30-60 μm. Some free Si visible.	Inclusions
AED Nitrasil batch 1 1978	2.52	29,920	2-10	85	Many clusters 20-40 μm unevenly distributed. Little free Si.	Inclusions, some with pores
2 1978	2.50	27,000	2-10	50	Avg. clusters 25-35 μm with some free Si unevenly distributed	Primarily inclusions, some pores
4 1978	2.60	30,730	1-5	50	Avg. clusters 20-40 μm evenly distributed.	Inclusions and inclusions with pores
5 1980	2.62	26,080	2-10	70	Unevenly distributed clusters 20-50 μm. uneven free Si.	Primarily dark inclusions
Georgia Tech	2.50-2.60	26,240	0.5-5	18	Even, fine porosity. Fine, even free Si. Clusters of pores 5-10 μm	Primarily light inclusions
AME	2.10	7,470	--	35	Much interconnected porosity. Large area of free Si unevenly distributed	Undetermined due to material porosity
AiResearch RBN-104	2.80	40,270	1-5	24	Fine, even porosity with clusters 8-10 μm	Subsurface pores and inclusions.
1977 Norton NC-350	2.38	29,450	0.5-3.0	12	Evenly distributed clusters 5-12 μm	Pores, pore agglomerates.

61

TABLE 11 (concluded)

Material	Bulk Density, g/cm³	Mean 25°C Bend Strength, psi	Grain size,[a] μm		Approximate Pore Size,[b] μm		Nature of Porosity	Room-Temperature Fracture Origin
			Average	Maximum	Average	Maximum		
SiAlON MATERIALS								
US Bureau of Mines SiAlON[d]								
● Billet 1 (5% ZrSiO₄)	~.900 (2.08-3.06)	26,660	.1	--	.5	20	fine interconnected pore structure	subsurface and surface-connected pores
● Billet 2 (5% Y₂O₃)	3.038	35,330	1	--	10	30-100	generally discrete pore structure with wide size variation.	large subsurface pores.
● Billet 4 (5% ZrSiO₄)	2.632	13,190	1	--	5-10 agglomerated	5C single pores	much interconnected porosity.	mostly undetermined due to ill-defined fracture features.
● Billet 5 (5% ZrSiO₄)	2.646	17,160	1	--	2-10	20-30, agglomerated	much interconnected porosity.	mostly undetermined, some large pores and large grains identified as fracture initiation sites

aFrom overall visual inspection of micrographs, not statistically determined by lineal analysis.

bVoid features with rounded corners were judged to be porosity void features with sharp/angular corners were judged to be polishing pullouts.

cSee Reference 5.

dRefer to Reference 36 for details of processing and compositional modifications. All SiAlON compositions were nominally 80% Si_3N_4-20% Al_2O_3, with 5% additive (either Y_2O_3 or $ZrSiO_4$) to promote sintering.

Pore size, rather than grain size, was characterized for the reaction-sintered silicon nitride materials since porosity is generally the strength-limiting feature of the microstructure of RS-Si₃N₄. With reference to Table 11, it is seen that a wide range of average and maximum porosity was observed. The materials with the finest pore structures were Norton N_-350 and AiResearch RBN-122. Average pores ranged in size from 0.5–3.0 μm, while the largest pores were 12-20 μm in size. In some of the other RS-Si₃N₄ materials, average pore sizes were as great as 15 μm, and the maximum pores approached 100 μm in size.

6.1.2 Flexural Strength/Fracture Sources and Elastic Properties

The room temperature 4-point bend strength and elastic moduli (static and dynamic) of all Si₃N₄ materials evaluated to date are tabulated in Tables 12 and 13. Strength data are plotted as a function of bulk density and volume fraction porosity in Figures 14 and 15, respectively. Density (and thus strength) generally increases with respect to processing method in the following progression: reaction sintered with few additives, reaction sintered with iron additives, sintered with oxide additives, hot-pressed with magnesia additive, and finally hot-pressed with yttria additive. A least-squares regression of the linearized form of the exponential strength-porosity relation $\sigma = \sigma_0 e^{-bp}$ gives

$$\sigma = 87.1e^{-5.55P}$$

as shown in Figure 15. The strength behavior of the thirty-nine (39) hot-pressed, sintered, and reaction bonded Si₃N₄ materials is well described by the strength-porosity data fit. This empirical strength-porosity relation is not strictly valid at low porosity, however, even though it accurately describes the strength of the high density hot-pressed materials in this region. This is the case because the fracture strength of the hot-pressed materials is not expected to be related directly to porosity as

TABLE 12. SUMMARY OF ROOM-TEMPERATURE POROSITY, STRENGTH, AND ELASTIC MODULUS DATA FOR VARIOUS Si_3N_4 MATERIALS

Symbol in Figs. 14-16	Material	Bulk Density g cm^{-3}	Theoret.[a] Density	P Volume Fraction Porosity	4-Point Flexure Strength ksi	Static Young's Modulus[b] 10^6 psi
○	Norton NC-132 HP-Si_3N_4 (MgO)	3.177	3.2	.007	90.91	48.4
○	Norton NC-132 HP-Si_3N_4 (MgO)	3.186	3.2	.004	115.21	45.7
■	Kyocera SN-205 Sintered Si_3N_4	2.801	3.2	.125	37.77	27.9
◇	Norton NC-350 RB-Si_3N_4 (Diamond Ground) (1976)	2.523	3.2	.212	30.87	25.5
◇	Norton NC-350 RB-Si_3N_4 (Diamond Ground) (1976)	2.396	3.2	.251	23.53	23.5
⟩	Norton NC-350 RB Si_3N_4 (Diamond Ground) (1976)	2.539	3.2	.207	33.96	27.7
◀	Norton NCX-34 HP-Si_3N_4 + 8% Y_2O_3	3.372	3.391	.006	126.73	48.6
△	Raytheon Isopressed RS-Si_3N_4	2.447	3.2	.235	21.55	23.8
◣	AiResearch Slip-Cast RS-Si_3N_4 (RBN-101)	2.862	3.2	.106	37.92	32.0
◖	Kyocera SN-3 HP-Si_3N_4	3.072	3.2	.04	74.86	36.6
◆	Kyocera SN-201 Sintered Si_3N_4	3.005	3.2	.061	49.61	34.4
◗	Ford Injection Molded RS-Si_3N_4	2.742	3.2	.143	38.18	30.7
◆	Harbison-Walker HP-Si_3N_4 + 10% CeO_2	3.327	3.387	.018	76.78	46.9
○	Kawecki-Berylco RS-Si_3N_4	2.509	3.2	.216	23.27	21.5
○	Kawecki-Berylco RS-Si_3N_4	2.454	3.2	.233	21.80	21.1
○	Kawecki-Berylco RS-Si_3N_4	2.349	3.2	.266	19.08	20.0
●	Indussa/Nippon Denko RS-Si_3N_4	2.084	3.2	.349	10.58	11.9
△	AiResearch Injection Molded RS-Si_3N_4 (RBN-122)	2.660	3.2	.169	32.58	30.2
⊕	GTE Laboratories Sintered Si_3N_4 + 6% Y_2O_3	3.256	3.271	.005	78.00	42.1
●	Ceradyne Ceralloy 147A, HP-Si_3N_4 + 1% MgO	3.221	3.2	.00?	87.09	47.9
◑	Ceradyne Ceralloy 147-Y-1, HP-Si_3N_4 + 8% Y_2O_3	3.289	3.295	.002	83.25	45.4
◐	Ceradyne Ceralloy 147-Y, HP-Si_3N_4 + 15% Y_2O_3	3.369	3.383	.004	87.85	44.7
◆	Norton NC-350 RB-Si_3N_4 (as-fired) (1977)	2.385	3.20	.255	42.09	----

TABLE 12 (cont.)

Symbol in Figs. 14-16	Material	Bulk Density g/cm³	Theoret. Density[a]	P Volume Fraction Porosity	4-Point Flexure Strength ksi	Static Young's Modulus[b] psi 10⁶
✕	Fiber Materials HP-Si₃N₄ (4% MgO)	3.171	3.216	.014	66.84	--
◇	Harbison-Walker HP-Si₃N₄ (10% CeO₂) b. ch 2	3.353	3.387	.010	87.89	45.0
◑	Norton NC-350 RS-Si₃N₄ (1979)	2.354	3.200	.264	37.56	22.1
⊕	Annawerk Ceranox NR-115H RS-Si₃N₄	2.571	3.200	.197	28.87	26.4
▷	AED Nitrasil RS-Si₃N₄	2.547	3.200	.204	29.06	26.3
●	AiResearch Sintered Si₃N₄ (8% Y₂O₃, 4% Al₂O₃)	3.144	3.323	.054	77.89	44.8
□	Rocketdyne SN-46 Sintered Si₃N₄ (14% Y₂O₃, 7% SiO₂)	3.433	3.47	.011	54.02	39.4
◆	Rocketdyne SN-50 Sintered Si₃N₄ (6% Y₂O₃, 4% Al₂O₃)	3.252	3.77	.020	51.60	40.8
◁	Rocketdyne SN-104 Sintered Si₃N₄ (14% Y₂O₃, 7% SiO₂)	3.365	3.47	.030	57.64	34.1
◺	Toshiba HP-Si₃N₄ (4% Y₂O₃, 3% Al₂O₃)	3.245	3.266	.006	105.7	47.5
◣	Toshiba HP-Si₃N₄ (3% Y₂O₃, 4% Al₂O₃, SiO₂,	3.204	3.261	.017	83.60	41.3
◢	Westinghouse HP-Si₃N₄ 4% Y₂O₃, SiO₂)	3.250	3.247	0	90.98	44.2
◻	Georgia Tech RS-Si₃N₄	2.542	3.200	.206	26.22	23.9
◇	AME RS-Si₃N₄	2.118	3.200	.338	7.47	--
◁	AiResearch RBN-104 RS-Si₃N₄	2.785	3.200	.130	40.27	--
■	NASA/AVCO/Norton HP-Si₃N₄ (10% ZrO₂)	3.36?	3.360	0	45.19	..?
--	BuMines Sintered SiAlON (Billet 1, 5% ZrSiO₄)	2.865	--	--	26.66	28.1
--	BuMines Sintered SiAlON (Billet 2, 5% Y₂O₃)	3.049	--	--	35.33	33.0
--	BuMines Sintered SiAlON (Billet 4, 5% ZrSiO₄)	2.627	--	--	13.19	19.4
--	BuMines Sintered SiAlON (Billet 5, 5% ZrSiO₄)	2.635	--	--	17.16	22.3

[a] The theoretical density of all sintered and reaction bonded Si_3N_4 materials was assumed to be 3.200 g/cm^3. The theoretical density of the HP-Si_3N_4 + .1% MgO materials was also assumed to be 3.200 g/cm^3. The theoretical density of the Y_2O_3- and CeO_2-doped HPSN was computed from the nominal chemical composition assuming $\rho(CeO_2)$ = 7.13 and $\rho(Y_2O_3)$ = 5.01. The only exception to this is for NCX-34, which contains .2% tungsten; the composition of NCX-34 was assumed to be 88% Si_3N_4 + 9% Y_2O_3 + 3% WC.

[b] Young's modulus determined with strain gages in 4-point flexure.

TABLE 13. SUMMARY OF ROOM-TEMPERATURE RELAXED AND DYNAMIC ELASTIC MODULUS DATA FOR VARIOUS Si$_3$N$_4$ MATERIALS

Symbol in Fig. 17	Material	Bulk Density (sonic), g cm^{-3} [a]	Theoret. Density [b]	Volume fraction Porosity [a]	Young's Modulus (sonic), 10^6 psi [c]	Static Young's Modulus and (bulk density), 10^6 psi [a]
◆	Norton NC-132 HP-Si$_3$N$_4$ + 1° MgO	3.177	3.2	.007	45.0	48.4 (3.177)
◆	Norton NC-132 HP-Si$_3$N$_4$ + 1% MgO	3.162	3.2	.012	44.5	45.7 (3.186)
△	Norton NCX-34, HP-Si$_3$N$_4$ + 8% Y$_2$O$_3$	3.386	3.391	.001	44.5	49.6 (3.372)
◁	Ceradyne Ceralloy 147-A, HP-Si$_3$N$_4$ + 1% MgO	3.312	3.2	0	45.8	47.9 (3.271)
▱	Ceradyne Ceralloy 147-Y, HP-Si$_3$N$_4$ + 15% Y$_2$O$_3$	3.370	3.333	.004	41.6	44.7 (3.360)
○	Ceradyne Ceralloy 147-Y-1, HP-Si$_3$N$_4$ + 8° Y$_2$O$_3$	3.218	3.295	.023	42.8	45.4 (3.280)
◁	Kyocera SN-3 HP-Si$_3$N$_4$	3.060	3.2	.044	35.9	36.6 (3.072)
◇	Kyocera SN-201 Sintered Si$_3$N$_4$	2.994	3.2	.064	34.7	34.4 (3.005)
◁	Kyocera SN-205 Sintered Si$_3$N$_4$	2.819	3.2	.119	27.6	27.9 (2.801)
◕	Norton NC-350 RS-Si$_3$N$_4$ (1976)	2.470	3.2	.228	25.6	25.5 (2.523)
◑	Norton NC-350 RS-Si$_3$N$_4$ (1976)	2.392	3.2	.253	22.7	23.5 (2.396)
⊕	Norton NC-350 RS-Si$_3$N$_4$ (1976)	2.524	3.2	.211	26.8	27.7 (2.539)
◐	Kawecki-Berylco (KBI) RS-Si$_3$N$_4$	2.325	3.2	.273	18.6	21.5 (2.599)
◑	KBI RS-Si$_3$N$_4$	2.347	3.2	.267	18.8	21.1 (2.454)
◑	KBI RS-Si$_3$N$_4$	2.432	3.2	.240	23.1	20.0 (2.349)
○	Ford (IM) RS-Si$_3$N$_4$	2.762	3.2	.137	28.3	30.7 (2.742)
▷	AiResearch (SC) RS-Si$_3$N$_4$	2.881	3.2	.099	31.4	32.0 (2.862)
▷	AiResearch (IM) RS-Si$_3$N$_4$	2.646	3.2	.173	26.6	30.2 (2.660)
□	Raytheon (IP) RS-Si$_3$N$_4$	2.602	3.2	.240	21.5	23.0 (2.447)
⊠	Fiber Materials HP-Si$_3$N$_4$ (4% MgO)	3.197	3.216	.006	46.2	--
◆	Harbison-Walker HP-Si$_3$N$_4$ (10% CeO$_2$) batch 2	3.343	3.387	.014	44.6	45.0 (3.353)
◑	Norton NC-350 RS-Si$_3$N$_4$ (1979)	2.422	3.200	.243	22.7	22.1 (2.354)
✧	Annawerk Ceranox NR-115U PS-Si$_3$N$_4$	--	3.200	--	--	26.4 (2.571)
▶	AED Nitrasil RS-Si$_3$N$_4$	2.561	3.200	.200	25.7	26.3 (2.547)

TABLE 13 (cont.)

Symbol in Fig. 17	Material	Bulk Density (sonic) g/cm3[a]	Theo Density[b]	Volume Fraction Porosity[a]	Young's Modulus (sonic) 10^6 psi[c]	Static Young's Modulus[d] and (bulk density), 10^6 psi
◪	Toshiba HP-Si$_3$N$_4$ (4% Y$_2$O$_3$, 3% Al$_2$O$_3$)	3.253	3.266	.004	47.0	47.5 (3.245)
◩	Toshiba HP-Si$_3$N$_4$ (3% Y$_2$O$_3$, 4% Al$_2$O$_3$, SiO$_2$)	3.217	3.261	.013	42.0	41.3 (3.204)
◢	Westinghouse HP-Si$_3$N$_4$ (4% Y$_2$O$_3$, SiO$_2$)	3.286	3.247	0	44.6	44.2 (3.250)
●	Georgia Tech RS-Si$_3$N$_4$	2.590	3.200	.191	25.6	23.9 (2.542)
⬓	NASA/AVCO/Norton HP-Si$_3$N$_4$ (10% ZrO$_2$)	3.338	3.360	.007	45.0	44.3 (3.367)
—	BuMines Sintered SiAlON (Billet 1, 5% ZrSiO$_4$)	2.813	--	--	30.6	28.1 (2.865)
—	BuMines Sintered SiAlON (Billet 2, 5% Y$_2$O$_3$)	3.049	--	--	34.5	33.0 (3.049)
—	BuMines Sintered SiAlON (Billet 4, 5% ZrSiO$_4$)	2.601	--	--	19.2	19.4 (2.627)
—	BuMines Sintered SiAlON (Billet 5, 5% ZrSiO$_4$)	2.634	--	--	22.0	22.3 (2.635)

[a] Average values for dynamic modulus samples.
[b] Theoretical density computed from nominal chemical composition.
[c] Dynamic elastic modulus determined by flexural resonant frequency method.
[d] Determined with strain gage transducers during 4-point flexure strength test at 0.02 ipm.
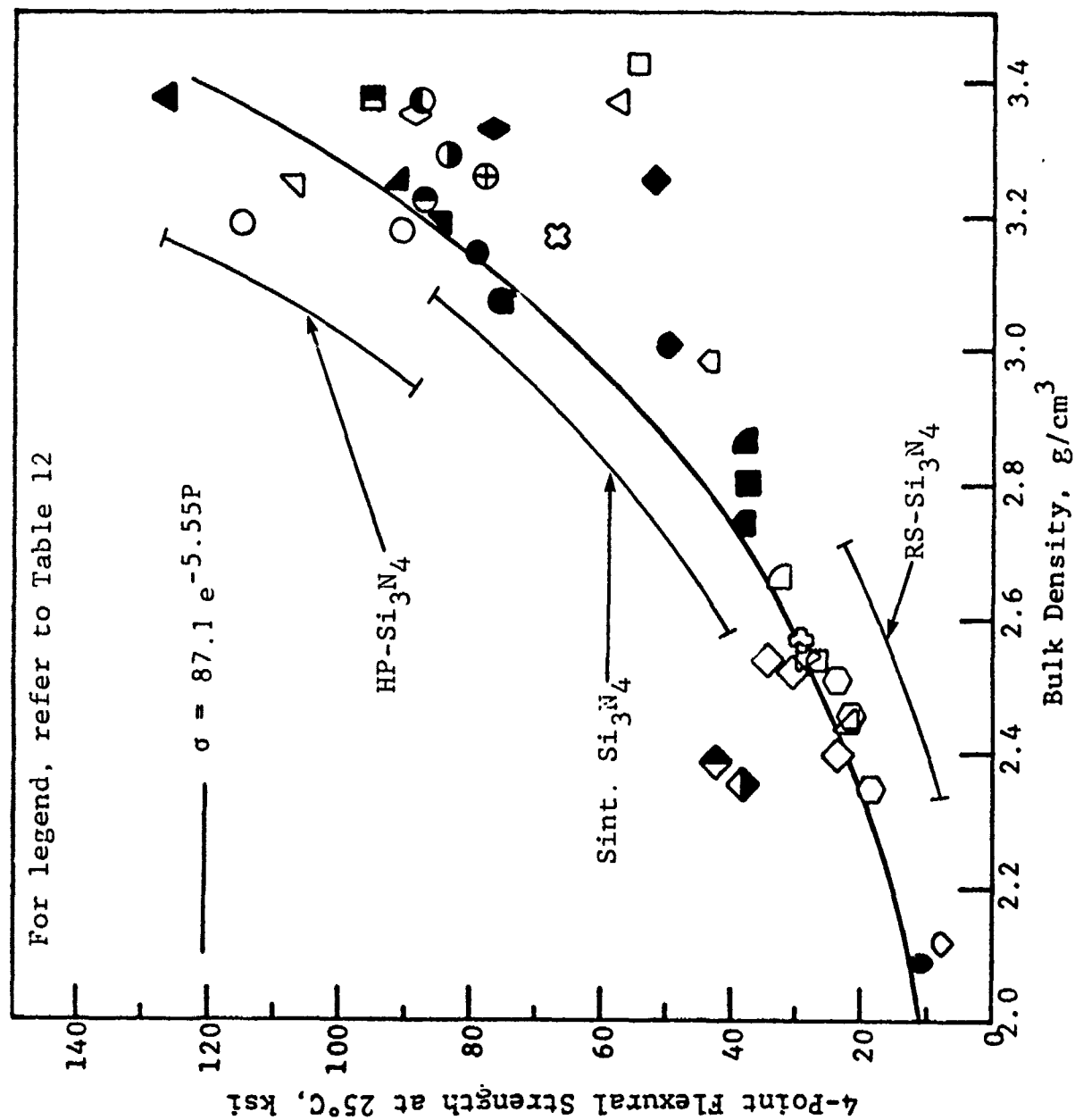
Figure 14. Room-temperature flexural strength vs. bulk density for various Si_3N_4 materials.
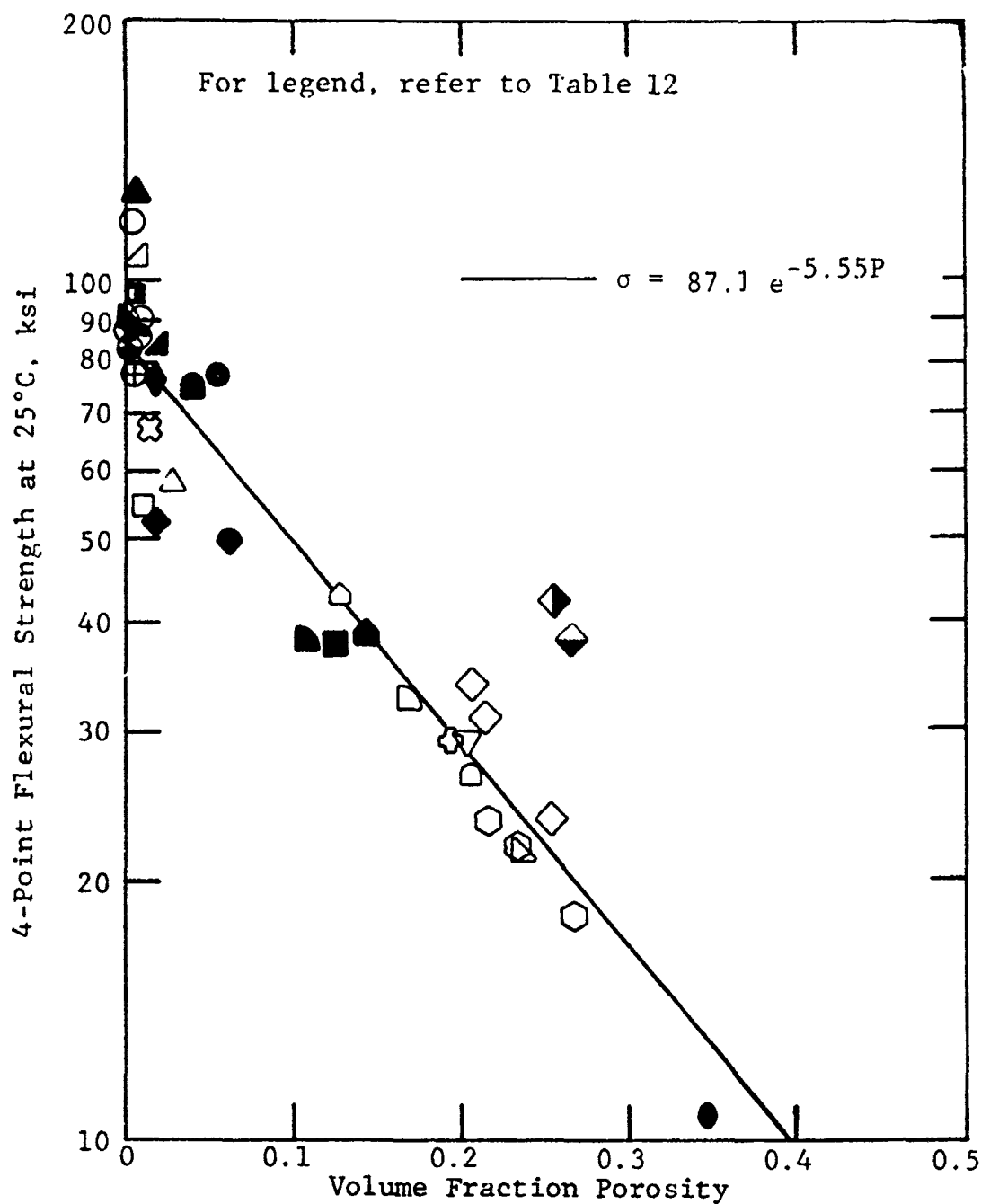
Figure 15. Room-temperature flexural strength vs. volume fraction porosity for various Si_3N_4 materials.

it is for the lower density sintered and reaction-bonded materials. That is, the critical strength-controlling flaws in the lower density materials are expected to be pores or pore clusters, while fracture sources in high density hot-pressed materials have typically been traced to large grains, metal inclusions, unreacted particles, surface or subsurface machining damage, or a single isolated pore not affecting the overall density.

The hot-pressed materials with strengths greater than 100 ksi are Norton NC-132 (1% MgO), Norton NCX-34 (8% Y_2O_3), and Toshiba (4% Y_2O_3, 3% Al_2O_3) materials. For RS-Si_3N_4, it is noted that the strength of two Norton NC-350 materials is ~40 ksi, well above the trend line.

Fracture surface analysis was conducted on this program with a 6-60X stereoscopic optical microscope with photographic attachment. The objective of this examination was to attempt to identify the general nature of the fracture origins. Room temperature fracture sources in Si_3N_4 are tabulated in Table 11. It is observed that the Norton hot-pressed materials (NC-132 and NCX-34) were relatively processing-mature in that the fracture sources that could be identified were predominantly machining induced flaws at the diamond-ground surface. All other hot-pressed materials exhibited fracture origins consisting of inclusions and other subsurface processing defects.

The fracture sources in the various sintered Si_3N_4 materials were a mixture of inclusions and porosity (surface and subsurface). Porosity and inclusion particles were also the predominant fracture sources in RS-Si_3N_4 materials. The inclusions are most probably unreacted silicon particles and iron-rich particles. Iron is a common impurity (and sintering aid) in RS-Si_3N_4. Spectrographic analysis results (Table 7) indicate as much as 1.3% Fe impurity in these materials. However, porosity is the predominant microstructural feature in RS-Si_3N_4 that can be described as detrimental to those properties necessary for high performance.

70

Evans[37] presents an enlightening analysis of the sensitivity of HP-Si$_3$N$_4$ materials to various types of processing defects. As summarized in Figure 18, the fracture stress is relatively insensitive to tungsten carbide inclusions, and progressively more sensitive to Fe, C, and voids. Unreacted silicon particles and surface cracks were found to have the strongest effect on strength.

The relaxed elastic moduli obtained during flexure testing of all Si$_3$N$_4$ materials are plotted as a function of porosity in Figure 16 (data compiled in Table 12). The dynamic moduli (obtained by a flexural resonant frequency method) of all Si$_3$N$_4$ materials are compiled in Table 13 (where the static moduli are repeated for comparison). The 25°C relaxed and dynamic elastic moduli for all Si$_3$N$_4$ materials are plotted as a function of volume fraction porosity in Figure 17. Good agreement is obtained between the static and dynamic moduli at room temperature. The data fit for all Si$_3$N$_4$ static and dynamic moduli has the exponential form:

$$E = 45.1e^{-2.99P}$$

6.2 SiC MATERIALS

Silicon carbide materials are processed in hot-pressed, sintered, and silicon-densified forms. All are essentially fully dense. There is no analogy to porous reaction-sintered silicon nitride for the SiC system.

Silicon carbides have high elastic modulus compared to Si$_3$N$_4$ materials. The Young's modulus is typically 50-60 x 10^6 psi. This is ~50% higher than the elastic modulus of dense HP-Si$_3$N$_4$. The strength of hot-pressed and sintered SiC is intermediate to the strength of hot-pressed and reaction sintered Si$_3$N$_4$. Room-temperature strength in SiC is usually controlled by the grain size. Hot-pressed SiC using Al$_2$O$_3$ as a densification aid has higher strength than when B$_4$C is used. Al$_2$O$_3$ inhibits grain growth, the grain size is typically 1-2 μm, and the strength is
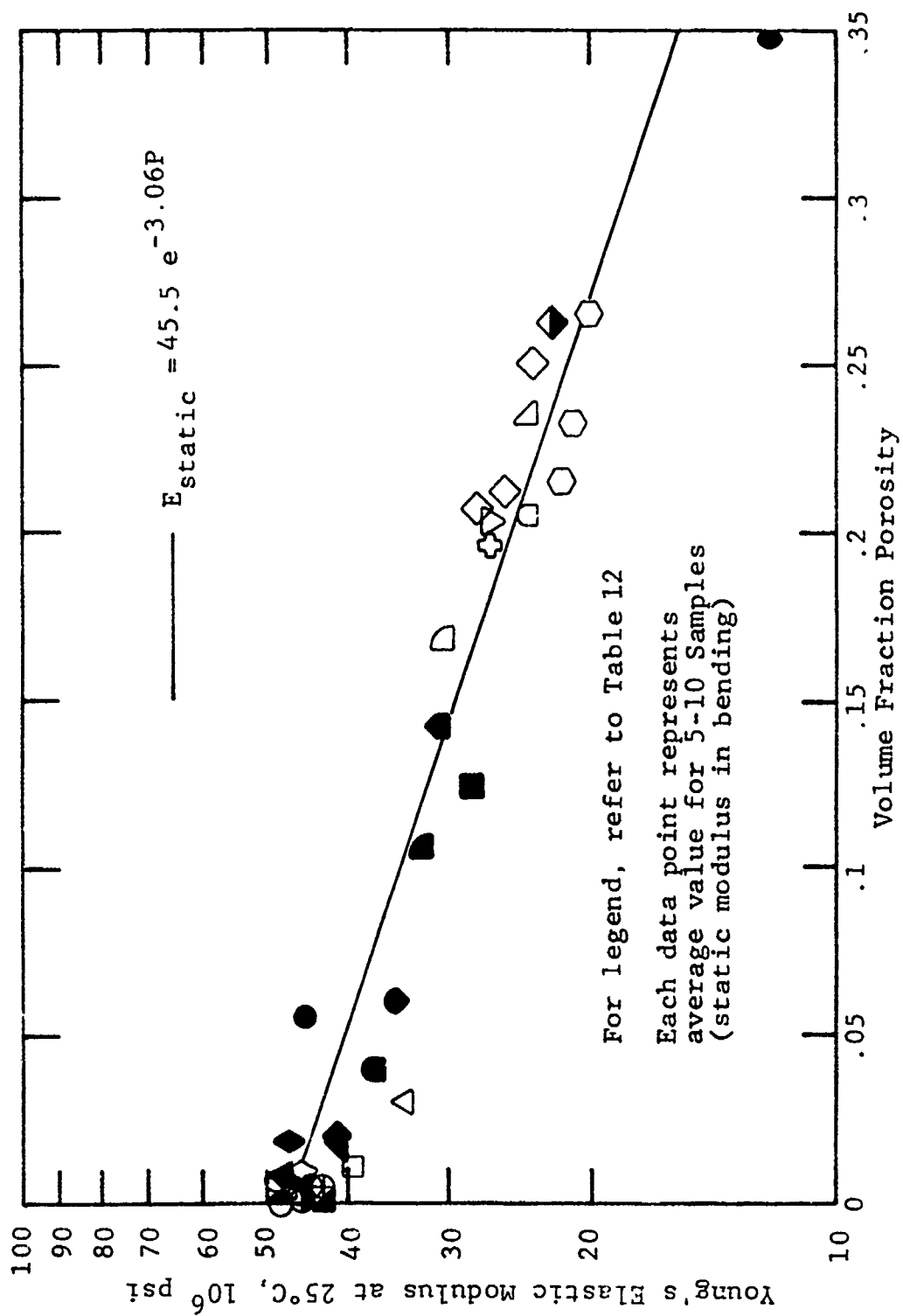
Figure 16. Room-temperature elastic modulus vs. porosity for various Si_3N_4 materials.

$E_{static} = 45.5 \ e^{-3.06P}$

For legend, refer to Table 12

Each data point represents average value for 5-10 Samples (static modulus in bending)

Volume Fraction Porosity

Young's Elastic modulus at 25°C, 10^6 psi
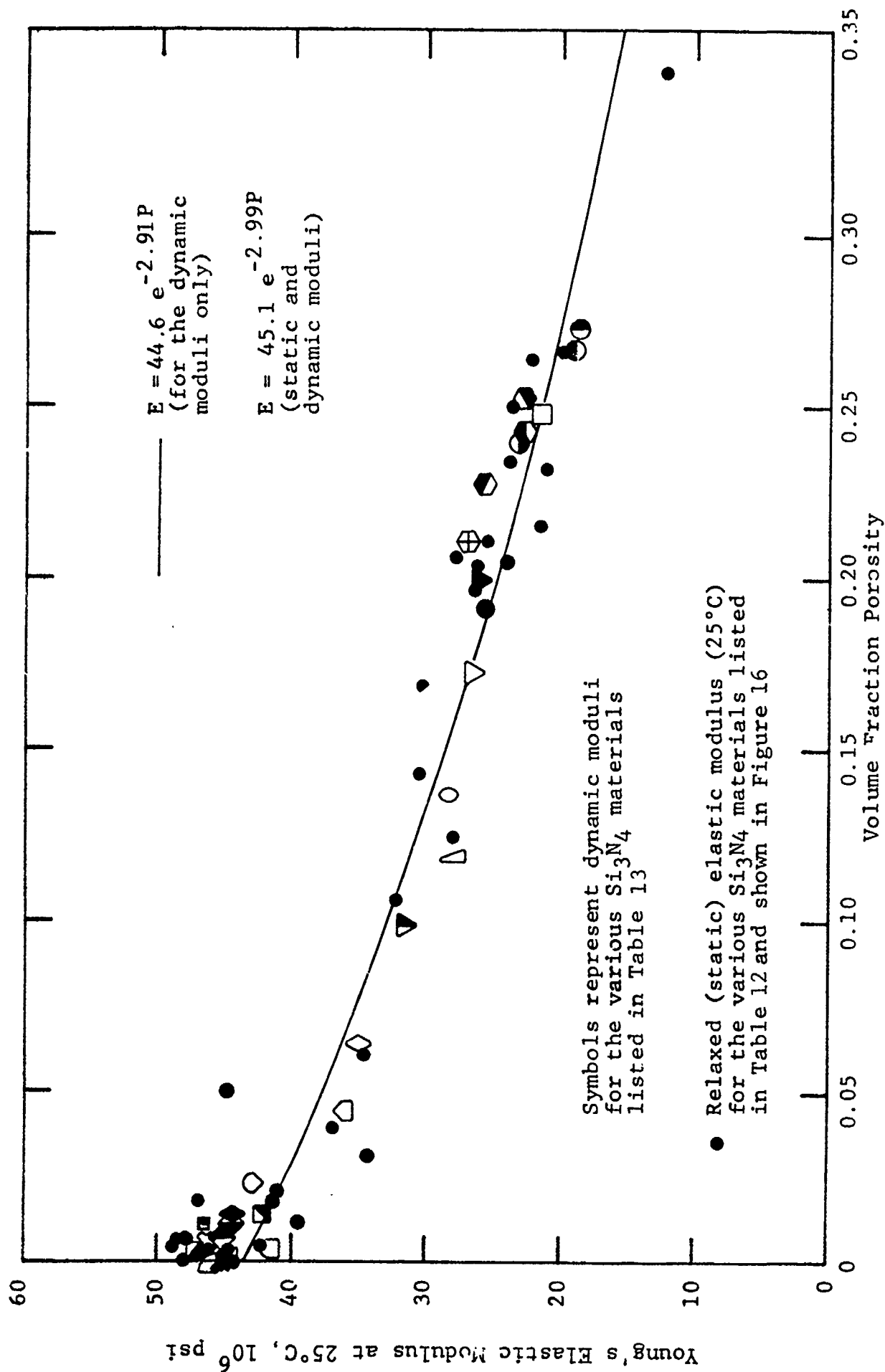
Figure 17. Comparison of relaxed and dynamic elastic moduli for various Si_3N_4 materials.
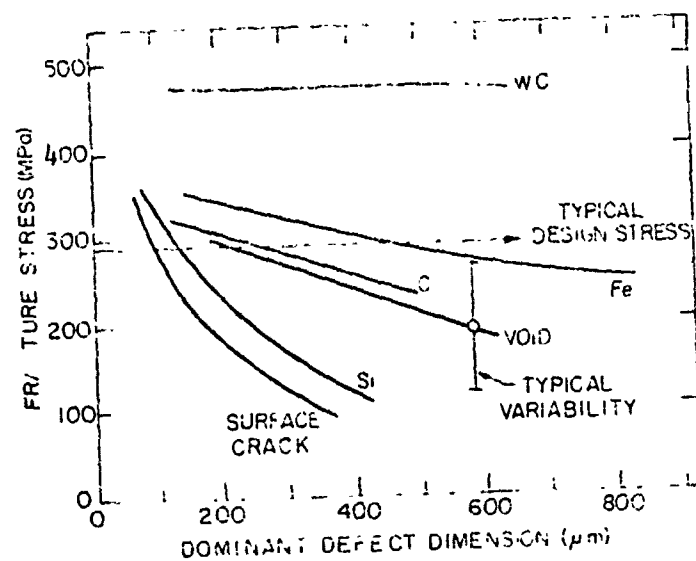
Figure 18. Strength, size relations for various fracture-initiating defects in silicon nitride (from Evans[37]).

nigh. The converse is true for HP-SiC doped with B_4C, where the grain size ranges from 10-40 μm.

Sintered SiC is processed in α- and β-SiC crystal structures (predominantly hexagonal and cubic, respectively). Bend strengths are typically 45-65 ksi. The β-SiC structure appears consistently stronger than α-SiC. Fracture origins in α-SiC are often large (~50 μm) individual needles/platelets that have experienced exaggerated grain growth during processing. Single isolated surface-connected pores are also found in α-SiC. Both forms of SiC fracture predominantly in the transgranular mode. It is for this reason that fracture phenomena in SiC are more often associated with grain size, rather than porosity or intergranular phases. The predominance of transgranular fracture also makes fracture surface analysis and the identification of fracture origins more difficult than in $HP-Si_3N_4$, where the fracture path is usually intergranular. Details are presented in the following paragraphs.

6.2.1 Strength-Grain Size Relation

The results of the microstructural analysis of all SiC materials evaluated to date are summarized in Table 14. In this tabulation we include the density, mean room-temperature fracture strength, average and maximum grain size, and the location of any porosity. The approximate grain size determination was made by an overall visual inspection of the micrographs, and not quantitatively determined by lineal analysis or other statistical techniques. In assessing the location of porosity, void features with rounded corners were judged to be actual porosity, whereas void features with sharp/angular corners were judged to be polishing pullouts. The comments in Table 14 regarding fracture origins and fracture mode were derived from the fracture surface analysis of bend bars broken at room temperature. The strength and elastic moduli of all SiC materials evaluated, as correlated with density/porosity, are tabulated in Tables 15 and 16. The modulus-porosity data for SiC are plotted in Figure 19.

TABLE 14. MICROSTRUCTURAL ANALYSIS SUMMARY FOR SiC MATERIALS

Material	Density g/cm³	Mean 25°C Bend Strength, psi	Approximate Grain Size, μm Avg.	Max.	Location of Porosity[b]	Room Temperature Fracture Origins; General Fracture Mode
HOT-PRESSED SiC						
Ceradyne Ceralloy 146-A (2% Al₂O₃)	3.22	60,060	4-12	30	In grain boundaries	Undetermined; primarily transgranular
Ceradyne Ceralloy 146-I (2% B₄C)	3.21	45,620	10-30	50	3/4 in grain boundaries 1/4 within grains	Some machining damage, primarily undetermined; transgranular
Norton NC-203 (2% Al₂O₃)	3.32	101,810	1-4	10	In grain boundaries	Undetermined; transgranular
SINTERED SiC						
General Electric β-SiC	3.04	63,770	0.5-2(5)	100(?)	Undetermined	Primarily inclusions or large grains; transgranular
Carborundum 1977 α-SiC (SC)	3.16	44,230	2-8	15	2/3 in grain boundaries 1/3 within grains	Primarily inclusions or large grains. transgranular
Kyocera 1980 SC-201 α-SiC	3.14	56,080	1.5-5	10	In grain boundaries	Primarily undetermined, some surface and subsurface pores; transgranular
Carborundum 1981 α-SiC (IM)	3.09	47,230	2-5	15-18	Mostly intergranular	Primarily surface and subsurface 1-4 μm pores
ESK α-SiC	3.16	41,660	3-8	60-120	2/3 in grain boundaries 1/3 within grains	Surface and subsurface porosity.
SILICONIZED SiC						
Norton NC-435	2.96	57,200	1-6	12	In grain boundaries	Pores or large grains, some undetermined; intergranular
UKAEA/BNF Refel[a]						
• As-processed	3.09	33,600	0.5-5	15	In grain boundaries	Some large grains, primarily undetermined; combination intergranular and transgranular
• Diamond-ground	3.11	44,920	0.5-3.	15-50	In grain boundaries	Large grains; combination intergranular and transgranular
Norton NC-430	3.1	30,420	2-10[d]	50-175[c]	Mostly between small grain boundaries, some within large grains	Undetermined; combination intergranular and transgranular
Coors (1979, SC-1)	3.0	50,620	1.5-6	12	In grain boundaries, between Si phase	Mostly undetermined, some machining damage
Coors (1981, SC-2)	3.09	45,410	0.5-3.5 5-12	20		Slightly less Si in Coors 1981.
Coors (1982, SC-2)	3.10	43,010	0.5-2 5-10	15		Primarily large grains.

[a] Diamond-ground and as-processed refer to the material condition for the strength tests; the microstructure analyses for grain size and Si distribution were made on bulk material well below the surface. The near-surface microstructural features are different for the diamond-ground and as-processed conditions.

[b] For overall visual inspection of micrographs; not statistically determined by lineal analysis, etc.

[c] Void features with rounded corners were judged to be porosity; void features with sharp/angular corners were judged to be polishing pullouts.

[d] Bimodal size distribution of SiC grains.

TABLE 15. SUMMARY OF ROOM-TEMPERATURE STRENGTH AND POROSITY DATA FOR VARIOUS SiC MATERIALS

Material	Bulk Density, g cm^{-3}	Theoret. Density[a]	Volume Fraction Porosity[b]	4-Point Bend Strength, ksi
Norton NC-435 Siliconized SiC, batch 1	2.936	3.0396	.0341	50.5
Norton NC-435 Siliconized SiC, batch 3	2.997	3.0396	.0140	66.0
Norton NC-435 Siliconized SiC, batch 4	2.962	3.0396	.0255	55.2
General Electric Sintered β-SiC	3.032	3.217	.0575	63.8
Carborundum Sintered α-SiC (1977)	3.159	3.217	.0180	44.2
UKAEA/BNF Refel Si/SiC, Diamond Ground	3.101	3.1283	.0087	44.9
UKAEA/BNF Refel Si/SiC, As-Processed	3.090	3.1283	.0122	33.6
Ceradyne Ceralloy 146A, HP-SiC (2% Al$_2$O$_3$)	3.224	3.2293	.0016	60.1
Ceradyne Ceralloy 146I, HP-SiC (2% B$_4$C)	3.211	3.1993	0	45.6
Norton NC-203 HP-SiC (2% Al$_2$O$_3$)	3.318	3.375	.017	101.8
Coors Si/SiC (1979, SC-1)	3.001	3.099	.032	50.6
Kyocera SC-201 Sintered SiC	3.148	3.217	.021	56.1
Norton NC-430 Si/SiC	3.105	3.217	.035	30.4
Carborundum 1981 Hexoloy SY-05 SSC	3.???	?.???	.03?	47.2
Coors Si/SiC (1981, SC-2)	3.037	3.099	?	45.4
Coors Si/SiC (1982, SC-2)	3.100	3.099	0	43.3
General Electric Silcomp Si/SiC (CC)	2.886	3.067^{c}	.057	26.0
ESK Sintered α-SiC	3.160	3.217	.018	41.7

[a] Theoretical density computed from nominal chemical composition assuming $\rho_{SiC} = 3.217$, $\rho_{Si} = 2.33$, $\rho_{B_4C} = 2.52$, $\rho_{Al_2O_3} = 3.97$ g cm^{-3}.

The effective theoretical density for NC-435 and Refel siliconized SiC was computed by relation $\rho = v_1\rho_1 + v_2\rho_2$, assuming 20 vol% and 10 vol% silicon phase, respectively.

The effective theoretical density of all other materials was computed from their nominal chemical composition using the relation $1/\rho = x_1/\rho_1 + x_2/\rho_2$, where x_1 and x_2 refer to the wt% of each phase present.

[b] $P = 1 - \rho_{Bulk}/\rho_{Theoret}$.

[c] Estimate.

TABLE 16. SUMMARY OF ROOM-TEMPERATURE RELAXED AND DYNAMIC ELASTIC MODULUS DATA FOR VARIOUS SiC MATERIALS

Symbol in Fig. 19 Static Modulus	Symbol in Fig. 19 Dynamic Modulus	Material	Bulk Density (sonic)[a] g cm^{-3}	Theoret. Density[b]	Volume Fraction Porosity	Young's Modulus (sonic),[c] 10^6 psi	Static Young's Modulus[d] (with corresponding density), 10^6 psi
○	●	Norton NC-435 Siliconized SiC, batch 1	2.953	3.217	.0821	49.1	53.9 (2.936)
□	■	Norton NC-435 Siliconized SiC, batch 3	2.973	3.217	.0758	49.6	49.5 (2.997)
◇	◆	Norton NC-435 Siliconized SiC, batch 4	2.991	3.217	.0703	50.6	48.8 (2.962)
△	▲	General Electric Sintered β-SiC	3.031	3.217	.0578	54.6	54.8 (3.032)
△	▲	Carborundum Sintered α-SiC (1977)	3.159	3.217	.0180	62.1	58.2 (3.159)
◁	◀	UKAEA/BNF Refel Si/SiC, Diamond Ground	3.086	3.217	.0407	56.2	57.5 (3.101)
◁	◀	UKAEA/BNF Refel Si/SiC, As-Processed	3.049	3.217	.0522	49.1	52.5 (3.090)
◇	◆	Ceradyne Ceralloy 146A, HP-SiC + 2% Al$_2$O$_3$	3.255	3.229	0	63.5	67.2 (3.224)
◁	◀	Ceradyne Ceralloy 146I, HP-SiC + 2% B$_4$C	3.229	3.217	0	62.6	65.3 (3.211)
◇	◆	Norton NC-203 HP-SiC (2% Al$_2$O$_3$)	3.331	3.375	.013	64.7	--
○	●	Norton NC-430 Si/SiC	3.130	3.217	.027	58.4	58.7 (3.105)
△	▲	Coors Si/SiC (1979, SC-1)	3.026	3.099	.024	52.3	51.1 (3.001)
○	●	Kyocera SC-201 Sintered SiC	3.113	3.217	.032	58.5	60.5 (3.148)
—	◐	Carborundum 1981 Hexoloy SX-05 SSC	-	3.217	-	-	55.9 (3.117)
■	■	Coors Si SiC (1981, SC-?)	3.118	3.099	0	58.0	53.8 (3.097)
—	◇	Coors Si/SiC (1982, SC-2)	-	3.099	-	-	54.2 (3.130)
◀	▲	General Electric Silcomp Si/SiC (CC)	2.919	3.062[e]	.047	48.0	43.7 (2.886)
—	◑	ESK Sintered α-SiC	-	3.217	-	-	61.0 (3.160)

[a] Average values for dynamic modulus samples.

[b] Theoretical density computed from nominal chemical composition only for Ceradyne 146A. All other materials: Theoretical density assumed to be ρ_{Th} = 3.217 g cm^{-3}.

[c] Dynamic elastic modulus determined by flexural resonant frequency method.

[d] Determined with strain gage transducers during 4-point flexure strength test (0.02 ipm crosshead deflection).

[e] Estimate.

78
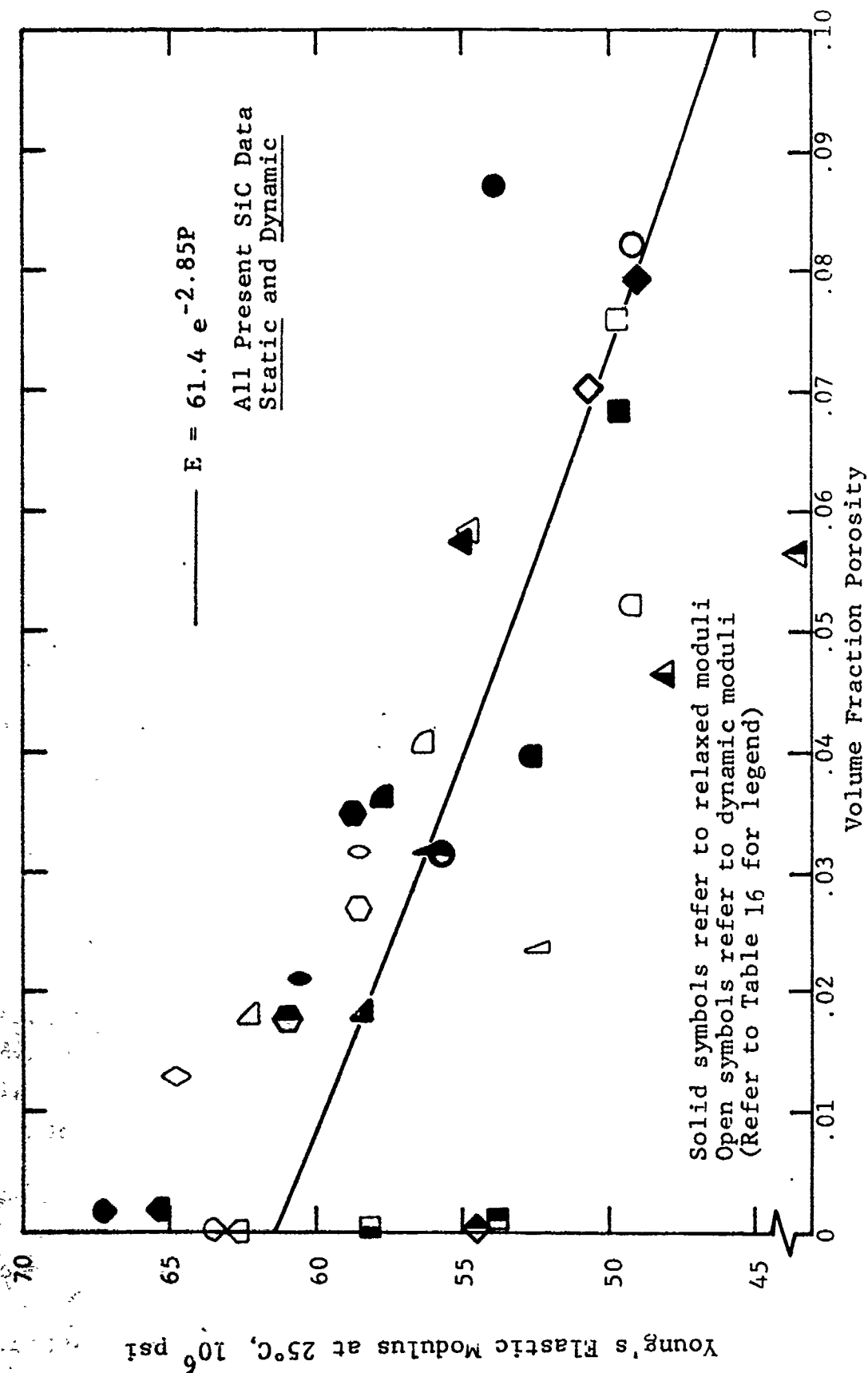
Figure 19. Comparison of relaxed and dynamic elastic moduli for various SiC materials (including hot-pressed, sintered, and silicon-densified forms of SiC).

79

(a) Hot-pressed SiC. The room-temperature strength of SiC can be correlated with grain size in general, as would be expected since the fracture path in SiC is predominantly transgranular. For instance, the strengths of the three fully dense hot-pressed (HP) SiC materials evaluated on this program are compared in Table 14.* The reflected light micrographs of these three materials are presented in Figure 20. Norton NC-203 HP-SiC, doped with ~2% Al_2O_3, has very high strength (σ >100 ksi) since it is so fine-grained. Its grain size averages 1-4 μm, with the largest grains being ~10 μm in size (see Table 14). All grains in NC-203 are equiaxial. This information is seen in the micrograph presented in Figure 20c. The strength of the companion Ceradyne material, Ceralloy 146-A which also contains nominally 2% Al_2O_3 as a densification additive, is much lower, i.e., ~60 ksi at room temperature. Figure 20a illustrates a larger grain size for Ceralloy 146-A than for NC-203, i.e., and average grain size ~4-12 μm, with a ~30 μm maximum. Thus, the grain size of the Ceradyne material is a factor of four larger than the grain size of NC-203, and the strength of the Ceralloy 146-A is roughly half that of NC-203. This is exactly what would be predicted from the known strength-grain size relation for ceramics; that is, the strength being inversely proportional to the square root of the grain diameter.[38,39]

The room-temperature strength of Ceradyne Ceralloy 146-I HP-SiC, which is doped with ~2% B_4C to promote densification, is even lower, ~45 ksi as shown in Table 14. Figure 20b illustrates the microstructure of Ceralloy 146-I. The average grain size is shown to be even larger than for the Al_2O_3-doped HP-SiC materials (i.e., 10-30 μm average grain diameter, with a maximum of ~50

---

*In this discussion of grain size we are only concerned with room temperature strength; at elevated temperature other factors affect the strength, mainly the amount of oxide intergranular phase and resulting subcritical crack growth (refer to Section 7.2).

(a) Ceradyne Ceralloy 146-A HP-SiC (2% Al_2O_3) etched 9.6 min with boiling Murikami's reagent.
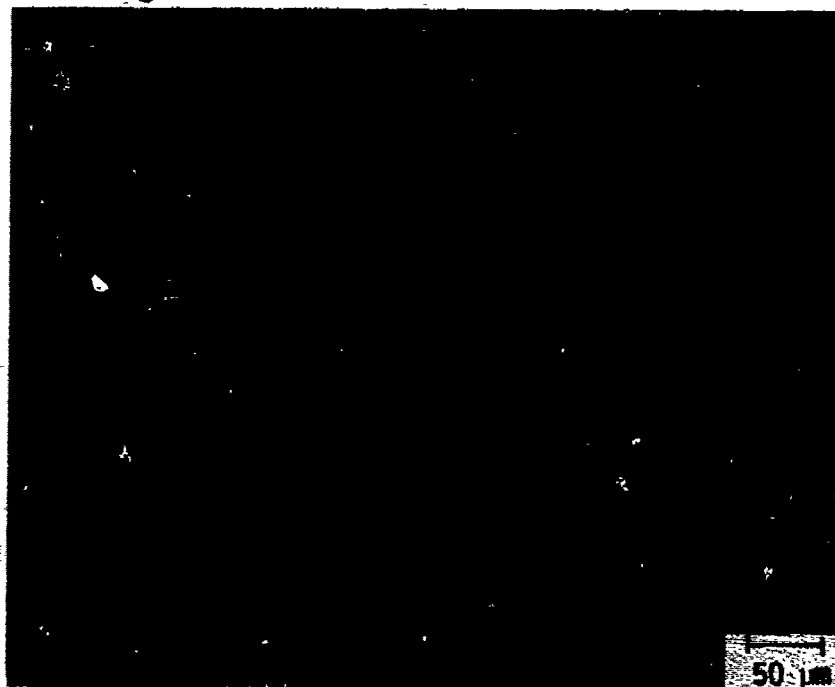
(b) Ceradyne Ceralloy 146-I HP-SiC (2% B_4C) etched 8.6 min with boiling Murikami's reagent.

Figure 20. Reflected light micrographs of hot-pressed silicon carbide materials.
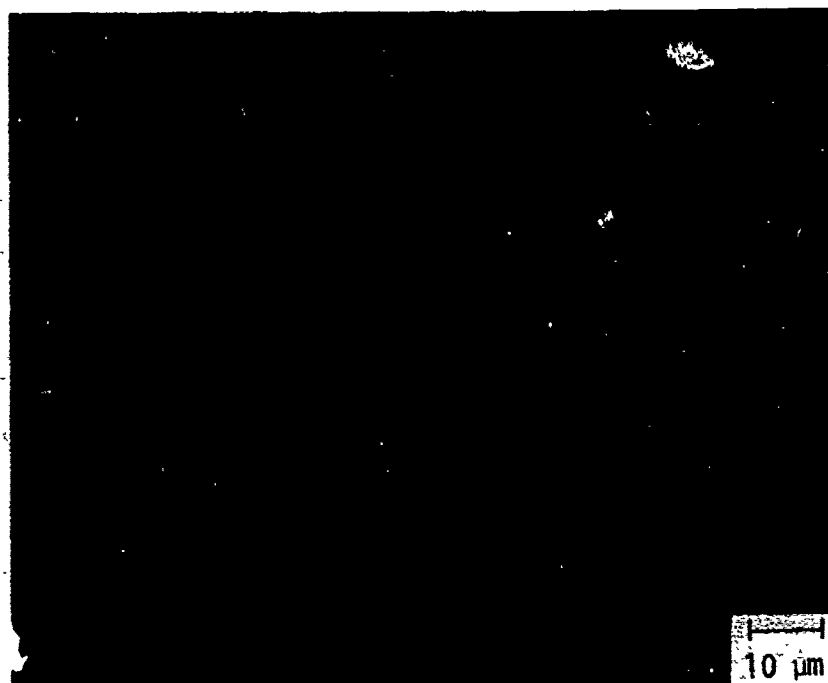
(c) Norton NC-203 HP-SiC ($\sim$2% Al_2O_3) etched
    9.6 min with boiling Murikami's reagent.

Figure 20 (cont.)

μm). Again, the data follow the inverse square root strength-grain diameter relation. The grain size of Ceralloy 146-I is about an order of magnitude larger than that of NC-203, and the room-temperature strength is about one third that of NC-203. The reason for the factor of three grain size difference in the two Ceralloy materials has to do with the effect of the oxide additive on grain growth during processing. The presence of Al_2O_3 inhibits grain growth; B_4C promotes grain growth in SiC. The resulting effect on strength is shown in the present data. The grain growth in the B_4C-doped material is apparently anisotropic, since the grain morphology in Ceralloy 146-I is largely tabular, with an aspect ratio of approximately 3:1.

(b) Sintered SiC. Sintered SiC materials from General Electric, Carborundum, Kyocera, and ESK[*] were evaluated on this program. Sintered SiC is processed in the α and β crystal structures (predominantly hexagonal and cubic, respectively). The General Electric material used to be referred to as boron-doped β-SiC. The materials from Carborundum (1977 and 1981 vintages) and Kyocera (SC-201 1980 vintage) are of the α crystalline form. The ESK material is also α-SiC. All, except ESK, employ boron as the primary sintering aid. Emission spectrographic analysis indicates all have ~0.4-0.5 wt% boron and ~0.2-0.3 wt% iron impurities (refer to Table 7). On the other hand, Al_2O_3 was the primary sintering aid for the ESK material (high Al impurity as shown in Table 7).

Strength data for these sintered SiC materials are shown in Table 14. The reflected light micrographs for these materials are presented in Figure 21. The various microstructural analysis parameters are summarized in Table 14. The β-SiC structure appears consistently stronger than α-SiC. Table 14 shows that General Electric β-SiC is a nominally 65 ksi material. Figure

---

[*]Elektroschmelzwerk Kempten, Kempten, FRG.

(a) 1980 Kyocera SC-201 sintered α-SiC etched
8 min with boiling Murikami's reagent.

(b) General Electric sintered β-SiC etched
5 min with boiling Murikami's reagent
(α-etch).

Figure 21. Reflected light micrographs
of sintered silicon carbide materials.
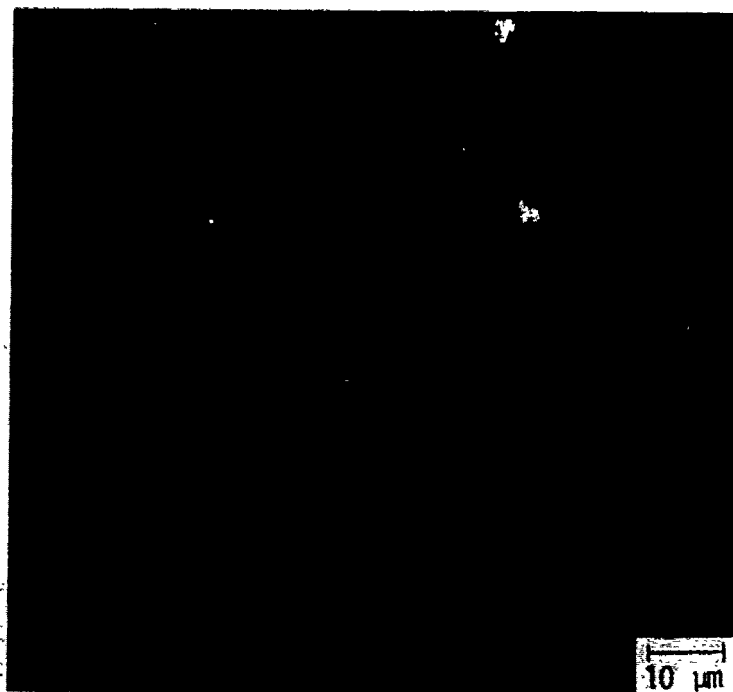
(c) General Electric sintered β-SiC etched 5 min with boiling Murikami's reagent (α-etch) and 1.5 min with a fused salt mixture of KOH and KNO_3 (β-etch).
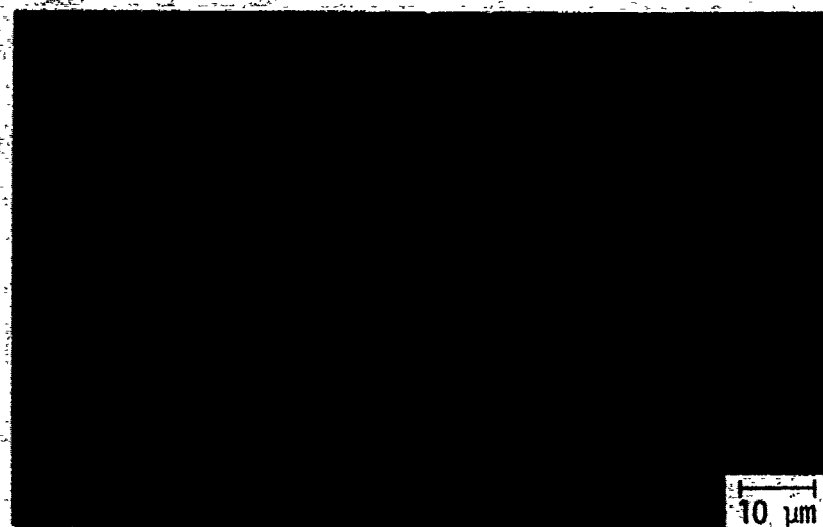
(d) 1977 Carborundum sintered α-SiC etched 10.3 min with boiling Murikami's reagent.

Figure 21 (cont.)

(e) 1981 Carborundum sintered α-SiC polished and etched 7.5 min with boiling Murikami's reagent.
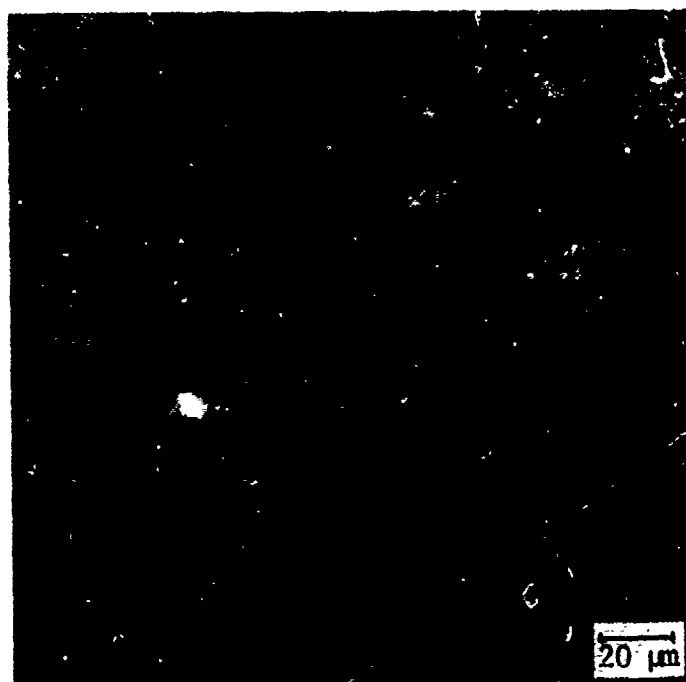
Figure 21 (cont.).

(f) ESK sintered α-SiC polished and etched
8 min with boiling Murikami's reagent.

(g) ESK sintered α-SiC.

Figure 21 (cont.)

21c i.lustrates that this high strength is achieved by obtaining a very fine β-SiC grain size (typically 0.5-2 μm). This material actually has a small amount of the α-structure present. Figure 21b shows some evidence of long needles/platelets of α-SiC in the overall structure. The X-ray diffraction results shown in Table 6 confirm that a small amount of the α-structure can be present in this β-SiC from General Electric. The acicular α-phase grains can become quite large (i.e., ~100 μm long in Figure 21c), but apparently are so few in number as to not override the influence of the much smaller β-crystals and not be detrimental to the strength of the overall structure. Since this would appear to be a violation of the weakest link theory, perhaps these long α-needles impart a whisker-like reinforcement to the structure. The two etching procedures used to delineate the features of the α and β crystal phases shown in Figures 21b and 21c are explained in Table 9. The development of the microstructure in General Electric β-SiC is described in detail by Johnson and Prochazka.[40]

The α-SiC materials from Carborundum and Kyocera are lower in strength compared to General Electric β-SiC. Carborundum 1977 α-SiC has a room-temperature 4-point bend strength of nominally 45 ksi, whereas the strength of Kyocera 1980-vintage SC-201 α-SiC is on the order of 55 ksi. The reflected light micrographs shown in Figures 21a and 21d illustrate the equiaxed grain configuration for these materials. The grain diameter of the Kyocera α-SiC is slightly smaller than that of the Carborundum material. The average grain diameter of Kyocera SC-201 ranges from ~1.5 to 5 μm. An occasional 10 μm grain is observed. The average grain size range and maximum grain diameter of 1977 Carborundum α-SiC are 2-8 μm and 15 μm, respectively. Therefore, the higher strength of the Kyocera material appears to be related to its slightly smaller grain size. No evidence of exaggerated growth of α grains is observed for these materials.

Carborundum 1981 sintered α-SiC (Hexoloy SX-05) was injection-molded and supplied in the as-fired condition (the 1977 material was slip-cast and diamond ground). The 1981 material

had slightly lower density. Both materials had similar phase content (α-SiC, with similar polytype structures) and cation impurities. The microstructures of these materials are similar. The more recent material was slightly stronger (refer to Table 14).

The ESK material exhibited a room-temperature 4-point bend strength of 41.7 ksi. This is on the low end of the range of strengths exhibited by the other sintered SiC materials evaluated. Microstructural analysis yields two explanations: exaggerated α-grain growth and large intergranular porosity, as illustrated in the micrographs shown in Figure 21 f and g. The average size of the α-grains is 3-8 μm. Most of these grains are not equiaxed, but have an aspect ratio of ~1:7. A number of large α-grains have grown to platelet size, 60-120 μm. Some pores are as large as 10 μm in diameter. Fracture surface analysis indicated that surface and subsurface pores were the primary fracture origins at room temperature, so it may be that the large α-grains had no effect on the strength. At this time the composition of the light areas on the micrograph shown in Figure 21g is not known; they may be Al_2O_3-rich areas.

(c) Silicon-Densified SiC. Bend strength data for the silicon-densified SiC materials are presented in Table 14. The micrographs are shown in Figure 22, and the microstructural parameters are also summarized in Table 14. The strongest materials at 25°C are Norton NC-435 and Coors 1979 SC-1 Si/SiC (51-57 ksi). The micrographs illustrate that these materials have the smallest grain size, which accounts for their high strength. The average grain size range for these two materials is ~1-6 μm; the maximum grain size observed is ~12 μm. The reflected light micrographs in Figures 22a and 22f illustrate that the grains of NC-435 are equiaxial, whereas about 25% of the Coors 1979 SC-1 Si/SiC grains are tabular with approximate aspect ratio of 10:1. The distribution of the continuous silicon phase is about the same in both materials, uniform, and appearing to be ~10-20% by volume in extent.

89

(a) Norton NC-435 siliconized SiC
   electrolytically etched 4 min
   with 20% KOH.

Figure 22.   Reflected light micrographs of
   siliconized silicon carbide materials.

(b) UKAEA/British Nuclear Fuels Refel siliconized SiC; microstructure of diamondground material, electrolytically etched 2 min with 20% KOH.

(c) UKAEA/British Nuclear Fuels Refel siliconized SiC; dense interior microstructure of as-processed material, electrolytically etched 3 min with 20% KOH.

Figure 22 (cont.)

91

(d) UKAEA/British Nuclear Fuels Refel silicon-
ized SiC, as-processed with high purity
SiC and silicon-rich surface layers in-
tact; electrolytically etched 3 min with
20% KOH.
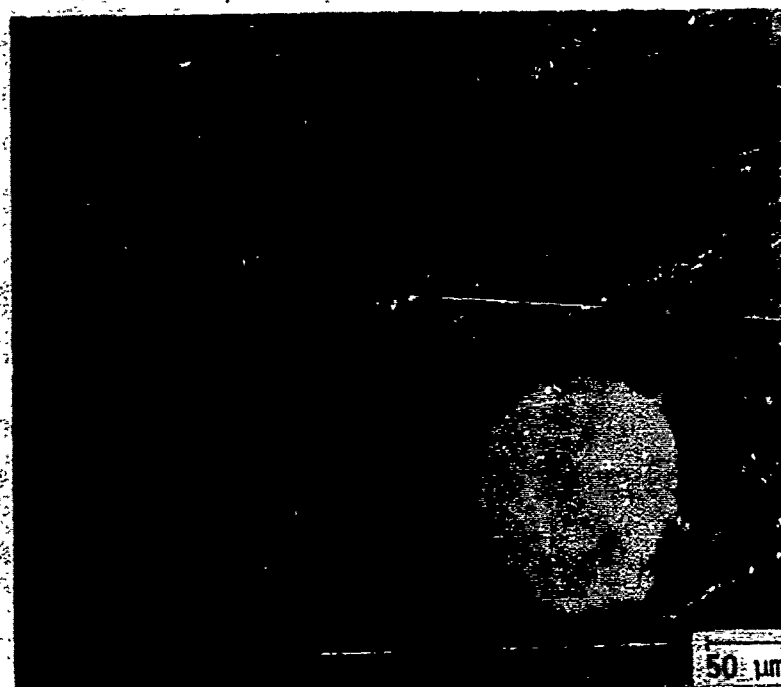
(e) Norton NC-430 siliconized SiC, electro-
lytically etched 2 min with 20% KOH.

Figure 22 (cont.)
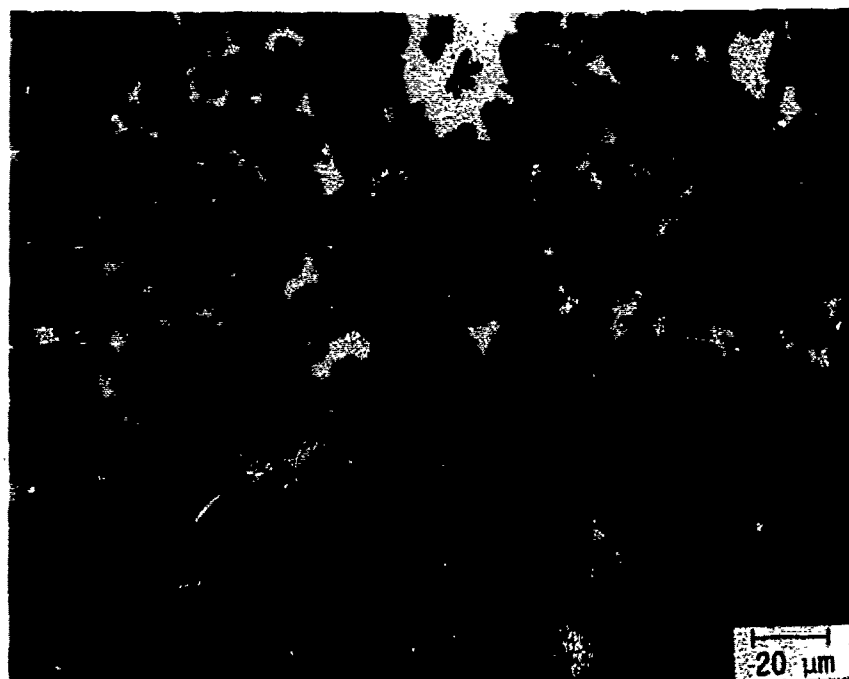
(f) Reflected light micrograph of 1979 Coors SC-1
siliconized SiC, electrolytically etched
3.0 min with 20% KOH.
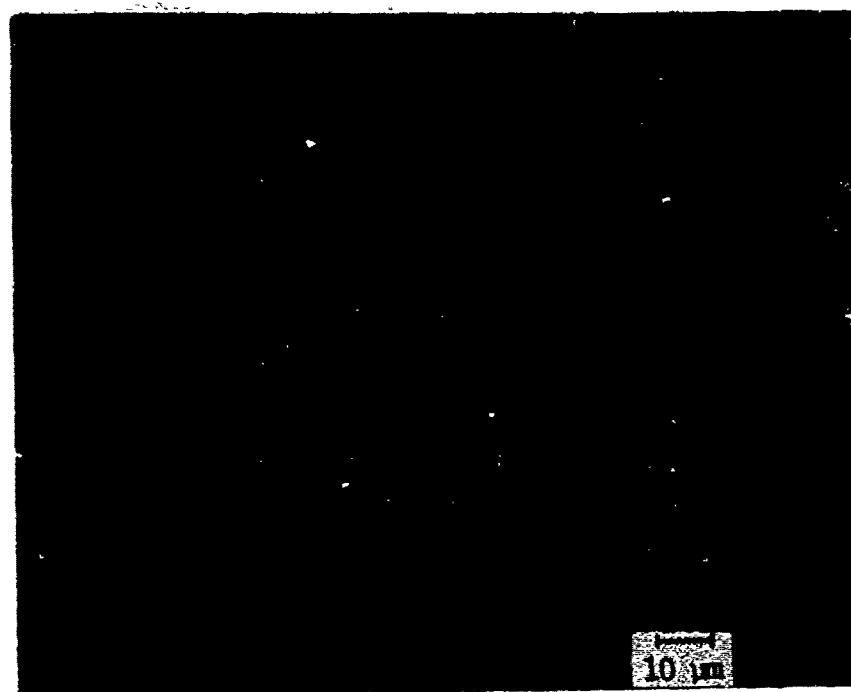
(g) Reflected light micrograph of 1981 Coors SC-2
siliconized SiC, electrolytically etched
2.5 min with 20% KOH.

Figure 22 (cont.)
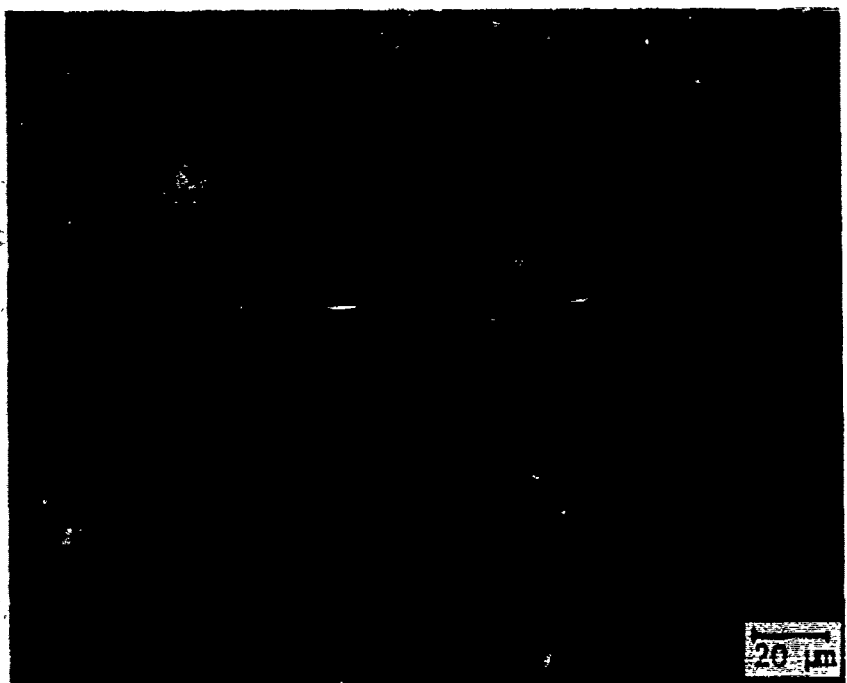
(h) Reflected light micrograph of 1982 Coors SC-2
siliconized SiC, electrolytically etched
1.5 min with 20% KOH.

Figure 22 (cont.)

The UKAEA/BNF Refel Si/SiC was received from the manufacturer in two conditions, diamond-ground and as-processed. The difference in these two conditions mainly involves the near-surface microstructure, and was described by Kennedy et al.,[41] and discussed in a previous report on this program.[42] With reference to Figure 22d, as-processed material has a highly crystalline ~25 μm layer of silicon carbide on the outer surface. Below this thin surface layer is a ~100 μm thick layer of silicon-rich material (~38 vol% silicon by manufacturer's estimate). Both of these outer layers are clearly seen in Figure 22d. Below these two outer layers of the as-processed material is the dense bulk Si/SiC, which the manufacturer states to contain 8-10 vol% continuous silicon phase. The micrograph presented in Figure 22d clearly shows all three microstructural regions of the as-processed material. It would be expected that the diamond-ground version of Refel would have two outer layers removed and exhibit the microstructure of the dense bulk material. This fact is confirmed in the micrographs in Figures 22b and 22c, and summarized in Table 14: the interior sections of both diamond-ground and as-processed material had average grain diameters ranging from approximately 0.5 to 4 μm, and the silicon phase looked relatively uniformly distributed in both.

Another silicon-densified SiC material evaluated on this program is Norton NC-430. The strength is seen in Table 14 to be only 30 ksi, the lowest of the Si/SiC materials. The microstructure shown in Figure 22e explains this; NC-430 is an extremely coarse-grained material. Actually, NC-430 exhibits a bimodal distribution of SiC grains: a network of relatively fine 2-10 μm SiC grains, and a distribution of extremely angular, extremely large 50-175 μm SiC grains. This structure is bonded together by the continuous silicon metal phase, but it is rather nonuniform in NC-430, as evidenced by the large silicon-rich region shown in the micrograph presented in Figure 22e.

It is noted that Coors has supplied three Si/SiC materials to this program. Spectrographic analysis results reveal about

the same level of cation impurities in all the materials (Table 7). X-ray studies indicate all generations of material contain similar SiC polytype structures (Table 6). The most recent material, 1982 SC-2, has about the same density (3.097 g cm^{-3}) as 1981 SC-2, and about 3% higher than 1979 SC-1.

Reflected light micrographs of these three materials are presented in Figures 22f-h. The micrographs reveal that 1982 SC-2 has about the same silicon metal content as 1981 SC-2. The earlier 1979 SC-1 material had slightly higher silicon content, and a smaller and more uniform SiC grain size. Again, like 1981 SC-2, there are two distinct size ranges of SiC grains in 1982 SC-2 Si/SiC. In the more recent material the finer, submicron grains appear to be evenly distributed around the larger grains, instead of clustered together as was seen in the 1981 material.

6.2.2 Effect of Porosity

All forms of SiC thus far evaluated on this program (i.e., hot-pressed, sintered, and silicon-densified) are essentially nearly fully dense, at least compared to the range of densities obtained for the various processing methods for silicon nitride (i.e., fully dense hot-pressed to reaction-sintered, which has up to 20% porosity). Therefore, porosity is not a major limiting factor in the behavior of SiC, as it is for RS-Si$_3$N$_4$, for example. High elastic modulus and high thermal expansion are usually cited as the most limiting factors of SiC from a properties standpoint.

However, porosity in SiC does exist and can affect properties. Thus it is informative to view the porosity in SiC. The micrographs shown for hot-pressed (Figure 20), sintered (Figure 21), and silicon-densified (Figure 22) forms of SiC show that the porosity is almost entirely in the grain boundaries. Knowing this location of the porosity in SiC helps to interpret the transgranular fracture mode observed for all forms of SiC (see Table 14). Rice[38] points out that in general, other factors being equal, the advancing crack front usually follows the most

96

porous path. For example, intergranular failure occurs with predominantly intergranular pores, and conversely, a transgranular fracture mode is obtained with intragranular porosity. The predominance of a transgranular fracture mode in SiC in the presence of intergranular porosity means that either (a) there is not enough grain boundary porosity in SiC to make the fracture path intergranular, or (b) the low cleavage energy of the SiC crystals promotes transgranular fracture and overrides the effect of the intergranular porosity. We suspect that the latter explanation may be the reason.

6.2.3 Fracture Origins

The fracture origins for all forms of SiC evaluated on this program are summarized in Table 14. Strength is correlated (inversely) with grain size in SiC since the fracture mode is transgranular, and since minimal porosity and intergranular impurity phases are present. Fracture origins in SiC are typically large grains, with some impurity inclusions and some isolated surface-connected porosity. Fracture in both α and β forms of sintered SiC can sometimes be traced to exaggerated grain growth of the α-phase, leading to very acicular (needle-shaped) SiC crystals. However, sometimes this microstructural feature is there, but not found to be detrimental. While a noticeable number of large grains/α-needles were observed in the 1981 Carborundum sintered α-SiC, the fracture origins were mostly surface and subsurface pores. The most dramatic example of this is the ESK material, for which the strength-limiting flaw was almost always porosity, even though some α-platelets were 60-120 μm in size.

In general, fracture source identification in SiC is more difficult than it is in Si_3N_4. This is due to the transgranular fracture path in all forms of SiC, and to the heterogeneous nature of the siliconized-SiC materials. In such cases the conditions are not favorable for the development of fracture surface features that permit the straightforward assessment of the source of fracture.

7. ELEVATED TEMPERATURE STRENGTH AND TIME DEPENDENCE

The most fundamental driving force for the use of structural ceramics in heat engine applications is the ability to extend operating temperatures upward beyond the limits of metallic superalloys. Therefore, elevated temperature properties for ceramics are generated, thereby exposing deficiencies that are often related to processing variables. This leads to process iterations with the aim of improving elevated temperature performance.

Perhaps the most crucial issue in the high temperature behavior of ceramics is time dependence of strength. This is the central theme in the developing of life prediction methodologies. The most general term to describe the time dependence of strength in silicon base ceramics is static fatigue--i.e., a reduction in strength as a function of no other externally applied variable other than time (as opposed to mechanical or thermal fatigue). Quinn[43] reviews the published static fatigue data in generally early forms of silicon nitride and silicon carbide. It is pointed out that static fatigue is the general name for this observed time dependence, but that various origins and mechanisms can be involved, either acting singly or simultaneously operable. For instance, stress corrosion is environmentally assisted strength degradation in materials subjected to an externally applied stress. The mechanism involves the growth of cracks by chemical reaction with and attack by one or more elements or compounds present in the surrounding gaseous or liquid environment. The material at the existing crack tip is chemically changed and/or the local stress intensity is increased at the crack tip in an atomistic-level process. Alternatively, microcracks may nucleate (be created) in certain cases of stress corrosion.

Another form of static fatigue is creep rupture or creep fracture. This phenomenon refers to diffusion or

98

cavitation-related deformation that results in the formation of extensive microcrack networks throughout the body. The microcracks eventually coalesce to form larger cracks which in time cause rupture at a lower value of stress than the fast fracture strength.

A third form of static fatigue is slow or subcritical crack growth (SCG). The concept of SCG involves the growth of pre-existing flaws under the applied stress, to the extent that the critical stress intensity at the crack tip is reached (thus leading to rapid fracture) at a lower macroscopic stress level than if the cracks were stable and unable to grow. The exact mechanism of SCG is related to material microstructure. For example, in many hot-pressed Si_3N_4 materials, the deformation of the intergranular phase leads to grain-boundary sliding. This promotes slow crack growth leading to lowered strength. The pre-exisiting flaws in HP-Si_3N_4 are often thought to be voids existing at intergranular triple points. Their extension is the mechanism to accommodate the grain-boundary sliding. As the flaws get larger, the strength, of course, decreases. Current materials research involves ways of achieving full densification with more deformation resistant intergranular phases.

Another form of strength degradation at elevated temperature, which can be termed static fatigue, is the generation of surface flaws by high temperature oxidation or gaseous corrosion mechanisms. This also includes the deposition of foreign elements on the material by the fuel. The concept here is that the intrinsic volume flaw population in the material is changed to a surface-related critical flaw population. This effect may or may not be related to the stress corrosion mechanism discussed above.

The following subsections of this report overview the elevated temperature strength observed for various silicon-base ceramics evaluated on this program. The observables are the strength and stress-strain behavior of the various materials. The existence or lack of strength or elastic modulus degradation

99

is correlated with the nature of the fracture surfaces as viewed in the optical microscope, and the material impurities and micro-structure. The results are usually interpreted assuming that slow crack growth is the predominant mechanism leading to strength reduction. This is readily observed on the fracture surfaces.

7.1 SILICON NITRIDE MATERIALS

The following sections overview the nature of high-temperature fracture in hot-pressed, sintered, and reaction-sintered forms of silicon nitride. Many of the basic differences in these materials were discussed in the final report of the predecessor to this program, AFML-TR-79-4188,[1] and presented at various conferences and symposia.[7,11,14,15,44]

7.1.1 Hot-Pressed Si_3N_4

The basis for the comparison of all hot-pressed Si_3N_4 materials is the behavior of Norton NC-132. This material is the most processing-mature, and was the most-utilized material in early component development programs. Its limitations form the basis for all of the strategies for improving high temperature properties through grain-boundary modification. During the time of the current program, significant developments have been accomplished. We can trace the need for such improvements and the path taken for realizing them by considering the behavior of the various HP-Si_3N_4 materials evaluated on this program.

(a) MgO Additives. The oxide additives used in hot-pressing Si_3N_4 to achieve full densification can result in the creation of intergranular phases in processed bodies that can deform readily at elevated temperature leading to strength reduc-tion by subcritical crack growth. Evidence for subcritical crack growth in HP-Si_3N_4 is observed in both stress-strain data and directly on the fracture surfaces. Figure 23 illustrates the 4-point bend strength of HP-Si_3N_4 materials containing various amounts of MgO additives. The baseline here is the behavior of

100
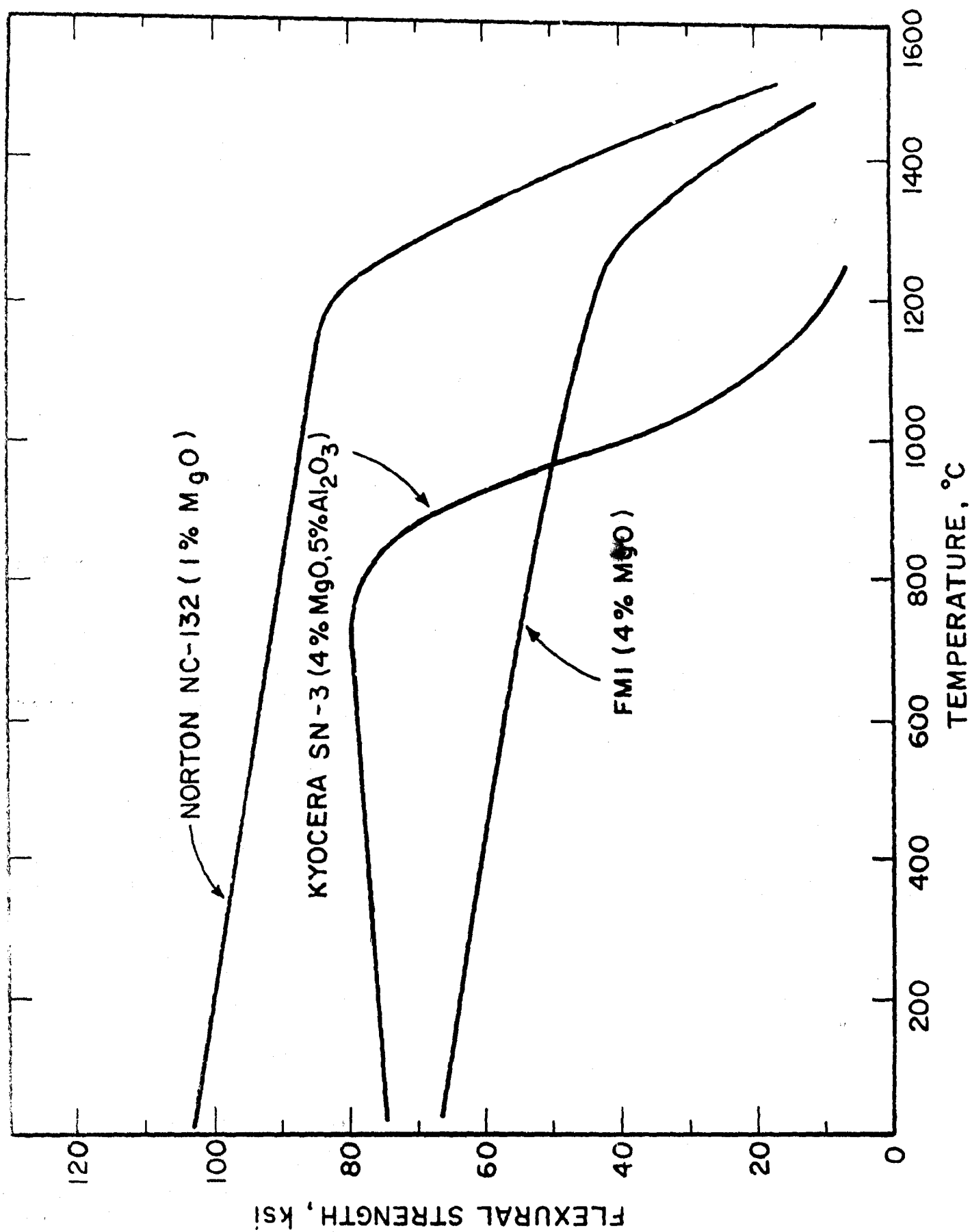
Figure 23. Flexural strength of hot-pressed silicon nitride materials.

Norton NC-132, which contains nominally 1% MgO. It is well documented in the ceramic literature how the presence of magnesia results in an amorphous intergranular phase in NC-132. Plasticity in the grain boundary silicate glass phase in NC-132 leads to strength reduction by SCG at temperatures T > 1250°C as shown in Figure 23. Evidence for increased plasticity at T > 1250°C is shown in the stress-strain behavior illustrated in Figure 24. The stress-strain curve is linear at 1200°C, and increasingly nonlinear with large increases in the strain-to-failure at 1350°C and 1500°C. The absence of SCG at 1200°C is confirmed by the appearance of the fracture surface, as shown in Figure 25. At higher temperatures SCG is observed on the fracture surfaces of NC-132, but the features of crack branching that indicate an operative slow crack growth mechanism are generally obscured by rapid oxidation at 1350°C and 1500°C. At 1500°C we have observed SCG to propagate through about 40% of the sample cross-section in NC-132.

With the behavior of NC-132, containing nominally 1% MgO, serving as a baseline, we can describe what happens when greater amounts of oxide additives are used to achieve densification. This applies, for instance, in the early development of a material, or in cases where the material is being developed for lower temperature applications, where economic considerations lead to larger amounts of oxide additives being used in processing. Kyocera, for instance, has developed a HP-Si_3N_4 with 4% MgO and 5% Al_2O_3 additives. Figure 23 illustrates that the low temperature strength is only maintained out to ~750°C. The stress-strain behavior correlates with this observation. Figure 26 illustrates that linear stress-strain behavior is exhibited for Kyocera SN-3 at 750°C, with distinctly nonlinear behavior obtained at 1000°C and above. Table 8 shows that this material contains ~10% oxide intergranular phase. Since this material is MgO-doped, it is expected that this phase is largely amorphous and deforms quite readily leading to strength reduction caused by SCG. Figure 27 shows the appearance of the fracture surface of
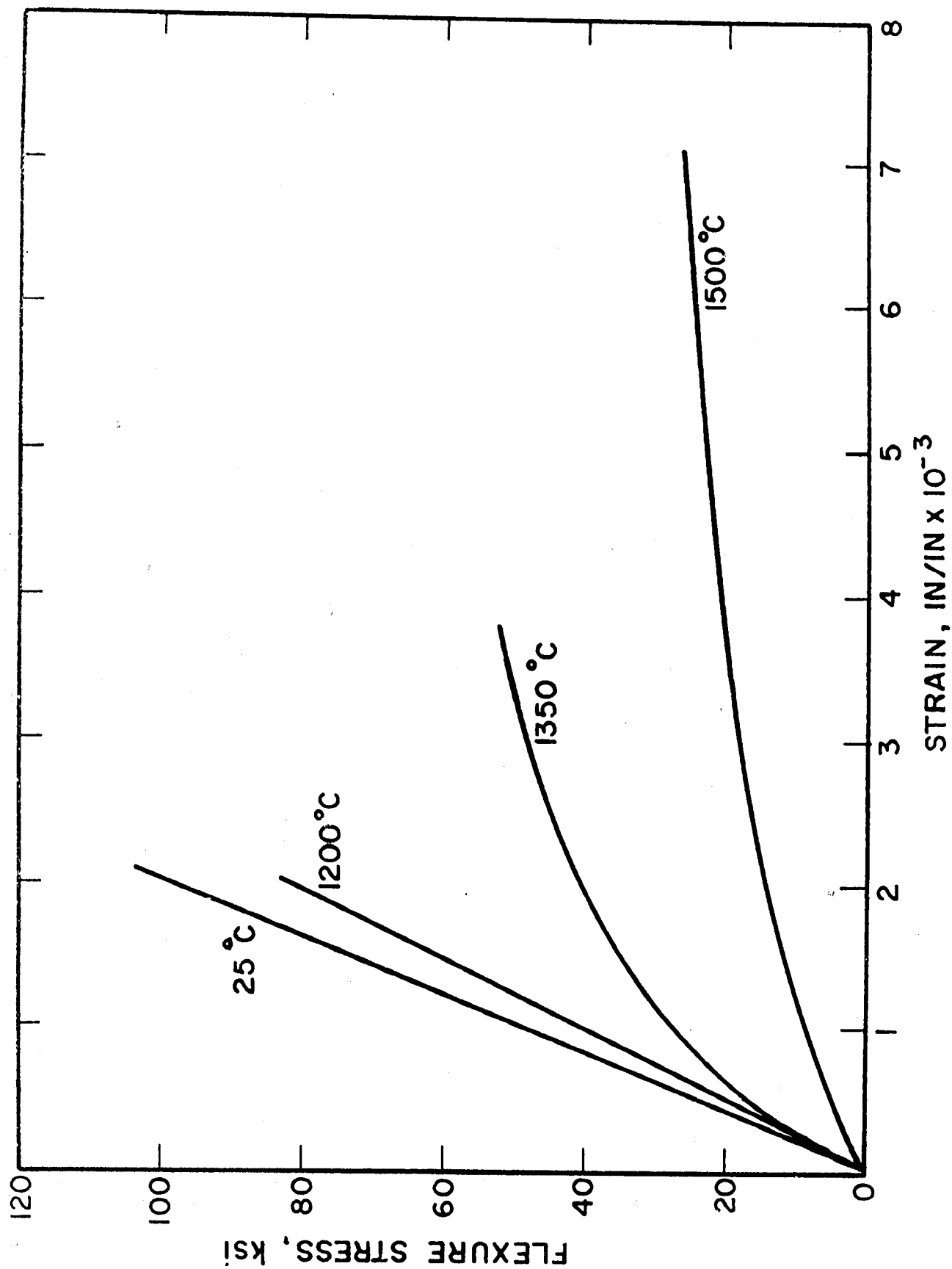
Figure 24. Representative flexural stress-strain behavior of Norton NC-132, HP-Si$_3$N$_4$ (1% MgO).

Figure 25. Fracture Surface (Tensile Surfaces Together) of Norton NC-132 HP-Si$_3$N$_4$ (1% MgO) Broken in Flexure at 1200°C.
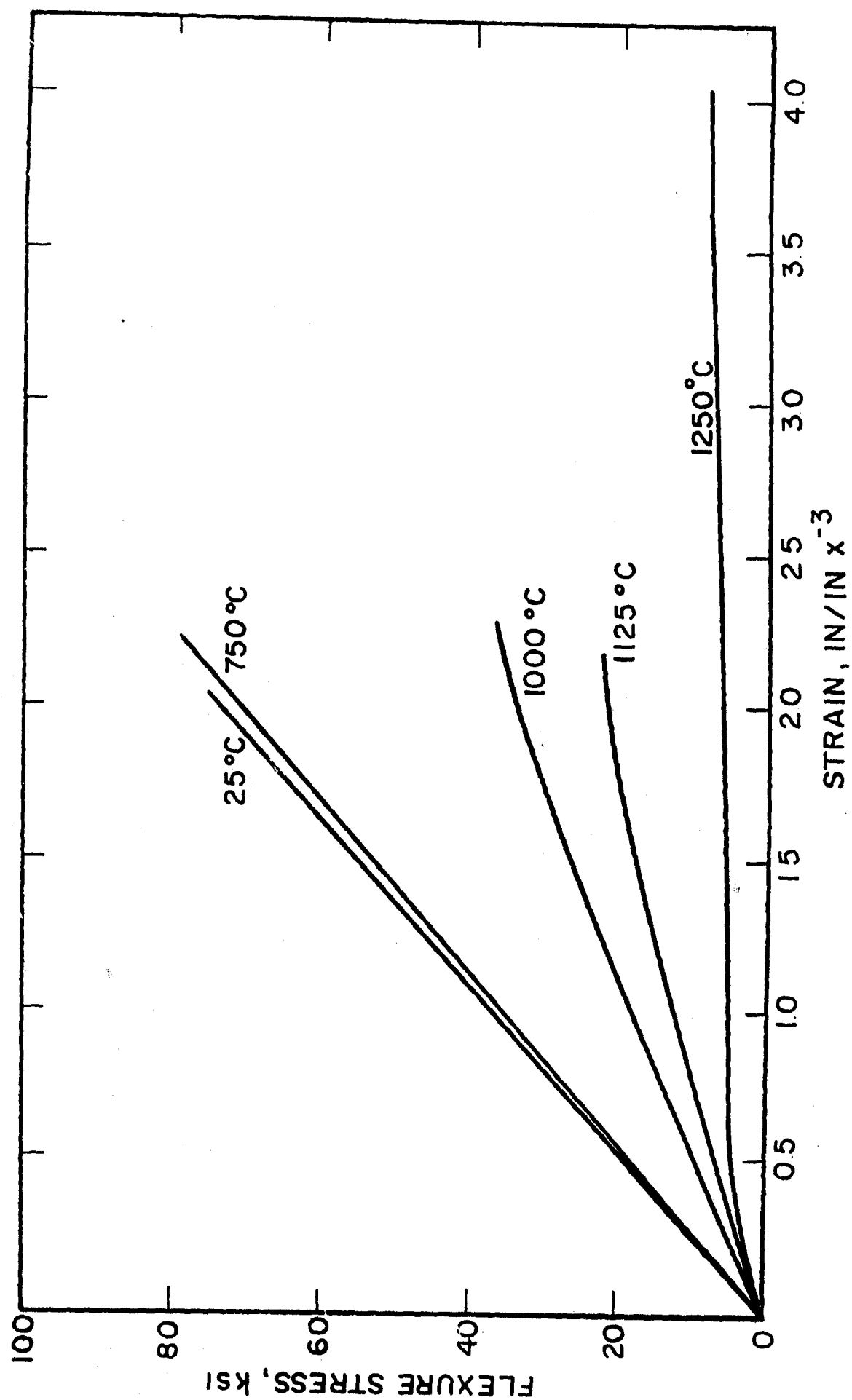
Figure 26. Flexural stress-strain behavior of Kyocera SN-3 HP-Si$_3$N$_4$ (4% MgO, 5% Al$_2$O$_3$).
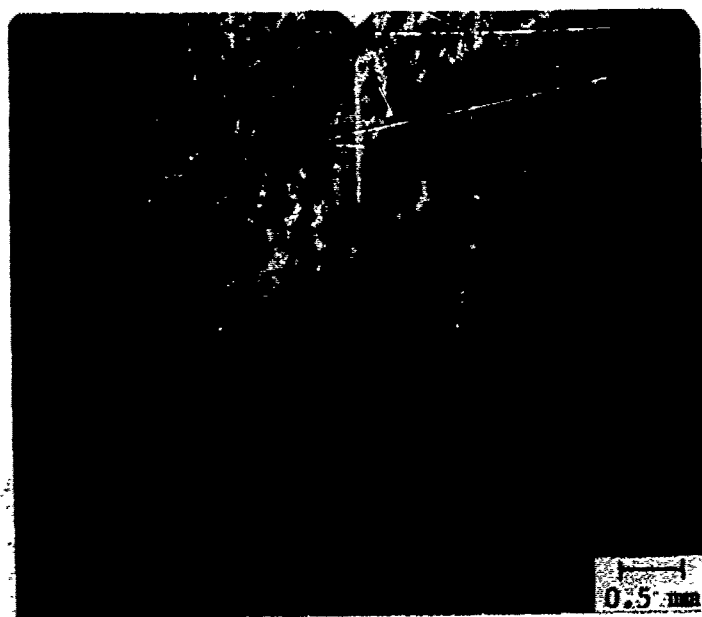
Figure 27. Fracture surface (tensile
surfaces together) of Kyocera SN-3
HP-Si$_3$N$_4$(4% MgO, 5% Al$_2$O$_3$) tested
in flexure at 1125°C.

the Kyocera material tested at 1125°C. The extensive subcritical crack growth is evident. Similar reasoning can be used to explain the behavior of the FMI HP-Si$_3$N$_4$ containing nominally 4% MgO. The stress-strain behavior presented in Figure 28 illustrates distinctly nonlinear behavior at 1250°C.

(b) Y$_2$O$_3$ Additives. It was recognized by the early-to-mid 1970's that MgO additives resulted in amorphous magnesium silicate ("glassy") grain boundary phases in HP-Si$_3$N$_4$. We discussed the use of CeO$_2$ and Y$_2$O$_3$ as alternate additives in the final report on Contract F33615-75-C-5196 (AFML-TR-79-4188).[44] The graphical results are presented for early versions of such materials in Figures 29 and 30. The problem with these materials was generally that while good densification was achieved, a major problem existed at intermediate temperatures in the form of accelerated oxidation of one of the phases present, leading to material destruction. This is discussed in detail in Section 11, dealing with cumulative oxidation results to date.

A major emphasis in the Si$_3$N$_4$ technical community during the time of the present program was finding a suitable location in the Y$_2$O$_3$-SiO$_2$-Si$_3$N$_4$ phase diagram in which to process to avoid the oxidation instability problem. The Y$_2$O$_3$-modified HP-Si$_3$N$_4$ materials from Westinghouse and Toshiba evaluated on the present program illustrate the improvements that have been achieved.

Figure 31 illustrates that these two Y$_2$O$_3$-modified Si$_3$N$_4$ materials show much promise for improved high temperature strength. This is particularly evident for Toshiba HP-Si$_3$N$_4$ (4% Y$_2$O$_3$, 3% Al$_2$O$_3$). Figure 31 illustrates the improved strength at T > 1200°C for this material relative to NC-132. The stress-strain behavior for the Toshiba material shown in Figure 32 confirms the decreased intergranular plasticity when compared to NC-132. No evidence of SCG is visible on the fracture surface of Toshiba 4% Y$_2$O$_3$, 3% Al$_2$O$_3$-modified Si$_3$N$_4$ tested at 1350°C, as illustrated in Figure 33. Oxidation of this Y$_2$O$_3$, Al$_2$O$_3$-doped material was rapid enough at 1500°C to completely obscure the fracture
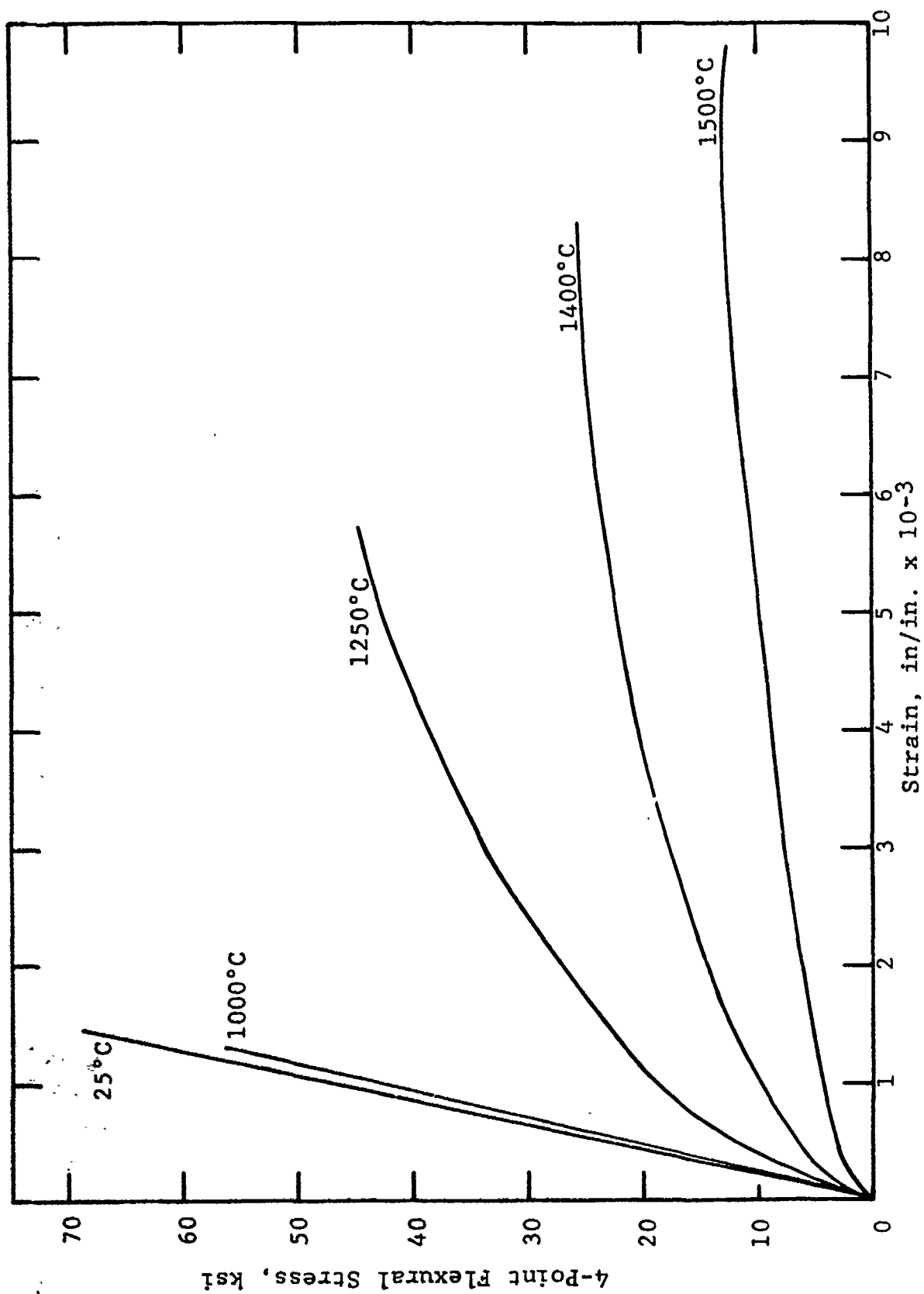
Figure 28. Representative flexural stress-strain behavior of Fiber Materials, Inc. HP-Si$_3$N$_4$ (4% MgO)
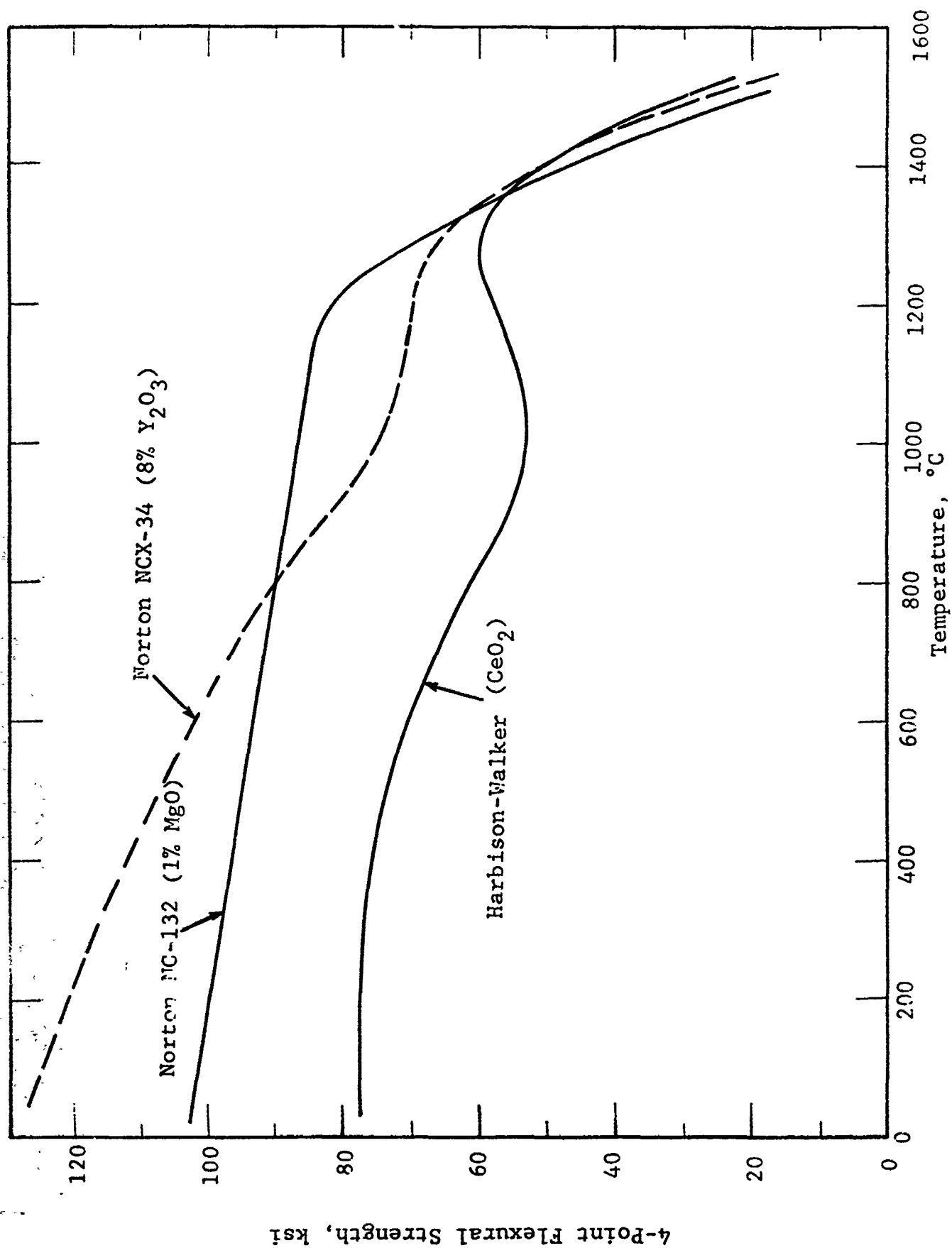
Figure 29. Flexural strength of hot-pressed silicon nitride materials.

109
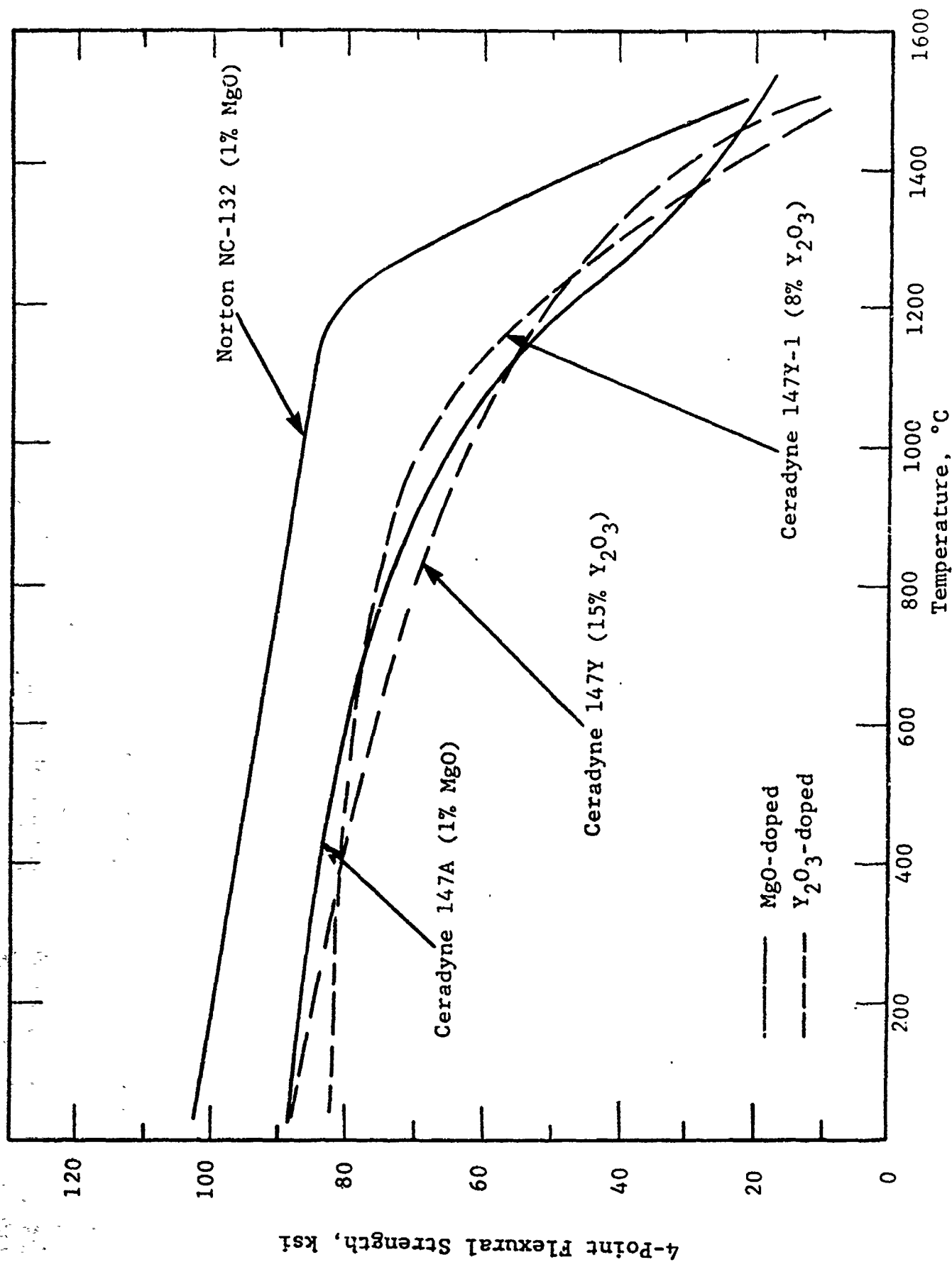
Figure 30. Flexural strength of MgO- and Y_2O_3-doped HP-Si_3N_4 materials
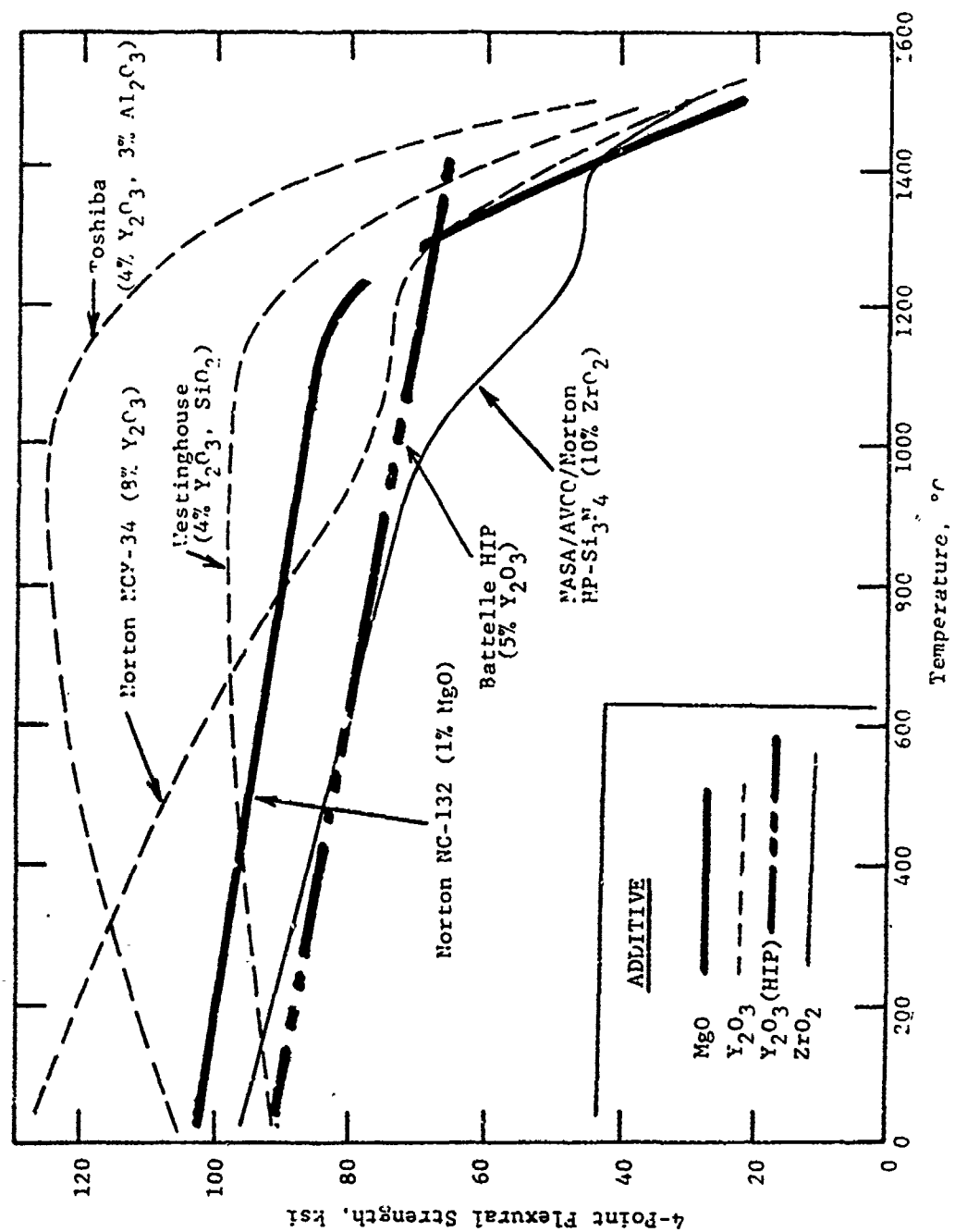
Figure 31. Flexure strength of various HP- and HIP-MgO, Y_2O_3, and ZrO_2-containing silicon nitride materials.

111
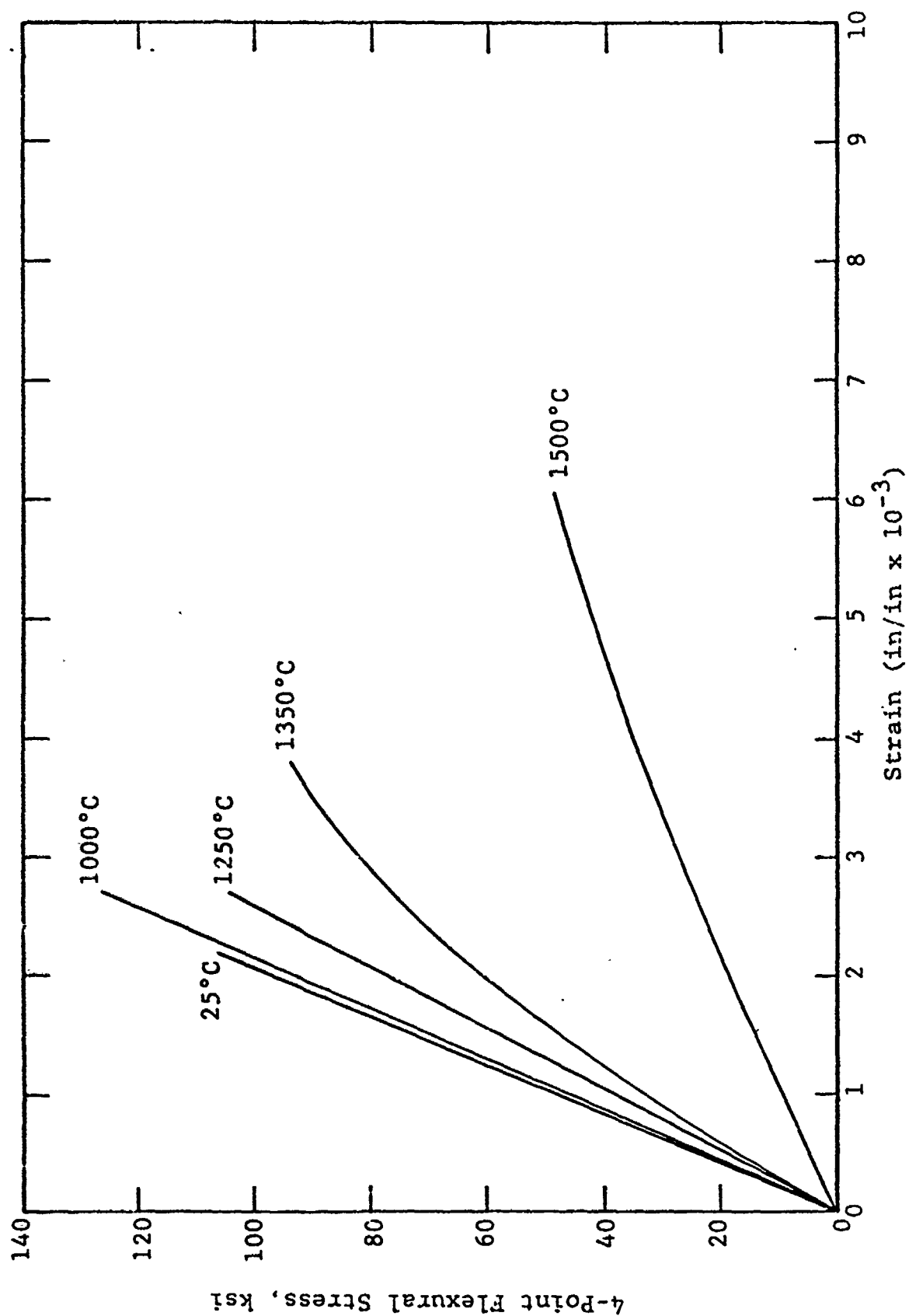
Figure 32. Representative flexural stress-strain behavior of Toshiba HP-Si$_3$N$_4$ (4% Y$_2$O$_3$, 3% Al$_2$O$_3$).
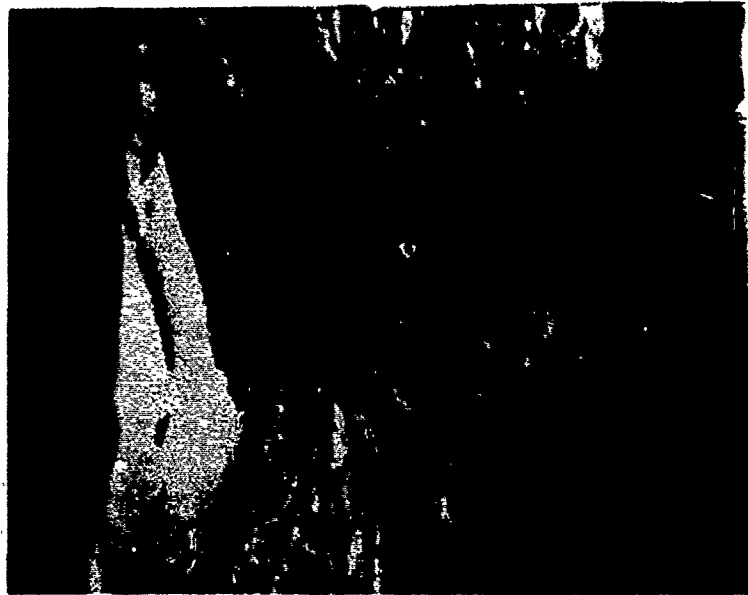
16X

Figure 33.   Fracture surface (tensile surfaces
together) of Toshiba HP-Si_3N_4 (4% Y_2O_3, 3%
Al_2O_3) broken in flexure at 1350°C (sample
T01F30).

features. However, the oxidation rate of Y_2O_3, SiO_2-modified Si_3N_4 structures is lower, and the fracture features at both 1350° and 1500°C are readily observed for Westinghouse $HP-Si_3N_4$, as shown in Figure 34. This material exhibited improved strength when compared to NC-132 (Figure 31), with no detectable SCG at 1350°C. At 1500°C, some SCG is visible on the fracture surface, as shown in Figure 34. These observations correlate with the shape of the stress-strain curve for the Westinghouse material, presented in Figure 35. Note that at 1250°C nearly linear behavior was obtained, whereas the stress-strain relationship is distinctly non-linear at 1500°C.

The improved elevated temperature strength of the Westinghouse and Toshiba materials is the result of the use of Y_2O_3 as a densification additive. Y_2O_3 dopants result in an oxide intergranular phase that can be crystallized by post-densification heat treatment. This results in more deformation resistant grain boundaries, and less grain boundary sliding, resulting in less subcritical crack growth. The stress-strain behavior and appearance of the fracture surfaces confirm this. X-ray diffraction studies, however, were inconclusive in attempts to identify crystallinity within intergranular regions. Higher resolution techniques such as transmission electron microscopy are required to detect the presence of a crystalline intergranular phase.

These results for the Westinghouse and Toshiba materials using Y_2O_3 as a processing additive illustrate the potential of ceramics to be successfully utilized in structural high temperature applications. It is judged that the Westinghouse material has extended the temperature limit approximately 100°C beyond that of MgO-doped NC-132 $HP-Si_3N_4$. The ~90 ksi room-temperature strength is maintained out to 1250°C, where linear stress-strain behavior is still observed. At 1350°C, the strength drops to ~63 ksi, but there is only a slight departure from stress-strain linearity, and SCG is not visible optically on fracture surfaces. The Toshiba $HP-Si_3N_4$, modified by 4% Y_2O_3 and 3% Al_2O_3 addition, also extends the potential use temperature of silicon nitride out

114

16X

(a) 1350°C

12X

(b)   1500°C

Figure 34.   Fracture surfaces (tensile
surfaces together) of Westinghouse
HP-S$_3$N$_4$ (4% Y$_2$O$_3$, SiO$_2$) tested at
1350°and 1500°C.
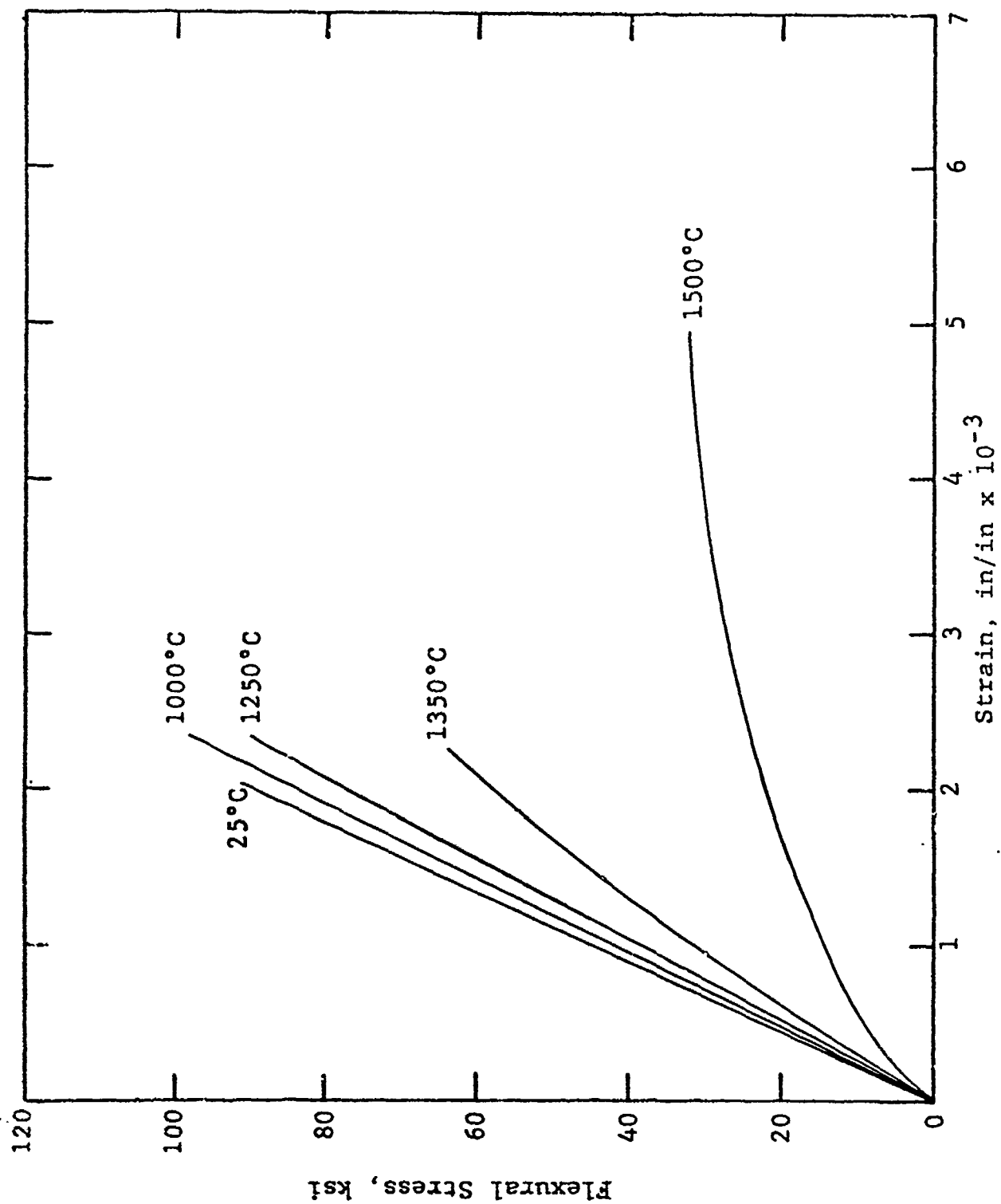
Figure 35. Representative flexural stress-strain behavior of Westinghouse $HP-Si_3N_4$.

116

to 1350°C. This material exhibited a bend strength of 94 ksi at this temperature, with nearly linear stress-strain, and no optically discernible evidence of subcritical crack growth on the fracture surfaces. However, the Toshiba HP-Si_3N_4 (4% Y_2O_3, 3% Al_2O_3) appears to be oxidation-limited at 1500°C. This is thought to be due to the Al_2O_3 additive.

These results are encouraging. They demonstrate that Y_2O_3 additions can be used to achieve a deformation-resistant intergranular phase that results in improved properties at elevated temperature. The Toshiba material achieved this through the use of Y_2O_3 and Al_2O_3 additives. The Westinghouse material achieved this through the use of Y_2O_3 and SiO_2 additives. Other oxide additives, or combinations of successful ones, however, can have an adverse effect on high temperature strength. For instance, Figure 36 illustrates another Toshiba material, which was developed for a lower temperature application. It exhibited rapid strength degradation after T ~1000°-1100°C. This material contained 3% Y_2O_3, 4% Al_2O_3, and an undetermined amount of SiO_2. The stress-strain behavior shown in Figure 37 further illustrates that degradation occurs at above 1100°-1200°C. Note the extremely nonlinear behavior at 1350°C. Figure 38 confirms that significant crack-branching was observed on the fracture surfaces at temperatures as low as 1250°C. Table 8 showed that almost twice as much oxygen was present compared to the other Toshiba material. Apparently SiO_2 was present in significant quantities, and either resulted in amorphous silicate grain boundary phases or inhibited the crystallization of yttrium silicate intergranular phases. However, the presence of SiO_2 does increase the oxidation resistance of Y_2O_3 and Y_2O_3-Al_2O_3 modified silicon nitride materials.

The success of Y_2O_3 as a densification aid for HP-Si_3N_4 lies in the fact that the resulting yttrium silicate intergranular phase can be crystallized. If more than 4% Y_2O_3 is used (i.e., 8% or more), we have found that there is a strong tendency to be in that part of the Si_3N_4-Y_2O_3-SiO_2 phase triangle that results

117
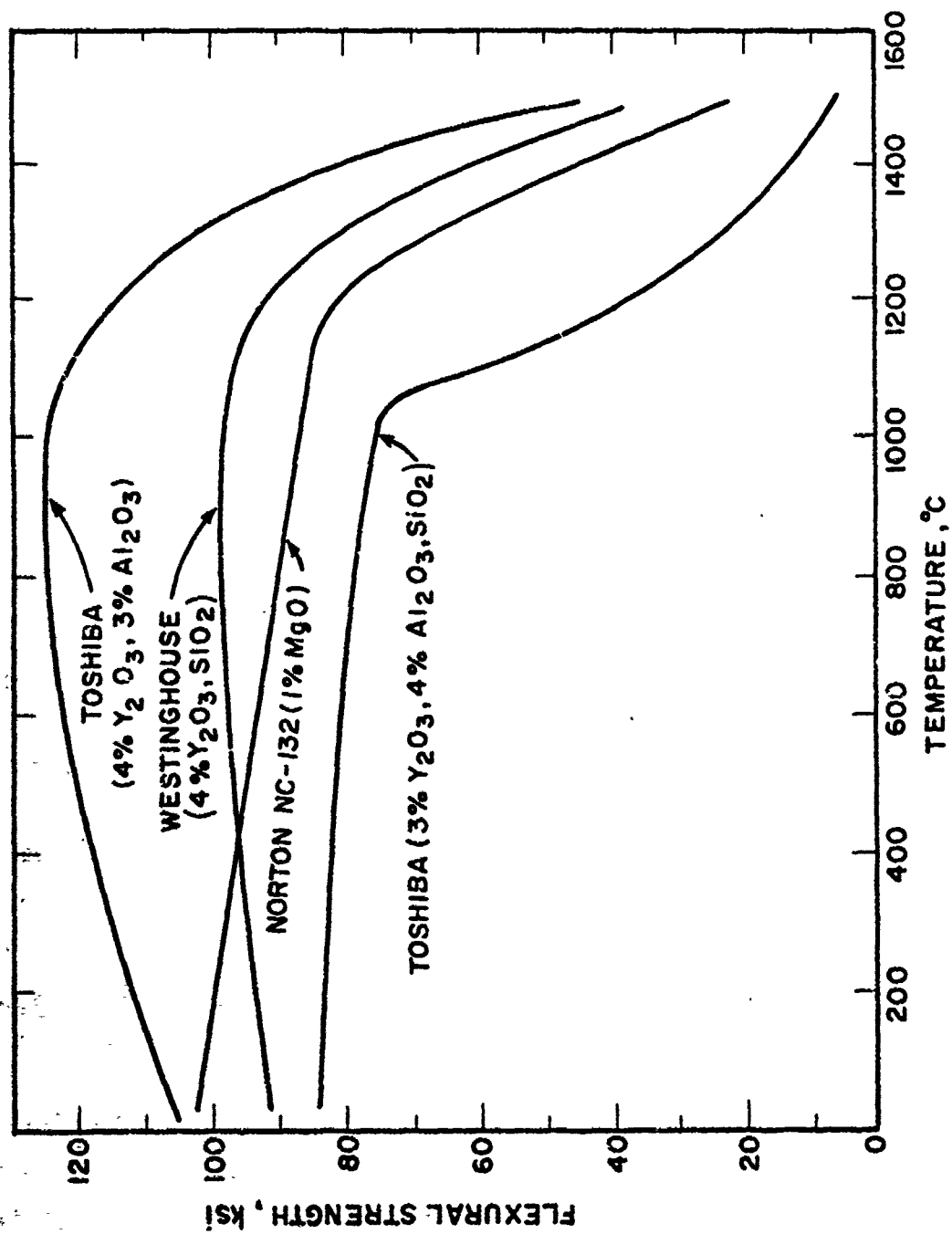
Figure 36. Flexural strength of MgO- and Y_2O_3-doped HP-Si_3N_4 materials.

118
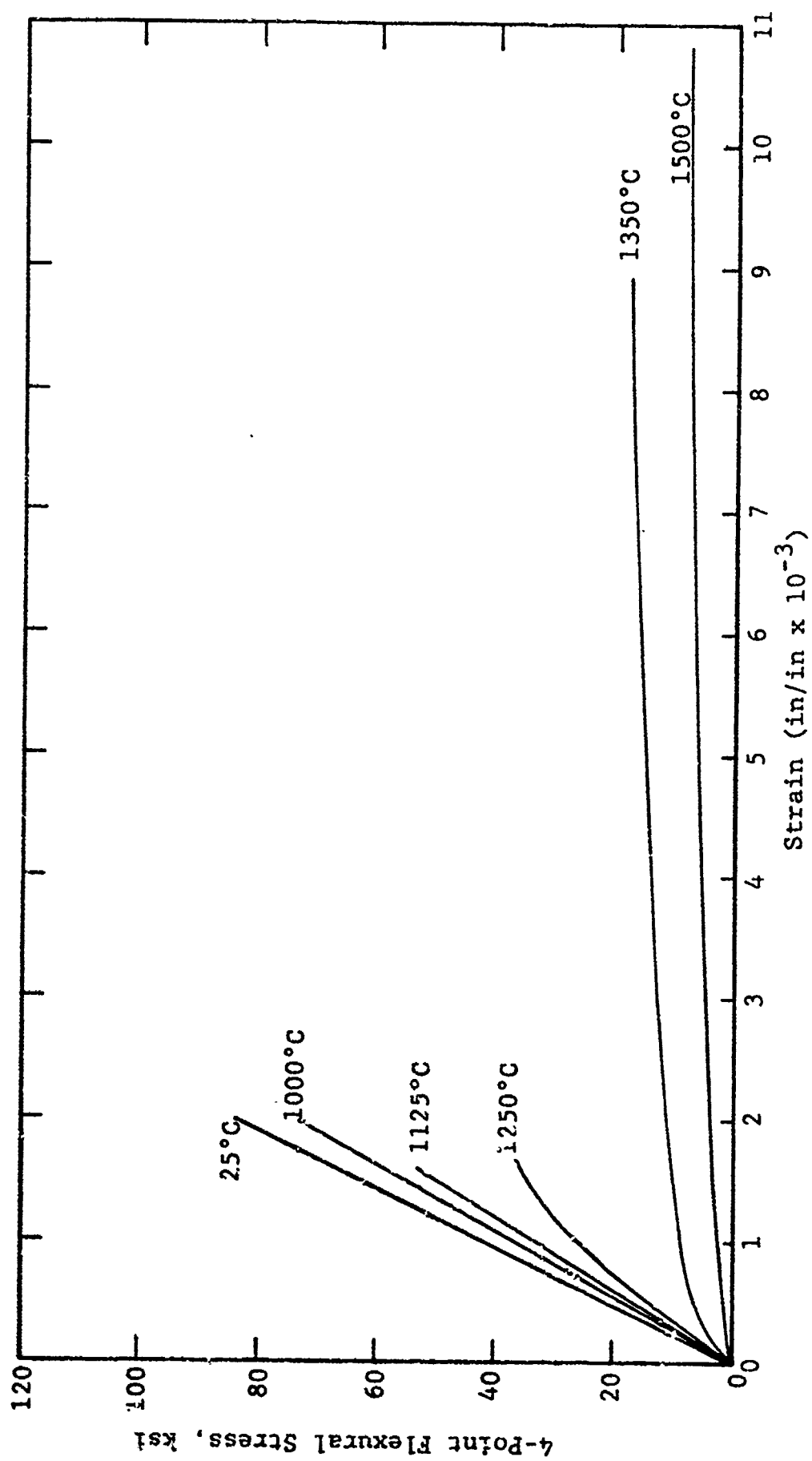
Figure 37. Representative flexural stress-strain behavior of Toshiba HP-Si$_3$N$_4$ (3% Y$_2$O$_3$, 4% Al$_2$O$_3$, SiO2).
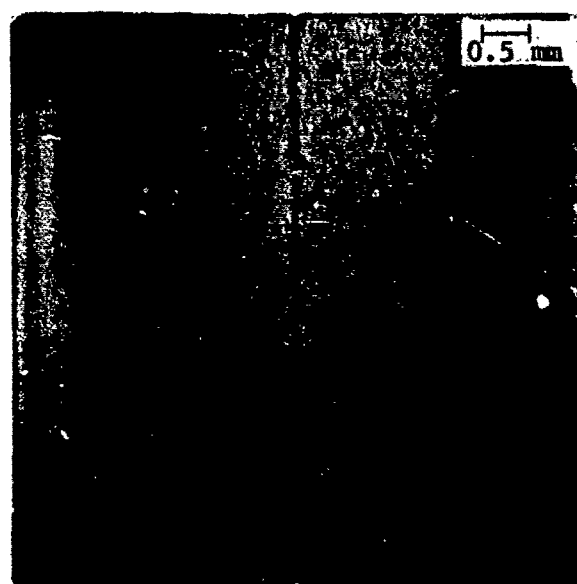
(a) 1250°C
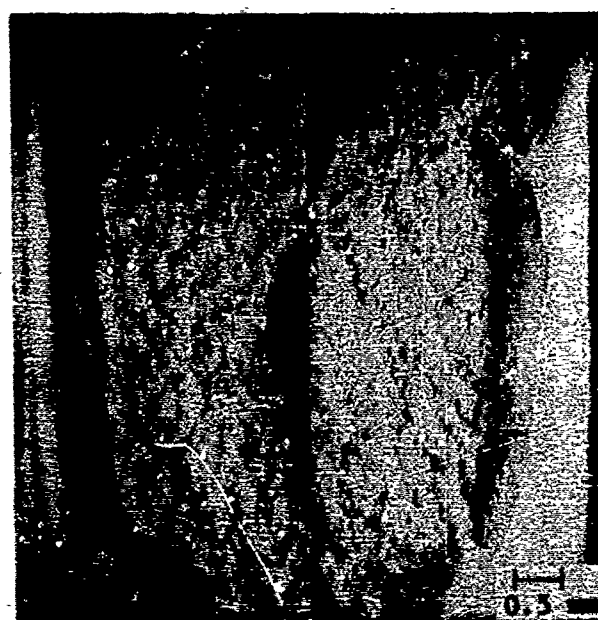
(b) 1350°C

Figure 38. Fracture surface (tensile
surfaces together) of Toshiba HP-
Si_3N_4 (3% Y_2O_3, 4% Al_2O_3, SiO_2)
broken in flexure at 1250°C and
1350°C.

120

in oxynitride phases that are unstable in oxidizing environments. These phases experience accelerated oxidation, with resulting macrocracking of the ceramic body. This will be discussed in detail in Section 11, Oxidation.

(c) HIP-Si_3N_4 (Y_2O_3). The use of Y_2O_3 densification additives for Si_3N_4 discussed above illustrates that intergranular crystallinity greatly impedes the relative movement of grains, thereby reducing the phenomenon of slow crack growth accommodated by cavity nucleation, extension of pre-existing triple-point voids, etc. There is one other route to decreasing SCG being investigated by several laboratories: hot isostatic pressing. HIP'ing is performed at much higher pressures than can be achieved in uniaxial hot pressing (e.g., 30,000 psi). Thus, the Si_3N_4 powder can be compacted to full density using a lower concentration of oxide additive, thereby minimizing slow crack growth, and improving the elevated temperature strength and creep resistance. HIP'ing has the additional economic advantage of the potential for near-net-shape fabrication of complex components.

A small quantity of Battelle HIP-Si_3N_4 containing nominally 5% Y_2O_3 was available for evaluation on this program. This material was prepared by isopressing Si_3N_4 powder at 30,000 psi, followed by HIP'ing at 1725°C for 1 hr at 30,000 psi.[45] The material was reported to consist of submicron equiaxed Si_3N_4 grains and a thin amorphous intergranular film that is very refractory. Battelle compressive creep data for this material are compared to flexural creep data for various Y_2O_3-containing HP-Si_3N_4 evaluated on the present program in Figure 39. This material exhibits low creep rates and shows much promise. Accordingly, time-dependent flexure tests were conducted on the present program at 1400°C in air. In this test the fracture stress is compared with the time-to-failure. These tests are sometimes referred to as dynamic fatigue or differential strain rate tests, and yield a quantitative measure of the time-dependent strength degradation by the phenomenon of subcritical crack growth. These tests are essentially regular flexure tests where the
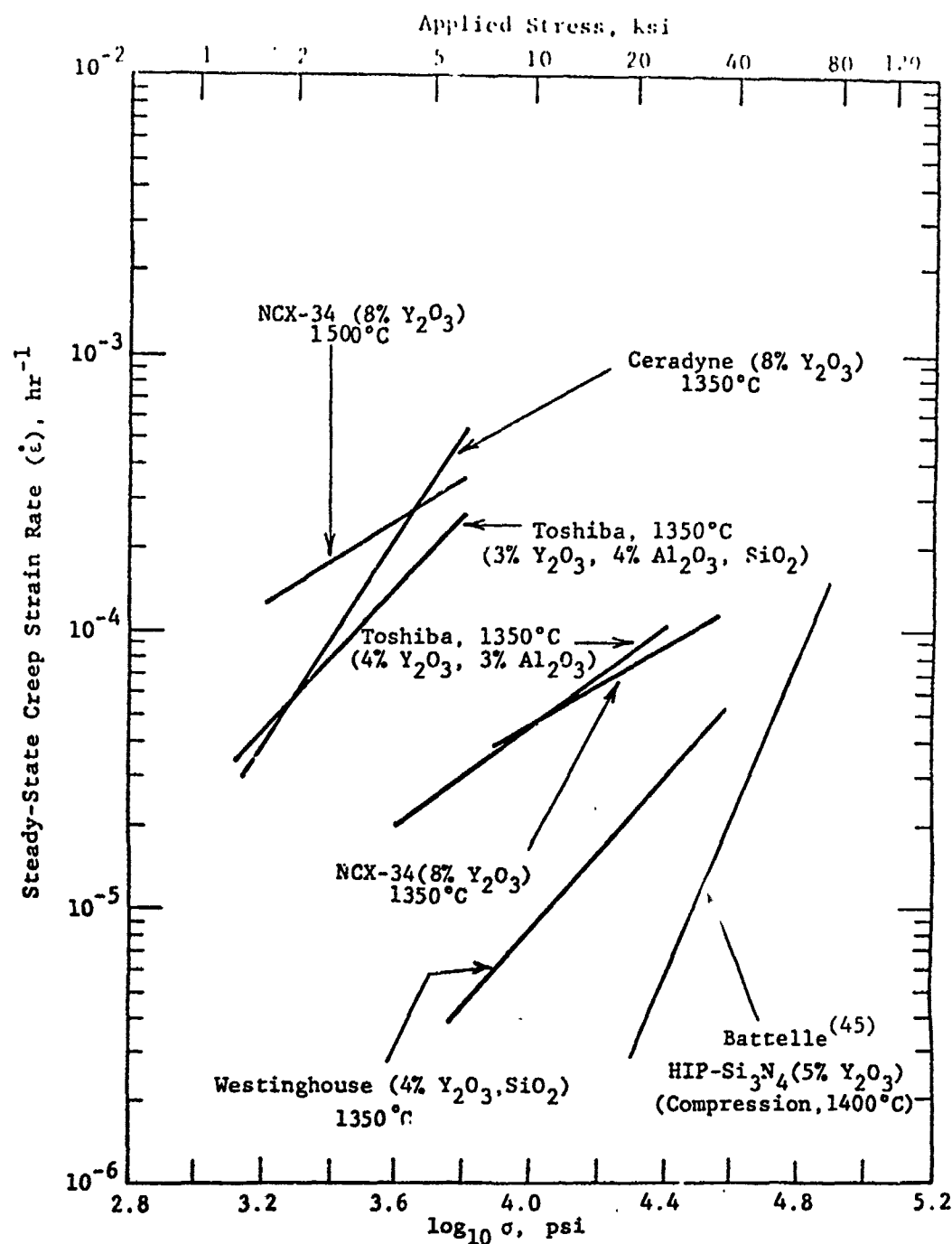
Figure 39. Steady-state flexural creep rate vs. applied stress for various Y_2O_3-modified Si_3N_4 materials.

time-to-failure is varied by adjusting the testing machine cross-head speed. Regression analysis of the resulting fracture strength vs. time relation yields a value for n in the relation v = AK^n, where v is the crack velocity, A is a constant, and K is the stress intensity at the crack tip. A large value of n indicates very little subcritical crack growth, and thus time-invariant strength.

The results of these tests are plotted in Figure 40 along with (a) Battelle data on the same material, tested at 1400°C, but at a machine crosshead speed a factor of 25 faster (0.005 ipm), and (b) our fast fracture results (crosshead speed 0.02 ipm) for various other Y_2O_3-containing HP-Si_3N_4 materials evaluated on this program. It is seen that the Battelle HIP-Si_3N_4 (5% Y_2O_3) material has a room-temperature strength of ~90 ksi. The 1400°C strength of the HIP'ed material is very good, ~63 ksi. The present IITRI data agree with the Battelle generated strength. This material has a 1400°C fracture strength about the same as we previously found for Westinghouse HP-Si_3N_4, which is doped with nominally 4% Y_2O_3 and an undetermined amount of SiO_2. What is significant here is that the Battelle and IITRI strengths were measured at crosshead deformation rates a factor of 25 and 100, respectively, slower than the Westinghouse and other materials, as shown in Figure 40. This means that there is apparently very little subcritical crack growth occurring prior to fracture in the HIP'ed material (however, the Westinghouse material was not subjected to the slow (0.0002 ipm) flexure test, so no direct comparison can be made).

Figure 41 illustrates the fracture surfaces of the Battelle HIP-Si_3N_4 (5% Y_2O_3) material after slow 1400°C flexure testing, where the time-to-failure was typically 113 min. We see only slight evidence of crack branching on the fracture surfaces, the SCG region extending over about 3% of the test bar cross-section. Battelle[45] indicated that it was reasonable to assume that this material would exhibit some SCG prior to fracture at 1400°C, but they could not detect any in optical examination of the fracture

123
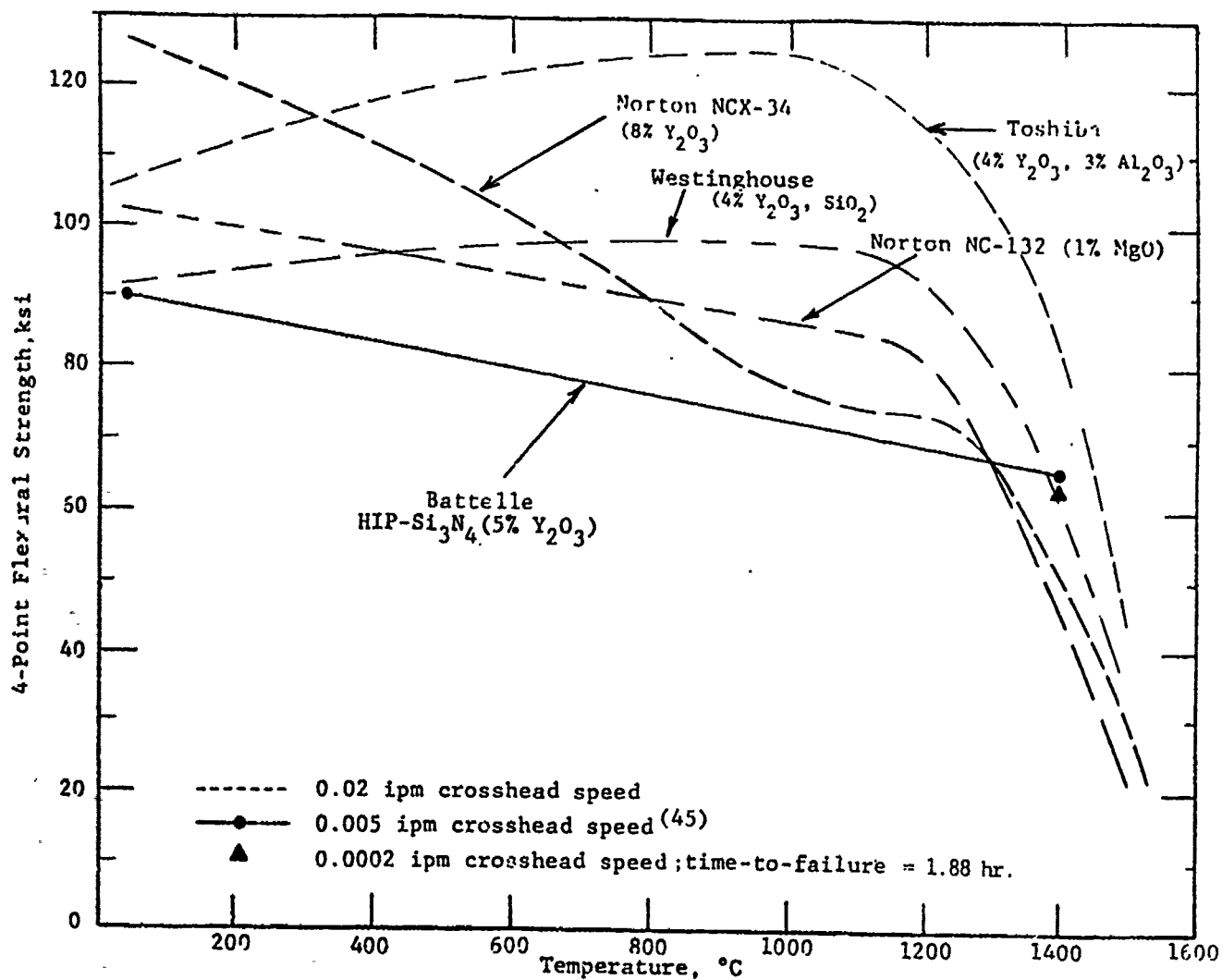
Figure 40. Flexural strength of MgO- and Y_2O_3-doped HP-Si_3N_4 materials.

17X

(a) Sample BW1F1

17X
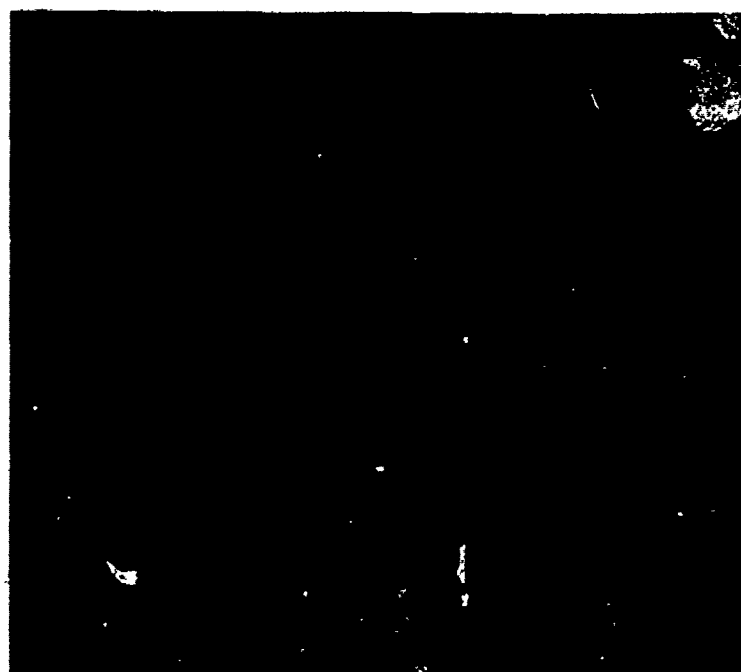
(b) Sample BW1F2

Figure 41. Fracture surfaces of Battelle HIP-Si$_3$N$_4$ (5% Y$_2$O$_3$) after time-dependent flexure test at 1400°C. (The time-to-failure was typically 113 min; the machine crosshead speed was 0.0002 ipm.)

surfaces. However, their test was conducted at a deformation rate a factor of 25 faster than the present IITRI tests. The time-to-failure in the Battelle test was ~5 min (by IITRI estimate, as no time-to-failure data were reported by Wills and Brockway). Thus, the IITRI and Battelle results are consistent: very good strength retention at 1400°C, and only slight evidence of SCG phenomena when the fracture times approach 2 hr.

It is interesting to compare our present slow-flexure results on this HIP'ed material with results we have obtained for Norton NC-132 HP-Si_3N_4 (1% MgO) and Norton NCX-34 HP-Si_3N_4 (8% Y_2O_3). In this case, direct comparison of the materials is possible since all were flexure-tested at a crosshead deformation rate of 0.0002 ipm, which resulted in fracture times on the order of 2-3 hr. The comparison of these materials is presented in Figure 42, where fracture stress is plotted against time-to-failure. It is seen that Norton MgO- and Y_2O_3-doped HP-Si_3N_4 materials experienced significant strength degradation at 1400°C, the degree of subcritical crack growth being characterized by n values of 16 and 12, respectively. In contrast, the 1400°C n value of Battelle HIP-Si_3N_4 (5% Y_2O_3) was estimated to be much higher, n ~30, which indicates much less SCG.

The fracture surface features of these three materials are consistent with this interpretation. The appearance of the fracture surface of NC-132 HP-Si_3N_4 (1% MgO) after 0.0002 ipm flexure testing is presented in Figure 43. The strength of NC-132 was 33% lower than the 1400°C fast fracture strength, the time-to-failure was typically 44 min, and slow crack growth extended over ~20% of the sample cross-section. For NCX-34 HP-Si_3N_4 (8% Y_2O_3), the strength for the same test conditions was 47% lower than the 1400°C fast fracture strength; but the failure time was typically 206 min, considerably longer than for NC-132. Figure 44 illustrates that the degree of SCG was lower in NCX-34, the SCG markings only extending over ~10% of the bend bar transverse section. These two fracture surfaces for NC-132 and NCX-34 are compared to the fracture surface for Battelle HIP-Si_3N_4 (5% Y_2O_3) that was
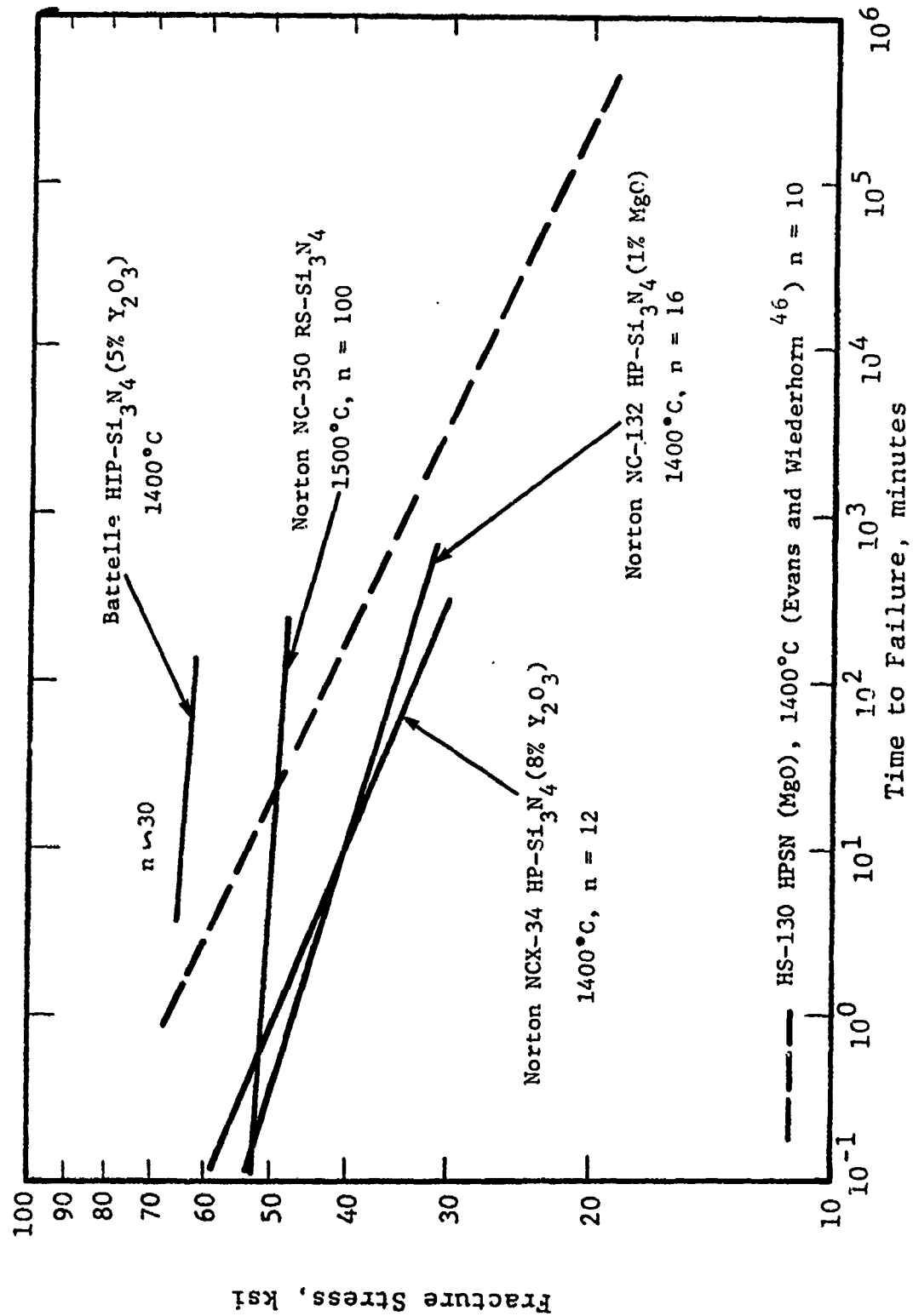
Figure 42. Strength degradation by subcritical crack growth.

127
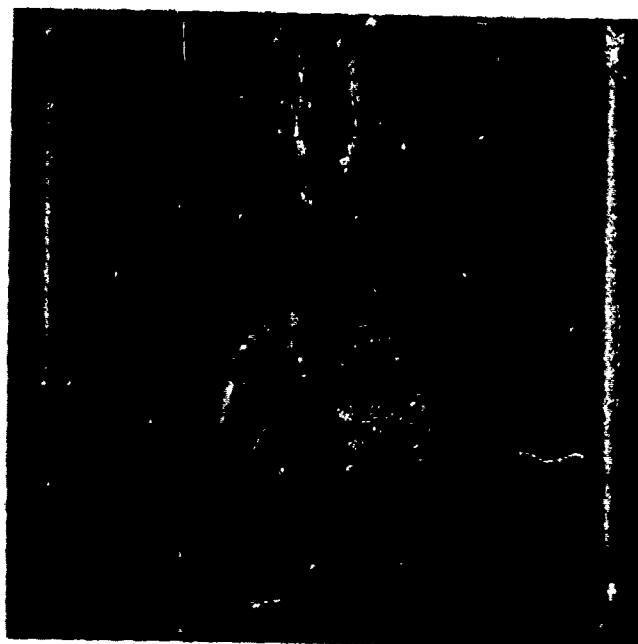
12X

Figure 43. Fracture surface of Norton NC-132 HP-Si₃N₄ (1% MgO) after time-dependent flexure test at 1400°C. (The strength was 33% lower than the 1400°C fast fracture strength; the time-to-failure was typically 44 min; the machine crosshead speed was 0.0002 ipm.)

12X

(a) Sample 51F60
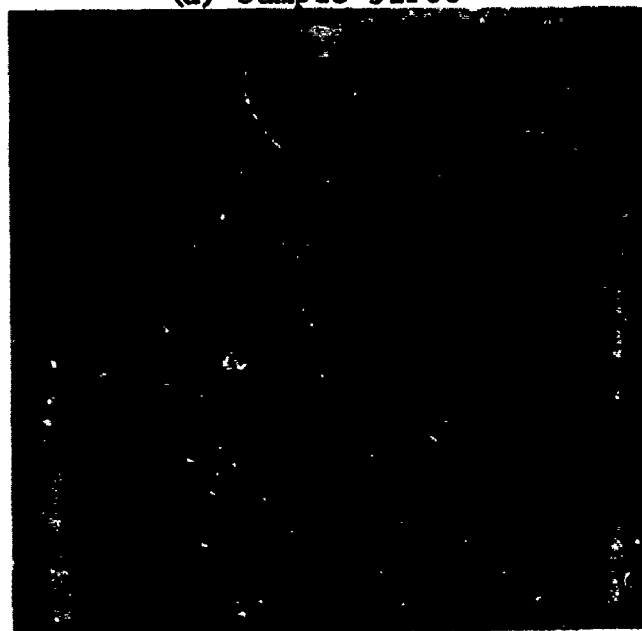
12X

(b) Sample 51F58

Figure 44. Fracture surfaces of Norton NCX-34
HP-Si$_3$N$_4$ (8% Y$_2$O$_3$) after time-dependent flex-
ure test at 1400°C. (The strength was 47%
lower than the 1400°C tast fracture strength;
the time-to-failure was typically 206 min;
the machine crosshead speed was 0.0002 ipm.)

presented in Figure 41. As discussed above, SCG features only
extended over ~3% of the cross-sectional area of the HIP'ed
material.

Therefore, the present results indicate that the degree of
subcritical crack growth and associated strength degradation can
be substantially reduced by utilizing the high pressure attain-
able with the HIP'ing process to attain full density with a lower
concentration of oxide additive. The ultimate behavior goal
might be to achieve the time-invariant strength of additive-free
reaction-sintered Si_3N_4.[*] Figure 42 illustrates the results for
Norton NC-350 RS-Si_3N_4 in the slow flexure tests. The test tem-
perature was 1500°C (100°C higher than for the HP- and HIP-Si_3N_4
materials), and for all practical purposes the strength did not
vary with time (n = 100). This goal may not be reached for hot-
pressed or HIP'ed Si_3N_4, because some small amount of oxide addi-
tive may always be necessary to achieve full density in pressure-
assisted sintering of Si_3N_4 powder.

(d) ZrO_2-containing Si_3N_4. Yttria and ceria are not the
only potential additives for HP-Si_3N_4 being investigated. It has
been thought for some time that zirconia compounds in intergranu-
lar regions would be quite resistant to deformation. Furthermore,
zirconia-based materials might not exhibit the intermediate-
temperature phase instabilities often associated with yttria
additives.

NASA-Lewis supplied a HP-Si_3N_4 (10% ZrO_2)[**] material to this
program that has proven to be quite interesting. The material

---

[*]This comment is made only with respect to the absence of inter-
granular SCG at high temperature. Certainly, it is recognized
that the denser forms of Si_3N_4 have advantages over porous RS-
Si_3N_4 such as higher low-temperature strength and lower surface
area. Internal oxidation is one of the major disadvantages of
reaction-sintered Si_3N_4.

[**]AFWAL-developed Zyttrite, a fully stabilized ZrO_2 containing 6
mol% (10.8 wt%) Y_2O_3.

concept was developed by Vasilos et al[47] at AVCO in an attempt to improve the stress rupture behavior and creep strength of Si_3N_4 by using ZrO_2 additives to create a zirconium oxynitride grain boundary phase. The actual material evaluated in this program was fabricated at Norton Company, using the same starting powder and procedures used for NC-132. We have thus termed this material NASA/AVCO/Norton HP-Si_3N_4 (10% ZrO_2). Our verification of its improved creep properties will be presented in Section 8.

Figure 31 illustrated that the high-temperature strength of this material is generally lower than that of the other high-performance Si_3N_4 materials shown. However, fracture origins at all elevated temperatures were the same shiny dark inclusion particles that were the sources of fracture at room temperature. Thus, the NASA/AVCO/Norton material is distinctly different from the others. Its elevated-temperature strength is controlled by the same inclusion-related fracture origins that were dominant at 25°C. There is no evidence of subcritical crack growth in this material, even at 1500°C in the fast fracture test. Evidence for this is shown in Figure 45b. The optical photograph of the fracture surface reveals no observable markings that would indicate operative slow crack growth (SCG). Note also in Figure 45b that the 1500°C fracture surface features are not obscured at all by oxidation. Thus, it can be expected that ZrO_2 additives lead to superior oxidation resistance when compared to other oxide additives (such as MgO). For comparison, the 1500°C fracture surface of the Westinghouse HP-Si_3N_4 (4% Y_2O_3, SiO_2) material was shown in Figure 34b. Note the region of SCG extending across ~20% of the bend bar cross section. Figure 31 illustrates that the Toshiba HP-Si_3N_4 (4% Y_2O_3, 3% Al_2O_3) was the strongest Si_3N_4 evaluated on this program. Its fracture surfaces were badly obscured by oxidation at 1500°C. Thus, no estimate of the extent of SCG was possible (no attempts were made to remove the oxide, such as by soaking in hydrofluoric acid).

The stress-strain behavior for the NASA/AVCO/Norton material also indicates the presence of a deformation-resistant grain

131

24X
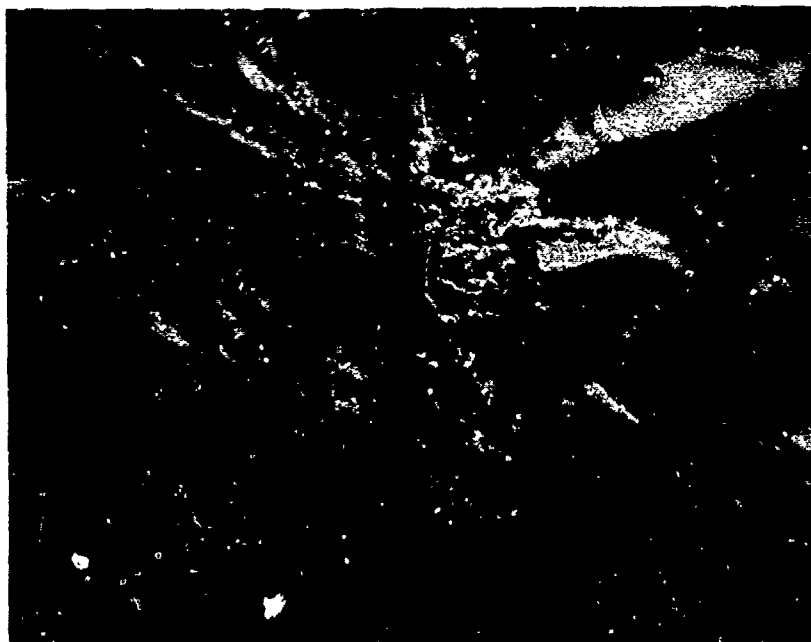
(a) Sample NA1F5 tested at room temperature

12X

(b) Sample NA1F14 tested at 1500°C

Figure 45. Fracture surfaces of NASA/AVCO/
Norton HF-Si_3N_4 (10% ZrO_2).

132

boundary phase. Figure 46 illustrates linear behavior in the limited testing at 1500°C. This is the first evidence of such behavior that has been observed for any hot-pressed Si_3N_4 evaluated on this program. The stress-strain behavior of the Y_2O_3-doped Toshiba and Westinghouse materials was presented in Figures 32 and 35, respectively. Note the nonlinearity at 1500°C, especially for the Westinghouse material.

The linear stress-strain behavior and the absence of observable SCG markings on the fracture surfaces of the NASA-AVCO/Norton HP-Si_3N_4 (10% ZrO_2) material in 1500°C fast fracture tests illustrate that this material has a very refractory intergranular phase. This will explain the excellent creep resistance for this material which is reported in Section 8. It would be expected, then, that this material would exhibit noticeably better time-dependent flexure strength and stress rupture behavior as well. Accordingly, fast and slow flexure strength tests were conducted at 1400°C, and the time-to-failure was recorded. The results of these constant stress rate tests are summarized in Figure 47, which illustrates the fracture stress vs. time for various silicon nitride materials evaluated on this program. The slope of the curves is -1/n, where n is the exponent in the $v = AK^n$ relation describing crack velocity vs. stress intensity. A high value of the n parameter in Figure 47 indicates less time dependence of the strength, and thus less subcritical crack growth. It is observed that the NASA/AVCO/Norton material exhibits the highest n value of any HP-Si_3N_4 material evaluated on this program (n = 36). This agrees with the fast fracture results discussed above. This material exhibits surprisingly little SCG and resultant strength degradation at elevated temperature. The fracture surface of a typical NASA/AVCO/Norton HP-Si_3N_4 (10% ZrO_2) material broken in slow flexure is shown in Figure 48. Note the absence of SCG markings. Corresponding fracture surfaces of the other hot-pressed silicon nitride materials compared in the stress-time plot of Figure 47 were shown in Figures 41, 43, and 44. The of SCG seen on the fracture surfaces
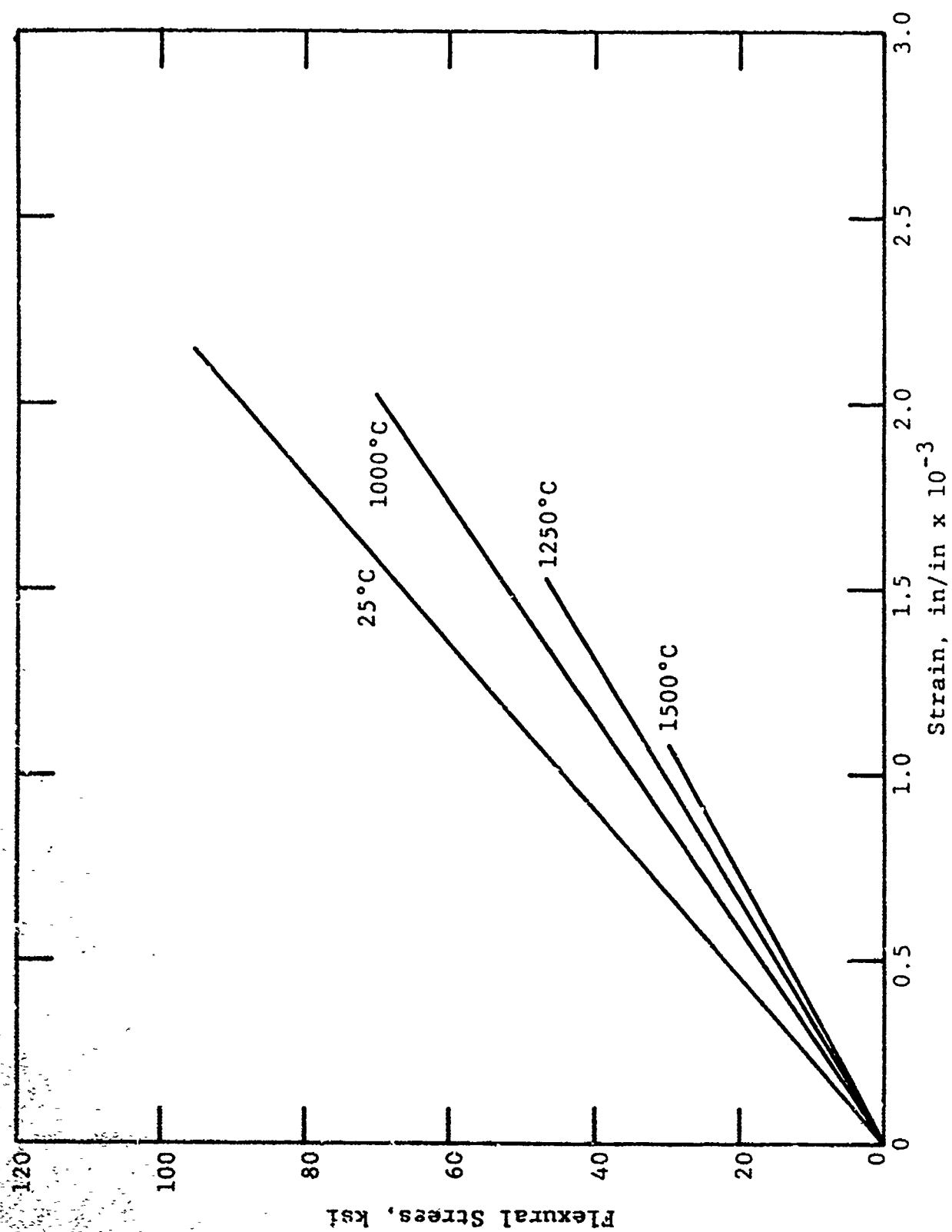
Figure 46. Flexural stress-strain behavior of NASA/AVCO/Norton HP-Si$_3$N$_4$ (10% ZrO$_2$).
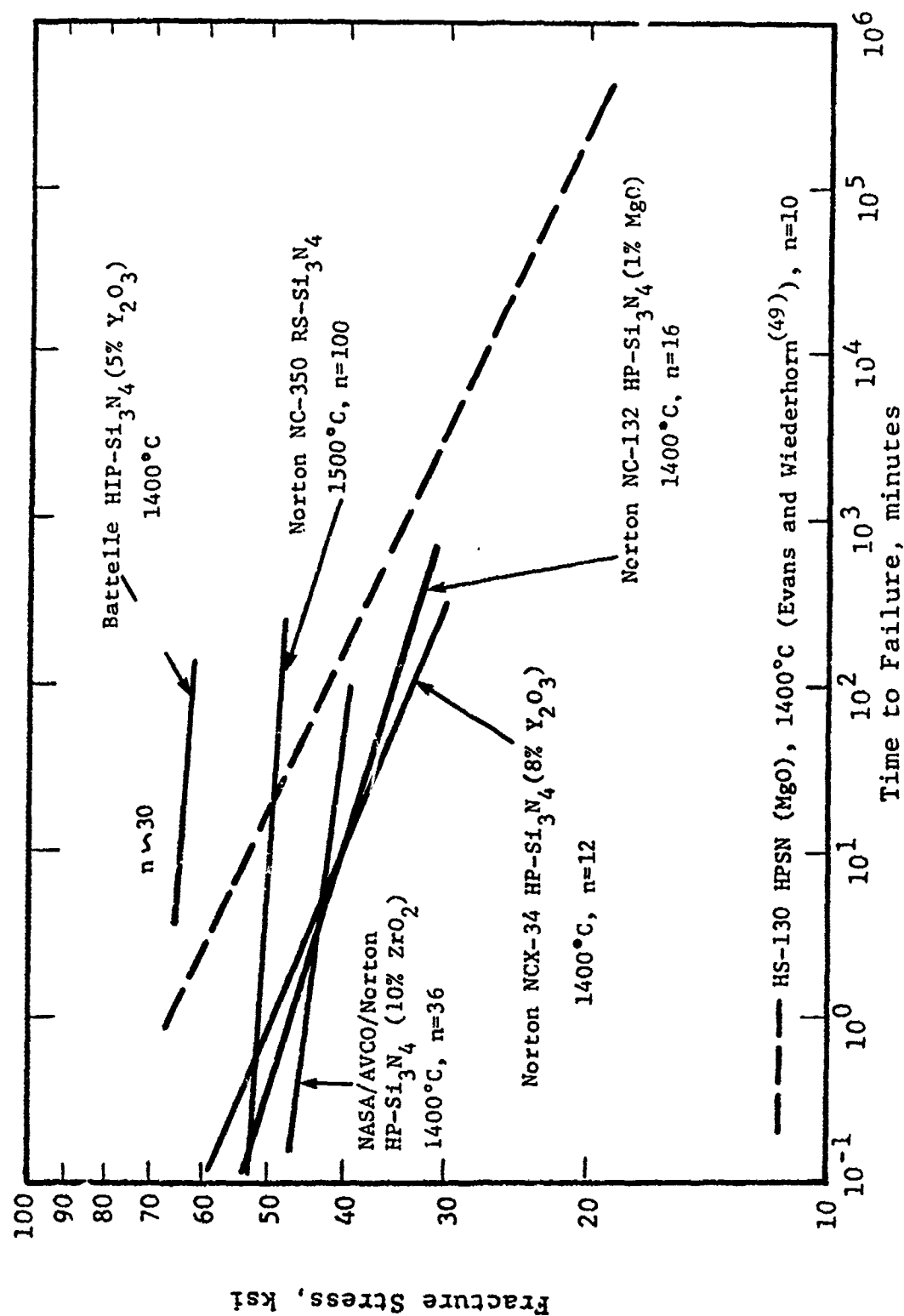
Figure 47. Strength degradation by subcritical crack growth.

135

Sample NA1F40   12X

Figure 48. Fracture surface of NASA/AVCO/Norton
HP-Si$_3$N$_4$ (10% ZrO$_2$) after time-dependent flexure
test at 1400°C. (The strength was typically 13%
lower than the 1400°C fast fracture strength;
the time-to-failure was typically 90 min; the
maching crosshead speed was 0.0002 ipm.)

136

correlates with the amount of strength degradation with time seen in Figure 47.

Since the NASA/AVCO/Norton material exhibited no noticeable SCG in fast fracture tests, and very good behavior in the slow flexure tests where the failure times were typically 1-2 hr, it was of interest to evaluate this material at much longer times. Accordingly, flexural stress rupture tests were conducted, where a constant stress was applied, and the time to failure was recorded. The tests were conducted at 1400°C in air atmosphere. The results are summarized in Figure 49. It is observed that at an applied stress of 30 ksi (65% of the 1400°C fast fracture strength) sample failures were not obtained in times as long as over 1700 hr. Even when fracture was obtained, for instance at 209 hr at an applied stress of 35 ksi, Figure 50 illustrates the absence of significant SCG. This is a significant achievement in hot-pressed silicon nitride technology, and indicates the advantage of using ZrO_2 as an additive. In contrast, Figure 47 illustrates the much more rapid strength degradation of MgO-doped HP-Si_3N_4.

In summary, it has been shown that the NASA/AVCO/Norton HP-Si_3N_4 (10% ZrO_2) material exhibits superior high-temperature properties. This is the result of the zirconium oxynitride intergranular phase that results in significantly reduced slow crack growth and improved time-dependent strength.

7.1.2 Reaction-Sintered Si_3N_4

At the other end of the silicon nitride behavioral spectrum is reaction sintered (RS) Si_3N_4. Figures 51 and 52 illustrate the strength-temperature behavior of typical high performance RS-Si_3N_4 materials. The room-temperature strength is only 30-40 ksi at best, caused by the presence of 10-20% porosity. Fracture origins are typically large pores and pore agglomerates (Figure 53). However, RS-Si_3N_4 materials are very pure, and thus their strength is maintained at elevated temperatures (any strength increase observed at high temperature is thought to be caused by
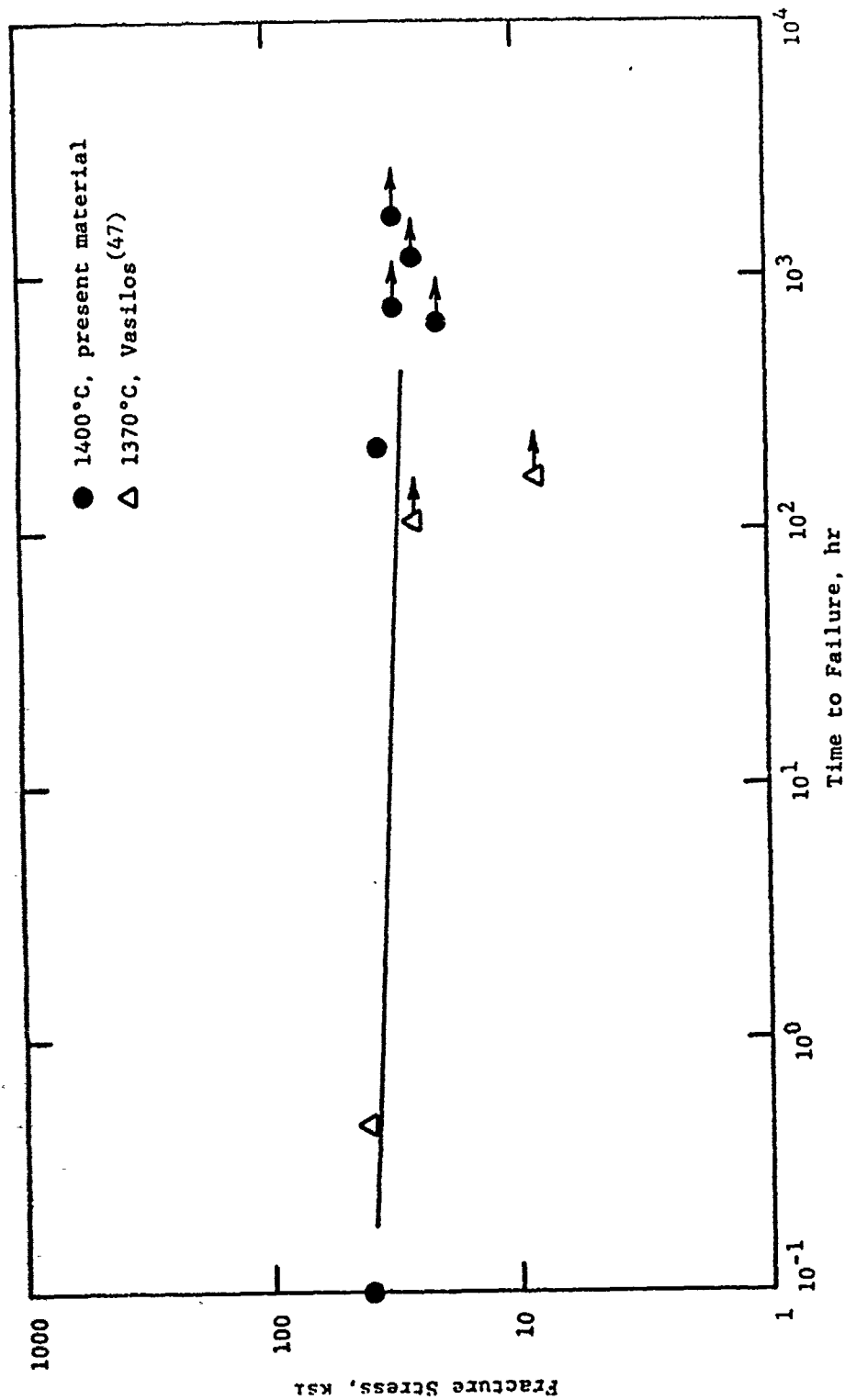
Figure 49. Flexural stress-rupture of NASA/AVCO/Norton HP-Si$_3$N$_4$
(10% ZrO$_2$) at 1400°C (air atmosphere).

138
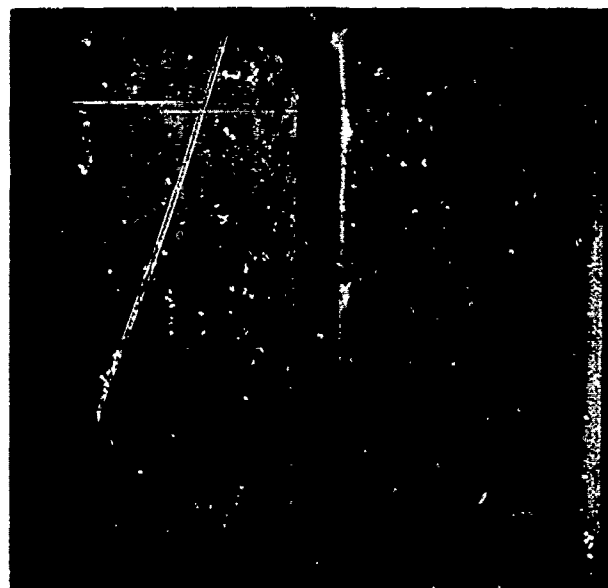
Figure 50. Fracture surfaces of NASA/AVCO/
Norton HP-Si$_3$N$_4$ (10% ZrO$_2$) after 1400°C
stress rupture test in air atmosphere
(the applied stress was 35 ksi; the sam-
ple failed at 209 hr; the sample was
soaked in HF to remove the oxide scale
to better observe the fracture surface
markings).
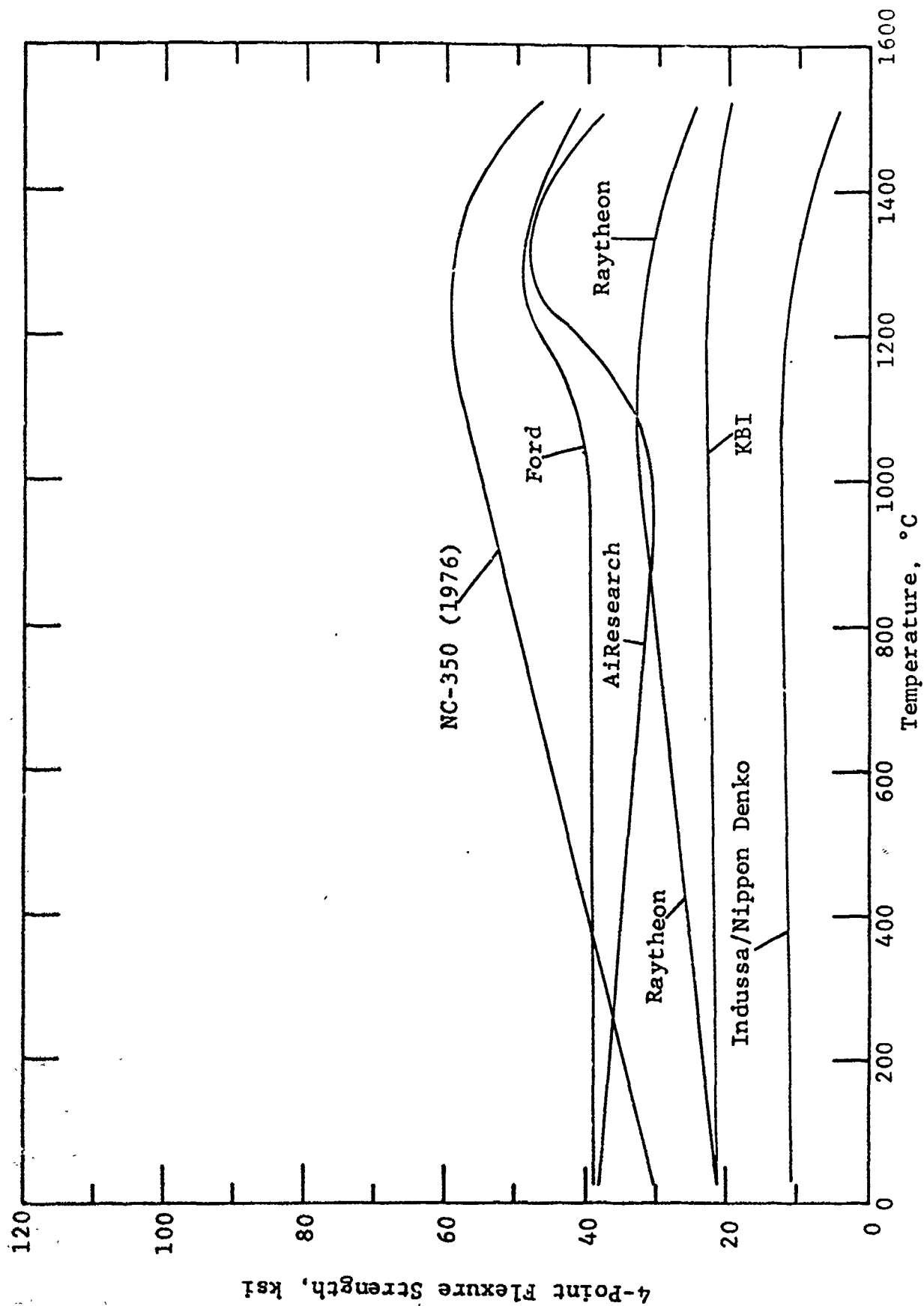
Figure 51. Flexure strength of reaction sintered Si_3N_4.

140
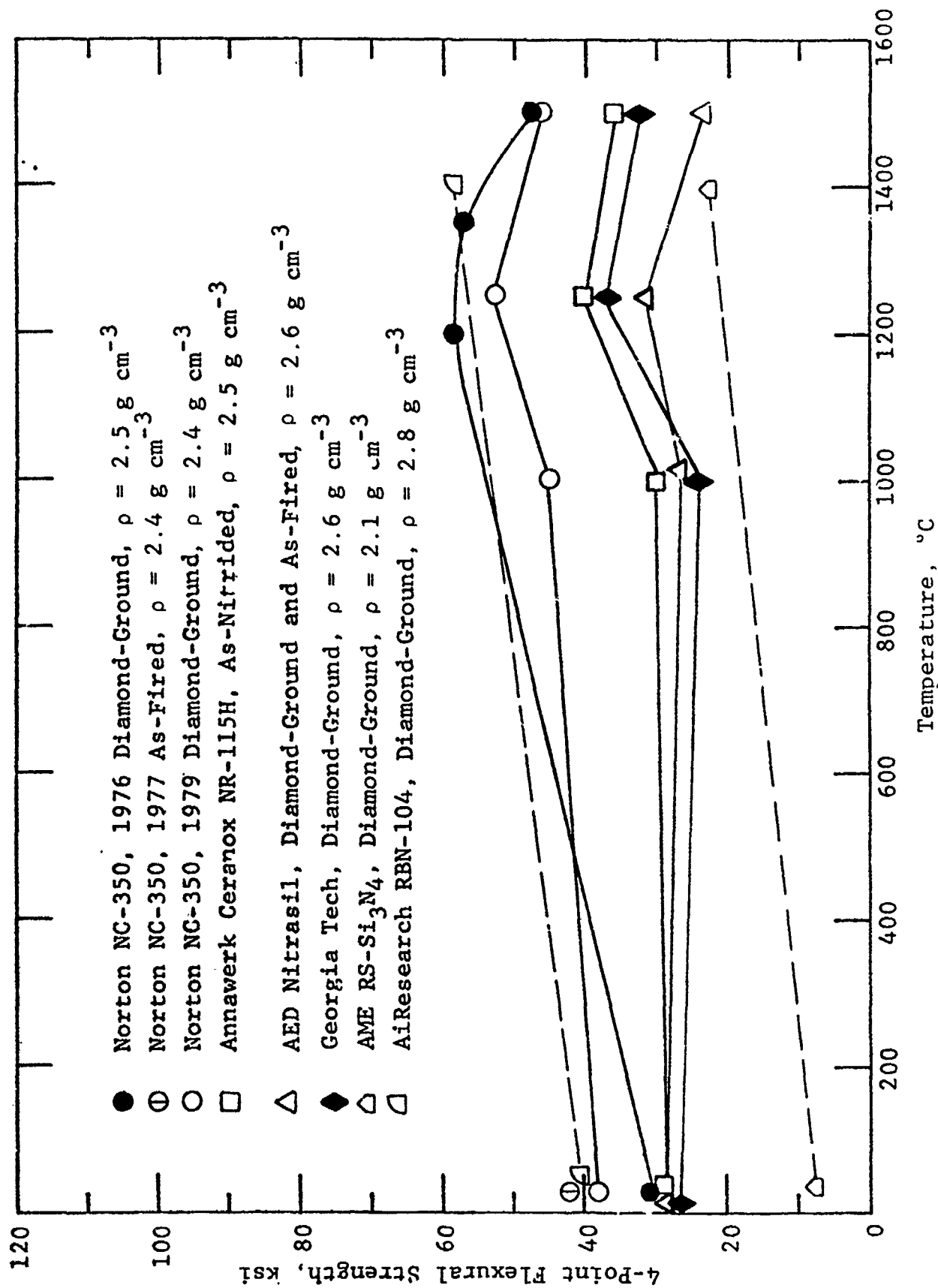
Figure 52. Flexural strength of RS-Si₃N₄.

Legend:
- Norton NC-350, 1976 Diamond-Ground, ρ = 2.5 g cm⁻³ (●)
- Norton NC-350, 1977 As-Fired, ρ = 2.4 g cm⁻³ (⊖)
- Norton NC-350, 1979 Diamond-Ground, ρ = 2.4 g cm⁻³ (○)
- Annawerk Ceranox NR-115H, As-Nitrided, ρ = 2.5 g cm⁻³ (□)
- AED Nitrasil, Diamond-Ground and As-Fired, ρ = 2.6 g cm⁻³ (△)
- Georgia Tech, Diamond-Ground, ρ = 2.6 g cm⁻³ (◆)
- AME RS-Si₃N₄, Diamond-Ground, ρ = 2.1 g cm⁻³ (◁)
- AiResearch RBN-104, Diamond-Ground, ρ = 2.8 g cm⁻³ (◁)

X-axis: Temperature, °C
Y-axis: 4-Point Flexural Strength, ksi

141

12X

(a) Sample tested at room-temperature
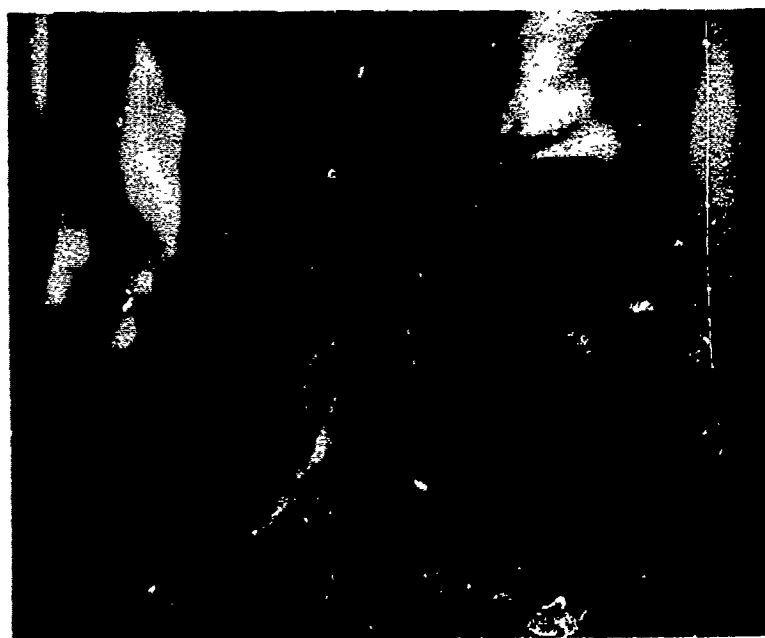
12X

(b) Sample tested at 1400°C

Figure 53. Fracture surfaces (tensile surfaces together) of AiResearch RBN-104 RS-Si_3N_4 tested at room temperature and 1400°C.

oxidation, i.e., blunting and rounding of sharp pore features). Indeed, Table 8 shows that the oxygen content of RS-Si$_3$N$_4$ materials is very low. Typical stress-strain curves are given in Figure 54. Note that linear behavior is obtained at 1500°C. Figure 55 shows the fracture surface appearance of Norton NC-350 RS-Si$_3$N$_4$ tested at 1500°C in air atmosphere. Note the absence of SCG markings on the fracture surface. Therefore, the absence of oxide intergranular phases is the reason for the excellent elevated temperature strength retent:-- in RS-Si$_3$N$_4$.

7.1.3 Sintered Si$_3$N$_4$

Sintered Si$_3$N$_4$ is similar to hot-pressed silicon nitride in that oxide additives are employed to achieve consolidation. Analagous to HP-Si$_3$N$_4$, this is accomplished somewhat at the expense of elevated temperature properties. However, sintered Si$_3$N$_4$ has one distinct advantage--the capability to produce net shapes of rather complex configuration. Only a few SSN materials were evaluated on this program. The results are summarized in Figures 56 and 57.

7.2 SiC MATERIALS

The effect of intergranular phases resulting from processing additives on subcritical crack growth and strength reduction is much less pronounced in SiC than it is in Si$_3$N$_4$. Figure 58 illustrates the strength-temperature behavior of the hot-pressed SiC materials evaluated on this program. The most successful HP-SiC contains ~2% Al$_2$O$_3$ as a densification aid. This results in aluminosilicate intergranular phases, the deformation of which is partially responsible for the strength reduction in HP-SiC at elevated temperature. Boron carbide, B$_4$C, results in a more deformation-resistant grain boundary. This is seen in Figure 58. However, as discussed in Section 6.2 above, B$_4$C promotes growth of SiC grains, which results in comparatively low strength.

With the successful development of fully dense sintered SiC, comparatively little work continues on HP-SiC. Sintered SiC

143
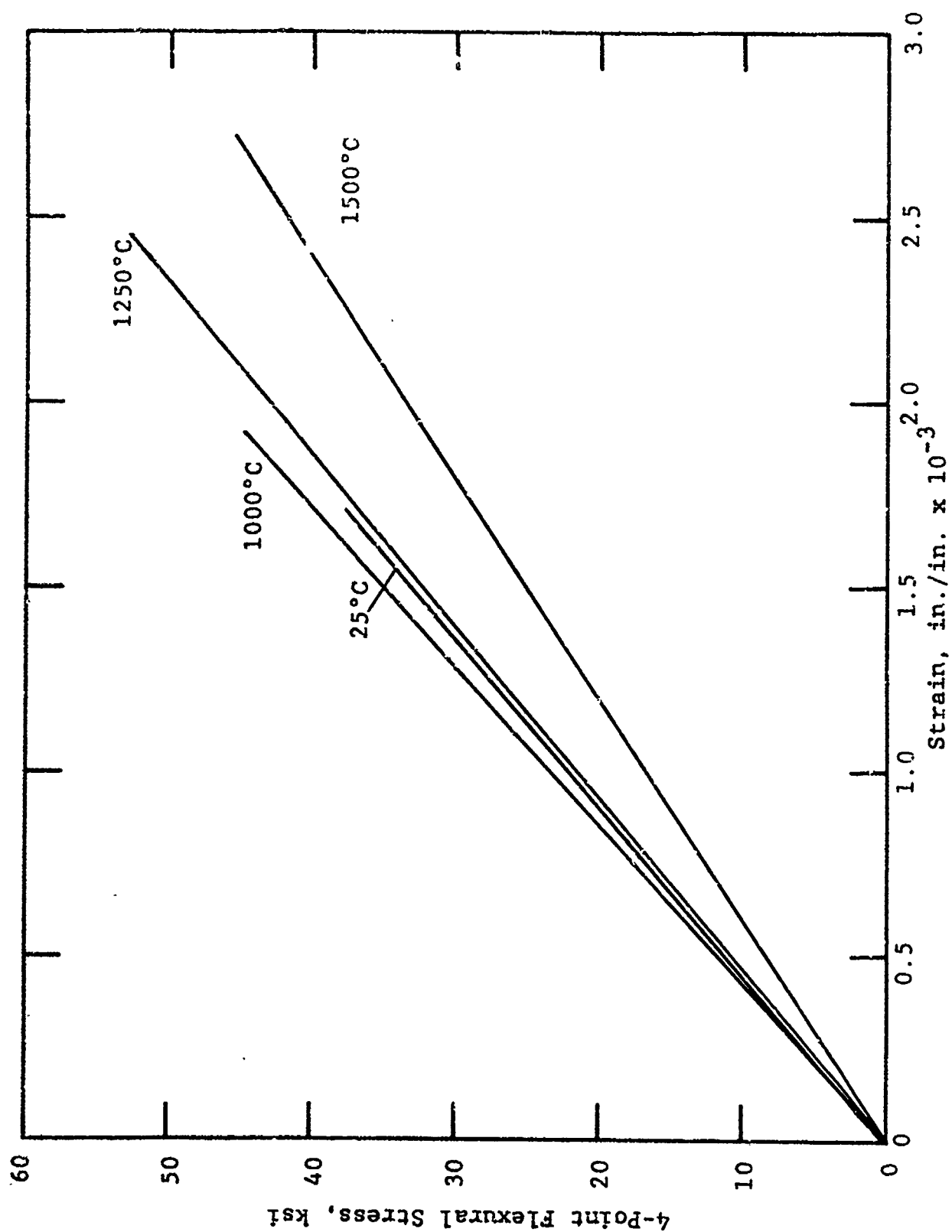
Figure 54. Representative flexural stress-strain behavior of Norton NC-350 RS-Si$_3$N$_4$ (1979).
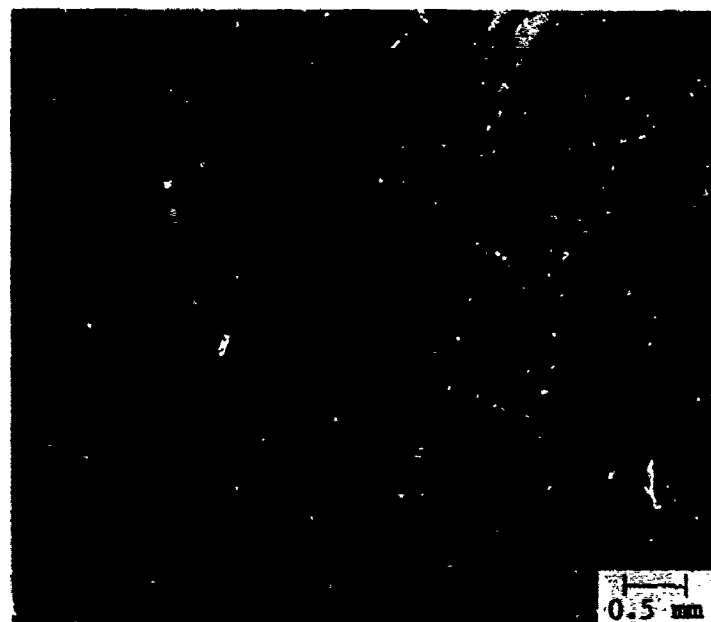
Figure 55. Fracture surface (tensile surfaces together) of Norton NC-350 RS-Si_3N_4 tested in flexure at 1500°C.
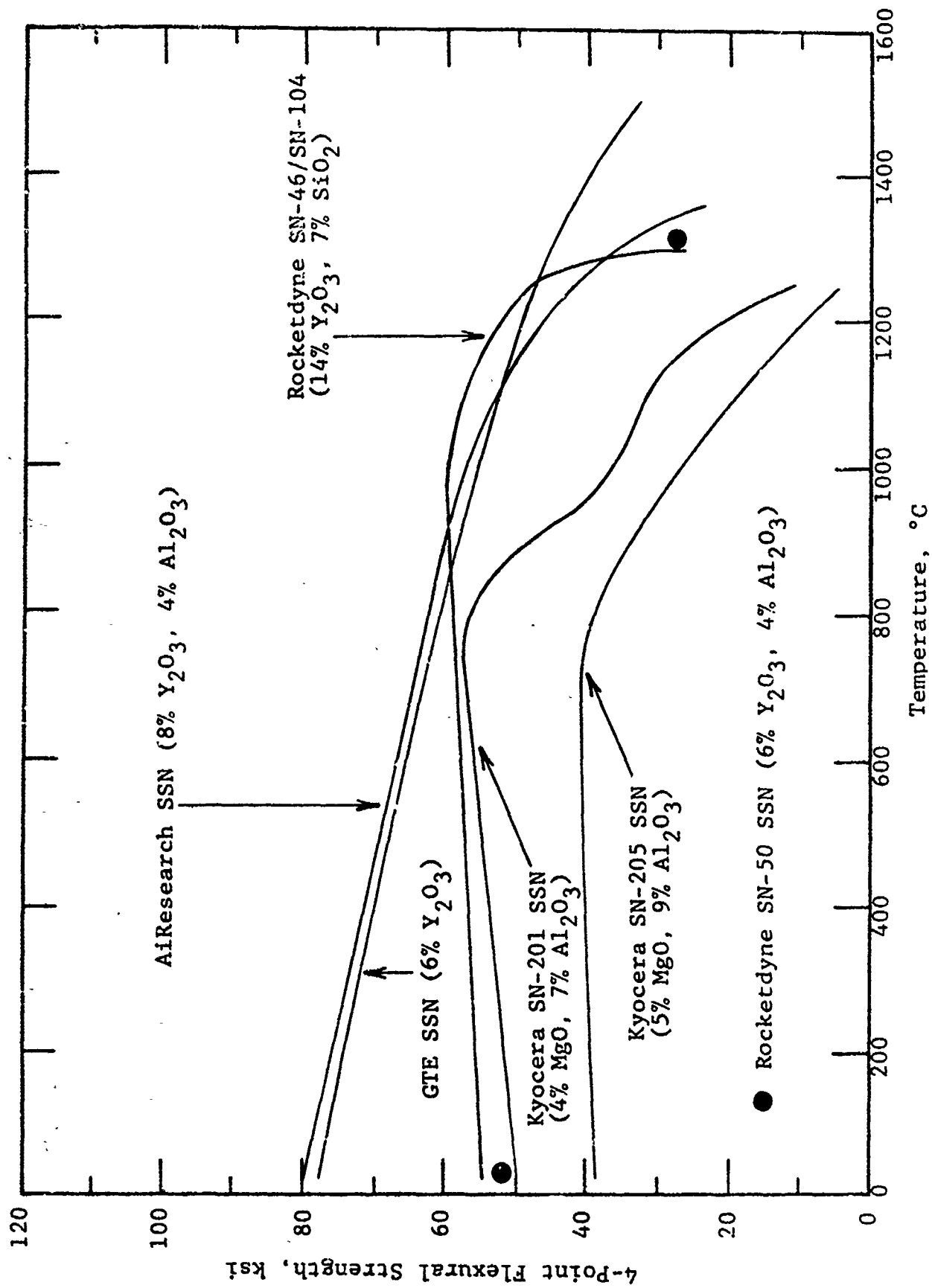
Figure 56. Flexural strength of sintered silicon nitride materials.
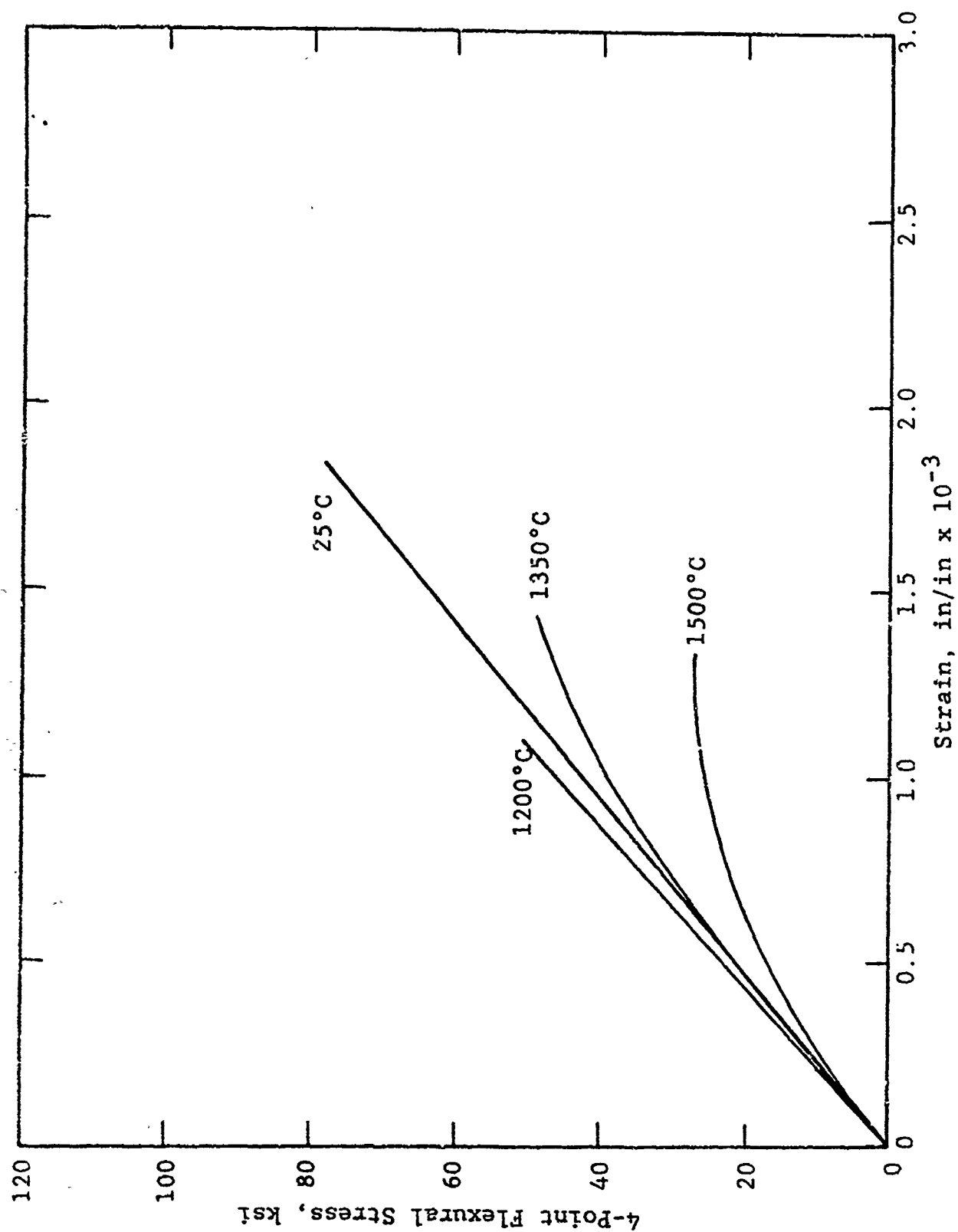
Figure 57. Representative flexural stress-strain of GTE sintered Si_3N_4 (6% Y_2O_3).
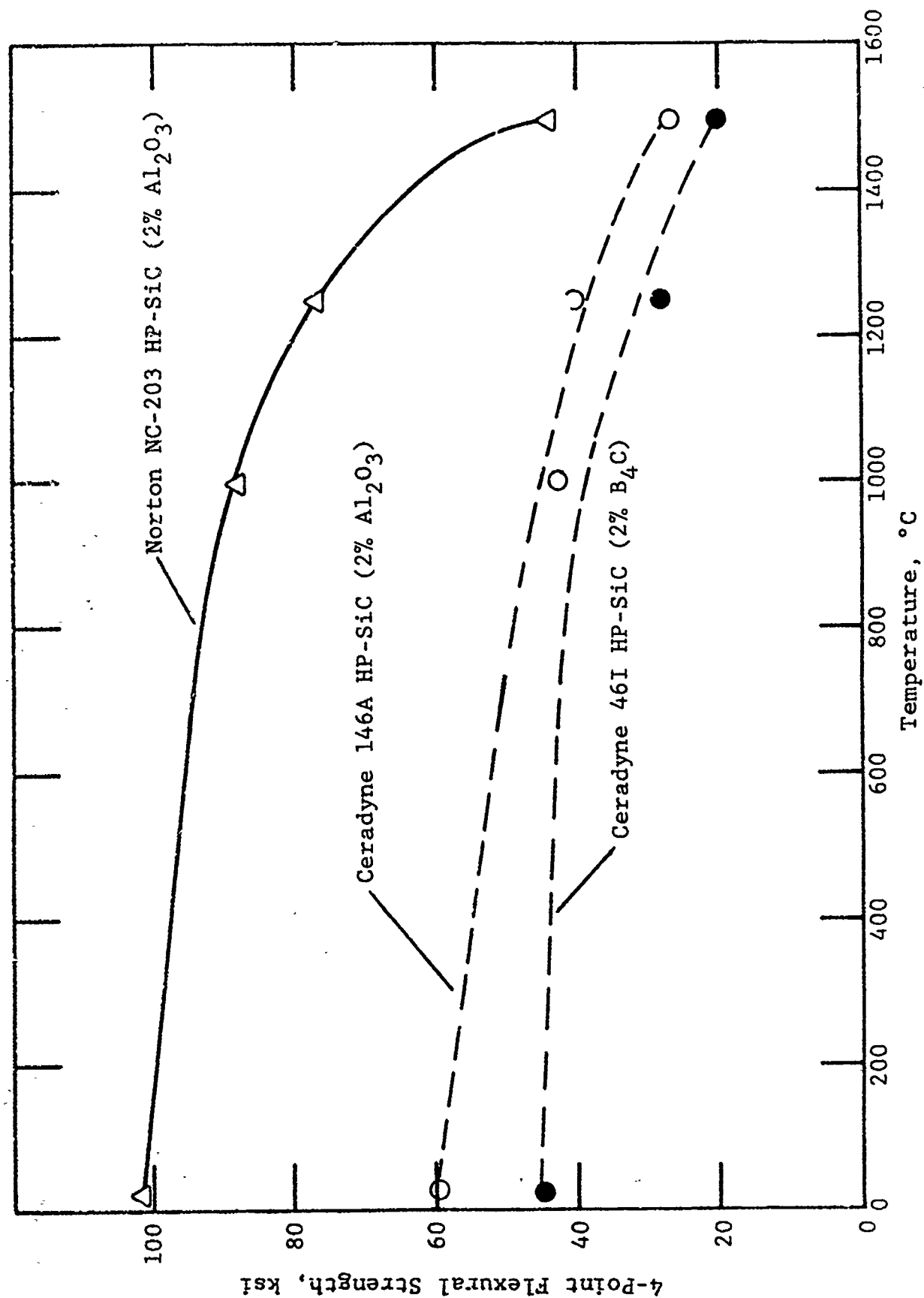
Figure 58. Flexural strength of hot-pressed silicon carbide materials.

offers the advantage of the fabricability of complex shapes. This technology has advanced by the incorporation of carbon and boron that permit sintering to full density. Furthermore, these additives do not result in elevated temperature strength degradation like the additives for silicon nitride. Figure 59 illustrates the strength-temperature behavior of sintered SiC, which contains few additives, if any. This is in contrast to that of hot-pressed SiC, which contains 1-2% Al_2O_3 additive to achieve densification, but which results in aluminosilicate grain boundary phases. The low temperature strength is maintained much better out to 1500°C for the sintered materials. Sintered SiC contains very little residual oxide impurity. Figures 60 and 61 (for the Carborundum Hexoloy SX-05 and Kyocera SC-201) show, analagous to high purity RS-Si_3N_4, that linear stress-strain behavior is obtained in sintered SiC at 1500°C. Figure 62 illustrates typical fracture surfaces for sintered SiC tested at 1000°, 1250°, and 1500°C. No fracture surface features are visible (at this level of magnification) that would indicate an operative slow crack growth mechanism. Oxide additives in HP-SiC do not affect the strength as much as they do in hot-pressed Si_3N_4. Figure 63 illustrates that only slightly nonlinear behavior is observed in 1500°C stress-strain data for Norton NC-203 HP-SiC, which contains ~2% Al_2O_3. Most HP-Si_3N_4 materials exhibit much more pronounced nonlinear stress-strain behavior at 1500°C. For the same reason, the temperature at which the strength begins to decrease precipitously is lower for Si_3N_4 (~1250°C). The reason for the less pronounced temperature dependence observed for SiC may be due to a combination of effects: (a) the absence of significant intergranular phases in sintered SiC, (b) the aluminosilicate intergranular phase in HP-SiC being relatively refractory, and (c) the fracture mode in SiC being predominantly transgranular, rather than intergranular as in Si_3N_4. A summary of the elevated temperature elastic properties of various sintered SiC materials evaluated on this program is presented in Table 17.

149
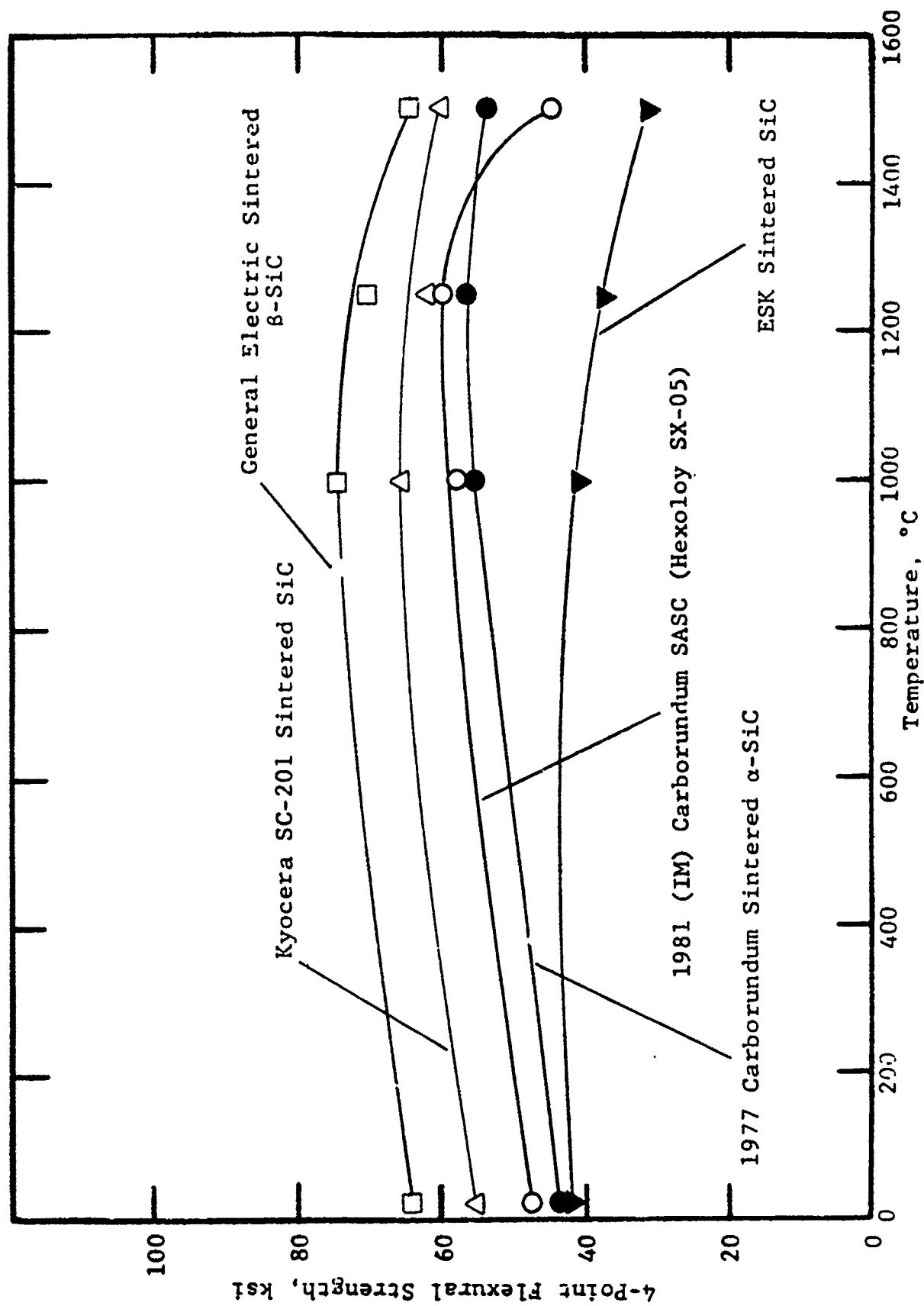
Figure 59. Flexural strength of sintered silicon carbide materials.
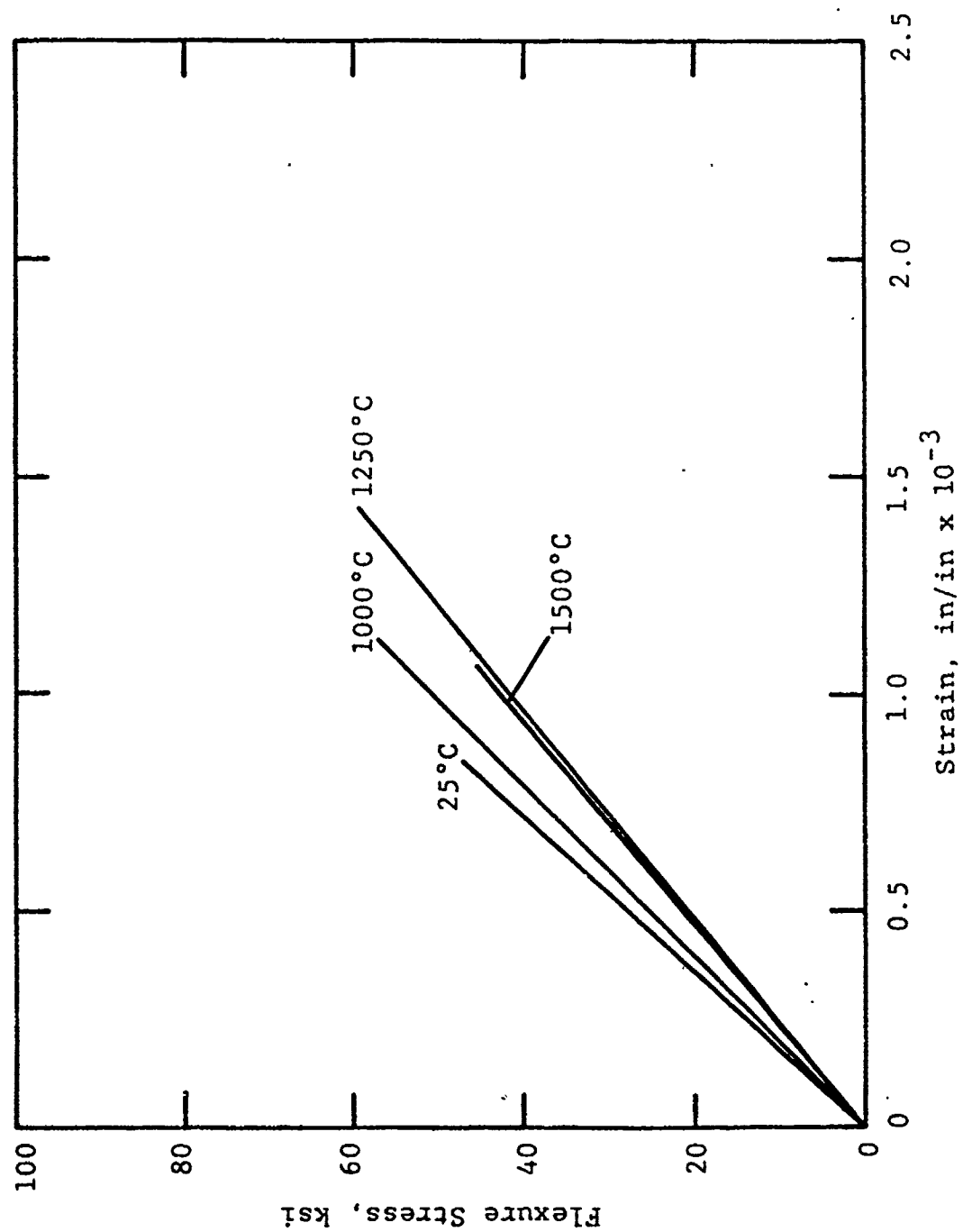
Figure 60. Flexural stress-strain behavior of 1981 Carborundum sintered α-SiC (Hexoloy SX-05).
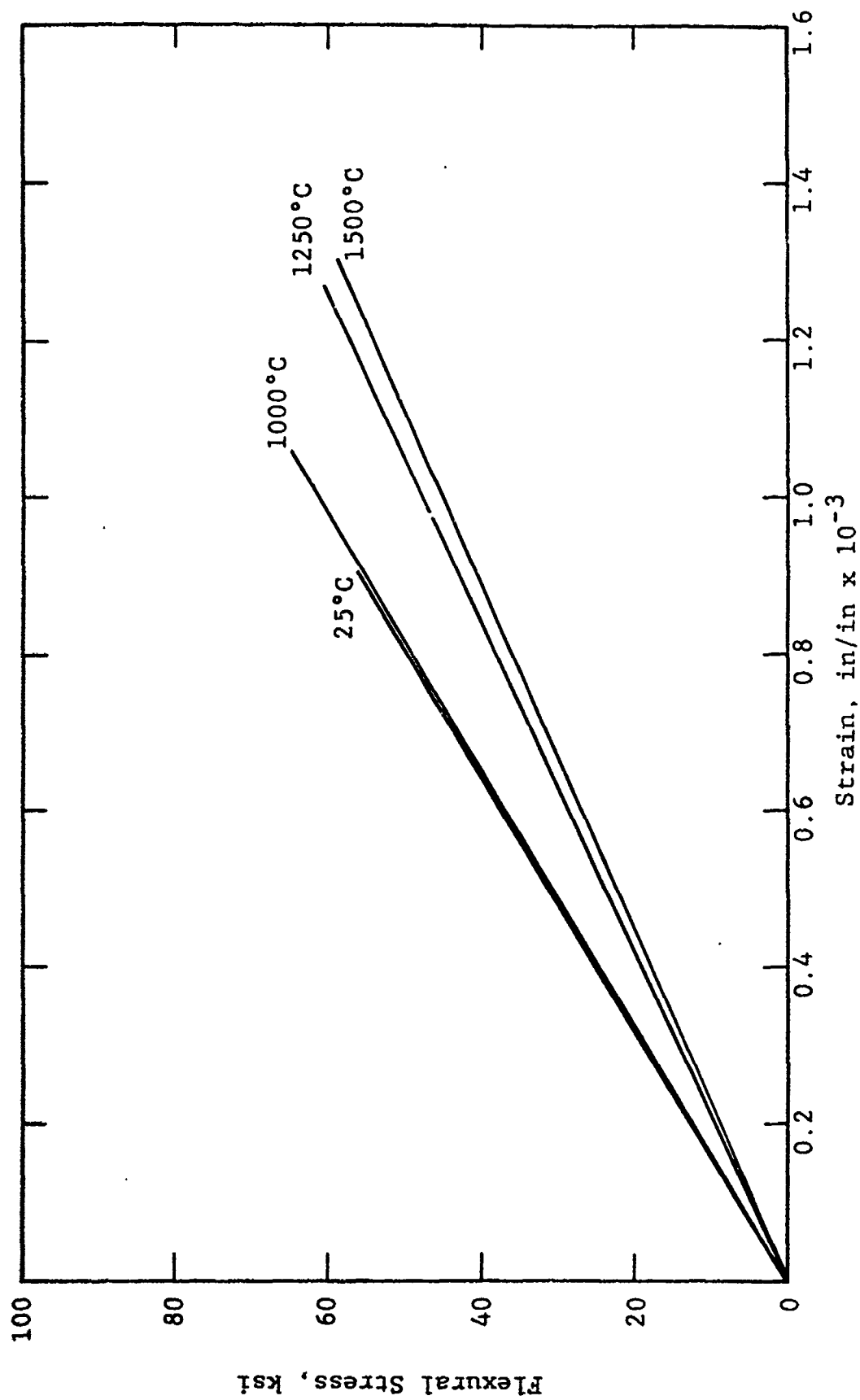
Figure 61. Representative flexural stress-strain behavior of Kyocera SC-201 sintered SiC.

(a) Kyocera SC-201 sintered SiC
tested at 1000°C.

(b) Kyocera SC-201 sintered SiC
tested at 1250°C.

(c) 1977 Carborundum sintered α-SiC
tested at 1500°C.

Figure 62. Fracture surfaces (tensile surfaces together) of Kyocera SC-201
sintered SiC and 1977 Carborundum sintered α-SiC.

153
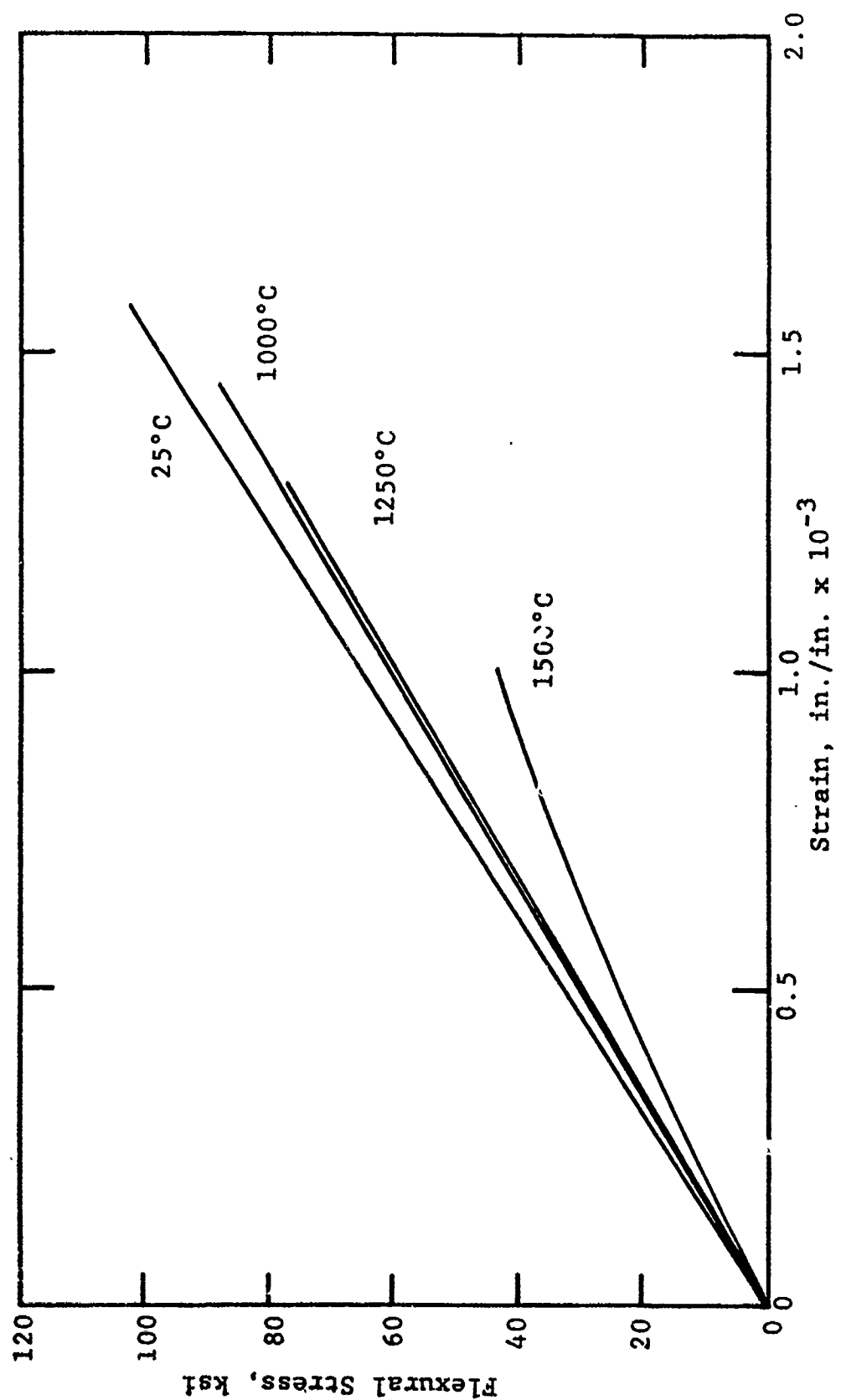
Figure 63.   Representative stress-strain behavior for Norton NC-203 HP-SiC (2% Al$_2$O$_3$).

Table 17

ELASTIC MODULUS OF SINTERED SiC

Temp., °C	Elastic Modulus, 10^6 psi[a]			
	Carborundum 1977 Slip Cast (α)	Carborundum 1981 Injection Molded (α)	General Electric Boron-Doped (β)	Kyocera SC-201 (α)
25	58.2	55.9	54.8	60.5
1000	67.0	51.1	63.2	60.5
1250	63.3	40.8	57.1	50.1
1500	54.7	42.1	58.3	44.9

[a]Secant Young's modulus determined using electromechanical deflectometer to continuously read outer fiber tensile strain during a 4-point bend test at a machine crosshead speed of 0.02 ipm in air atmosphere. The values tabulated are as-measured, and not corrected for porosity.

TABLE 18. ELASTIC MODULUS OF COORS SILICONIZED SiC

Temperature, °C	Elastic Modulus, 10^6 psi[a]		
	1979 SC-1	1981 SC-2	1982 SC-2
25	51.1	53.8	54.2
1000	42.6	55.5	55.5
1200	34.0	42.0	47.9
1350	29.6	33.9	40.7

[a]Secant Young's modulus measured during 4-point bend test. Not corrected for porosity.

Seven silicon-densified SiC materials were evaluated on this program. Their strength-temperature behavior is shown in Figure 64. At elevated temperature, their elastic properties are determined by the amount and distribution of the silicon metal phase. This is illustrated in Table 18 and in Figures 65 and 66.

As discussed above, static fatigue is of primary concern in structural ceramics. Figure 67 illustrates the fracture stress vs. time-to-failure from dynamic fatigue tests. The n value in Figure 67 is related to the slope of the strength-time relation, and is the exponent n in the relation $v = AK^n$, where v is the crack velocity and K is the stress intensity at the crack tip (A is a constant). A large value of n means little slow crack growth and time-invariant strength. As shown in Figure 67, SiC exhibits much less SCG and strength degradation than does Si_3N_4.

The mechanisms of SCG and strength degradation appear to be different in Si_3N_4 and SiC. In Si_3N_4 the existence of slow crack growth is usually correlated with a grain boundary sliding mechanism. Accommodation for this deformation is provided by the nucleation of intergranular voids or the extension of pre-existing grain triple-point voids. The result of this is readily observable on Si_3N_4 fracture surfaces.

The current speculation for SiC is that slow crack growth is an atomistic-level process occurring at the crack tip, being related to stress corrosion by an oxidation mechanism. The crack path is generally transgranular in SiC, and SCG is not readily observable on fracture surfaces at the level of magnificaition used on this program. Srinivasan et al.[50] report no detectable SCG in sintered α-SiC tested in argon at 1500°C. However, in air at 1500°C there was evidence of significant SCG, the mechanism being atmospheric attack of intergranular regions leading to grain separation. McHenry and Tressler[51] also indicate the mechanism of SCG in NC-203 HP-SiC to be stress-corrosion by oxidation.
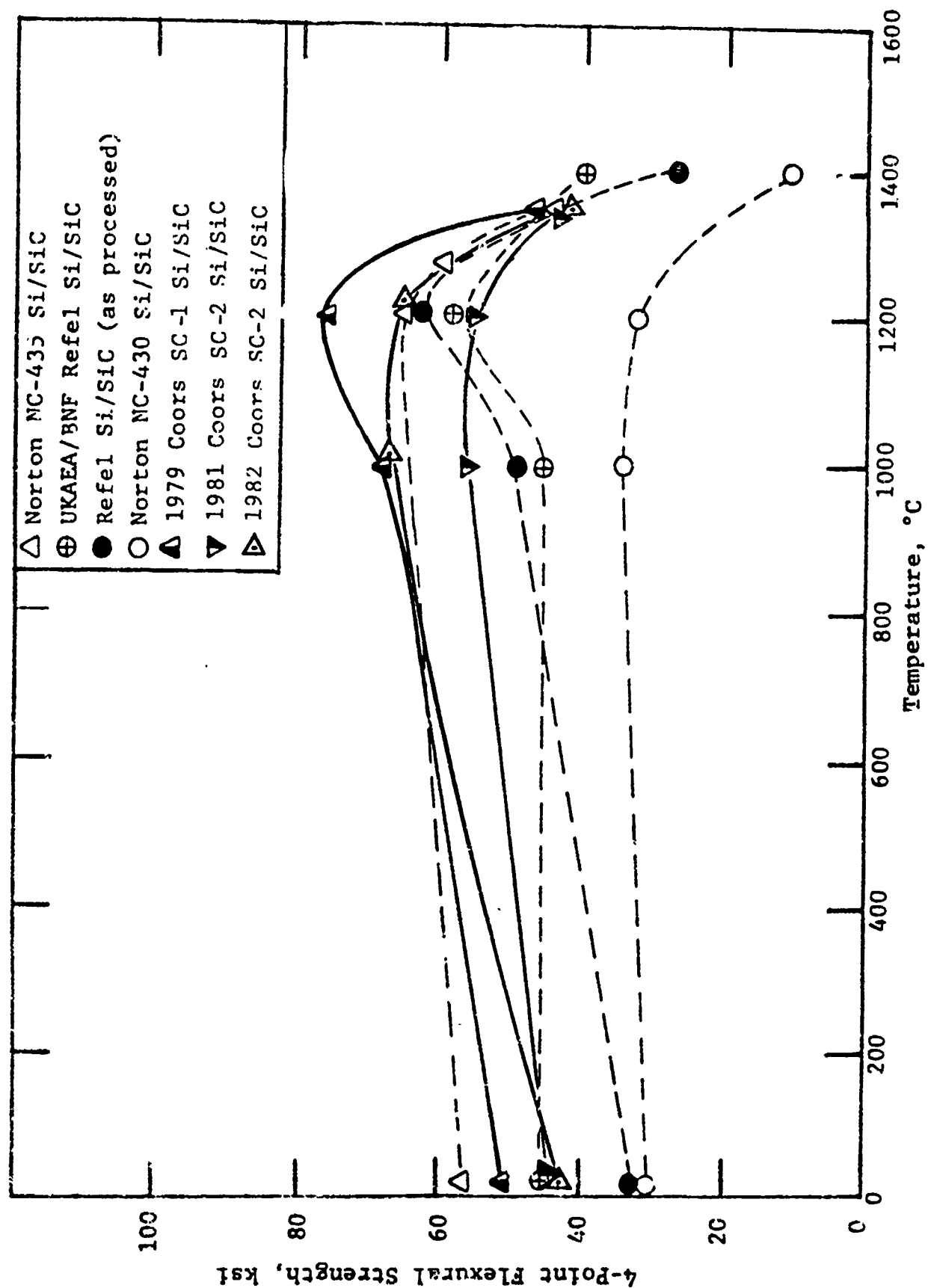
Figure 64. Flexural strength of siliconized silicon carbide materials.

157
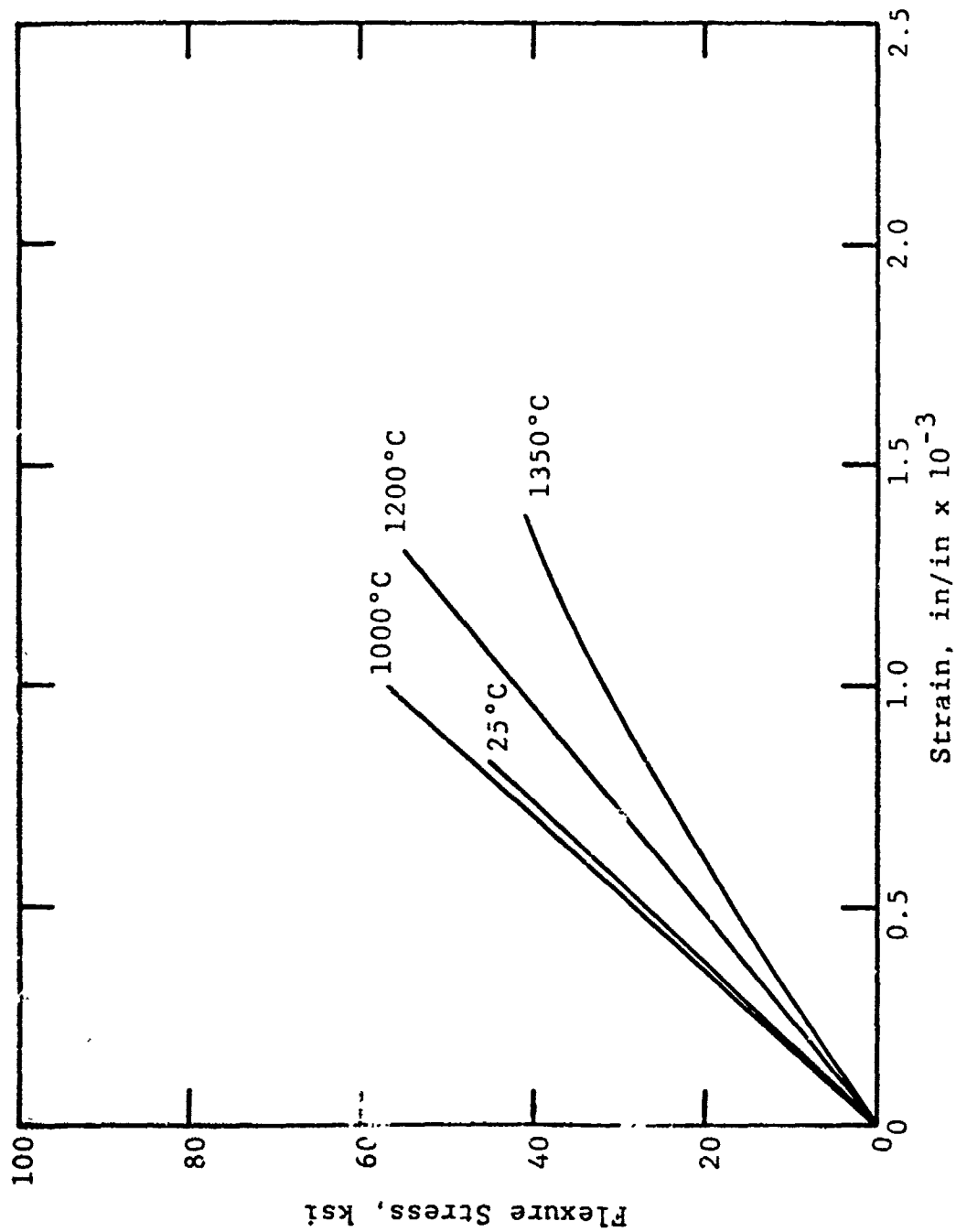
Figure 65. Flexural stress-strain behavior of 1981 SC-2 Coors Si/SiC.

158
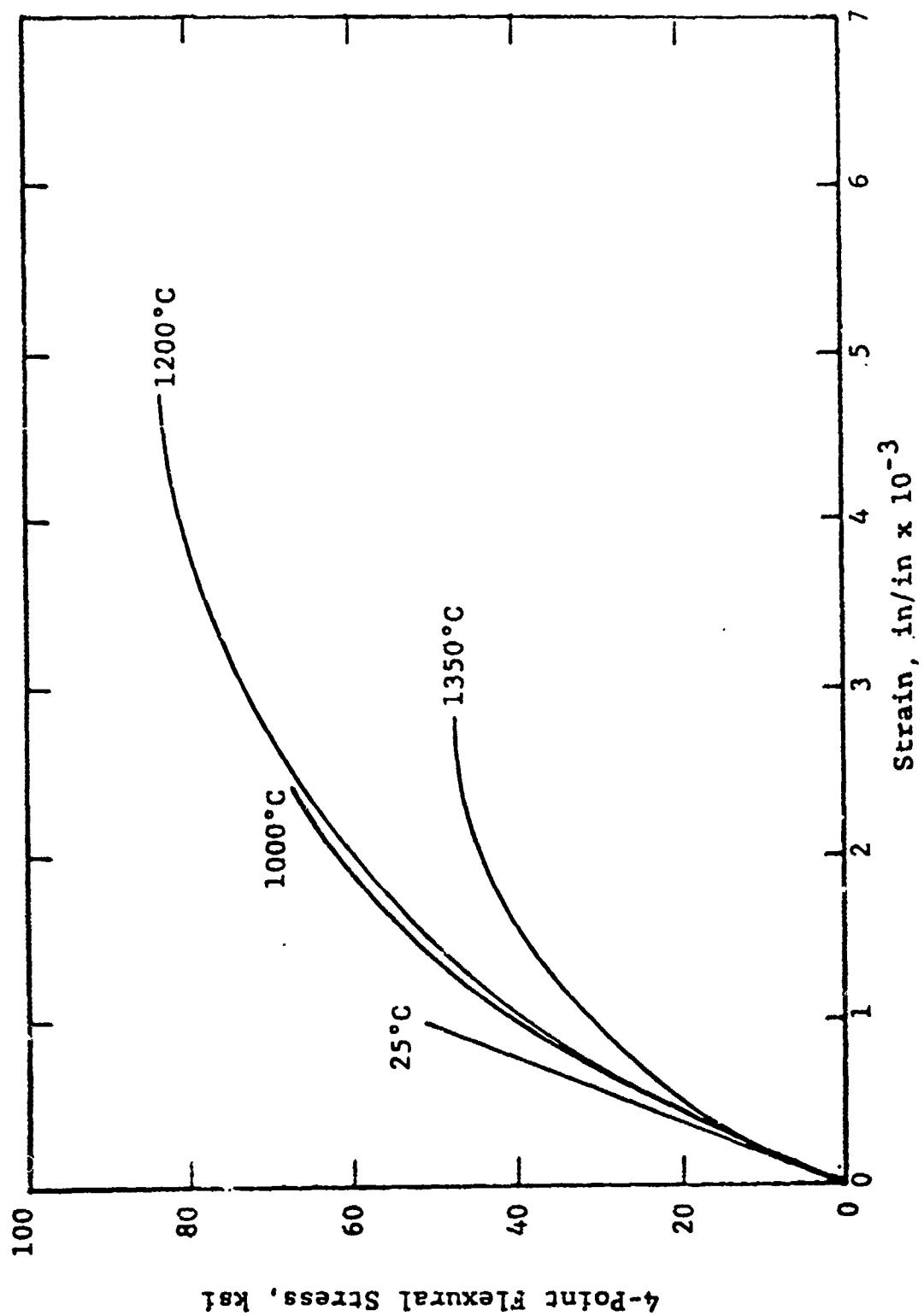
Figure 66. Representative flexural stress-strain behavior of 1979 SC-1 Coors Si/SiC.

159
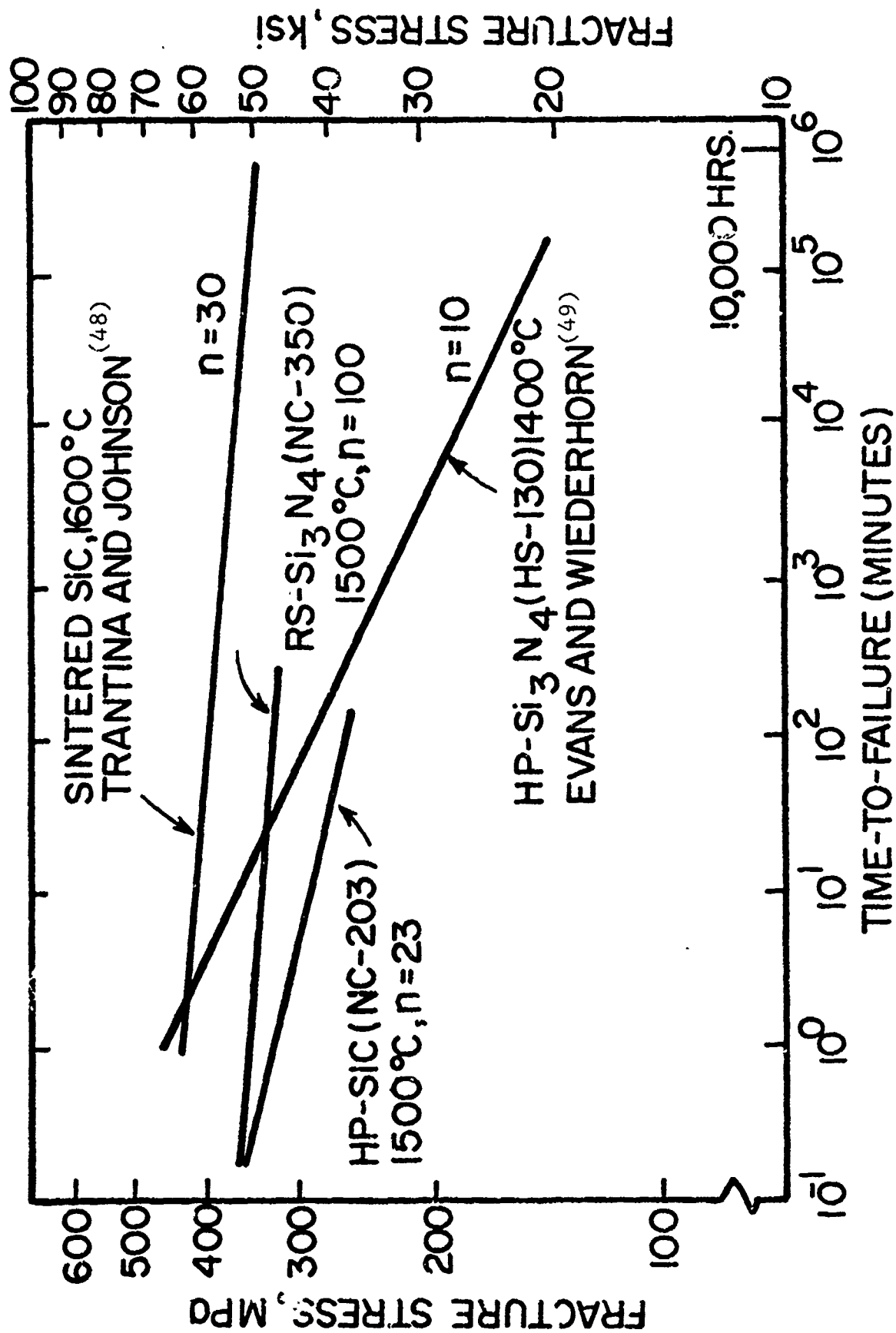
Figure 67. Strength degradation in silicon carbide and silicon nitride due to subcritical crack growth.

7.3 SUMMARY OF HIGH TEMPERATURE FRACTURE ORIGINS IN Si_3N_4 AND SiC

For convenience and reference, the sources of fracture at elevated temperature that have been observed on this program for both Si_3N_4 and SiC materials are tabulated in Table 19. It is noted that all fractography was performed with a low magnification optical binocular microscope.

TABLE 19. SOURCES OF FRACTURE AT ELEVATED TEMPERATURE - Si_3N_4 AND SiC MATERIALS

Material	Source of Fracture[a]
A. Hot-Pressed Si_3N_4	
Norton NC-132 HP-Si_3N_4 (1% MgO)	Machining and undetermined flaws at 1200°C; some SCG at 1350°C, 50% SCG at 1500°C
Norton NCX-3: HP-Si_3N_4 (8% Y_2O_3)	Primarily inclusions at 1000°C, surface oxidation and undetermined processing flaws at 1250°C, 50% SCG at 1500°C
Harbison-Walker HP-Si_3N_4 (10% CeO_2)	Some SCG at 1000°C, prevalent at 1250°C
Kyocera SN-3 HP-Si_3N_4 (4% MgO, 5% Al_2O_3)	Inclusions at 750°C, less than 10% SCG at 1000°C, ~50% SCG at 1125°C, 100% SCG at 1250°C
Ceradyne Ceralloy 147A, HP-Si_3N_4 (1% MgO)	Inclusions at 1000°C, ~10% SCG at 1250°C; 50-75% SCG at 1500°C
Ceradyne Ceralloy 147Y, HP-Si_3N_4 (15% Y_2O_3)	Undetermined processing flaws at 1000°C, less than 10% SCG at 1250°C, 100% SCG at 1500°C
Ceradyne Ceralloy 147Y-1, HP-Si_3N_4 (8% Y_2O_3)	Inclusions and undetermined processing flaws at 1000°C, less than 5% SCG at 1250°C, 100% SCG at 1500°C
Fiber Materials HP-Si_3N_4 (4% MgO)	Some SCG at 1000°C; 50% at 1250°C, much at 1400°C
Toshiba HP-Si_3N_4 (4% Y_2O_3, 3% Al_2O_3)	Dark inclusions at 1000°C, light inclusions at 1250°C; less than 10% SCG at 1350°C, ~50% SCG at 1500°C
Toshiba HP-Si_3N_4 (3% Y_2O_3, 4% Al_2O_3, SiO_2)	Inclusions at 1000°C, less than 10% SCG at 1125°C and 1250°C, >50% at 1350°C, 100% SCG or plastic deformation at 1500°C
Westinghouse HP-Si_3N_4 (4% Y_2O_3, SiO_2)	Primarily undetermined at 1000° and 1250°C, 25% SCG at 1500°C
NASA/AVCO/Norton HP-Si_3N_4 (10% ZrO_2)	Machining flaws at 1000°C, undetermined processing defects at 1250° and 1500°C; no SCG evident at 1500°C
Battelle HIP-Si_3N_4 (5% Y_2O_3)	SCG less than 5% at 1400°?

TABLE 19 (cont.)

Material	Source of Fracture
B. Reaction-Sintered Si₃N₄	
• 1976 Norton NC-350 RS-Si₃N₄	Pore agglomerates, pores, and undetermined processing defects at 1200°, 1350°, and 1500°C
• Kawecki-Berylco RS-Si₃N₄	Inclusions and pores at 1200° and 1350°C; pores and pore agglomerates, inclusions at 1500°C
• Ford Injection Molded RS-Si₃N₄	Inclusions at 1000°C, inclusions and some pores at 1250° and 1500°C
• AiResearch Slip Cast RS-Si₃N₄ (Airceram RBN-101)	Inclusions and pore clusters at 1000° and 1250°C, pores at 1500°C
• Raytheon Isopressed RS-Si₃N₄	Inclusions at 1000°C, inclusions and pores at 1250° and 1500°C; some oxidation pit origins at 1500°C
• Indussa/Nippon Denko RS-Si₃N₄	Primarily undetermined at 1250° and 1500°C, a few pores as fracture origins
• AiResearch Injection Molded RS-Si₃N₄ (Airceram RBN-122)	Large particles at 1000°, 1250°, and 1500°C; some with associated pores
• 1979 Norton NC-350 RS-Si₃N₄	Half inclusions, half undetermined at 1000°, 1250°, and 1500°C
• Annawerk Ceranox NR-115H RS-Si₃N₄	Primary inclusions, some pores at 1000°C, inclusions at 1250° and 1500°C
• Associated Engineering Developments (AED) Nitrasil RS-Si₃N₄	Even distribution of free Si particles and large pores as origins at 1000°, 1250°, and 1500°C
• Georgia Tech RS-Si₃N₄	Machining damage at 1000°C, pores as 1250°C, undetermined at 1500°C
• AME RS-Si₃N₄	Undetermined at 1400°C
• AiResearch RBN-104 RS-Si₃N₄	Subsurface inclusion at 1400°C

TABLE 19 (cont.)

Material	Source of Fracture
C. Sintered Si₃N₄	
Kyocera SN-205 Sintered Si₃N₄ (5% MgO, 9% Al₂O₃)	Pores and inclusions at 750°C, less than 10% SCG at 1000°C, ~15% SCG at 1125°C, 25% SCG at 1250°C
Kyocera SN-201 Sintered Si₃N₄ (4% MgO, 7% Al₂O₃)	Inclusions at 750°C, less than 5% SCG at 1000°C, SCG more prevalent at 1125° and 1250°C
GTE Sintered Si₃N₄ (6% Y₂O₃)	Inclusions at 1200°C, ~50% SCG at 1350°C, 100% SCG at 1500°C
AiResearch Sintered Si₃N₄ (8% Y₂O₃, 4% Al₂O₃)	Surface porosity at 1000°C, less than 25% SCG at 1250°C, 75-100% SCG at 1350°C
Rocketdyne SN-50 Sintered Si₃N₄ (6% Y₂O₃, 4% Al₂O₃)	Inclusions at 1000°C, ~10% SCG at 1250°C, ~20% SCG at 1283°C, ~30% SCG at 1325°C
Rocketdyne SN-104 and SN-46 Sintered Si₃N₄ (14% Y₂O₃, 7% SiO₂)	Inclusions at 1000°C, pores at 1250°C, undetermined at 1325°C
D. Hot-Pressed SiC	
Norton NC-203 HP-SiC (~2% Al₂O₃)	Undetermined fracture sources at all elevated temperatures
Ceradyne Ceralloy 146A, HP-SiC (2% Al₂O₃)	Undetermined at 1000°, 1250°, and 1500°C; possibly some SCG at 1500°C
Ceradyne Ceralloy 146I, h SiC (2% B₄C)	Primarily undetermined at 1000° and 1250°C, undetermined and possibly some SCG at 1500°C
E. Sintered SiC	
General Electric Sintered β-SiC	Regions of incomplete sintering as origins at 1000°, 1250°, and 1500°C
Carborundum Sintered α-SiC (1977 vintage)	Subsurface pore fracture origins at 1000°, 1250°, and 1500°C
Kyocera SC-201 Sintered α-SiC (1980 vintage)	Open and subsurface pores at 1000°C and 1250°C; subsurface pores at 1500°C

164

TABLE 19 (cont.)

Material	Source of Fracture
• Carborundum 1981 SASC (Hexoloy SA-05)	Subsurface pores and surface finish at 1000° and 1250°C, subsurface pores at 1500°C
• ESK Sintered α-SiC	Subsurface and open porosity at 1000°, 1250°, and 1500°C
F. Silicon-Densified SiC	
• Norton NC-435 Si/SiC	Pores and large grains at 1200°C, undetermined processing flaws at 1275° and 1350°C
• UKAEA/BNF Refel Si/SiC	
● diamond-ground ● as-processed	Surface and subsurface porosity at 1000°, 1200°, and 1400°C Large grains and subsurface pores at 1000°C, undetermined processing flaws at 1200° and 1400°C
• Norton NC-430 Si/SiC	Undetermined at 1000° and 1200°C; undetermined at 1400°C, noticeable plastic deformation
• Coors Si/SiC (1979, SC-1)	Large SiC grains at 1000°C, undetermined at 1200° and 1350°C
• Coors Si/SiC (1981, SC-2)	Surface and subsurface pores at 1000°C, undetermined at 1200° and 1350°C
• Coors Si/SiC (1982, SC-2)	Oxidation pits at 1000° and 1200°C, undetermined at 1350°C

ᵃPercentages indicate amount of sample cross-section affected by subcritical crack growth as observed on the fracture surfaces. All fracture surface analysis performed with low magnification optical binocular microscope.

165

8. CREEP BEHAVIOR

Creep resistance is of primary concern in the rotating components of a turbine engine. High creep rates can lead to both excessive deformation and uncontrolled stresses.

Creep is a thermally activated process, characterized by a linear or power law stress dependence. After load application there is an instantaneous strain, followed by three regions of creep behavior. Primary creep (transient) is characterized by a creep rate that continually decreases with time. This is followed by secondary (steady-state) creep behavior where the creep rate remains constant with increasing strain and time. Tertiary creep can be observed just prior to fracture in some materials and is characterized by a rapid increase in creep rate. Steady-state secondary creep behavior is of greatest interest in structural applications. The steady-state creep rate, $\dot{\epsilon}$, is governed by an empirical relation, the general form of which is:

$$\dot{\epsilon} = A\sigma^n e^{-E/kT}$$

Creep deformation mechanisms are deduced in part by analysis of measured creep rates with respect to this relation. Experimental schedules normally cover a range of stress, σ, and temperature, T, which permit analytical determination of the stress exponent, n, and activation energy, E. The term A in the empirical relation above is a constant. A knowledge of the stress exponent and activation energy permits some mechanistic interpretation, which is important in understanding the measured behavior and eventually improving materials properties. However, this information alone is not sufficient for a comprehensive mechanistic study. Microstructural analysis of crept specimens using light microscopy and scanning, replica, and transmission electron microscopy can reveal features that suggest the rate-controlling mechanisms involved. Such features include grain boundary

166

sliding, nucleation of microcracks, porosity on grain boundaries, dislocations, diffusion within grains, diffusion along grain boundaries, etc.

The creep data obtained on this program and its predecessor for various HP-Si_3N_4 materials are presented in Figure 68, where the steady-state creep strain rate is plotted as a function of applied stress. The stress dependence and activation energy data are tabulated in Table 20. Figure 69 and Table 21 contain similar information for the reaction-sintered silicon nitride materials evaluated. The data for SiC are presented in Figure 70 and Table 22.

This information is summarized in Figure 71, where data bands of creep behavior for silicon nitride and silicon carbide materials are plotted as a function of processing method.

8.1 HP-Si_3N_4

For hot-pressed Si_3N_4, good results are beginning to be achieved in recent processing efforts to control the composition and thus properties of the grain boundary phases. Recall that MgO-doped HPSN had an amorphous intergranular phase that was not resistant to deformation under stress. Grain boundary plasticity and associated cavity nucleation and growth resulted in low high-temperature strengths and high creep rates. The high degree of stress dependence of the creep rate in such MgO-modified HP-Si_3N_4, characterized by $1.5 < n < 1.8$, suggested such a visco-elastic mechanism.

Efforts were then directed toward Y_2O_3-modified Si_3N_4 structures. At 1350°C, HP-Si_3N_4 materials by Ceradyne (8% Y_2O_3) and Toshiba (3% Y_2O_3, 4% Al_2O_3, SiO_2) did not exhibit improved creep resistance when compared to magnesia-doped Norton NC-132. This is illustrated in Figure 71, where curve A falls within the band of data for MgO-doped HP-Si_3N_4. We then evaluated two other Y_2O_3-doped materials at 1350°C, Norton NCX-34 (8% Y_2O_3) and Toshiba (4% Y_2O_3, 3% Al_2O_3). The results for these two materials are represented by curve B in Figure 71. It is observed that some

167
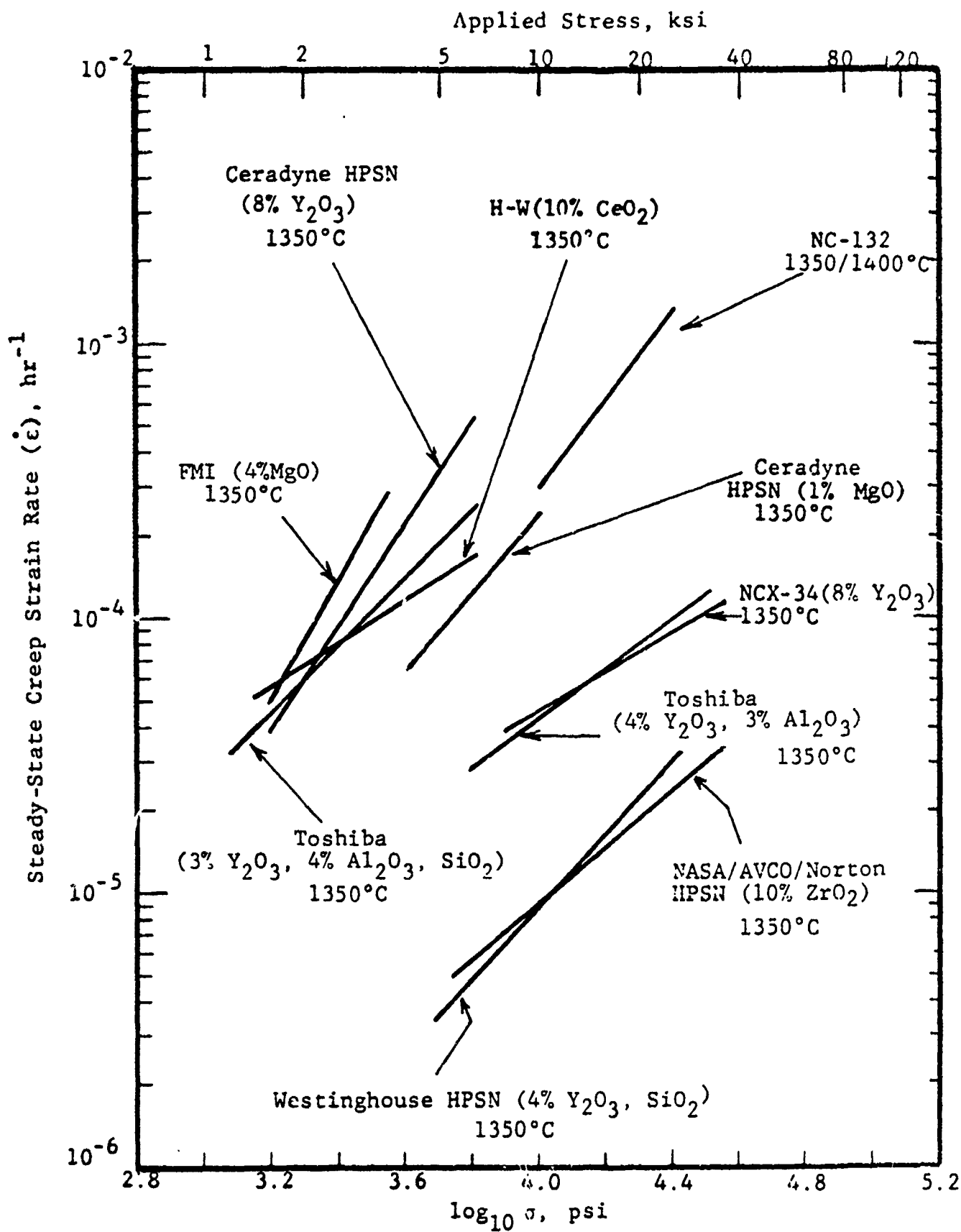
Figure 68.   Steady-state flexural creep rate vs. applied stress
for various hot-pressed Si_3N_4 materials at 1350°C.

TABLE 20. DERIVED CREEP STRESS DEPENDENCE AND ACTIVATION
ENERGY FOR VARIOUS Si_3N_4 MATERIALS EVALUATED.

Material	Temp., °C	Stress Exponent, n	Activation Energy, kcal/mole
Hot-Pressed			
Norton NC-132 (1% MgO)	1350 1500	1.6	130[a]
Ceradyne Ceralloy 147A (1% MgO)	1350	1.5	--
Norton NCX-34 (8% Y_2O_3)	1350 1500	0.7- 0.8	91
Ceradyne Ceralloy 147Y-1 (8% Y_2O_3)	1350	1.8	--
Ceradyne Ceralloy 147Y (15% Y_2O_3)	1350	0.9[b]	--
Fiber Materials (4% MgO)	1250 1350	∿0.5 2.3	--
Harbison-Walker (10% CeO_2)	1350	0.9	--
Toshiba (4% Y_2O_3, 3% Al_2O_3)	1350	0.9	--
Toshiba (3% Y_2O_3, 4% Al_2O_3, SiO_2)	1350	1.4	--
Westinghouse (4% Y_2O_3, SiO_2)	1350	1.3	--
NASA/AVCO/Norton (10% ZrO_2)	1350	1.0	--
Sintered			
Rocketdyne SN-46, SN-104 (14% Y_2O_3, 7% SiO_2)	1250 1350	1.1 --	114

[a]Computed from IITRI and Seltzer[52] data.

[b]Material decomposed, exhibited spontaneous catastrophic phase instability.

169
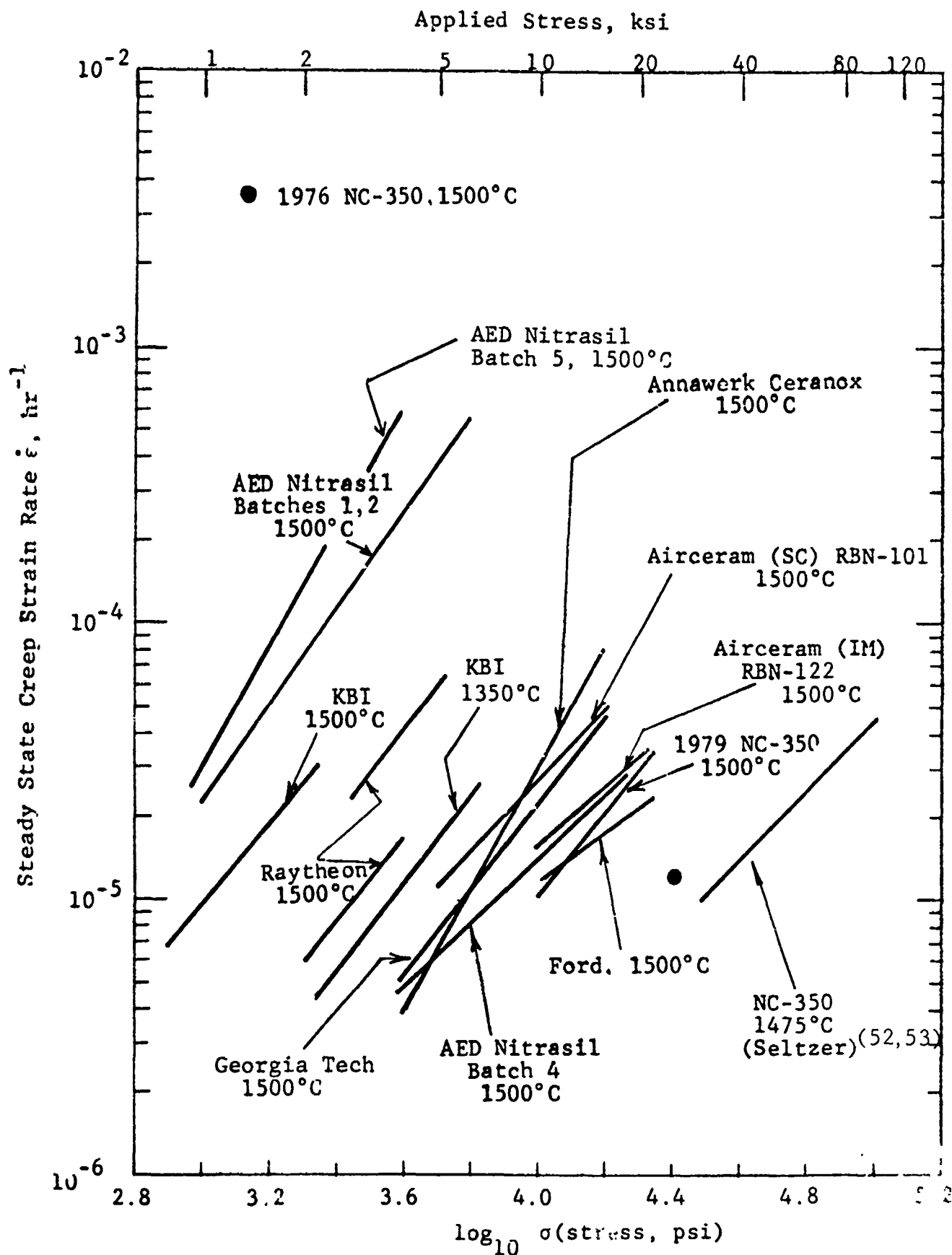
Figure 69. Steady-state flexural creep rate vs. applied stress for various reaction-sintered Si_3N_4 materials.

TABLE 21. DERIVED CREEP STRESS DEPENDENCE AND ACTIVATION ENERGY FOR VARIOUS RS-Si$_3$N$_4$ MATERIALS STUDIED

Material	Density g cm^{-3}	Temp., °C	Stress Exponent, n	Activation Energy, kcal/mole
Norton NC-350 (1976)	2.41-2.55	1500	1.3[a]	~90[b]
KBI	2.35-2.53	1350 1500	1.5-1.6	74
Ford (IM)	2.76	1500	0.9	--
AiResearch (IM) Airceram RBN-122	2.68	1500	1.1	--
AiResearch (SC) Airceram	2.88	1500	1.3	--
Norton NC-350 (1979)	2.34-2.47	1500	1.7	--
Annawerk Ceranox NR-115H	2.65	1500	2.2	--
AED Nitrasil				
Batch 1,2	2.52	1500	1.7	--
Batch 4	2.61	1500	1.2	--
Batch 5	2.63	1500	2.1	--
Raytheon (IP) RSSN	2.37-2.42	1500	1.7	--
Georgia Tech	2.49-2.64	1500	1.6	--

[a]Data of Seltzer. [52,53]

[b]Computed from IITRI and Seltzer data.
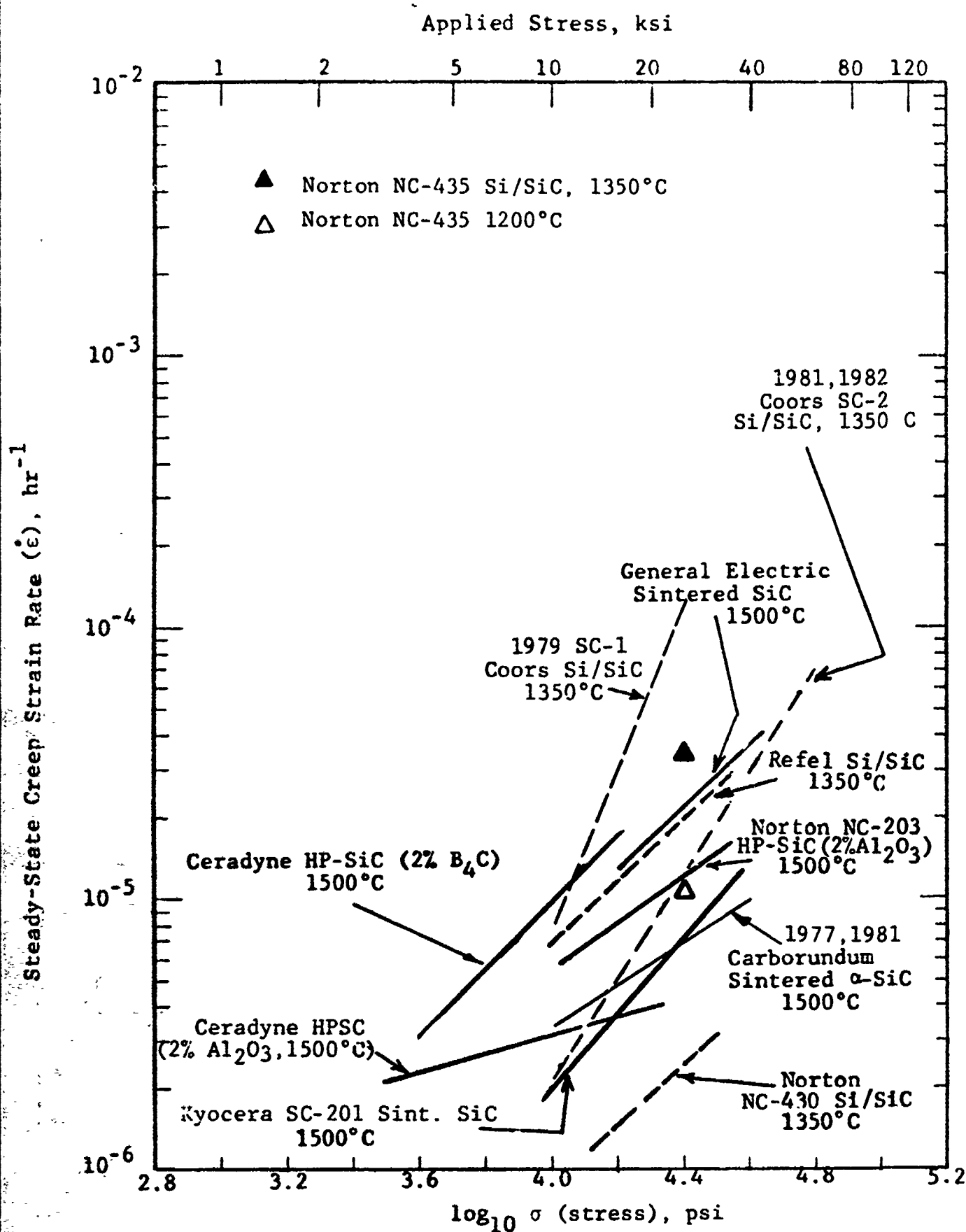
Figure 70. Steady-state flexural creep rate vs. applied stress for various silicon carbide materials.

TABLE 22.   DERIVED CREEP STRESS DEPENDENCE AND ACTIVATION ENERGY
FOR VARIOUS SiC MATFRIALS STUDIED

Material	Temp., °C	Stress Exponent, n	Activation Energy, kcal/mole
Sintered SiC			
General Electric Sintered SiC	1500	1.1-1.2	210-250[a]
1977, 1981 Carborundum Sintered SiC	1500	0.8-1.1	--
Kyocera SC-201 Sintered SiC	1500	1.4	--
Hot-Pressed SiC			
Ceradyne Ceralloy 146A HP-SiC (2% Al_2O_3)	1500	0.3	--
Ceradyne Ceralloy 146I HP-SiC (2% B_4C)	1500	1.5	--
Norton NC-203 HP-SiC (2% Al_2O_3)	1500	0.9	--
Silicon-Densified SiC			
Norton NC-435 Si/SiC	1200 1350	0.9[b]	235[c]
UKAEA/BNF Refel Si/SiC	1350	1.2	--
Norton NC-430 Si/SiC	1350	1.2	--
1979 Coors SC-1 Si/SiC	1350	2.9	--
1981, 1982 Coors SC-2 Si/SiC	1350	1.9	--

[a]General Electric data.[54]

[b]Data of Seltzer.[52,53]

[c]Computed from IITRI and Seltzer data.
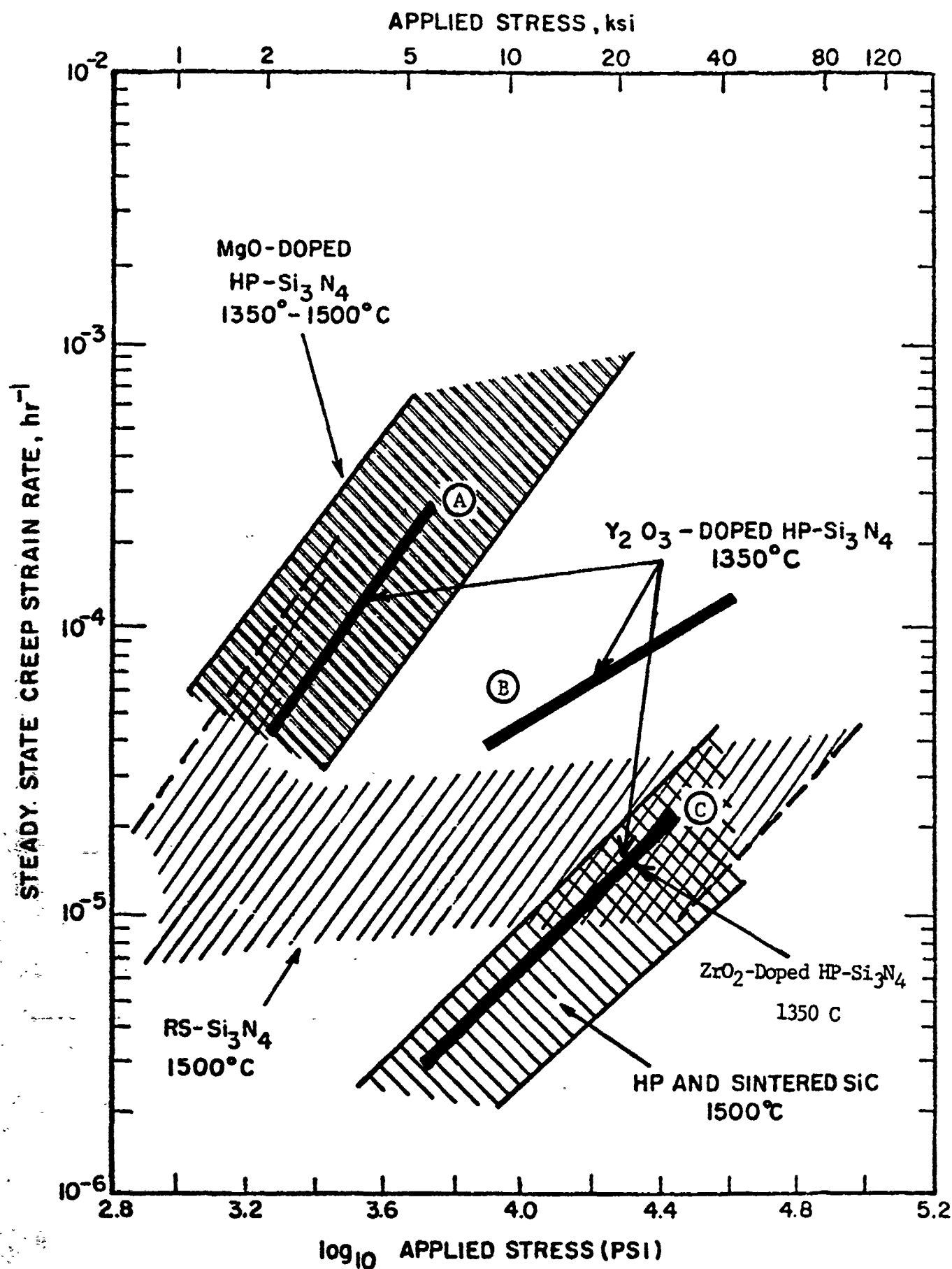
Figure 71. Flexural creep behavior of various Si_3N_4 and SiC materials.

improvement in creep resistance was beginning to be attained. This was accomplished by the controlled crystallization of the intergranular phase in these materials.

Our most recent results for hot-pressed Si_3N_4 are quite encouraging. Much improved creep resistance was observed for the Westinghouse material, doped with 4% Y_2O_3 and an undetermined amount of SiO_2. This is illustrated in Figure 71 by curve C (also shown in Figure 68). The same is true for the NASA/AVCO/ Norton material, which is prepared with nominally 10% ZrO_2 additive (also represented by curve C in Figure 71). Thus, Y_2O_3 and ZrO_2 dopants for Si_3N_4 are beginning to fulfill their promise of improved properties. Note that these two materials fall into the data band for SiC materials in Figure 71. Additionally, low stress-dependence is observed (1.0 < n < 1.3, Table 20). These are the best HP-Si_3N_4 materials investigated on this program. These creep results correlate with the good high temperature strength reported above.

Recall that the NASA/AVCO/Norton HP-Si_3N_4 (10% ZrO_2) material exhibited excellent long-term elevated temperature behavior in that a minimal amount of static fatigue was observed. The low creep rate and stress dependence obtained for the material is consistent with this, and is also a result of the deformation-resistant grain boundary phase. The Naval Research Laboratory has reported initial results in attempts to obtain more refractory silicate intergranular phases in HP-Si_3N_4 with zirconium-based densification additives such as ZrO_2, $ZrSiO_4$, ZrC, and ZrN.[55-57] We have evaluated early versions of ZrO_2-doped NRL HP-Si_3N_4 on the previous AFML program.[58] The concept here is that zircon ($ZrSiO_4$) would be present at the grain boundaries either by the direct use of it as an additive, or through the reaction of the additive binary zirconium compounds with surface-absorbed SiO_2. Rice and McDonough[55] have pointed out that zirconium silicate is a desirable intergranular compound since it has a reported melting point as high as 2500°C and solidus temperature of >1775°C (compared to >1500°C for magnesium silicate and

175

-1300°C for magnesium silicate with a few wt% CaO impurity).
Furthermore, the Young's elastic modulus and coefficient of
thermal expansion of $ZrSiO_4$ (~25 x 10^6 psi and 5 x 10^{-6} °C^{-1},
respectively) are generally better matched to those of Si_3N_4 (~45
x 10^6 psi and 3 x 10^{-6} °C^{-1}, respectively) than are those of the
lower modulus, higher expansion magnesium silicates (~20 x 10^6
psi and ~11 x 10^{-6} °C^{-1}, respectively).[55]

In summary, Y_2O_3 and ZrO_2 dopants for HP-Si_3N_4 are beginning
to fulfill their promise of improved properties. The creep re-
sults for the Westinghouse and NASA/AVCO/Norton materials fall
within the band of behavior we have previously reported for the
very creep-resistant SiC materials (Figure 71). This is a signi-
ficant advancement in Si_3N_4 technology.

8.2 RS–Si_3N_4 MATERIALS

The RS–Si_3N_4 materials studied to date generally have very
good creep strengths due to the lack of significant oxide impuri-
ty phases. Stress exponents are lower than for HP-Si_3N_4, being
typically 1.1 ± 0.2. Grain boundary sliding models have been
proposed for reaction sintered Si_3N_4,[59,60] where accommodation is
by microcracking and boundary separation. However, other inves-
tigators contend that the rate-controlling process in Si_3N_4 is
not the grain boundary sliding itself, but rather the microcrack
formation necessary to accommodate the relative crystal
movement.[61-63]

8.3 SiC MATERIALS

For all forms of SiC studied, especially hot-pressed and
sintered, creep rates are extremely low, and a linear stress
dependence is observed. This is observed in Figure 70 and Table
22. Siliconized SiC materials have substantially higher creep
rates, probably due to the presence of the continuous silicon
metal phase. This phase is very near its melting point under the
creep test conditions, and would be expected to exhibit high
rates of creep deformation. Since the creep strength of

176

hot-pressed and sintered SiC is so high (i.e., creep rate so low)
very few applications studies have identified creep deformation
to be a predominant failure mode for SiC. For this reason, only
a few mechanistic studies have been undertaken. The linear
stress dependence of the creep rate in SiC suggests that diffu-
sion is the rate-controlling process. A carbon-vacancy diffusion
mechanism has been proposed.[64,65]

9. THERMAL EXPANSION

One of the reasons that silicon-base ceramics are prime
candidates for use in advanced gas turbine applications is their
low expansion coefficient and high strength, which makes them
less susceptible than many other ceramics (especially oxides) t
thermal shock damage. However, it is recognized that such low
thermal expansion can be a disadvantage also; for instance, in
the creation of thermal expansion mismatch situations with higher
expansion metal engine components. As with many other aspects of
heat ɛ ᵗine materials selection and component design, many trade-
offs exist.

Thermal expansion is perhaps the least variable property of
silicon ceramics. It is mainly a function of the solid phase and
thus not strongly affected by porosity and minor impurities.
Figure 72 presents thermal expansion data bands for various sili-
con-based ceramics. Details for specific materials are contained
in Figure 73. Tabular data for the various forms of silicon
nitride and silicon carbide investigated on this program are
presented in Tables 23 and 24, respectively.

All forms of SiC have ~50% higher thermal expansion than all
forms of Si_3N_4. Within a given material performance band, the
effect of additives can be seen. For instance, within the ther-
mal expansion data band for SiC shown in Figure 72 exist curves
for additive-free sintered SiC, hot-pressed SiC (which contains
~2% Al_2O_3), and siliconized SiC (which contains ~10-20% silicon
metal). Siliconized forms of SiC exhibit the lowest expansion,
sintered SiC has intermediate expansion, and Al_2O_3-doped hot-
pressed SiC the highest expansion. The low expansion for Si/SiC
is due to the low expansion of the silicon metal phase. The high
expansion for hot-pressed SiC is caused by their slight alumino-
silicate grain boundary phase (oxides having much higher expan-
sion than pure SiC).

178
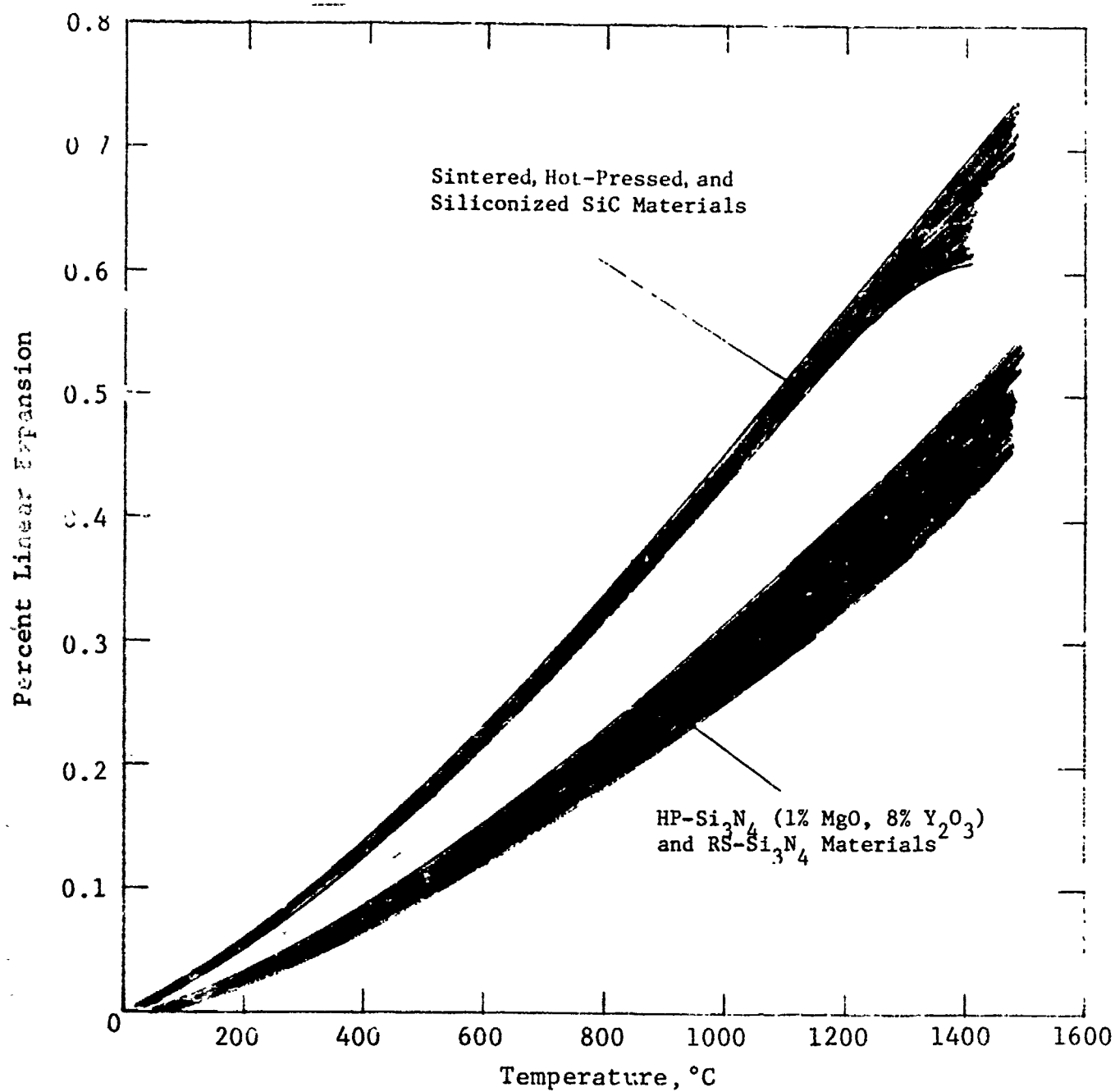
Figure 72. Thermal expansion data bands for Si_3N_4 and SiC materials.
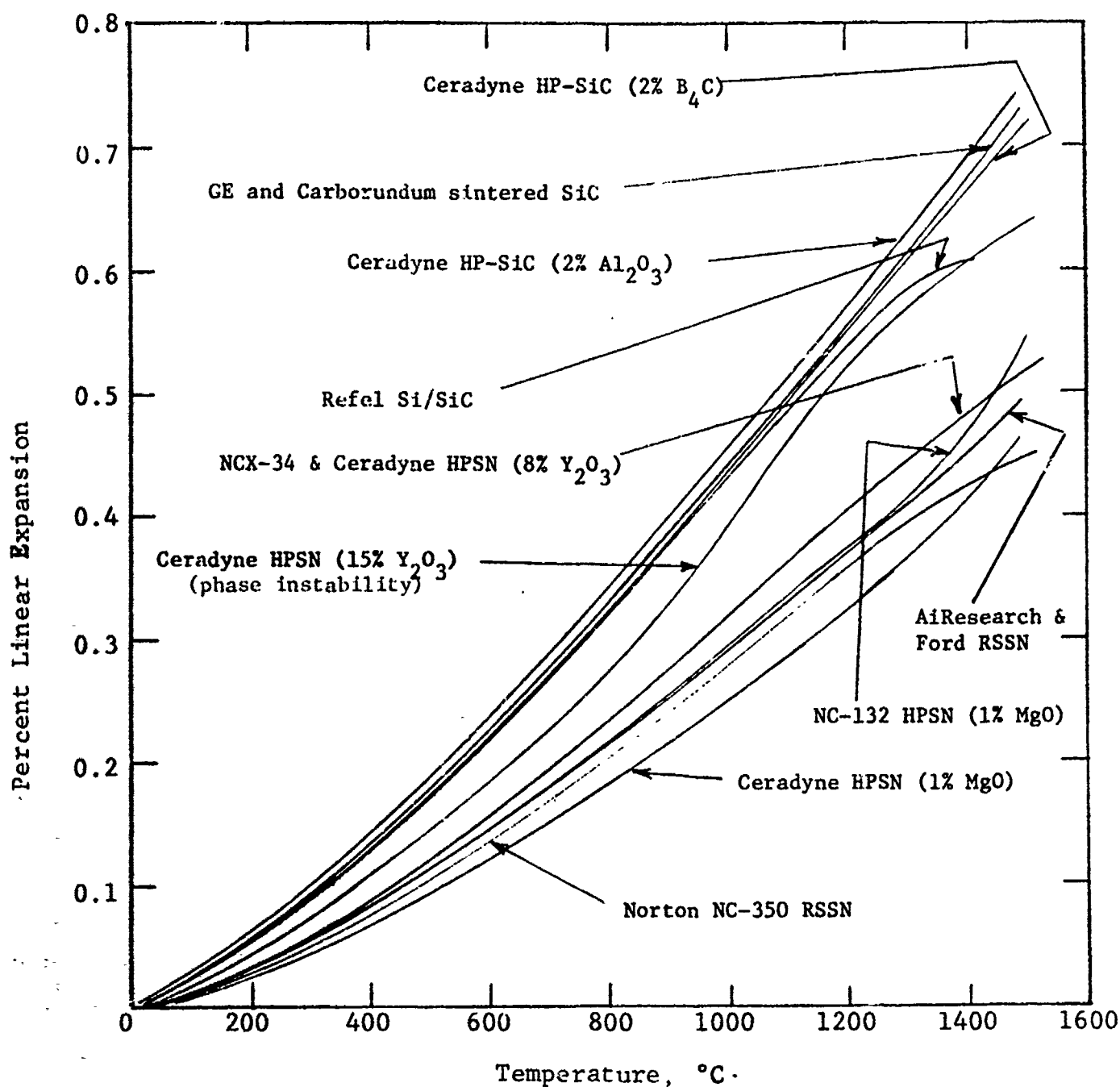
Figure 73. Thermal expansion of various Si_3N_4 and SiC materials.

TABLE 23. THERMAL EXPANSION OF Si_3N_4 MATERIALS

Material	Percent Linear Expansion at 1000°C	Mean Coefficient of Thermal Expansion, (20°-1000°C), $10^{-6}/°C$
Hot-Pressed Si_3N_4		
Norton NC-132 (1% MgO)	.295	3.01
Ceradyne 147A (1% MgO)	.299	3.05
Fiber Materials (4% MgO)	.336	3.43
Norton NCX-34 (8% Y_2O_3)	.315	3.21
Ceradyne 147Y-1 (8% Y_2O_3)	.322	3.29
Ceradyne 147Y (15% Y_2O_3)	.385	3.93
Harbison-Walker (10% CeO_2)	.341	3.48
Toshiba (4% Y_2O_3, 3% Al_2O_3)	.305	3.11
Toshiba (3% Y_2O_3, 4% Al_2O_3, SiO_2)	.316	3.22
NASA/AVCO/Norton (10% ZrO_2)	.355	3.62
Reaction-Sintered Si_3N_4		
Norton NC-350 (1976)	.274	2.80
Kawecki-Berylco	.280	2.86
Ford (IM)	.300	3.06
AiResearch (SC) RBN-101	.297	3.03
AiResearch (IM) RBN-122	.296	3.02
Raytheon	.289	2.95
Norton NC-350 (1979)	.292	2.98
AED Nitrasil (Batch 4)	.302	3.08
Georgia Tech	.268	2.73

TABLE 24. THERMAL EXPANSION OF SiC MATERIALS

Material	Percent Linear Expansion at 1000°C	Mean Coefficient of Thermal Expansion (20°-1000°C), 10^{-6}/°C
Hot Pressed SiC		
Ceradyne 146A (2% Al_2O_3)	.449	4.58
Ceradyne 146I (2% B_4C)	.438	4.47
Norton NC-203 (2% Al_2O_3)	.451	4.60
Sintered SiC		
Carborundum 1977 α-SiC	.438	4.47
General Electric β-SiC	.432	4.41
Kyocera SC-201 α-SiC	.445	4.54
Carborundum 1981 α-SiC (Hexoloy SX-05)	.430	4.39
Siliconized SiC		
Norton NC-435	.427	4.36
UKAEA/BNF Refel	.424	4.33
Norton NC-430	.424	4.33
Coors 1979 (SC-1)	.425	4.34
Coors 1981 (SC-2)	.420	4.29

Trends for Si_3N_4 materials are stronger and directly correlated with the amount of intergranular oxide phase present in the microstructure. This is seen by consideration of the tabular data in Table 23. In the limit of minimal intergranular phases, the lowest thermal expansion is observed. This represents the pure $RS-Si_3N_4$ materials. The hot-pressed forms of Si_3N_4 all contain varying amounts of the high expansion oxide phase in intergranular regions.

Compared to the various forms of Si_3N_4, the thermal expansion of SiC only varies a maximum of ~5% as a function of processing method. As shown in Table 23, the difference in thermal expansion between a reaction-sintered Si_3N_4 and a highly doped hot-pressed Si_3N_4 can be as much as 30%. As mentioned previously, this is another indication that the properties of the various forms of SiC are more intrinsic, and that the properties of Si_3N_4 are mainly dependent on the existence or the lack of an oxide grain boundary phase, and its specific character (i.e., phase composition, structure, and resulting mechanical properties).

10. THERMAL SHOCK RESISTANCE

The ability to withstand the thermal stresses generated during ignition, flame-out, and operating temperature excursions is an important consideration in evaluating potential ceramic heat engine materials. Thermally created stresses may initiate a fracture which can result in a catastrophic failure, or cause existing flaws to grow giving a gradual loss of strength and eventual loss of component integrity. However, the evaluation of thermal stress resistance is a complex task since performance is dependent not only on material thermal and mechanical properties, but is also influenced by heat transfer and geometric factors (i.e., heat transfer coefficient and component size).

Thermal shock resistance was determined on this program by the water quench method, with the initiation of thermal shock damage being detected by internal friction measurement. The methodology for this was discussed in detail in Section 5.5. In conducting this test, internal friction is measured before and after water quench from successively higher temperatures using the flexural resonant frequency Zener bandwidth method. A marked change in internal friction (specific damping capacity) indicates the onset of thermal shock damage (i.e., thermal stress-induced crack initiation). This defines the critical quench temperature difference, ΔT_c, which is compared to analytical thermal stress resistance parameters. The parameter which is most applicable to the experimental severe water quench is $R = \sigma(1 - \mu)/\alpha E$,[66] where σ is the strength, μ is Poisson's ratio, α is thermal expansion, and E is the elastic modulus. The details, interpretation, and limitations of this procedure for assessing relative thermal shock resistance was discussed previously.[67]

Hasselman's theory[68] unified considerations of thermal stress fracture initiation and the degree of damage due to subsequent crack propagation. It was demonstrated that the material

184

parameters that are required to give greatest resistance to thermal stress fracture initiation (high strength, low Young's elastic modulus, high thermal conductivity, low thermal expansion, etc.) are, in general, mutually exclusive to the requirements providing greatest resistance to crack propagation and material damage due to thermal stresses (low strength, high modulus, high fracture surface energy, etc.). These properties and the behavior of a material experiencing thermally created stresses are influenced by the initial size and density of cracks or flaws (i.e., the total flaw structure of the material). This structure affects the material's ability to store elastic thermal strain energy, the driving force for crack propagation. In general a material resistant to fracture has a low flaw density, so once a sufficiently high stress level (or level of stress intensity) is obtained in such a material, its high stored energy causes the most deleterious flaw to propagate catastrophically or in a kinetic manner. This occurs because the energy release rate is greater than that needed to merely balance fracture surface energy. Resistance to thermal stress damage means the material is resistant to crack propagation, as opposed to fracture initiation. When cracks are propagated due to thermal stresses in such a case, the propagation is quasi-static in that only enough crack length is generated to absorb the available strain energy. The rate of strain energy release is lower in such materials and less strain energy is available as a driving force for continued propagation. This usually occurs in a more highly flawed material. This discussion shows why internal friction, as a measure of the total flaw spectrum, is useful in monitoring thermal shock performance.

The baseline (unshocked) levels of internal friction for all silicon-base materials evaluated on this program are presented in Tables 25-27. Figure 74 compares the observed internal friction-quench temperature difference behavior for various general classes of silicon ceramics. Table 28 presents the various analytical thermal stress resistance parameters that have been

185

TABLE 25.   BASELINE UNSHOCKED LEVEL OF INTERNAL
FRICTION FOR HOT PRESSED Si_3N_4 MATERIALS

Material	Baseline Internal Friction Approximate Range, x 10^4
1. Norton NC-132 HPSN (1% MgO)	1.0
2. Norton NCX-34 HPSN (8% Y_2O_3)	0.5-0.8
3. Ceradyne 147A HPSN (1% MgO)	0.9-2.7
4. Ceradyne 147-Y-1 HPSN (8% Y_2O_3)	0.9-1.2
5. Ceradyne 147-Y HPSN (15% Y_2O_3)	0.7-1.3
6. Fiber Materials HPSN (4% MgO)	1.1-1.4
7. Harbison-Walker HPSN (10% CeO_2)	0.6
8. Toshiba HPSN (4% Y_2O_3, 3% Al_2O_3)	0.9
9. Toshiba HPSN (3% Y_2O_3, 4% Al_2O_3, SiO_2)	0.8-1.4
10. Westinghouse HPSN (4% Y_2O_3, SiO_2)	0.6-1.0
11. NASA/AVCO/Norton HPSN (10% ZrO_2)	3.5

TABLE 26. BASELINE UNSHOCKED LEVELS OF INTERNAL
FRICTION FOR REACTION SINGERED Si_3N_4 MATERIALS

	Material	Baseline Internal Friction Approximate Range, x 10^4
1.	Norton NC-350 RSSN (1976)	2-3
2.	Kawecki-Berylco RSSN	2-5
3.	Ford (IM) RSSN	1.7-2.5
4.	AiResearch (SC) Airceram RBN-101	4
5.	AiResearch (IM) Airceram RBN-122	1.4-2.6
6.	Raytheon (IP) RSSN	2.8-4.9
7.	Norton NC-350 RSSN (1979)	2.2-2.7
8.	AED Nitrasil RSSN	1.4-2.2
9.	Georgia Tech RSSN	1.9-2.2

TABLE 27. BASELINE INTERNAL FRICTION OF SiC MATERIALS

Material	Baseline Internal Friction Approximate Range, x 10^4
1. Norton NC-435 Si/SiC	1-2
2. Carborundum Sintered α-SiC	1.6-2.3 .
3. General Electric Sintered β-SiC	2-2.7
4. UKAEA/BNF Refel Si/SiC	0.6-2.7
5. UKAEA/BNF Refel Si/SiC	5-10
6. Ceradyne 146A HPSC (2% Al_2O_3)	1.4-2.4
7, Ceradyne 146I HPSC (2% B_4C)	1.2-3.7
8. Norton NC-203 HPSC (2% Al_2O_3)	1.2
9. Norton NC-430 Si/SiC	1-1.5
10. Coors Si/SiC (1979, SC-1)	0.9
11. Kyocera SC-201 Sintered SiC	2.7-3.3
12. 1981 Coors SC-2 Si/SiC	1.5
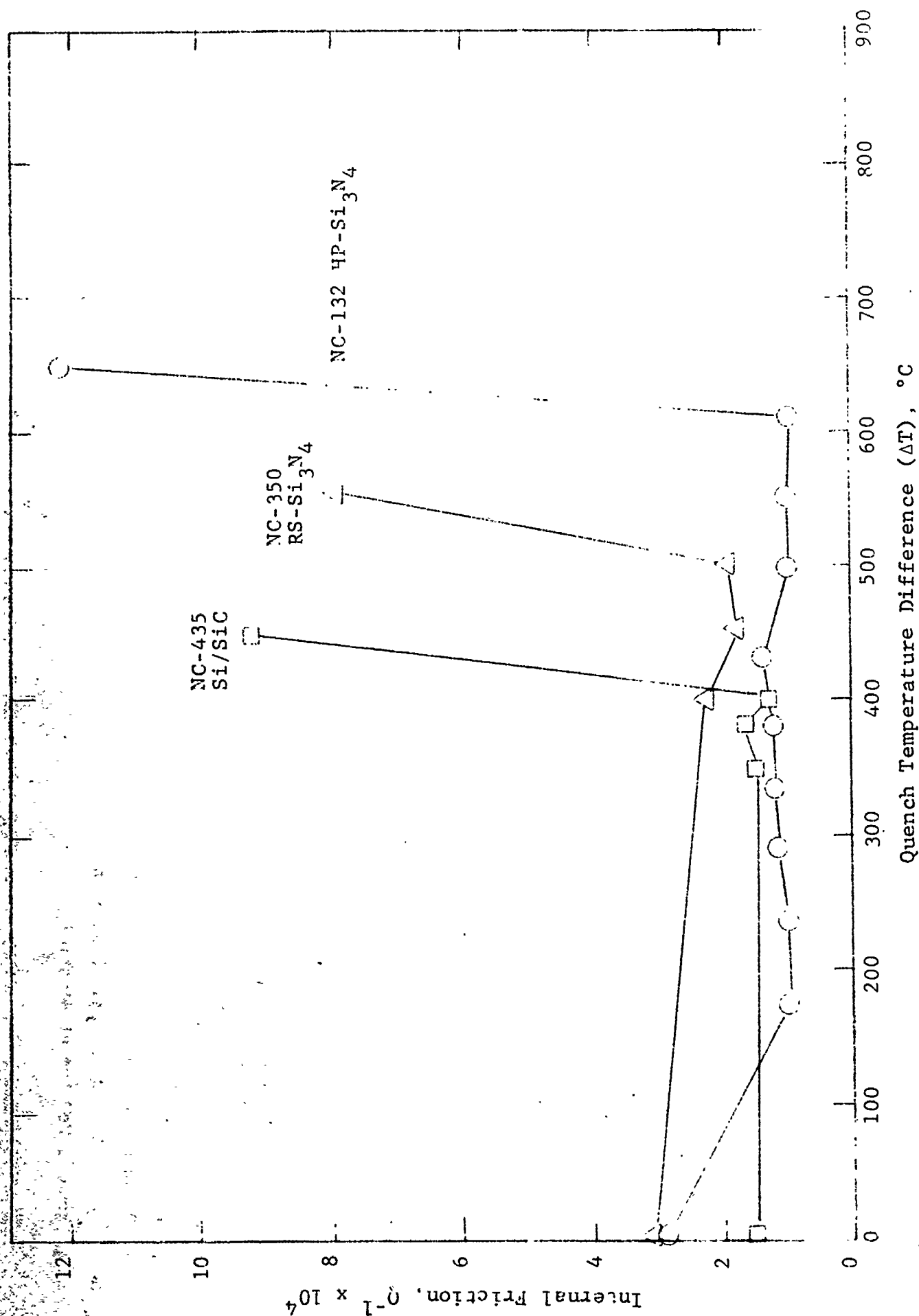
Figure 74. Intern. friction after water quench.

189

TABLE 28. THERMAL STRESS RESISTANCE PARAMETERS (66)

LITERATURE DESIGNATION	PARAMETER TYPE	PARAMETERS	PHYSICAL INTERPRETATION/ENVIRONMENT	TYPICAL UNITS
R	Resistance to Fracture Initiation	$\dfrac{\sigma_t\,(1-\mu)}{\alpha E}$	Maximum ΔT allowable for steady heat flow;	°C
R'	Resistance to Fracture Initiation	$\dfrac{\sigma_t(1-\mu)k}{\alpha E}$	Maximum heat flux for steady flow;	cal cm^{-1} sec^{-1}
R''	Resistance to Fracture Initiation	$\dfrac{\sigma_t\,(1-\mu)\alpha_{TH}}{\alpha E}$	Maximum allowable rate of surface heating;	cm^2°C sec^{-1}
R'''	Resistance to Propagation Damage	$\dfrac{E}{\sigma^2\,(1-\mu)}$	Minimum in elastic energy at fracture available for crack propagation	(psi)$^{-1}$
R''''	Resistance to Propagation Damage	$\dfrac{YE}{\sigma^2\,(1-\mu)}$	Minimum in extent of crack propagation on initiation of thermal stress fracture	cm
R_{st}	Resistance to further crack propagation	$\left[\dfrac{\gamma}{\alpha^2 E}\right]^{1/2}$	Minimum ΔT allowed for propagation long cracks	°Cm$^{-1/2}$

σ_t = Tensile Strength

μ = Poisson's ratio

α = Coefficient of Thermal Expansion

E = Young's Modulus of Elasticity

ρ = Density

C_p = Specific Heat

k = Thermal Conductivity

α_{TH} = Thermal Diffusivity

γ = Fracture Surface Energy

derived. For the water-quench test, it was mentioned above that the R parameter is most appropriate.

Cumulative analytical and experimental thermal shock results are compiled in Tables 29 through 31 for hot-pressed and reaction-sintered Si_3N_4, and SiC materials, respectively. The pertinent thermal and mechanical properties used to compute R, the analytical thermal stress resistance parameter, are also shown. The computed R value for each material represents the maximum ΔT allowable before shock initiation. The R parameter is compared with experimentally obtained ΔT_c values from the water quench tests, as shown. Figure 75 provides a direct comparison of the analytical and experimental thermal shock results for all materials investigated to date. The trend line is a linear least squares regression data fit for all materials. The materials evaluated follow a definite trend of thermal shock resistance as a function of material type and processing method as shown in Figure 75. That is, in descending order of resistance to damage by thermal shock, the materials are listed: (1) Y_2O_3-modified HP-Si_3N_4, (2) MgO-doped HP-Si_3N_4, (3) high density RS-Si_3N_4, (4) low density RS-Si_3N_4, and finally, (5) all forms of SiC.

A notable aspect of the results illustrated in Figure 75 is the relative thermal shock resistance of the 1976 and 1979 versions of Norton NC-350 RS-Si_3N_4. By virtue of its ~30% higher strength and ~10% lower expansion-modulus product, 1979 NC-350 has significantly increased thermal shock resistance. The more recent Norton NC-350 is the most thermal shock resistant reaction sintered Si_3N_4 evaluated on this program. Figure 75 illustrates that it is better than some of the denser hot-pressed Si_3N_4 materials.

The results for the Toshiba and Westinghouse HP-Si_3N_4 materials are also encouraging. As shown in Figure 75, Toshiba HP-Si_3N_4 (4% Y_2O_3, 3% Al_2O_3) and Westinghouse HP-Si_3N_4 (4% Y_2O_3, SiO_2) exhibited the highest experimentally determined critical quench temperature difference, ΔT_c, obtained to date, i.e., ΔT_c = 725°C and 750°C, respectively. These results for the Toshiba and

TABLE 29. THERMAL STRESS RESISTANCE PARAMETERS FOR HOT-PRESSED Si_3N_4 MATERIALS

Material	Flexural Strength,[a] ksi	Poisson's Ratio[b]	Thermal Expansion[c] 10^{-6}/°C	Elastic Modulus 10^6 psi	$R = \sigma(1-\mu)/\alpha E$,[d] °C	ΔT_c $(\Delta q^{-1})/\alpha$,[d,e] °C
Norton NC-132 HPSN (1% MgO)	103.1	0.27	2.50	47.1	639	600
Norton NCX-34 HPSN (8% Y_2O_3)	126.7	0.27	2.63	48.6	724	600-800
Ceradyne 147A HPSN (1% MgO)	b7.1	0.27	2.60	47.9	511	500-600
Ceradyne 147Y-1 HPSN (8% Y_2O_3)	83.3	0.29	2.61	45.4	499	500-700
Ceradyne 147Y HPSN (15% Y_2O_3)	87.6	0.28	3.0	44.7	470	400-500
Fiber Materials HPSN (4% MgO)	66.8	0.28	2.94	46.2	354	600
Harbison-Walker HPSN (10% CeO_2)	87.9	0.28	2.88	45.0	488	400-600
Toshiba (4% Y_2O_3, 3% Al_2O_3)	105.7	0.28 (est)	2.40	47.5	668	725
Toshiba (3% Y_2O_3, 4% Al_2O_3, SiO_2)	83.6	0.28 (est)	2.35	41.3	620	625
Westinghouse (4% Y_2O_3, SiO_2)	91.0	0.28 (est)	2.4 (est)	44.2	618	750
NASA/AVCO/Norton HPSN (10% ZrO_2)	95.2	0.28 (est)	2.99	45.0	509	600-650

[a] All properties at 25°C, unless otherwise noted; computed average of all samples tested; note that 4-point bend strength is used instead of tensile strength.

[b] Determine at AFML by resonant sphere technique, unless otherwise indicated.

[c] At 500°C.

[d] Analytical thermal stress resistance parameter; maximum ΔT allowable for steady heat flow.

[e] Critical ΔT determined by change in internal friction in water quench tests.

TABLE 30. THERMAL STRESS RESISTANCE PARAMETERS FOR REACTION-SINTERED Si_3N_4 MATERIALS

Material	Flexural Strength,[a] ksi	Poisson's Ratio[b]	Thermal Expansion,[c] $10^{-6}/°C$	Elastic Modulus, 10^6 psi	$R = \sigma(1-\mu)/\alpha E$,[d] °C	$\Delta T_c(\Delta Q^{-1})$,[e] °C
Norton NC-350 RSSN (1976)	29.5	0.22	2.29	25.6	393	400-500
Kawecki-Berylco RSSN	21.1	0.24	2.30	20.9	334	600-800
Ford (IM) RSSN	38.2	0.25	2.48	30.7	376	350-450
AiResearch (SC) Airceram RBN-101	37.9	0.24	2.42	32.0	372	400-600
AiResearch (IM) Airceram RBN-122	32.6	0.23	2.44	30.2	341	350-400
Raytheon (IP) RSSN	21.6	0.24(est.)	2.41	23.8	286	~400
Norton NC-350 RSSN (1979)	37.6	0.22(est.)	2.46	22.1	539	500
AED Nitrasil RSSN	29.1	0.24(est.)	2.67	26.6	311	425-475
Georgia Tech RSSN	26.2	0.24(est.)	2.00	23.9	417	500

[a]All properties at 25°C, unless otherwise noted; computed average of all samples tested; note that 4-point bend strength is used instead of tensile strength.

[b]Determine at AFML by resonant sphere technique, unless otherwise indicated.

[c]At 500°C.

[d]Analytical thermal stress resistance parameter; maximum ΔT allowable for steady heat flow.

[e]Critical ΔT determined by change in internal friction in water quench tests.

TABLE 31. THERMAL STRESS RESISTANCE PARAMETERS FOR SILICON CARBIDE MATERIALS

Material	Flexural Strength,[a] ksi	Poisson's Ratio[b]	Thermal Expansion,[c] $10^{-6}/°C$	Elastic Modulus, 10^6 psi	$R = \sigma(1-\mu)/\alpha E$,[d] °C	ΔT_c $(\Delta Q=1)$,[e] °C
Norton NC-435 Si/SiC	57.2	0.17	3.83	50.7	244	350-400
Carborundum Sint. α-SiC	44.2	0.16	3.8	58.2	168	300
General Electric Sint. β-SiC	63.8	0.16	3.78	54.8	259	375-400
UKAEA/BNF Refel Si/SiC	44.9	0.17	3.79	57.5	171	300-400
UKAEA/BNF Refel Si/SiC (as processed)	33.6	0.17	3.79	52.5	140	---
Ceradyne 146A HP-SiC (2% Al_2O_3)	60.1	0.16	4.0	67.2	188	~300 (est.)
Ceradyne 146I HP-SiC (2% B_4C)	45.6	0.16 (est.)	3.89	65.3	151	300
Norton NC-203 HP-SiC (2% Al_2O_3)	101.8	0.17	4.08	64.7	320	350
Norton NC-430 Si/SiC	30.4	0.17	3.85	58.7	112	300-350
Coors Si/SiC (1979 SC-1)	50.6	0.17 (est.)	3.50	51.1	235	400
Kyocera SC-201 Sint. SiC	56.1	0.17 (est.)	3.70	60.5	208	325
1981 Coors SC-2 Si/SiC	45.4	0.17 (est.)	3.95	56	170	375-400

[a]All properties at 25°C, unless otherwise noted; computed average of all samples tested; note that
4-point bend strength is used instead ot tensile strength.

[b]Determine at AFML by resonant sphere technique, unless otherwise indicated.

[c]At 500°C.

[d]Analytical thermal stress resistance parameter; maximum ΔT allowable for steady heat flow.

[e]Critical ΔT determined by change in internal friction in water quench tests.

194
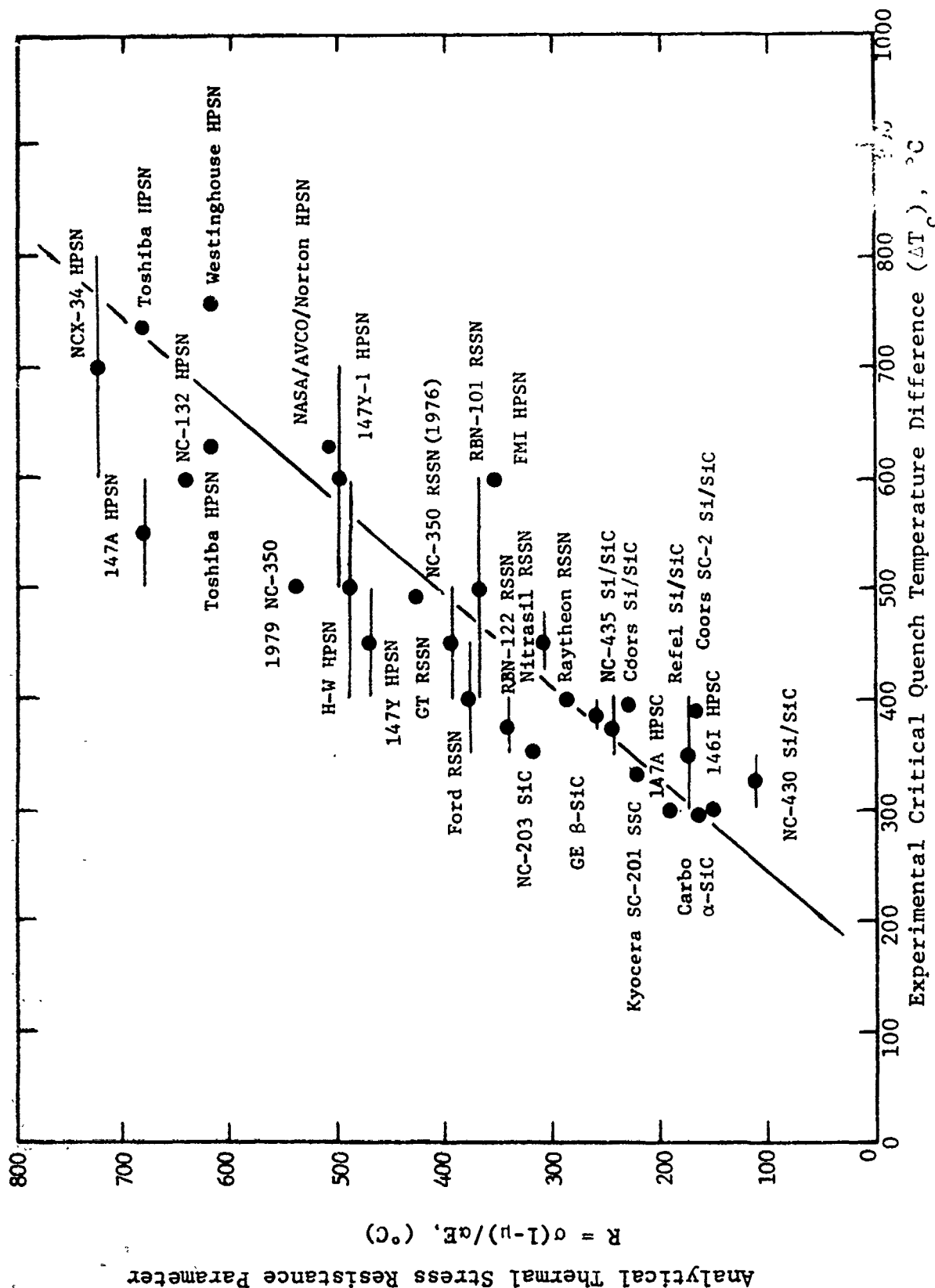
Figure 75. Analytical vs. experimental thermal shock results for various Si_3N_4 and SiC materials.

Westinghouse materials correlate with the high strength of these materials.

To summarize the results for SiC, it is noted that all forms of silicon carbide fall at the opposite extreme of thermal shock resistance when compared to HP-Si_3N_4. This is due to the extremely high thermal expansion and elastic modulus for SiC. It is interesting to note that despite the very high strength of Norton NC-203 HP-SiC (twice as strong as other SiC materials), its thermal shock resistance remains about the same as the other SiC materials. The reason for this is the overriding influence of the high αE product for SiC. For example, for NC-203 to exhibit an R value of 500°C (that is, approximately mid-range of the materials shown in Figure 75), it would have to have a strength of 160 ksi. For NC-203 HP-SiC to have an R value as high as the best HP-Si_3N_4, i.e., R = 750°C, it would have to have a strength of 240 ksi. Thus, SiC inherently has lower thermal shock resistance than Si_3N_4, and no conventional processing methods for SiC can overcome the high αE factor. In certain situations the higher thermal conductivity for SiC helps, but not enough to override the effect of high elastic modulus and high thermal expansion. It is for this reason that SiC has found application in combustors, where high thermal conductivity is useful to minimize hot spots and the temperature is relatively static.

11. OXIDATION BEHAVIOR

Oxidation of Si_3N_4 and SiC materials is strongly dependent on porosity for reaction sintered materials and specific impurities for hot-pressed materials. In this screening program test bars were exposed in static air for 100, 1000, and occassionally 2000 hr at specific temperatures, as listed in Table 32. The choice of exposure temperature was generally based on the projected upper use temperature for the material. Yttria- and ceria-doped HP-Si_3N_4 materials, however, were all exposed at 1000°C, since a destructive oxidation-related phase instability has sometimes been observed for such materials at intermediate temperatures. Post-exposure evaluation of materials is outlined in Table 33, and includes optical and SEM examination of the oxide scale morphology, weight change, retained strength and fracture source identification (with comparison to unexposed data), and identification of the oxide scale products by X-ray diffraction (XRD) and X-ray fluorescence (XRF) techniques.

The details of the weight change data for specific HP-Si_3N_4, sintered Si_3N_4, RS-Si_3N_4, and SiC materials are presented in Tables 34 through 37, respectively. Similarly, the residual strength and fracture origins for these materials are presented in Tables 38 through 41. The unexposed bend strength and fracture origins are also tabulated for each material for comparison. For convenience, the weight change data are combined and presented in summary form in Table 42. Note that when interpreting weight change data, it is important to recognize that a negligible change in weight does not necessarily mean that the environment was benign. Positive and negative weight changes due to competing mechanisms could conceivably occur at the same rate. The residual strength data are combined and summarized in Table 43. These data for each material can be discussed in terms of the purity and porosity of each material, the optical and SEM surface scale morphology, and the mechanistic interpretation for

TABLE 32. SCHEDULE FOR 100 AND 1000 HOUR
STATIC AIR EXPOSURE

Material	Temperature, °C
HP-Si_3N_4 (MgO)	1200
HP-Si_3N_4 (Y_2O_3)	1000
HP-Si_3N_4 (CeO_2)	1000
RS-Si_3N_4	1400
HP-SiC	1400[a]
Sintered SiC	1400[a]
Si/SiC	1200

[a]Also limited 2000 hr/1500 C exposures.

TABLE 33. POST-EXPOSURE EVALUATION PARAMETERS

Oxide Scale Morphology

- Optical
- SEM

Weight Gain

Residual Strength

- fracture origins

Scale Products

- XRD,[a] crystalline compounds
- XRF,[b] elemental

[a]X-ray diffraction.

[b]X-ray fluorescence.

TABLE 34. WEIGHT CHANGE AFTER OXIDATION EXPOSURE FOR VARIOUS HOT-PRESSED Si_3N_4 MATERIALS

Material	Exposure	Weight Change, %
Norton NCX-34 (8% Y_2O_3)	100 hr/1000°C	+0.02
	1000 hr/1000°C	+0.10
Ceradyne Ceralloy 147Y-1 (8% Y_2O_3)	100 hr/1000°C	+0.004
	1000 hr/1000°C	+0.05
Ceradyne Ceralloy 147Y (15% Y_2O_3)	100 hr/1000°C	+2.70
	1000 hr/1000°C	+0.03 to +5.1
Harbison-Walker (10% CeO_2)	100 hr/1000°C	+0.14
	1000 hr/1000°C	+0.34
Ceradyne Ceralloy 147A (1% MgO)	100 hr/1200°C	+0.17
	1000 hr/1200°C	+0.48
Fiber Materials (4% MgO)	100 hr/1200°C	+0.46
	1000 hr/1200°C	+2.62 (2.1 to 3.2)
Toshiba HP-Si_3N_4 (4% Y_2O_3, 3% Al_2O_3)	100 hr/1000°C	+0.14 (+0.1 to +0.3)
	1000 hr/1000°C	+0.06 to +0.58
Toshiba HP-Si_3N_4 (3% Y_2O_3, 4% Al_2O_3, SiO_2)	100 hr/1000°C	-0.03
	1000 hr/1000°C	-0.007
Westinghouse (4% Y_2O_3, SiO_2)	100 hr/1000°C	+0.003
	1000 hr/1000°C	+0.013

TABLE 35. WEIGHT CHANGE AFTER OXIDATION EXPOSURE
FOR SINTERED Si_3N_4 MATERIALS

Material	Exposure	Weight Change, %
Rocketdyne SN-50 Sintered Si_3N_4(6% Y_2O_3, 4% Al_2O_3)	100 hr/1000°C	+0.14
Rocketdyne SN-46 Sintered Si_3N_4(14% Y_2O_3, 7% SiO_2)	1000 hr/1000°C	+0.64 (+4% thickness change)
AiResearch Sintered Si_3N_4 (8% Y_2O_3, 4% Al_2O_3)	100 hr/1200°C 1000 hr/1200°C	+0.08 +0.21

TABLE 36. WEIGHT CHANGE AFTER OXIDATION EXPOSURE FOR VARIOUS REACTION-SINTERED Si$_3$N$_4$ MATERIALS

Material	Exposure	Weight Change %	Unexposed Fractional Porosity		
			Open	Closed	Total
Norton 1979 NC-350	100 hr/1400°C	+1.90	0.18-0.24	0.04(Avg)	0.23-0.27
	1000 hr/1400°C	+1.57 (1.21-2.05)			
Norton 1976 NC-350	100 hr/1400°C	--	0.12	0.08	0.20
	1000 hr/1400°C	+0.13			
Ford (IM)	100 hr/1400°C	+0.03	0.11	0.03	0.14
	1000 hr/1400°C	+0.83			
Airesearch Airceram RBN-101 (Slipcast)	100 hr/1400°C	-0.25	0.06	0.04	0.10
	1000 hr/1400°C	-0.02 to +0.09			
AiResearch Airceram RBN-122 (Injection-Molded)	100 hr/1400°C	+0.74	0.11	0.06	0.17
	1000 hr/1400°C	+1.16			
Annawerk Ceranox NR-115⁴	100 hr/1400°C	+0.84 (0.56-1.13)	0.12-0.15	0.06(Avg)	0.16-0.23
	1000 hr/1400°C	+0.98 (0.75-1.46)			
AED Nitrasil: ● Batch 1	100 hr/1400°C	+2.19	0.18	0.04	0.22
	1000 hr/1400°C	+2.60			
● Batch 2	100 hr/1400°C	+1.32	0.17	0.04	0.21
	1000 hr/1400°C	+2.50			
● Batch 3	100 hr/1400°C	+1.23	0.13	0.06	0.19
	1000 hr/1400°C	+1.49			
● Batch 4	100 hr/1400°C	+1.01	0.12	0.06	0.18
	1000 hr/1400°C	+1.09			
● Batch 5	100 hr/1400°C	+0.94	0.12	0.06	0.18
	1000 hr/1400°C	+1.52			
Georgia Tech RS-Si$_3$N$_4$	100 hr/1400°C	+0.42	0.16	0.03	0.19
	1000 hr/1400°C	+1.35			
AME RS-Si$_3$N$_4$	100 hr/1400°C	+8.87 (8.32-9.37)	0.32	0.02	0.34
	1000 hr/1400°C	+8.12 (6.90-9.14)			
AiResearch RBN-104	100 hr/1400°C	+0.11	0.08	0.05	0.13
	1000 hr/1400°C	+0.18			

TABLE 37. WEIGHT CHANGE AFTER OXIDATION EXPOSURE FOR VARIOUS SILICON CARBIDE MATERIALS

Material	Exposure	Weight Change %
Carborundum Sintered α-SiC	100 hr/1400°C	--
	1000 hr/1400°C	+0.07
General Electric Sintered SiC	100 hr/1400°C	-0.14 to +0.08
	1000 hr/1400°C	+0.01 to +0.23
	2000 hr/1500°C	0.39 to 1.21
Norton NC-203 HP-SiC (2% Al_2O_3)	100 hr/1400°C	+0.11
	1000 hr/1400°C	+0.10
	2000 hr/1500°C	+0.30
Ceradyne Ceralloy 146A HP-SiC (2% Al_2O_3)	100 hr/1400°C	+0.07
	1000 hr/1400°C	+0.20
Ceradyne Ceralloy 146I HP-SiC (2% B_4C)	100 hr/1400°C	+0.12
	1000 hr/1400°C	+0.19
UKAEA/BNF Refel Si/SiC ● Diamond-Ground	100 hr/1200°C	+0.01
	1000 hr/1200°C	+0.08
● As-Processed	100 hr/1200°C	+0.02
	1000 hr/1200°C	+0.05
Norton NC-430 Si/SiC	100 hr/1200°C	+0.01
	1000 hr/1200°C	+0.06
Coors Si/SiC	100 hr/1200°C	+0.06
	1000 hr/1200°C	+0.16
Kyocera SC-201 Sintered SiC	100 hr/1400°C	+0.03
	1000 hr/1400°C	+0.09

TABLE 38. RETAINED STRENGTH OF HOT-PRESSED Si_3N_4 MATERIALS

Material	Non-Exposed		Static Air Exposure	Exposed	
	Mean R.T. Strength, psi	Fracture Origins		Mean R.T. Strength, psi	Fracture Origins
Norton NCX-34 (8% Y_2O_3)	126,730	Machining flaws and processing defects.	100 hr/1000°C 1000 hr/1000°C	136,480 137,550	Machining flaws. Undetermined.
Ceradyne Ceralloy 147Y-1 (8% Y_2O_3)	83,250	Machining flaws and processing defects	100 hr/1000°C 1000 hr/1000°C	89,320 79,880	Undetermined. Dark inclusion
Ceradyne Ceralloy 147Y (15% Y_2O_3)	87,850	Undetermined	100 hr/1000°C 1000 hr/1000°C	5,590 or 102,000[a]	Internal cracking. Undetermined.
Harbison-Walker (10% CeO_2)	87,890	Primarily inclusions	100 hr/1000°C 1000 hr/1000°C	76,840 49,940	Dark inclusion. Oxidation pitting.
Ceradyne Ceralloy 147A (1% MgO)	87,090	Primarily inclusions	100 hr/1200°C 1000 hr/1200°C	57,590 58,250	Inclusions and oxidation pits. Oxidation pits.
Fiber Materials (4% MgO)	73,680	Dark-colored inclusions	100 hr/1200°C 1000 hr/1200°C	66,110 42,980	Oxidation pits. Oxidation pits.
Toshiba HP-Si_3N_4 (4% Y_2O_3, 3% Al_2O_3)	105,140	Dark, shiny inclusions	100 hr/1000°C 1000 hr/1000°C	102,410 112,730	Dark, shiny inclusions. Dark, shiny inclusions.
Toshiba HP-Si_3N_4 (3% Y_2O_3, 4% Al_2O_3, SiO_2)	84,100	Inclusions	100 hr/1000°C 1000 hr/1000°C	65,270 42,710	Inclusions} Inclusions} No breaks at joints
Westinghouse (4% Y_2O_3, SiO_2)	90,980	Dark, shiny inclusions	100 hr/1000°C 1000 hr/1000°C	112,050 93,730	Grain or inclusion. Machining defect

Note: The typical population of oxidized test bars for retained 4-point bend strength measurement was two to four samples. Sample failed in furnace due to destructive phase instability.

[a] psi: Gross macrocracking due to accelerated oxidation.

TABLE 39. RETAINED STRENGTH OF SINTERED Si_3N_4 MATERIALS

Material	Non-Exposed		Static Air Exposure	Exposed	
	Mean R.T. Strength, psi	Fracture Origins		Mean R.T. Strength, psi	Fracture Origins
Rocketdyne SN-50 Sintered Si_3N_4 (6% Y_2O_3, 4% Al_2O_3)	51,600	Porosity open to tensile surface	100 hr/1000°C	45,270	Inclusions and accelerated oxidation at surface pores
Rocketdyne SN-46 Sintered Si_3N_4 (14% Y_2O_3, 7% SiO_2)	51,600	Porosity open to tensile surface	1000 hr/1000°C	34,450	Oxidation at pre-existing surface pores
AiResearch Sintered Si_3N_4 (8% Y_2O_3, 4% Al_2O_3)	79,450	Surface and Subsurface porosity	100 hr/1200°C 1000 hr/1200°C	61,900 59,190	Surface porosity. Surface porosity.

Note: The typical population of oxidized test bars for retained 4-point bend strength measurement was two to four samples.

TABLE 40. RETAINED STRENGTH OF REACTION SINTERED Si_3N_4 MATERIALS

Material	Non-Exposed		Static Air Exposure	Exposed	
	Mean R.T. Strength, psi	Fracture Origins		Mean R T Strength, psi	Fracture Origins
Norton 1979 NC-350	37,560	Primarily subsurface inclusions	100 hr/1400°C 1000 hr/1400°C	37,690 34,480	Subsurface inclusions; Primarily subsurface inclusions
Norton 1976 NC-350	29,450	Pores, pore agglomerates	100 hr/1400°C 1000 hr/1400°C	36,600 30,360	Primarily oxidation pits. Primarily oxidation pits, some undeter.
Ford (IM)	38,180	Processing defects, inclusions and porosity	100 hr/1400°C 1000 hr/1490°C	33,060 25,280	Oxidation pits. Primarily oxidation pits.
AiResearch Airceram RBN-101 (Slipcast)	37,920	Primarily inclusions	100 hr/1400°C 1000 hr/1450°C	22,990 30,590	Oxidation pits Oxidation pits.
AiResearch Airceram RBN-122 (Injection-Molded)	32,580	Inclusions, some with adjoining pores	100 hr/1400°C 1000 hr/1400°C	18,390 5,960	Oxidation pits Primarily oxidation pits
Annawerk Ceranox NR-115H	28,870	Inclusions	100 hr/1400°C 1000 hr/1400°C	21,890 0,*19,100	Primarily oxidation pits. Primarily oxidation pits
AED Ultrasil: • Batch 1	29,920	Inclusions, some with adjoining pores	100 hr/1400°C 1000 hr/1400°C	20,680 15,980	Oxidation pits. Undetermined.
• Batch 2	27,400	Inclusions, some with adjoining pores	100 hr/1400°C 1000 hr/1400°C	19,060 16,710	Oxidation pits and inclusions Oxidation pits or undetermined
• Batch 3	28,190	Inclusions or subsurface pores	100 hr/1400°C 1000 hr/1400°C	17,800 11,840	Oxidation pits Undetermined
• Batch 4	30,730	Inclusions, some with adjoining pores	100 hr/1400°C 1000 hr/1400°C	18,690 14,730	Primarily oxidation pits. Primarily oxidation pits.
• Batch 5	26,080	Primarily dark inclusions	100 hr/1400°C 1000 hr/1400°C	18,990 21,210	Surface and subsurface porosity. Pore under oxide skin.
Georgia Tech RS-Si_3N_4	26,220	Primarily light-colored inclusions	100 hr/1400°C 1000 hr/1400°C	26,240 19,560	Oxidation pit Oxidation pit
AME RS-Si_3N_4	7,470	Undetermined due to porous nature of material	100 hr/1400°C 1000 hr/1400°C	ª0 1,400 1,750	Undetermined. Undetermined.
AiResearch RBN-104	40,270	Subsurface inclusions and pores	100 hr/1400°C 1000 hr/1400°C	33,640 36,590	Primarily oxidation pits Primarily oxidation pits

Note: The typical population of oxidized test bars for retained 4-point bend strength measurement was two to four samples.

ª0 psi: Gross macrocracking due to destructive phase instability. Sample failed in furnace under zero stress.

TABLE 41. RETAINED STRENGTH OF SiC MATERIALS

Material	Non-Exposed		Static Air Exposure	Exposed	
	Mean R.T. Strength, psi	Fracture Origins		Mean R.T. Strength, psi	Fracture Origins
Carborundum Sintered α-SiC	44,230	Primarily inclusions or large grains	100 hr/1400°C 1000 hr/1400°C	50,160 42,500	Subsurface inclusion or large grain. Oxidation pits.
General Electric Sintered SiC	63,770	Primarily inclusions or large grains	100 hr/1400°C 1000 hr/1400°C 2000 hr/1500°C	73,650 59,200 49,970	Undetermined. Internal processing defects. Oxidation pits.
Norton NC-203 HP-SiC (2% Al₂O₃)	101,810	Undetermined	100 hr/1400°C 1000 hr/1400°C 2000 hr/1500°C	91,890 91,470 103,670	Chips at non-chamfered edge. Undetermined. Undetermined.
Ceradyne Ceralloy 146A HP-SiC (2% Al₂O₃)	60,060	Undetermined	100 hr/1400°C 1000 hr/1400°C	43,880 54,010	Undetermined. Undetermined.
Ceradyne Ceralloy 146I HP-SiC (2% B₄C)	45,620	Some machining damage, primarily undetermined	100 hr/1400°C 1000 hr/1400°C	43,910 43,610	Undetermined. Oxidation pits.
UKAEA/BNF Refel Si/SiC • Diamond-Ground	44,920	Large grains	100 hr/1200°C 1000 hr/1200°C	a 63,890	Mixed internal processing defects and undetermined. Surface oxide pits and large grains
• As-Processed	33,600	Some large grains, primarily undetermined	100 hr/1200°C 1000 hr/1200°C	43,560 38,770	Undetermined. Undetermined.
Norton NC-430 Si/SiC	30,420	Undetermined	100 hr/1200°C 1000 hr/1200°C	29,640 40,110	Undetermined. Undetermined.
Coors Si/SiC	50,620	Mostly undetermined, some machining damage	100 hr/1200°C 1000 hr/1200°C	44,800 27,120	Undetermined Oxidation
Kyocera SC-201 Sintered SiC	56,080	Primarily undetermined, some surface and subsurface pores.	100 hr/1400°C 1000 hr/1400°C	59,540 50,720	Undetermined Oxidation pits (surface pores?)

Note: The typical population of oxidized test bars for retained 4-point bend strength measurment was two to four samples.

a Not all samples were standard (1/4 x 1/8 x 2-1/4 in.) dimensions. Dimensions and strengths were:

inches	psi
1/4 x 1/8 x 2	63,960
1/4 x 1/4 x 2	50,590
1/8 x 9/32 x 2-1/2	42,330
1/8 x 1/4 x 2-1/4	78,790

TABLE 42. SUMMARY OF WEIGHT CHANGE DATA

Material	Weight Gain, %
Si_3N_4 (Exposure: 1000 hr/1200°C)	
HP-Si_3N_4 (1% MgO)	0.48
HP-Si_3N_4 (4% MgO)	2.6
Sintered Si_3N_4 (8% Y_2O_3, 4% Al_2O_3)	0.21
HP-Si_3N_4 (Exposure: 1000 hr/1000°C	
HP-Si_3N_4 (8% Y_2O_3)	0.05-0.10
HP-Si_3N_4 (15% v. `	0.03-5.1
HP-Si_3N_4 (4% Y_2O_3, 3% Al_2O_3)	0.06-0.58
HP-Si_3N_4 (3% Y_2O_3, 4% Al_2O_3, SiO_2)	0
HP-Si_3N_4 (4% Y_2O_3, SiO_2)	0.01
HP-Si_3N_4 (10% CeO_2)	0.34
SiC Material (Exposure: 1000 hr/1400°C	
HP-SiC (2% A_2O_3)	0.1-0.2
HP-SiC (2% B_4C)	0.49
Sintered SiC	0.08 (α)
	0.01-0.23 (β)
Si/SiC[a]	0.06-0.16

[a] 1200°C exposure.

207

TABLE 43. SUMMARY OF STRENGTH CHANGES DUE TO 1000 HR STATIC AIR EXPOSURE

Material	Exposure Temp., °C	Strength Change/25°C	Fracture Origins Unexposed	Fracture Origins Exposed
A. HP-Si$_3$N$_4$ Materials				
HP-Si$_3$N$_4$ (1% MgO)	1200	-33%	Inclusions	Oxidation pits
HP-Si$_3$N$_4$ (4% MgO)	1200	-41%	Inclusions	Oxidation pits
HP-Si$_3$N$_4$ (8% Y$_2$O$_3$)	1000	+7%	Inclusions	Inclusions
HP-Si$_3$N$_4$ (15% Y$_2$O$_3$)	1000	+10% -100%	Inclusions	Internal cracking due to accelerated oxidation
HP-Si$_3$N$_4$ (4% Y$_2$O$_3$, 3% Al$_2$O$_3$)	1000	No change	Inclusions	Inclusions
HP-Si$_3$N$_4$ (4% Y$_2$O$_3$, SiO$_2$)	1000	+10%	Inclusions	Inclusions
HP-Si$_3$N$_4$ (10% CeO$_2$)	2000	-50%	Inclusions	Oxidation pits
B. RS-Si$_3$N$_4$ Materials				
Reaction sintered Si$_3$N$_4$	1400	+3% to -60%	Inclusions, porosity	Primarily oxidation pits
C. SiC Materials				
HP-SiC (2% Al$_2$O$_3$)	1400 1500[a]	-10% 0	Undetermined	Undetermined
HP-SiC (2% B$_4$C)	1400	-4%	Undetermined	Oxidation pits
Sintered α-SiC	1400	-8%	Inclusions, grains, pores	Oxidation pits
Si/SiC	1200	+30% to -46%	Undetermined	Mostly undetermined, some oxidation pits

[a]2000 hr.

the oxidation of silicon-base ceramics found in the literature.[69-91] The overview summary for each material type is presented below.

11.1 Si_3N_4 MATERIALS

The hot-pressed silicon nitride materials studied on this program have been doped with MgO, Y_2O_3, CeO_2, $Y_2O_3-Al_2O_3$, $Y_2O_3-SiO_2$, and $Y_2O_3-Al_2O_3-SiO_2$.

11.1.1 MgO-Doped HP-Si_3N_4

MgO-doped HPSN materials exhibit more rapid oxidation than Y_2O_3-doped materials. This is directly observed in the weight gain data for 1000 hr/1200°C exposure shown in Table 42. The Ceradyne and FMI materials contained 1% and 4% MgO additive, respectively. Table 42 illustrates the decreased resistance to oxidation as the additive content increases (i.e., increased weight gain). The surface scale morphology of these materials is presented in Figures 76 through 79. The SEM detects the thick crystalline scale products after 100 hr exposure. After 1000 hr exposure the scales are easily observed in the low magnification optical microscope.

Such MgO-doped materials form a SiO_2 scale upon oxidation which is quickly modified by the impurities in the unexposed material. These cation impurities are tabulated in the spectrographic analysis results presented in Table 7. Typically Mg, Al, Fe, Ca, and Mn impurities diffuse up through the grain boundary into the oxide scale where they either form mixed crystalline silicates or dissolve into the glass phase. This outward diffusion of impurity (Mg and Ca) cations from the amorphous grain boundary phase through the surface oxide film is thought to be the rate-controlling process in the oxidation of MgO-doped Si_3N_4.[69] The main crystalline scale product is usually $MgSiO_3$ (enstatite), with small amounts of cristobalite. These expected results were confirmed for the FMI and Ceradyne MgO-doped HPSN materials. X-ray diffraction (XRD) analysis for both these materials indicated the major scale products to be $MgSiO_3$ (enstatite,
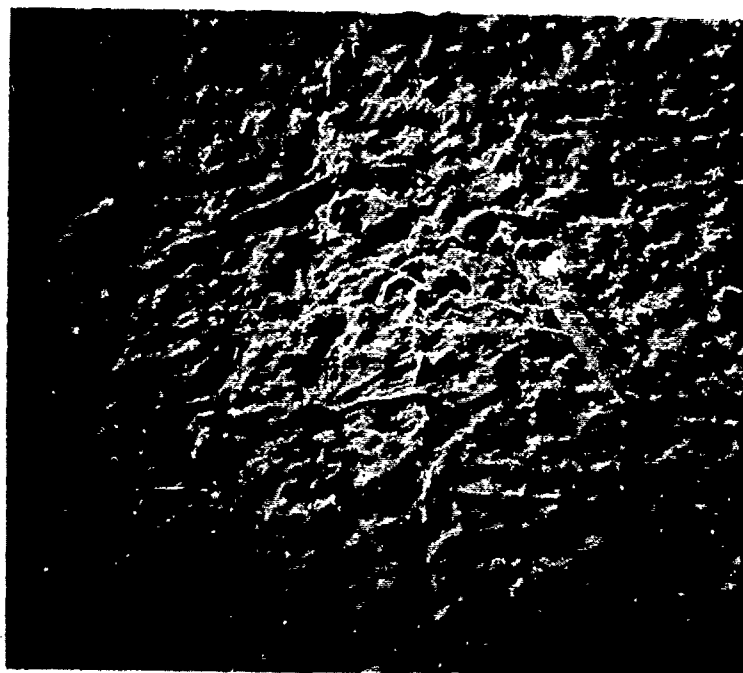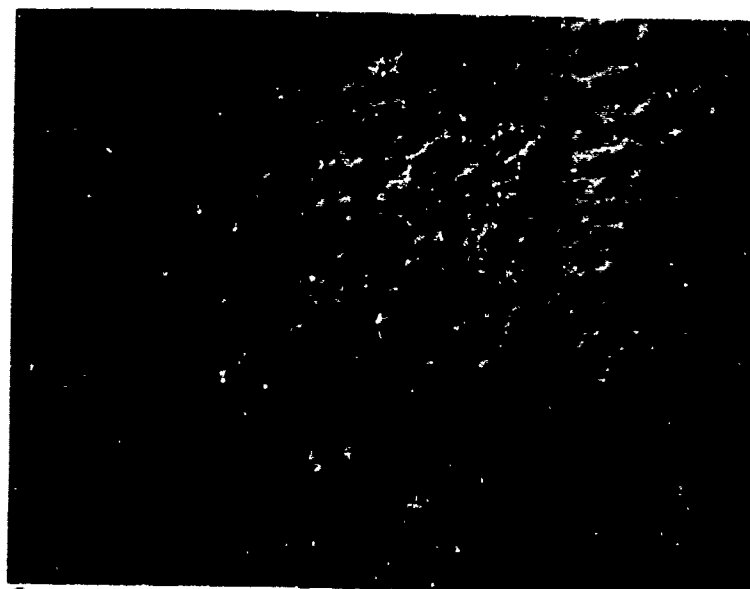
SEM, 200X

Figure 76. Surface of Ceradyne Ceralloy 147A,
HP-Si$_3$N$_4$ (1% MgO) sample after 100 hr/1200°C
static air exposure.
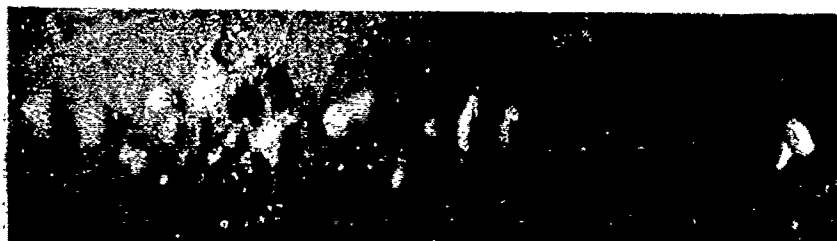

12X

Figure 77. Surface of Ceradyne Ceralloy 147A
HP-Si$_3$N$_4$ (1% MgO) sample after 100 hr/
1200°C static air exposure.

SEM   200X

Figure 78.   Surface of Fiber Materials, Inc.,
HP-Si$_3$N$_4$ (4% MgO) sample after 100 hr/
1200°C static air exposure.

5.3X

12X

Figure 79.   Surface of Fiber Materials, Inc., HP-
Si$_3$N$_4$ (4% MgO) sample after 1000 hr/1200°C
static air exposure.

211

which is orthorhombic, and clinoenstatite, which is monoclinic), and the minor crystalline scale product to be cristobalite. The X-ray fluorescence (XRF) scan of the oxide scale is shown in Figure 80. When these scale impurities are compared to the spectrographic analysis data (Table 7), we find that most of the major matrix material impurities have diffused up into the oxide scale. An exception is the original Al impurity that has apparently not migrated into the oxide scale. Phosphorus was not a major impurity detected by spectrographic analysis, and therefore its presemce in the XRF scan of the oxide scale is not understood at this time.

At short oxidation times, distinct oxide mounds are formed on the Si_3N_4 surface as shown in Figure 81a. The mound formation often contains a hole in the top which presumably was formed by the evolution of N_2 gas from the SiO_2/Si_3N_4 interface. At longer times $MgSiO_3$ is formed as discussed above. It is believed that $MgSiO_3$ reacts with Si_3N_4 to form pits at the scale/matrix interface. These pits become fracture origins as illustrated in Figure 81b. Table 38 illustrates for both Ceradyne 1% MgO- and FMI 4% MgO-modified Si_3N_4 materials, that oxidation pits were the fracture origins for 100 and 1000 hr exposure at 1200°C. Such oxidation can be responsible for as much as 40% strength loss.

11.1.2 CeO_2-Doped HP-Si_3N_4

CeO_2 dopants for $HP-Si_3N_4$ are being investigated in an attempt to form more deformation resistant intergranular phases than the amorphous grain boundary films present in MgO-doped materials. Harbison-Walker $HP-Si_3N_4$ (10% Ce_2O) was exposed in static air for 1000 hr at 1000°C. The weight gain data given in Table 42 indicate much more rapid oxidation for Ce_2O-containing silicon nitride compared to Y_2O_3-modified material. No direct comparison can be made with MgO-doped materials since the exposure temperatures were different. The strength and fracture origin data of Table 38 also illustrate the poor oxidation resistance when compared to Y_2O_3-containing materials. While good strength retention was obtained for the Harbison-Walker material
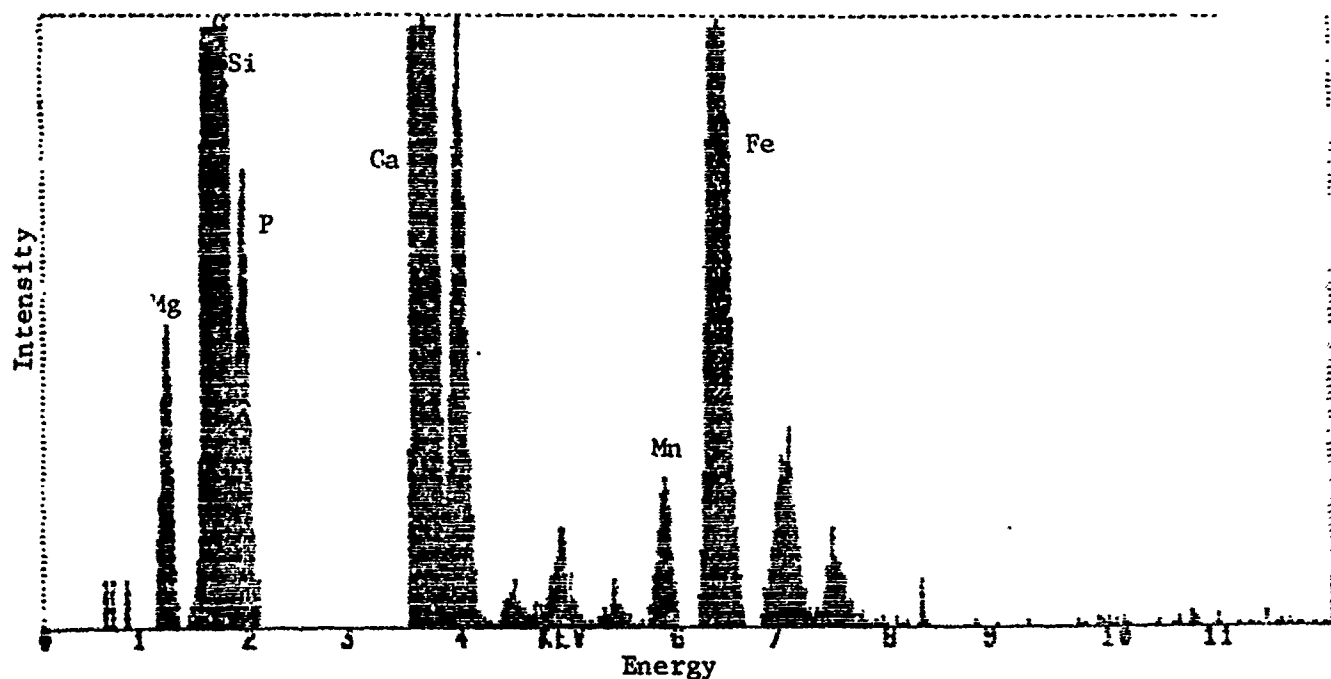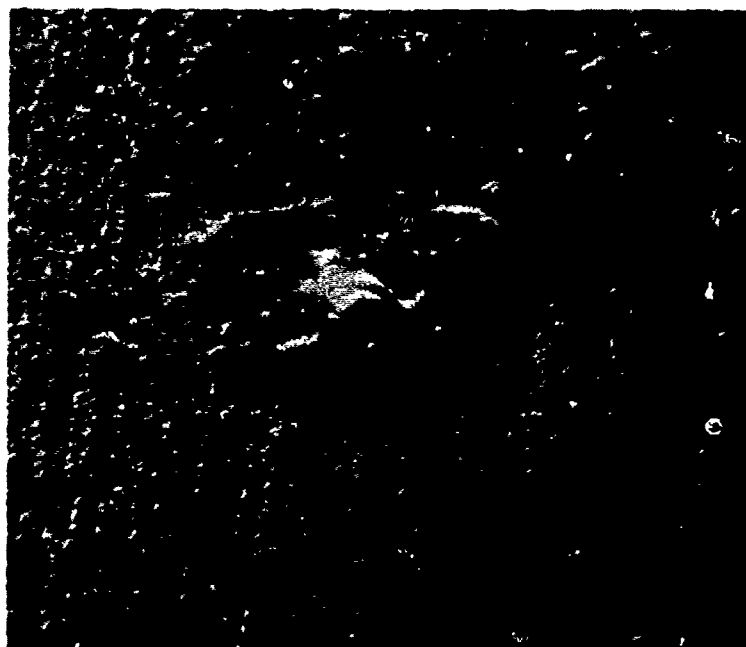
212

Figure 80. X-ray fluorescence scan of oxidation scale for Ceradyne Ceralloy 147A HP-Si$_3$N$_4$ (1% MgO) after 1000 hr/1200°C static air exposure.

200X

(a) Oxide mound on tensile surface of Norton
NC-132 (1% MgO) after 15 min/1350°C expo-
sure. (Photo courtesy of R. W. Rice, NRL.)

92X

(b) Oxidation pit as fracture origin in
Ceradyne Ceralloy 147A (1% MgO) ex-
posed for 100 hr/1200°C

Figure 31. Oxidation of MgO-doped HP-Si$_3$N$_4$.

214

after 100 hr exposure (Table 38), excessive oxidation pitting caused a 50% strength loss after 1000 hr exposure at 1000°C. The morphology of the oxide scale after 100- and 1000-hr exposures at 1000°C is shown in Figures 82 and 83. The crystalline scales shown were found by X-ray diffraction to be mainly cristobalite. No crystalline cerium compounds were identified. Figure 84 presents the XRF elemental scan of the oxide scale. The Ce present is apparently dissolved in an amorphous phase on the surface. The iron and calcium impurities present in the scale were in the unexposed material according to spectrographic analysis (Table 7). These impurities in ceria-containing Si_3N_4 diffuse to the oxide scale as they do in magnesia-doped material. As with MgO-modified Si_3N_4, the aluminum impurity is not detected in the surface oxide scales of CeO_2-doped material, as shown in Figure 84. Lange[81] discusses that ceria-containing silicon nitride may have unstable crystalline phases that experience accelerated oxidation in a manner similar to the Y_2O_3-doped materials discussed below. No such crystalline cerium phases were detected by X-ray diffraction for the Harbison-Walker material (Table 6). However, their existence might help to explain the relatively poor oxidation resistance exhibited by this material at 1000°C.[*]

11.1.3 Y_2O_3-Doped HP-Si_3N_4

Y_2O_3 has proven to be a promising densification aid for hot-pressed silicon nitride. Its main advantage is that an inter-granular phase is formed that can be crystallized, thus improving high-temperature strength and creep resistance when compared to MgO-doped Si_3N_4 materials, which have an amorphous grain boundary phase. We have demonstrated above that much less subcritical crack growth is evident in many Y_2O_3-doped Si_3N_4 materials.

---

[*]It is noted, however, that in-house work at AFWAL indicates that much better oxidation resistance is obtained with lower CeO_2 content Si_3N_4 materials.

SEM, 1000X

Figure 82.   Surface of Harbison-Walker HP-
   Si_3N_4 (10% CeO_2) sample after 100 hr/
   1000°C static air exposure.

SEM, 1000X

Figure 83.   Surface of Harbison-Walker HP-Si_3N_4
   (10% CeO_2) sample after 1000 hr/1000°C static
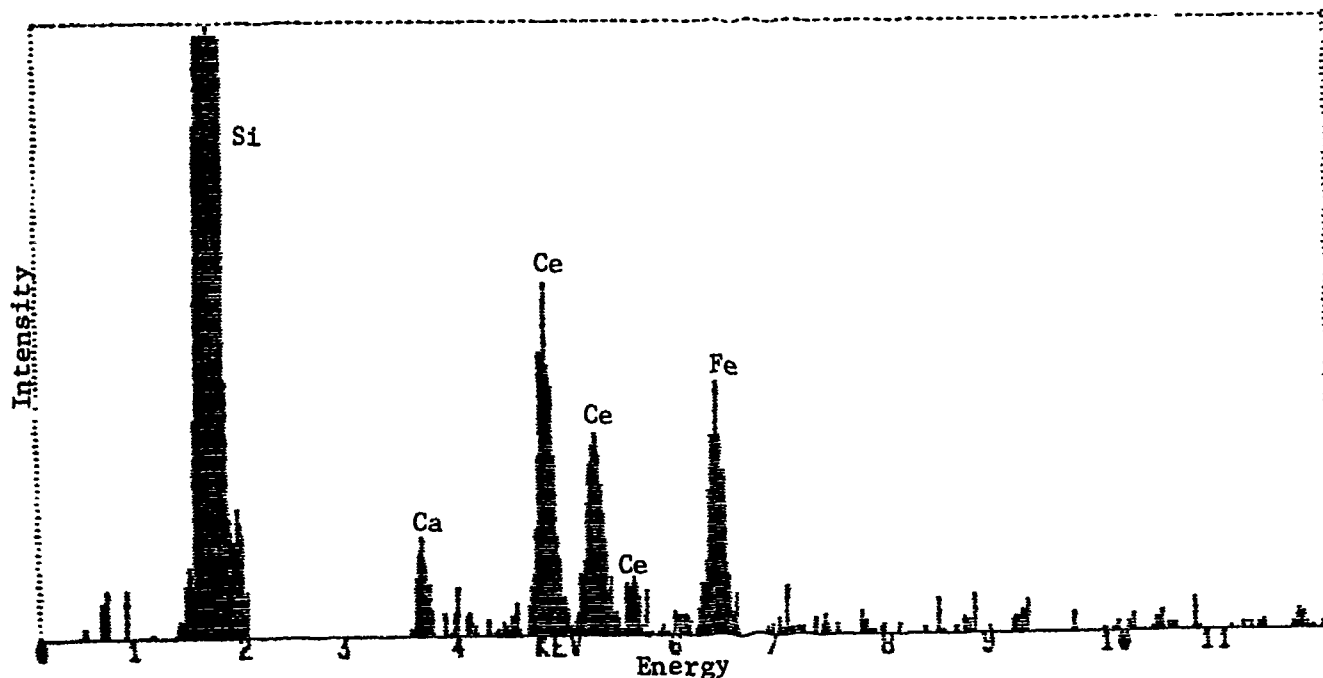   air exposure.

Figure 84. X-ray fluorescence scan of oxidation scale for Harbison-Walker HP-Si$_3$N$_4$ (10% CeO$_2$) after 1000 hr/1000°C static air exposure.

	Percent Weight Change
	+3.0
	+2.4
(a) 100 hr/1000°C	
	+5.1
	+0.03
(b) 1000 hr/1000°C	

Figure 85. Photographs of Ceradyne HP-Si$_3$N$_4$ (15% Y$_2$O$_3$) samples after static air exposure.

We have also demonstrated that such Y_2O_3-containing mate-rials can have interesting oxidation behavior. Catastrophic results such as illustrated in Figure 85 for a 15% Y_2O_3-doped Si_3N_4 can result at temperatures between ~750° and 1000°C. It is thought that such behavior is caused by accelerated linear oxidation of $Si_3Y_2O_3N_4$, $YSiO_2N$, or $Y_{10}Si_7O_{23}N_4$ phases in these materials. Such materials exist in the Si_3N_4-SiO_2-Y_2O_3 phase fields labeled A, B, and C in Figure 86.[69] However, if the processed material is in the phase triangle containing crystalline Si_2N_2O and $Y_2Si_2O_7$ phases (i.e., phase field D in Figure 86), then parabolic kinetics are observed and the oxidation rates are very low. Other mechanistic interpretations of this effect involve the influence of W and WC contamination[86] and carbon impurity effects.[85].

Several Y_2O_3-containing materials have been investigated on this program, and the results are consistent with this mechanistic interpretation. The Ceradyne 15% Y_2O_3-doped material that exhibited the catastrophic oxidation (shown in Figure 85) indeed contained $YSiO_2N$ as a minor crystalline phase, as shown in the X-ray diffraction results presented in Table 6. The Westinghouse material, however, doped with 4% Y_2O_3 and an unknown amount of SiO_2, contained $Y_2Si_2O_7$ as a minor phase and did not develop nonprotective oxide scales when exposed at 1000°C. The appearance of the Westinghouse material after 100 and 1000 hr exposure at 1000°C is shown in Figure 87. Figure 88 presents an SEM view of the surface of Norton NCX-34 (8% Y_2O_3-doped) after 1000 hr/ 1000°C. This material only exhibited a slight evidence of the phase instability, better seen in the optical photograph in Figure 89. Thus, the goal in processing these materials is to keep the Y_2O_3 content lower than ~6-8%. Several attempts are currently being made with a 4% Y_2O_3 content, similar to the Westinghouse material.

The weight change and strength/fracture origin information presented in Tables 34-37 and Tables 38-41, respectively, illustrates that if the catastrophic oxidation effect is avoided, then
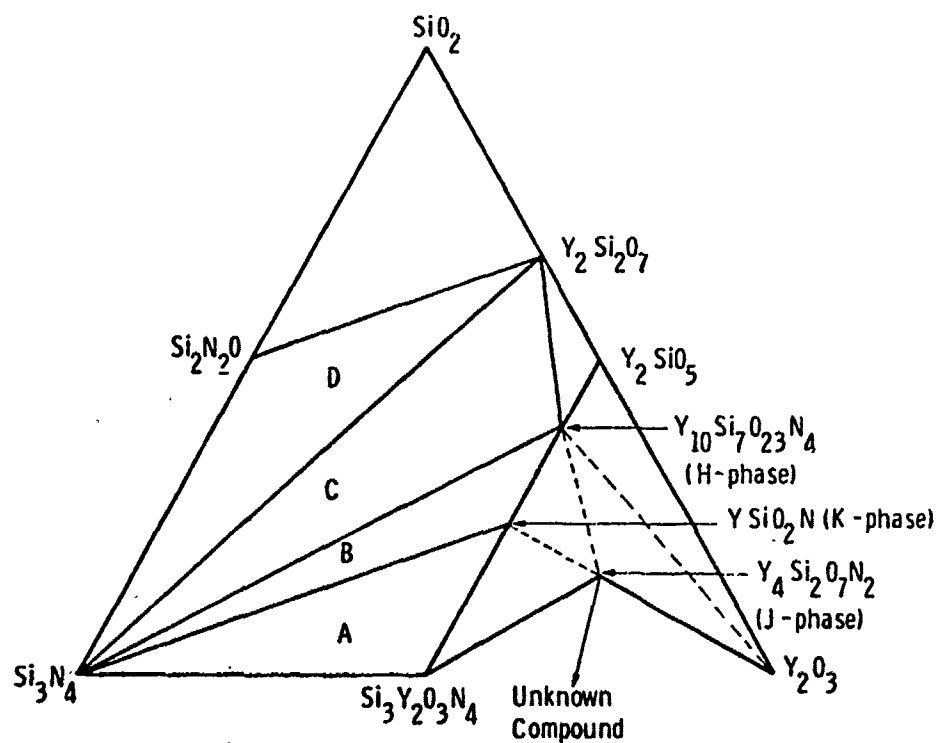
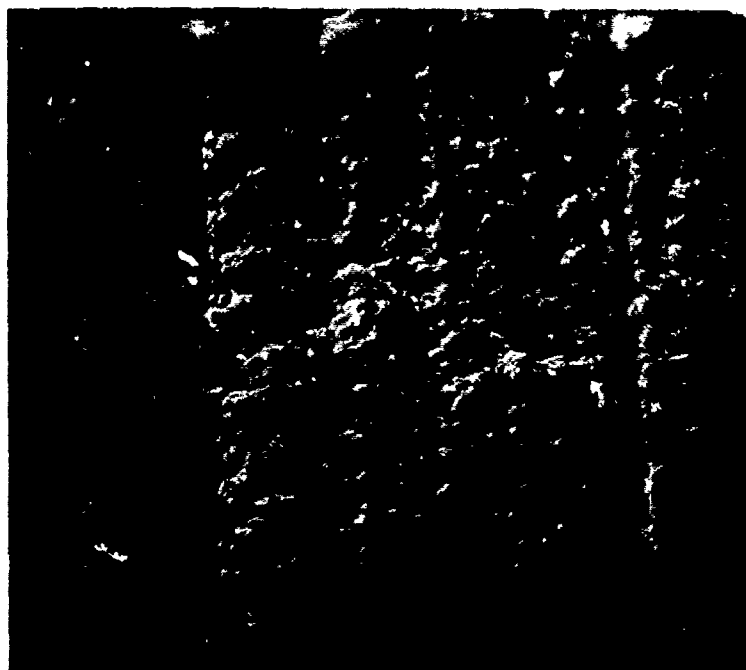Figure 86. Phase relationships in the Si_3N_4-SiO_2-Y_2O_3 system at 1600°-1750°C (after Singhal).[69]

(a) 100 hr/1000°C exposure   12X

(b) 1000 hr/1000°C exposure   12X

Figure 87. Surfaces of Westinghouse HP-Si$_3$N$_4$
(4% Y$_2$O$_3$, SiO$_2$) after 1000°C static air
exposure.

1000X

Figure 88. SEM view of surface of Norton
NCX-34 HP-Si$_3$N$_4$ (8% Y$_2$O$_3$) sample after
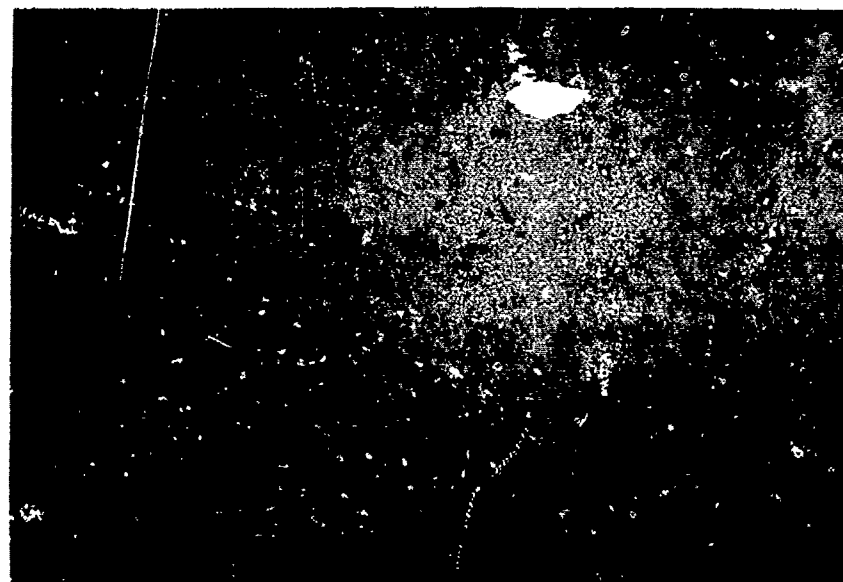1000 hr/1000°C static air exposure.

12X

Figure 89. Optical macrograph of surface of
Norton NCX-34 HP-Si$_3$N$_4$ (8% Y$_2$O$_3$) sample
after 1000 hr/ 1000°C static air exposure.

221

Y_2O_3-containing materials have good oxidation resistance. Weight gain during oxidation is very low, and the exposed strength is equivalent to the unexposed strength. This is mainly evident for the 8% Y_2O_3-doped materials from Norton and Ceradyne. It is further noted in Table 38 that exposed and non-exposed fracture origins were the same for these two materials, which is indicative of the absence of oxidation pitting. The oxide scales on these materials were too thin to remove for XRD and XRF analysis of the scale products.

Toshiba has developed a very significant HP-Si_3N_4 doped with 4% Y_2O_3 and 3% Al_2O_3. The high strength of this material was discussed above. The weight gain data in Table 34 show that the addition of Al_2O_3 has decreased the oxidation resistance when compared to materials modified by Y_2O_3 only, as evidenced by larger weight gain. However, when SiO_2 is also added, with or without Al_2O_3, the oxidation resistance is very good. This is illustrated by the weight gain data in Table 34 for the Toshiba (3% Y_2O_3, 4% Al_2O_3, SiO_2) modified Si_3N_4 and the Westinghouse 4% Y_2O_3-SiO_2 modified Si_3N_4. In general, the nonexposed bend strengths were maintained for these materials, and fracture origins remained unchanged. Figures 90 and 91 illustrate the nature of the oxide scales on the two Y_2O_3-Al_2O_3-doped Toshiba materials, with and without SiO_2 addition. Oxide scale products could only be identified for the Toshiba HP-Si_3N_4 (4% Y_2O_3, 3% Al_2O_3) material. X-ray diffraction indicated that the scale consisted of cristobalite. No crystalline aluminum silicate or mullite compounds were identified.

11.1.4 RS-Si_3N_4 Materials

The properties of RS-Si_3N_4 materials can vary widely, and depend on the specific nature of the porosity, pore size, and pore size distribution. Impurities only have an effect in some cases, since RSSNs are generally very pure, containing typically 0.5-1% cation impurities (spectrographic analysis, Table 7). As discussed by Singhal,[70] oxidation in RS-Si_3N_4 materials occurs in two stages. First, internal oxidation occurs within the network
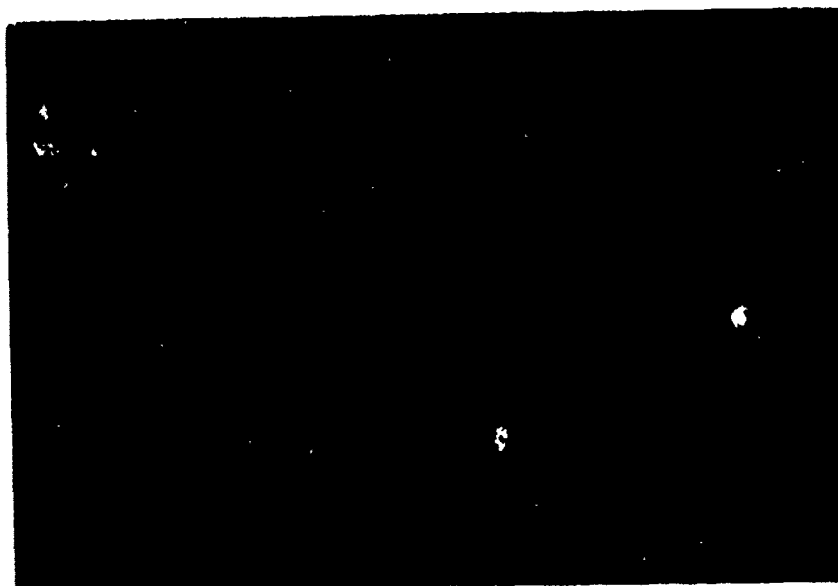
222

12X

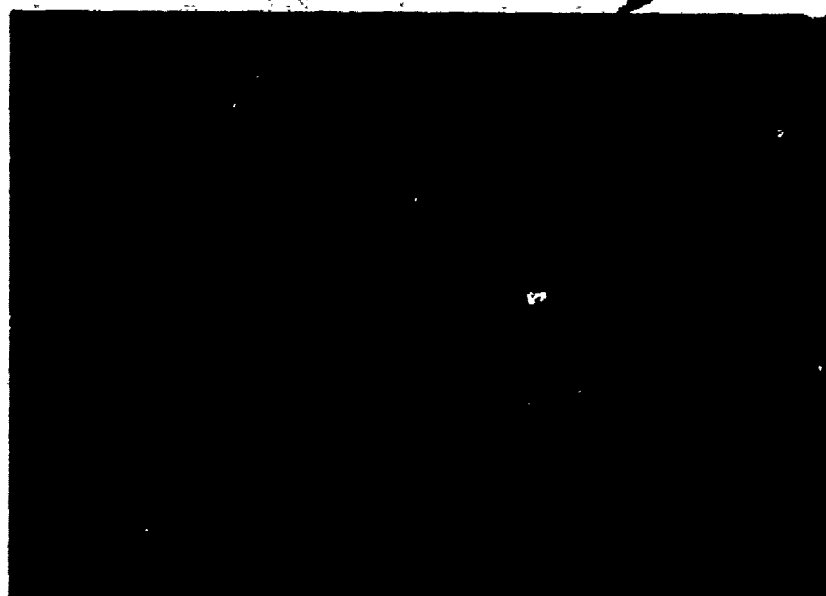(a)   100 hr/1000°C exposure

12X

(b)   1000 hr/1000°C exposure

Figure 90.   Surfaces of Toshiba HP-Si$_3$N$_4$ (4% Y$_2$O$_3$,
3% Al$_2$O$_3$) samples after 1000°C static air
exposure.

(a) 100 hr/1000°C exposure

(b) 1000 hr/1000°C exposure

Figure 91. Surfaces of Toshiba HP-Si$_3$N$_4$ (3% Y$_2$O$_3$, 4% Al$_2$O$_3$, SiO$_2$) sample after 1000°C static air exposure.

of open porosity until the pores are completely filled, or until the surface is sealed, which limits the supply of oxygen to the interior. The second stage of oxidation then occurs only on the external surface. In both stages, oxidation follows parabolic behavior due to the diffusion-controlled process of inward oxygen transport through the SiO_2 scale to the Si_3N_4/SiO_2 interface. The oxidation rates are higher in the first stage, since the surface area is much greater (the interconnected open porosity is exposed). For many RS-Si_3N_4 materials, experience has shown that up to 1100°C most of the oxidation is internal. However, at ~1200°C a transition occurs from first to second stage oxidation at very short times. However, much internal oxidation can occur prior to the transition at temperatures of 1200°C and above. We have demonstrated this for the very porous AME material (ρ = 2.1 g cm^{-3}). After 15 min/1400°C exposure, the oxide penetrated half the thickness of the test sample. After 100 hr/1400°C exposure the oxide had penetrated through all of the open porosity. This may be an extreme example, since this material contained very large open porosity, i.e., 32%. After 1000 hr exposure, significant second-stage external oxidation had occurred in this material, since cracks were observed in the scale upon cooling, as shown in Figure 92.

The higher density (ρ = 2.5-2.8 g cm^{-3}) RS-Si_3N_4 materials studied on this program were also exposed for 100 and 1000 hr at 1400°C. The transition to second stage oxidation apparently occurred rapidly, since only surface scales were observed, with no major internal attack. Oxidation was still controlled by the open porosity though, in the sense that higher open porosity means a greater Si_3N_4 surface area at the Si_3N_4/SiO_2 interface. This is illustrated in Figure 93, where percent weight gain is plotted as a function of fractional open porosity for all RSSN materials oxidized for 1000 hr at 1400°C. The tabular data are presented in Table 36. No such correlation was found when weight gain data were plotted as a function of total metallic impurity content, or the amount of any specific impurity present (e.g., Al
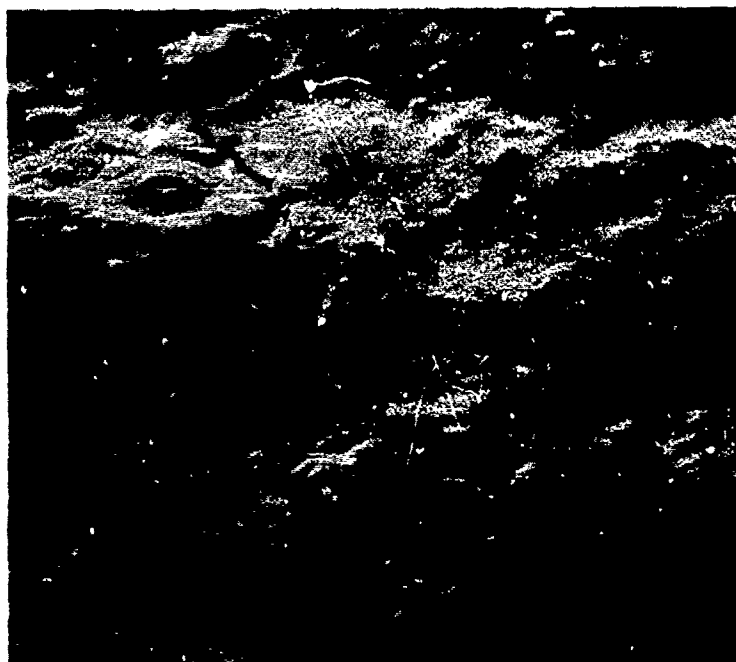
SEM, 200X

Figure 92.   Surface of AME RS-Si$_3$N$_4$ sample
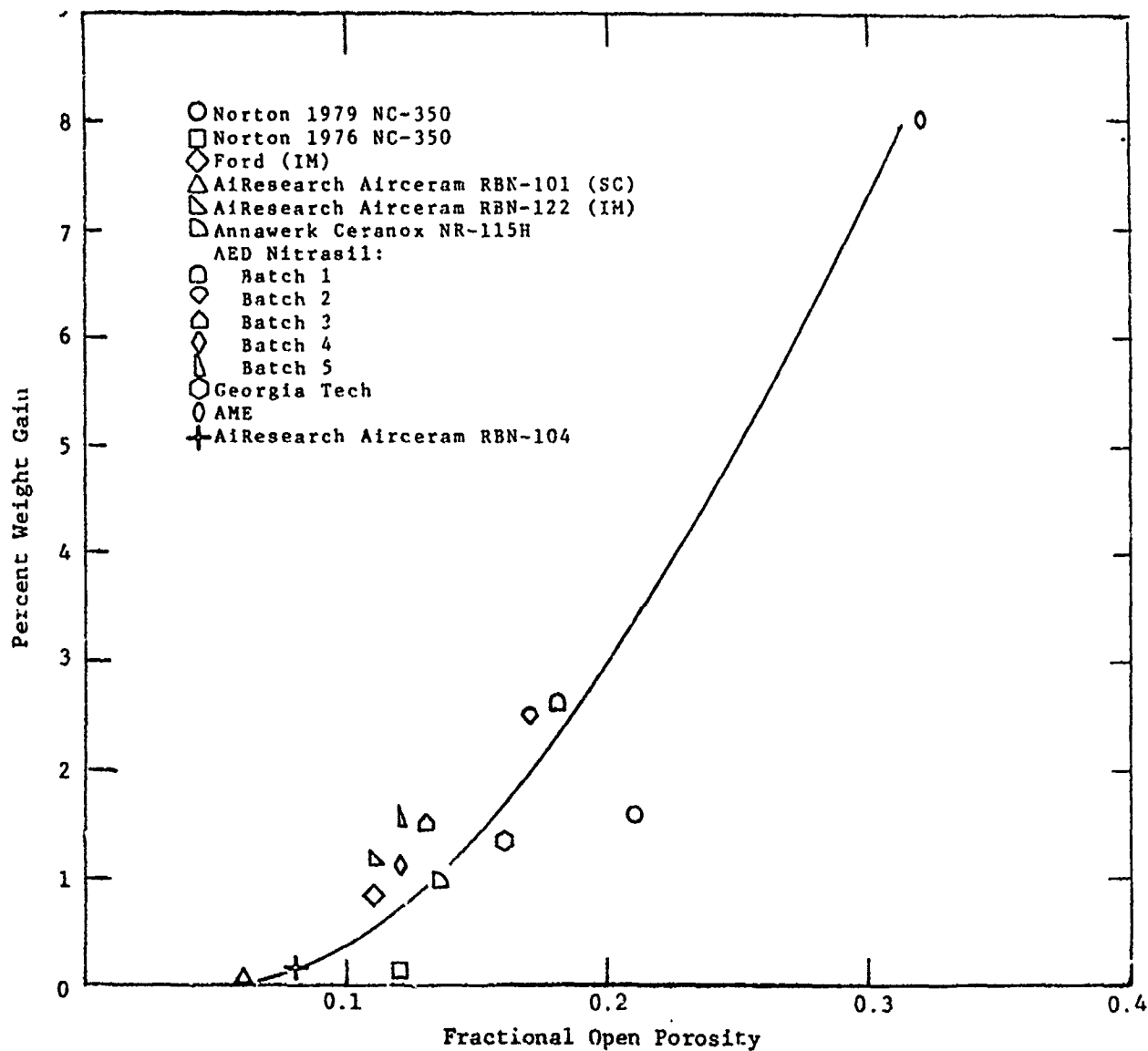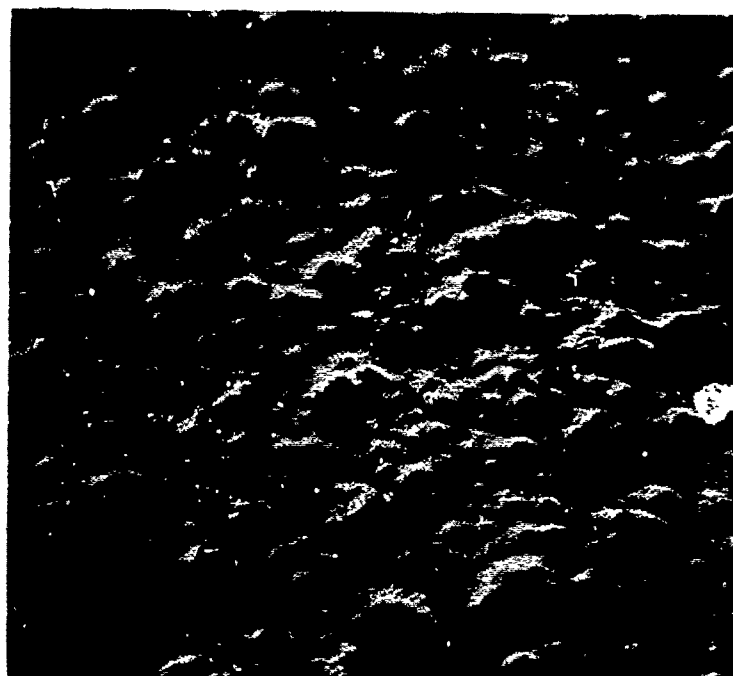after 1000 hr/1400°C static air exposure.

226

Figure 93. Weight gain-porosity relation for RS-Si$_3$N$_4$ materials exposed in static air for 1000 hr at 1400°C.[4]

or Fe). Thus, oxidation in RS-Si_3N_4 materials, as measured by weight gain, is determined by the open porosity.

The residual strength of oxidized RS-Si_3N_4 materials has been found to be either lower or higher than the unexposed strength, depending on the extent of internal and external oxidation, the nature of the SiO_2 formed, the temperature of the strength measurement, and whether or not any thermal cycling had occurred. In general, if only a small amount of internal oxidation occurs, we would expect a strength increase due to rounding off of internal pores. If gross internal oxidation occurs, we would expect to see internal cracking upon cooling as was seen with the AME material If stage two oxidation occurred (i.e., if a thick cristobalite layer is formed on the surface), then we would expect the high-temperature strength to increase due to blunting of surface pore features, and the room-temperature strength to decrease due to cracking of the cristobalite layer upon cooling through its 250°C phase inversion.

The residual strength data for all RS-Si_3N_4 materials exposed for 100 and 1000 hr at 1400°C are contained in Table 40 and summarized in Table 43. Most materials experienced sufficient oxidation scale cracking and pitting to result in up to 60% reduction in strength when compared to unexposed material. An SEM view of a typical surface scale after 1000 hr/1400°C static air exposure is shown in Figure 94. The two Norton NC-350 materials (1976- and 1979-vintage) are particularly interesting materials. The 1976 NC-350 experienced no reduction in strength after 1000 hr/1400°C exposure. However, fracture origins were oxidation pits, and the surface scale was cracked as shown in Figure 95. The 1979 NC-350 experienced only marginal strength loss after similar exposure as shown in Table 40. However, Table 36 illustrates that the 1979 material had a much greater open porosity, and experienced an order of magnitude greater weight gain for both exposure times. It is notable that 1979 NC-350 experienced no change in fracture origins due to exposure. As shown in Table 40, subsurface inclusions were the fracture origins under all
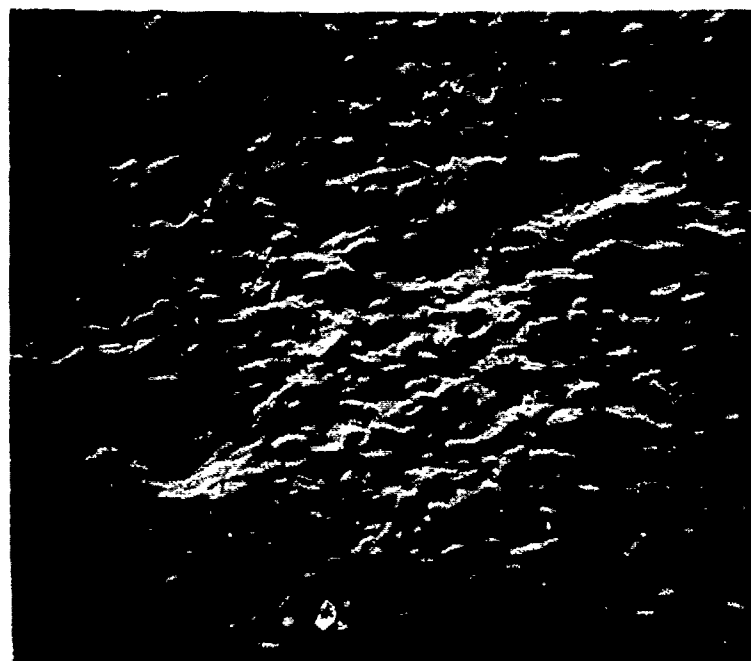
228
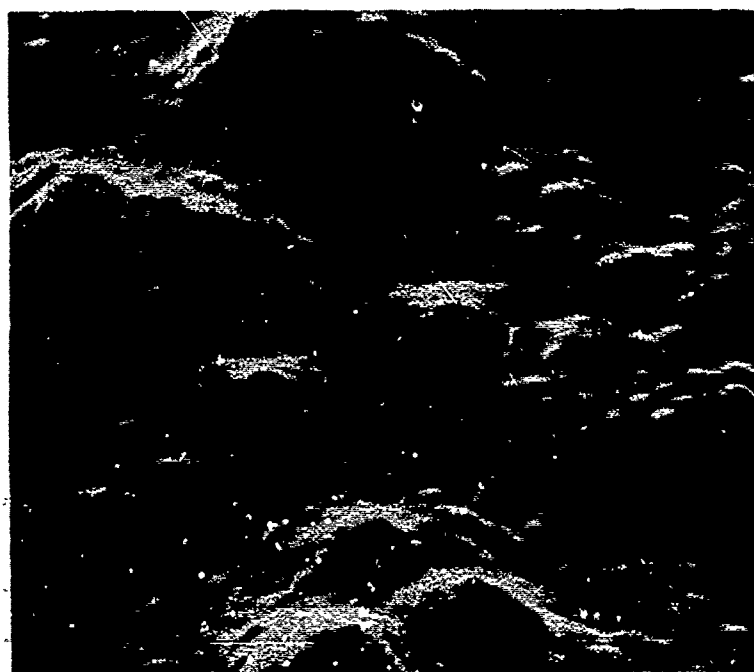
(a)   SEM, 100X

(b)   SEM, 500X

Figure 94. Surfaces of AiResearch injection
molded RS-Si₃N₄ (Airceram RBN-122) samples
after '.\ '؟/1400°C static aiᵣ exposure.

229

SEM, 1000X

Figure 95. Surface of 1976 vintage Norton
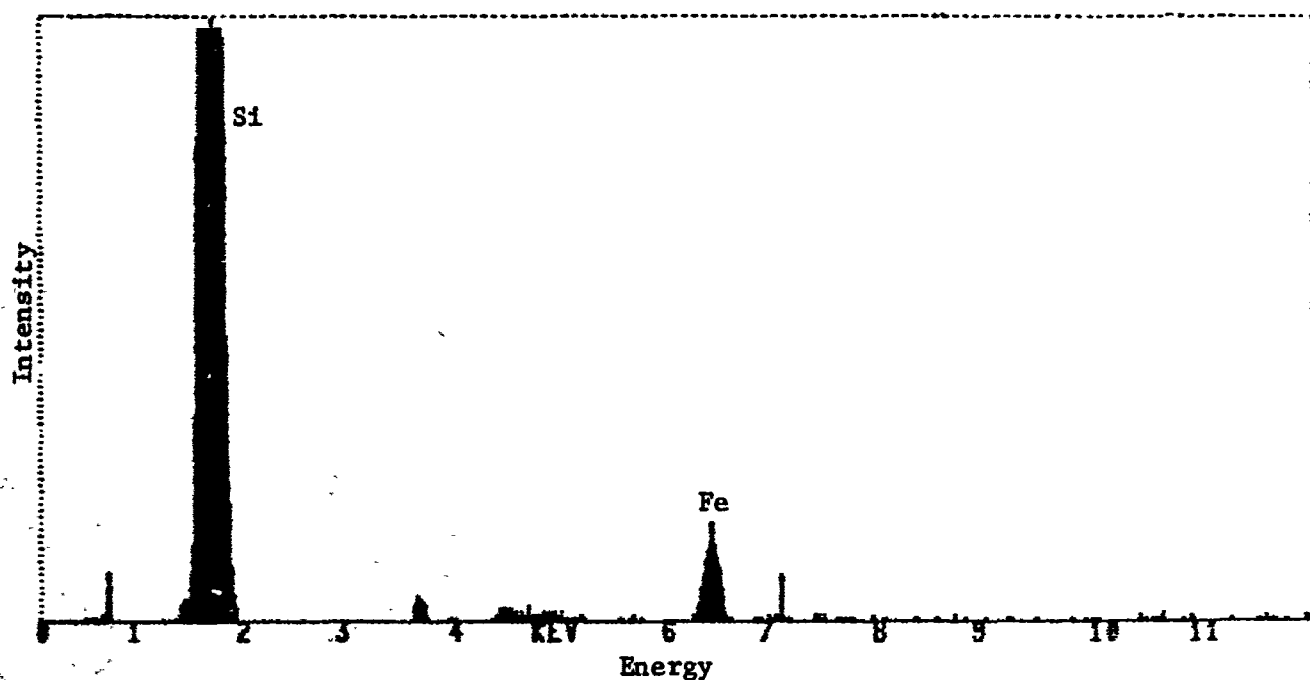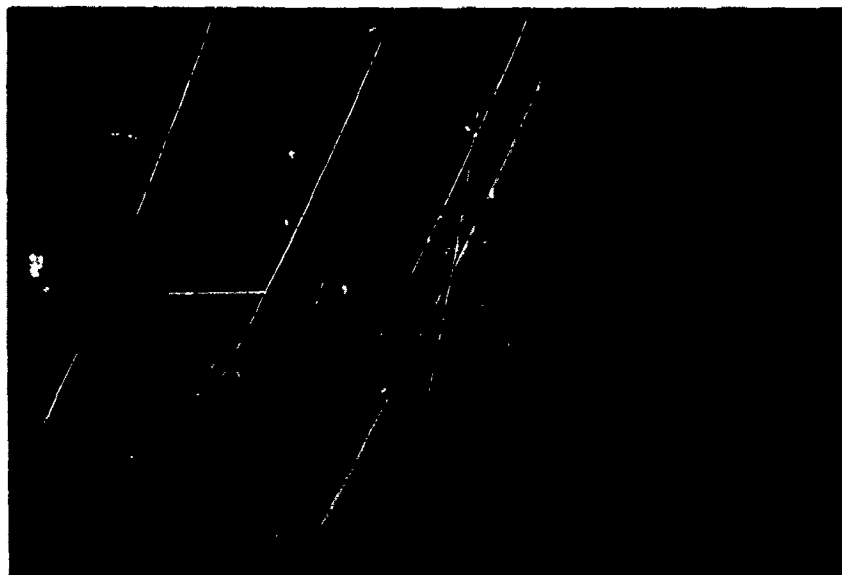NC-350 RS-Si$_3$N$_4$ after 1000 hr/1400°C
static air exposure.

Figure 96. X-ray fluorescence scan of oxidation scale for Norton NC-350
RS-Si$_3$N$_4$ after 1000 hr/1400°C static air exposure.

test conditions for this material. Thus, even though 1979 NC-350 experienced a relatively large weight gain upon exposure, the strength and critical flaw structure remained unchanged.

The crystalline oxide scale was identified for all RS-Si_3N_4 materials by XRD to be cristobalite. Elemental X-ray fluorescence scans indicated Fe was typically present in the scales. An XRF scan for NC-350 scale is shown in Figure 96. The spectrographic analysis results in Table 7 indicate that iron is the major impurity in RS-Si_3N_4. Figure 97 illustrates the surface scale of AED Nitrasil after 1000 hr/1400°C exposure. These two batches of material had a total of almost 2% Fe, Al, and Ca impurities (Table 7). The surface scale for a newer batch of Nitrasil is shown in Figure 98. Figure 99 illustrates an anomalous effect for Annawerk Ceranox material that was discussed previously. The sample shown in Figure 99 spontaneously fractured during 1000 hr/1400°C static air exposure. No definite ¬nation for this is currently available. However, an inclusion-Si_3N_4 thermal expansion mismatch seems a plausible cause.

11.2 SiC MATERIALS

Silicon carbide materials have much better oxidation resistance than Si_3N_4 materials. Two views are found in the literature regarding the rate-controlling mechanisms of oxidation in SiC. During oxidation CO gas is formed at the SiC-SiO_2 interface, and its desorption from the interface has been found by some investigators to control the rate of oxidation.[69] Others contend that oxidation kinetics are determined by the rate of inward oxygen diffusion through the surface SiO_2 layer.[77] All investigations have found that processing additives such as Al_2O_3, B, and B_4C increase oxidation rates over additive-free CVD-SiC, but that parabolic kinetics are still observed. The additives are thought to decrease the viscosity of the surface SiO_2 layer, which results in increased oxygen diffusion through the scale, leading to greater rates of oxidation. The oxide scales are typically cristobalite, and an amorphous phase in
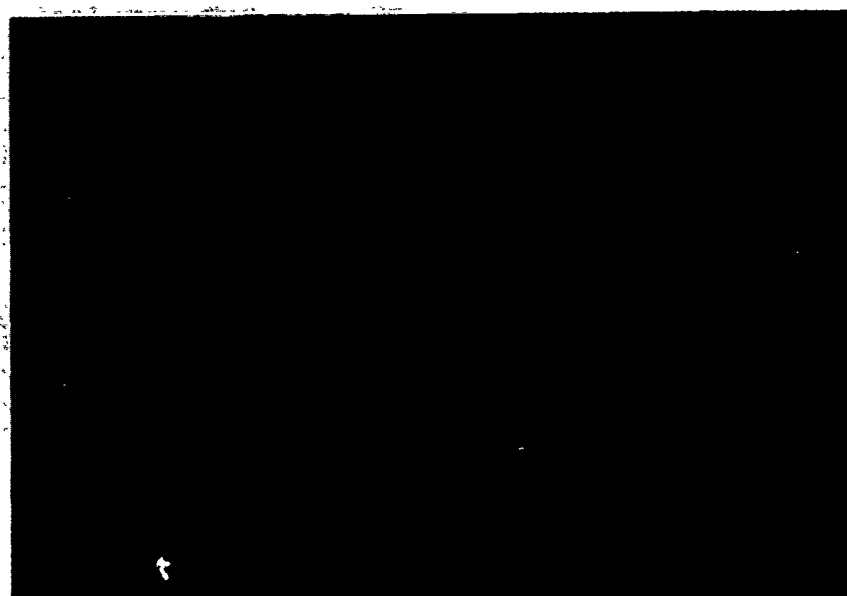
231

(a)　　　Batch 1　　　　　　　12X

(b)　　　Batch 2　　　　　　　12X

Figure 97.　Surface of AED Nitrasil RS-Si$_3$N$_4$
after 1000 hr/1400°C static air exposure.

(a)　100 hr/1400°C exposure

12X

(b)　1000 hr/1400°C exposure

12X

Figure 98.　Surfaces of AED Nitrasil (batch 5)
RS-Si₃N₄ samples after 1400°C static air
exposure.

5.3X

8X

Figure 99. Spontaneous fracture of Annawerk
Ceranox NR-115H RS-Si$_3$N$_4$ sample during
1000 hr/1400°C static air exposure.

which impurities such as Al and Fe concentrate. Boron impurities may be found in the scale also. Thus the outward diffusion of impurities from the matrix into the scale is analogous to the case for hot-pressed silicon nitride. In Al_2O_3-doped HP-SiC some mullite (3 $Al_2O_3 \cdot 2$ SiO_2) and aluminum silicate (Al_2SiO_5) are sometimes found in the surface scale, primarily for oxidation temperatures below 1300°C.[69]

Various hot-pressed, sintered, and silicon-infiltrated forms of silicon carbide have been exposed in static air environment on this program. The usual exposure was for 100 and 1000 hr at 1200° or 1400°C. Selected materials were exposed for 2000 hr at 1500°C. The weight change data were presented in Table 37 and summarized in Table 42.

11.2.1 HP-SiC

Hot-pressed and sintered materials were exposed at 1400°C. The use of B_4C instead of Al_2O_3 in HP-SiC is seen to result in up to a factor of five increase in weight gain. The optical photographs in Figure 100 and 101 illustrate a much thicker and more crystalline surface scale for the B_4C-doped material, even though the exposure conditions for that material were not as severe as for the Al_2O_3-doped material (1000 hr/1400°C vs. 2000 hr/1500°C). The surface scale for the B_4C-doped SiC was identified as cristobalite. Calcium and iron were found in the scale by X-ray fluorescence. The element boron cannot be (... cted with the equipment used. The surface scales on the Al_2O_3-doped HP-SiC were very thin, smooth, and shiny. The shiny nature of the scale in these materials has been thought to be indirect evidence that the scale was liquid at the exposure temperature. This coincides with the concept of Al matrix impurities entering the SiO_2 scale and reducing its viscosity. SEM views of the surface scales of such HP-SiC materials containing 2% Al_2O_3 are presented in Figures 102 and 103. The hole in the scale, shown in Figure 102, was presumably made by escaping CO gas. Note the cracking and spallation of the scale shown in Figure 103. Even though the B_4C-doped HP-SiC developed a thicker, more crystalline scale than did the
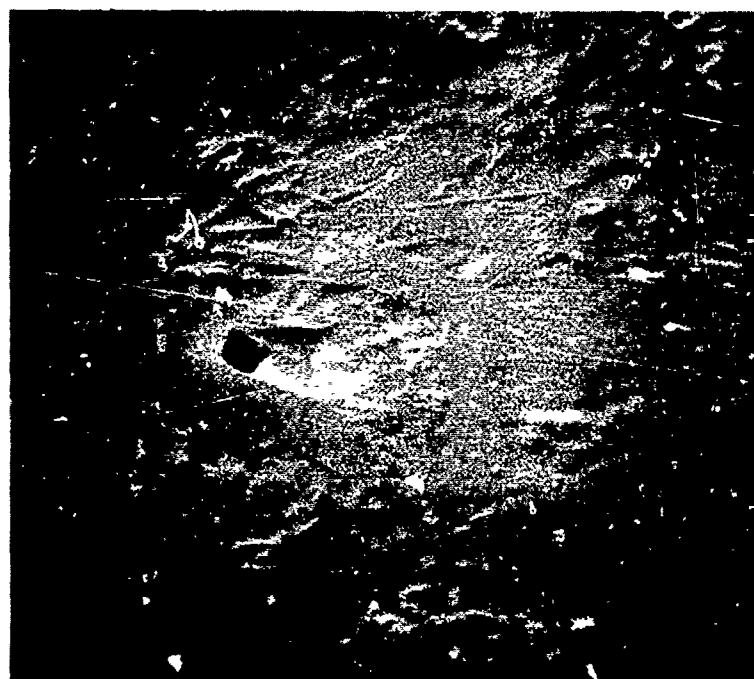
235

12X

Figure 100. Optical view of surface of Norton
NC-203 HP-SiC (2% Al$_2$O$_3$) after 2000 hr/1500°C
static air exposure.
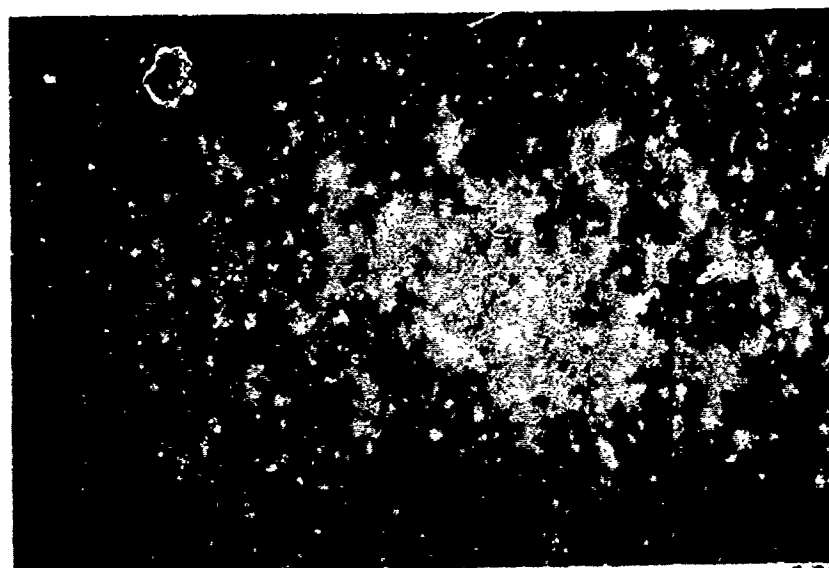
12X

Figure 101. Optical view of surface of Ceradyne
Ceralloy 146I HP-SiC (2% B$_4$C) after 1000 hr/
1400°C static air exposure.

236

1000X

Figure 102. SEM view of surface of Norton
NC-203 HP-SiC (2% Al₂O₃) after 2000 hr/
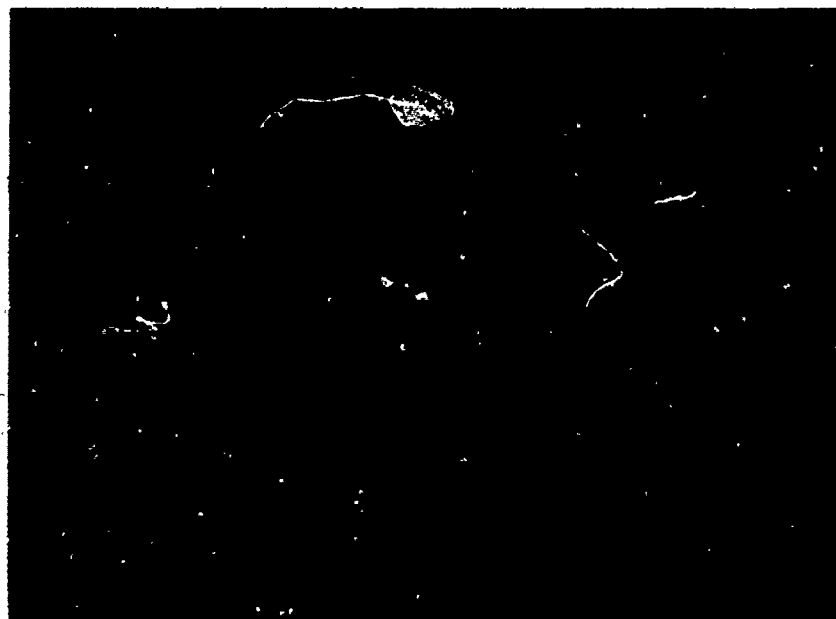1500°C static air exposure.

500X

Figure 103. SEM view of surface of Ceradyne
Ceralloy 146A HP-SiC (2% Al₂O₃) after
1000 hr/1400°C static air exposure.

237

Al_2O_3-doped material, T₂ jle 41 shows that its bend strength was not as affected by the exposure. For 1000 hr/1400°C exposure, the Al_2O_3-doped material retained ~90% of its unexposed strength, whereas the B_4C-doped material retained about 95% of its original strength. It is interesting to note that even after the 2000 hr/1500°C exposure, Norton NC-203 has the same room-temperature strength as in nonexposed material.
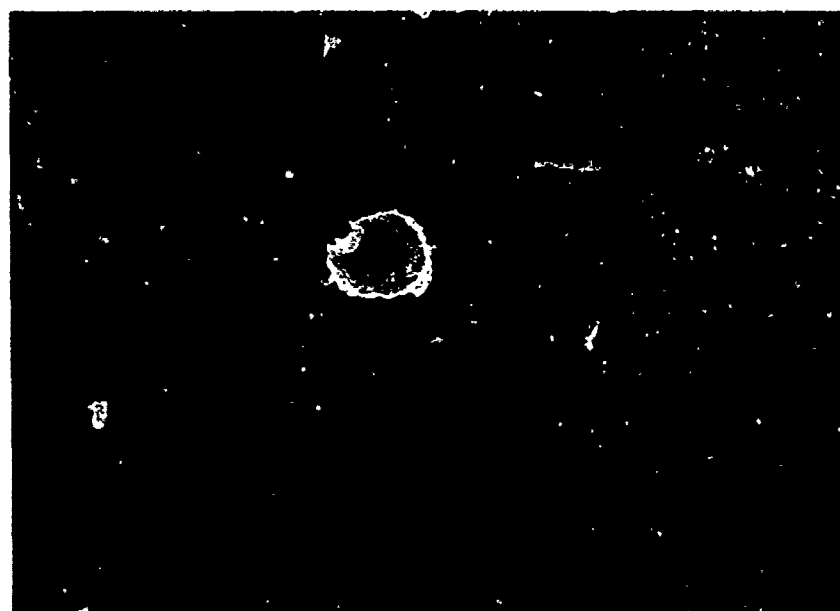
11.2.2 Sintered SiC

Three sintered SiC materials were evaluated: Carborundum (1979) α-SiC, Kyocera α-SiC, and General Electric β-SiC. They were exposed for 100 and 1000 hr at 1400°C. Table 42 summarized the weight change data. The α-form generally has about a factor of two lower weight gain than the best hot-pressed material (i.e., Al_2O_3 doped). This illustrates the adverse effect of impurities on oxidation resistance. The sintered materials are very pure, typically containing only ~0.5% metallic impurity, which is mainly the boron that is used as a sintering aid. The sintered β-SiC was a bit more variable, as shown in Table 42. Some samples experienced much more crystalline scale formation than the α-SiC materials, which were very uniform.

The oxide surface scales on sintered α-SiC are very thin and dull, as shown in the optical photographs in Figures 104 and 105. The SEM view of the scale formation on the Carborundum and Kyocera materials provided in Figures 106 and 107 are much more informative. The holes in the scale of the Carborundum material were presumably made by escaping CO gas. The surface of the Kyocera material appears similar. After 100 hr oxidation at 1400°C, both materials gain ~5-10% in strength, presumably due to blunting of machining marks or isolated surface porosity. After 1000 hr exposure, both α-SiC materials lose about 5-10% of their original unexposed strength, oxidation pits becoming the predominant fracture origins. The β-SiC behaves in a similar manner.

12X

Figure 104. Optical view of surface of Carborundum
sintered α-SiC after 1000 hr/1400°C static air
exposure.

(a)   100 hr/1400°C exposure   12X

(b)   1000 hr/1400°C exposure   12X

Figure 105.   Optical view or surfaces of Kyocera
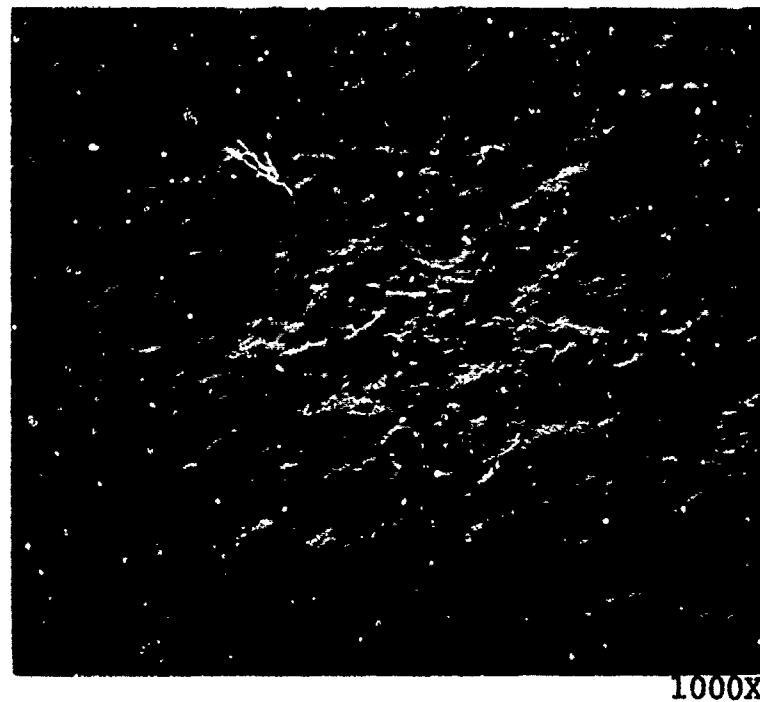SC-201 sintered α-SiC after 1400°C static air
exposure.

240

1000X

Figure 106. SEM view of surface of Carborundum
sintered α-SiC after 1000 hr/1400°C static
air exposure.

1000X

Figure 107. SEM view of surface of Kyocera
SC-201 sintered α-SiC after 1000 hr/1400°C
static air exposure.

11.2.3 Silicon-Infiltrated SiC

Silicon-infiltrated (or siliconized) SiC materials contain typically 5-15% free Si metal to densify the originally porous structure. They contain nominally 0.5% other metals (impurities), mainly aluminum and iron. Refel, Norton NC-430, and Coors 1979 SC-1 Si/SiC were exposed for 100 and 1000 hr at 1200°C. Table 42 illustrates that they experienced about the same weight gain as HP-SiC (2% Al_2O_3) had at a temeprature 200°C higher. Their surface scales were generally smooth, dull, and very thin, as shown in Figure 108. The Coors material, however, exhibited some crystalline portions of the scale, as shown in Figure 109.

The most interesting aspect of Si/SiC materials is their retained strength after exposure. Table 41 detailed and Table 43 summarized the residual strength data. It is observed that a range from a 30% strength increase to a 50% strength loss was observed for these materials. This large difference and discrepancy when compared to the retained strength of the other silicon carbide materials must be related to the silicon phase in these materials. Strength data are difficult to analyze in Si/SiC materials, since fracture source identification is usually inconclusive due to the heterogeneous nature of the two-phase material.

The Coors 1979 SC-1 Si/SiC appears to exhibit anomalous oxidation behavior when compared to the Refel and Norton NC-430 materials. The weight gain for Coors material was higher, and it was the only material to exhibit a strength loss after exposure. This behavior is probably somehow related to the specific nature of the silicon phase in this material. A few large crystalline features on the surface of exposed samples were associated with what appeared to be silicon metal that had exuded from within the structure. Figure 110 illustrates a macroscopic crack that spontaneously developed in the Norton NC-430 material during exposure. The damaged area appears to be associated with a band of silicon-rich material that has exuded from within the composite
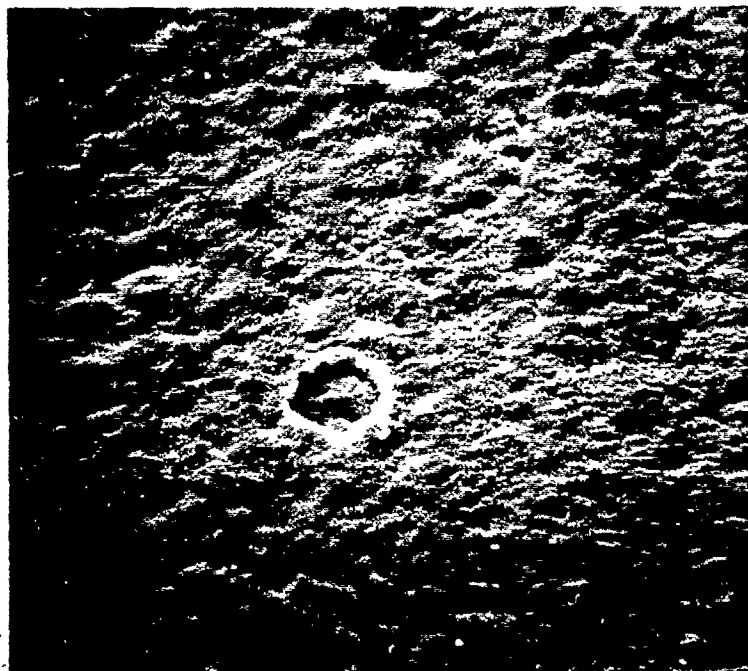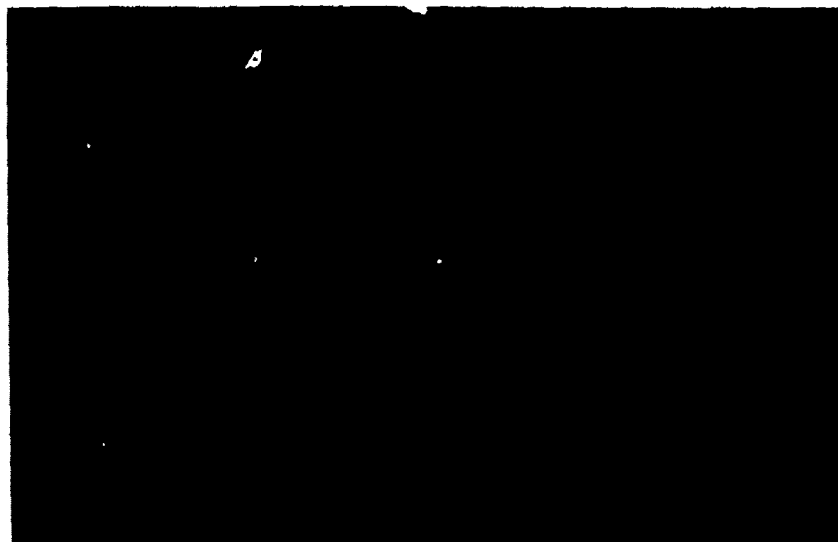
Figure 108. SEM view of surface of Refel
Si/SiC after 1000 hr/1200°C static air
exposure.
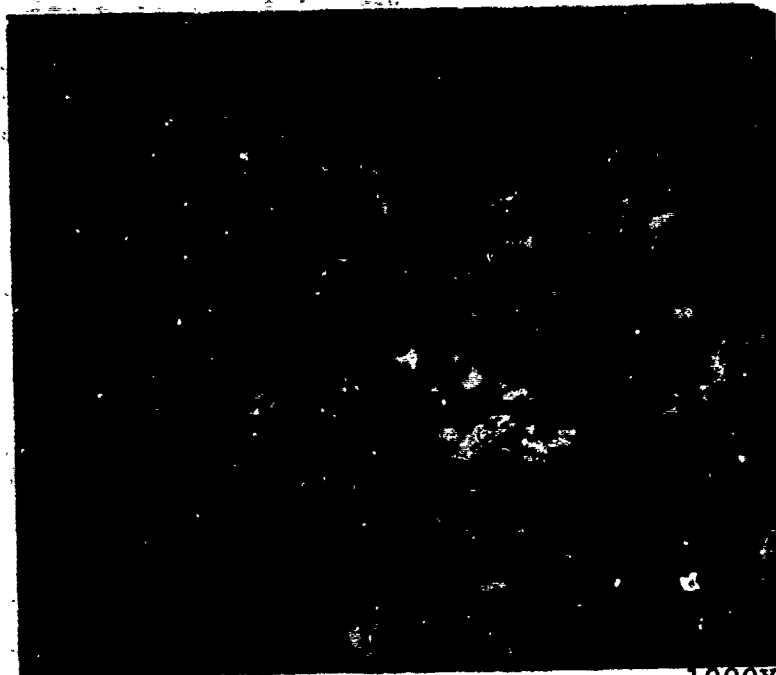
Figure 109. SEM view of surface of Coors 1979
SC-1 Si/SiC after 1000 hr/1200°C static air
exposure.

243

12X

Figure 110.   Surface of Norton NC-430 Si/SiC Sample
after 1000 hr/1200°C static air exposure.

body. Behavior similar to this could certainly explain the large strength loss for the exposed Coors material.

11.3 SUMMARY OF OXIDATION IN SILICON CERAMICS

Silicon carbide materials are, in general, more stable in long term high-temperature applications than are Si_3N_4 materials. The strength distribution in SiC appears to be altered less by environmental effects such as oxidation. Weight gain by oxidation is lower in SiC, and the oxide scale thickness is less when compared to Si_3N_4. This is the case because, in general, SiC materials are of higher purity and higher density than Si_3N_4 materials. Oxidation in HP-Si_3N_4 is mainly affected by the alkali impurities that segregate in grain boundaries and then migrate to and modify the oxide scale causing increased rates of oxidation. Reaction-sintered Si_3N_4 is admittedly very pure, but a trade-off is made; the porosity is high (10-20%) in RS-Si_3N_4, and thus surface area and total oxidation are large. Sintered SiC is both pure and dense, and thus has excellent oxidation resistance. Recent forms of HP-Si_3N_4, however, show much promise for good oxidation resistance. A particular example is a Westinghouse HP-Si_3N_4 that contains nominally 4% Y_2O_3, and an undetermined amount of SiO_2.

12. ZIRCONIA CERAMICS FOR DIESEL ENGINES

Zirconia ceramics have considerable promise for use in diesel engines. The following sections outline their promise, the concept of transformation-toughening, and properties of various commercial varieties. It is important to recognize that transformation-toughened zirconia is essentially a low-temperature material. It will be demonstrated below that extended high-temperature exposure can lead to overaging with resultant loss of properties.

12.1 THE ADVANTAGES OF ZIRCONIA IN DIESEL ENGINES

Zirconia is currently the ceramic material that has been the most successful in the U.S. Army TACOM Adiabatic Diesel Engine program at Cummins Engine Company.[92-95] The concept of that program is to insulate the high-temperature components of the engine such as the piston (cap), cylinder head, valve hardware, cylinder liner, and exhaust ports. Additional power and improved efficiency result from this concept since thermal energy normally lost to the cooling water and exhaust gas (almost two-thirds of the energy input in a conventional diesel engine) is converted to useful power through the use of turbocompounding. By reducing the lost energy and eliminating the need for a conventional water-cooling system, the adiabatic diesel has been demonstrated to improve fuel economy and increase power output.

The performance advances that have been achieved by the Adiabatic Diesel Engine have largely been realized through the use of one generic class of ceramic material, transformation-toughened partially stabilized zirconia.[96,97] This particular ceramic has been successful in this application for three reasons: (a) it is highly refractory; (b) it possesses a very low thermal conductivity; and (c) significant increase in fracture toughness has been attained in this ceramic material by a

phenomenon known as phase transformation-toughening. Additionally, zirconia has a high thermal expansion (for ceramics), almost as high as cast iron. This means that the shrink-fit of a zirconia liner in a cast iron block will be maintained at elevated temperatures.

Much work is currently being done within the ceramics industry on transforma. -toughened zirconia (TTZ). Various manufacturers are beginning to supply newly developed materials to various engine demonstration and component development programs. It is now an appropriate time to develop a data base for such zirconia ceramics.

12.2 POLYMORPHISM AND PHASE STABILIZATION IN ZIRCONIA

Pure zirconia (i.e., nonstabilized) exhibits three crystal structures between room-temperature and its melting point. Zirconia is normally monoclinic up to ~1100°C, where it transforms to tetragonal symmetry, followed by a final transformation to the cubic structure at 2370°C. The problem with pure ZrO_2 arises upon cooling through the martensitic tetragonal-to-monoclinic transformation at ~1100°C. There, approximately a 3% volume expansion occurs leading to extensive macrocracking in pure zirconia bodies.

This problem can be avoided by doping the zirconia with additions of CaO, MgO, or Y_2O_3. Thus, the material is stabilized to its high-temperature form, the cubic crystal structure. This material is termed fully stabilized zirconia (FSZ). FSZ can be cycled from room temperature to its melting point without any destructive phase transformations. Yttria has been found to be the best stabilizer, since it is less volatile than calcium and magnesium compounds at elevated temperature. Thus, destabilization of the FSZ body is less likely to occur. However, fully stabilized zirconia has disadvantages in structural applications. It is generally a coarse-grained structure, of fairly low strength, and not very tough. Its biggest drawback, perhaps, is its high thermal expansion coefficient and resulting poor thermal

247

shock resistance. However, it is noted that the low thermal con-
ductivity of zirconia, which is an advantage for cylinder liner
application, is also a major contribution to poor thermal shock
resistance in zirconia.

If less stabilizer (CaO, MgO, Y_2O_3) is incorporated into the
structure than is required to fully retain the ZrO_2 cubic struc-
ture, the material is termed partially stabilized. It has long
been known that this has distinct advantages, si .ce the thermal
expansion of PSZ is lower than that of FSZ, and thus PSZ has
better thermal shock resistance. However, thermal shock resis-
-ance is still the performance-limiting factor of PSZ in many
engineering applications.

Partially stabilized zirconia typically consists of cubic
zirconia grains with second phase tetragonal and/or monoclinic
precipitates. Recall that the stable structure at room tempera-
ture is monoclinic, and that a large shape and volume change is
associated with the martensitic tetragonal-to-monoclinic trans-
formation at ~1100°C. Through appropriate processing, it has
recently been demonstrated how the tetragonal precipitates in PSZ
can be held (in a metastable condition) within the cubic matrix
at room temperature. It was found that they would revert to
their stable monoclinic structure with the application of a cer-
tain stress field.

Thus originated the partially stabilized zirconia that is
transformation-toughened (TTZ). Such TTZ bodies show much im-
proved strength and toughness (about a factor of three), and are
responsible for the birth (or rebirth) of zirconia as a struc-
tural engineering material, toughness being a central issue in
the utilization of ceramics in structural applications.

12.3 CONCEPT OF TRANSFORMATION-TOUGHENING

The most mature form of transformation-toughened zirconia
(TTZ) consists of precipitates of metastable tetragonal zirconia
in a magnesia-stabilized cubic zirconia matrix.[98-113] The
tetragonal precipitates are dispersed within much larger cubic

243

grains. The tetragonal precipitates that are within a certain size range are constrained from transforming to the monoclinic structure by the surrounding matrix. However, under an applied stress the transformation occurs. The stress-induced tetragonal-to-monoclinic phase transformation is accompanied by a volume expansion. This results in the generation of stress fields around the transformed region and microcrack generation. Such two-phase transformation-toughened materials exhibit dramatic increases in strength, fracture energy, and fracture toughness. This effect has been observed in ZrO_2, Al_2O_3, and Si_3N_4 matrices, all with a dispersed ZrO_2 (tetragonal) phase.

Current mechanistic interpretations of the improved fracture properties of transformation-toughened zirconia include: (1) deflection of the advancing crack front by interation with the stress fields around the transformed areas; and/or (c) microcrack generation leading to crack branching and an increase in the energy necessary to continue crack propagation. A third mechanism is sometimes discussed as a minor contributor, i.e., energy absorption by the phase transformation process itself. Whatever the mechanism, it is known that the stress-induced phase transformation in front of an advancing crack tip does absorb energy, arrest crack propagation, and thereby increase strength and toughness.

It is important to understand that the microstructure and properties of TTZ are strongly dependent on the particle size of the initial powder, the concentration of stabilizing oxide, the time-temperature processing schedule, post-fabrication heat treatment, and surface preparation. It is possible to fabricate dense ZrO_2 bodies with various phase assemblages (in particular, varying amounts of tetragonal phase), with various amounts of microcracking, and with a varying martensitic phase transformation temperature. Generally, TTZ is considered a low temperature material. High-temperature isothermal aging is known to cause coarsening of the tetragonal phase and loss of toughness.[98] The specific time-temperature conditions that result in coarsening

depend on the amount and type of rare-earth oxide used, the initial particle size, and the nature of the overall phase assemblage, etc.

12.4 EVALUATION OF VARIOUS COMMERCIAL ZIRCONIA MATERIALS

Various foreign and domestic zirconia ceramics were characterized. They were supplied to this program by R. Kamo of Cummins Engine Company. Investigated were crystal phases, stabilization, microstructure, thermal expansion, strength, elastic modulus, and fracture mode. Interpretation is made with respect to transformation-toughening, phase stability, and overaging phenomena. Five different foreign and domestic transformation-toughened zirconia materials were investigated. We have used the identifying notations A, G, J, and U to designate material from Australian, German, Japanese, and domestic sources, respectively.

12.4.1 Density, Phase Assemblage

The bulk density of each material is shown in Table 44. All are in the range $5.7-5.8$ g cm^{-3}. Table 45 presents results for spectrographic cation analysis. Materials A-1, A-2, G-1, and U-4 are magnesia stabilized, whereas the Japanese material is stabilized with Y_2O_3. Note that materials A-1 and U-4 apparently contain only half the magnesia stabilizer compared to materials A-2 and G-1. Note also that the Y_2O_3-stabilized material contains a substantial amount of Al and Si. Presumably, there is a fair amount of SiO_2 at the grain boundaries. The detrimental result of this in high temperature deformation will be discussed later.

Table 46 presents the results of X-ray diffraction analysis. Note th..t the low MgO content in material A-1 has resulted in very little retention of the cubic phase. All other materials exhibited substantial cubic content. Additionally, A-2, J-1, and U-4 exhibited major tetragonal peaks. Recall that it is the metastable tetragonal phase that results in increased toughness in TTZ. Note also in Table 46 that the two Australian materials each contain a major monoclinic phase. Monoclinic ZrO_2 was only detected as a minor phase in the other materials.

250

TABLE 44.   ZIRCONIA MATERIALS EVALUATED

Material Supplied[a]	Bulk Density, $g\ cm^{-3}$	Measured Open Porosity, %
A-1	5.719	0.02
A-2	5.757	0.02
G-1	5.776	0.01
J-1	5.791	0.00
U-4	5.739	0.01

[a]The notations A, G, J, and U refer to
Australian, German, Japanese, and
domestic sources, respectively.

TABLE 45.   SPECTROGRAPHIC ANALYSIS[a] OF MAJOR IMPURITIES
IN ZIRCONIA CERAMICS

Material[b]	Analysis, approximate weight percent[c]
A-1	1.1 Mg, ~1.0 Hf, 0.2 Fe, 0.1 Si
A-2	3.0 Mg, 0.1 Hf, 0.07 Si
G-1	3.0 Mg, 0.1 Hf, 0.05 Cr
J-1	(P)Y, 1.0 Al, 1.0 Si, 0.1 Hf, 0.05 Mg, 0.05 Ti
U-4	0.9-1.5 Mg

[a]Performed at AFWAL.

[b]The A, G, J, and U notations refer to Australian, German,
Japanese, and domestic sources, respectively.

[c]The P notation refers to a primary constituent (e.g., Zr);
it is used here to indicate two materials that are yttria-
stabilized (i.e., Y-PSZ).

TABLE 46.   X-RAY DIFFRACTION ANALYSIS RESULTS[a]

| Material[b] | Phases Present[c] | |
	Major	Minor
A-1	tet., mono.	
A-2	cubic, tet., mono.	
G-1	cubic	tet., mono.
J-1	cubic, tet.	mono. (trace)
U-4	tet., cubic	mono.

[a]Performed at AFWAL/ML.

[b]A. G. J. and U notations refer to Australian, German, Japanese, and domestic sources, respectively.

[c]The notations tet and mono. refer to the tetragonal and monoclinic crystal structures, respectively.

12.4.2 Microstructure

The microstructure of these materials was studied by reflected light microscopy. Materials A-1, A-2, G-1, and U-4 look similar, as shown in Figures 111-114. These are all magnesia-stabilized, and consist of large ~50 µm grains. From the XRD results, it would be inferred that these large grains were typically cubic. However, note that cubic ZrO_2 was not detected, even as a minor constituent, for material A-1. This is not understood at present, since both A-1 and A-2 exhibited total extinction when viewed in the petrographic microscope with crossed polars. This would be expected for the isotropic cubic crystal, but not for anisotropic tetragonal or monoclinic crystals. Figure 115 illustrates that in contrast to the large grain magnesia-stabilized materials, the Y_2O_3-stabilized Japanese material (J-1) is very fine grained (~1-5 µm). Some submicron, presumably tetragonal, particles are also observed in the SEM micrograph of the fracture surface of J-1 shown in Figure 115.

12.4.3 Strength, Deformation, and Fracture

The strength of these five transformation-toughened materials is shown in Figure 116. Tests were generally conducted in four point flexure at 25° and 1000°C. Note that the fine grain J-1 material has the highest strength, ~105 ksi at 25°C. This shows the promise of Y_2O_3-stabilized material. However, it is demonstrated that this fine grained Y_2O_3-stabilized material deforms more at elevated temperature than the MgO-stabilized materials. This appears to be a long-term creep effect rather than a short-time effect. It will be shown below that the J-1 material deformed badly during the thermal expansion test. This may be attributed to enhanced grain boundary creep due to the fine grain size of this material. Also, Table 45 illustrated that the J-1 material had substantial Si impurity, which is usually associated with SiO_2 in intergranular regions, resulting in large high temperature deformation. However, at short times this is not as obvious. Figure 117 illustrates that the J-1 material exhibited linear stress strain behavior at 1000°C. This would
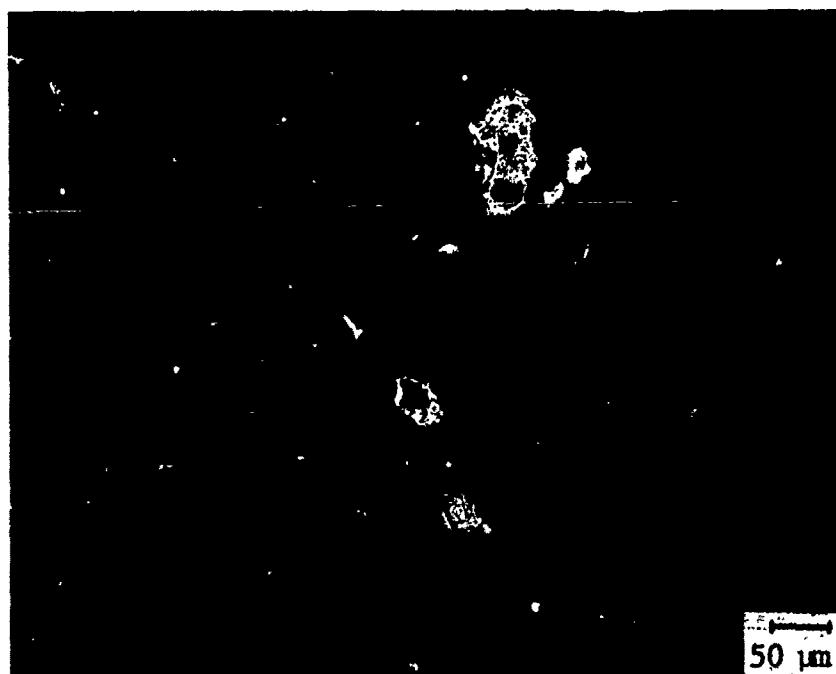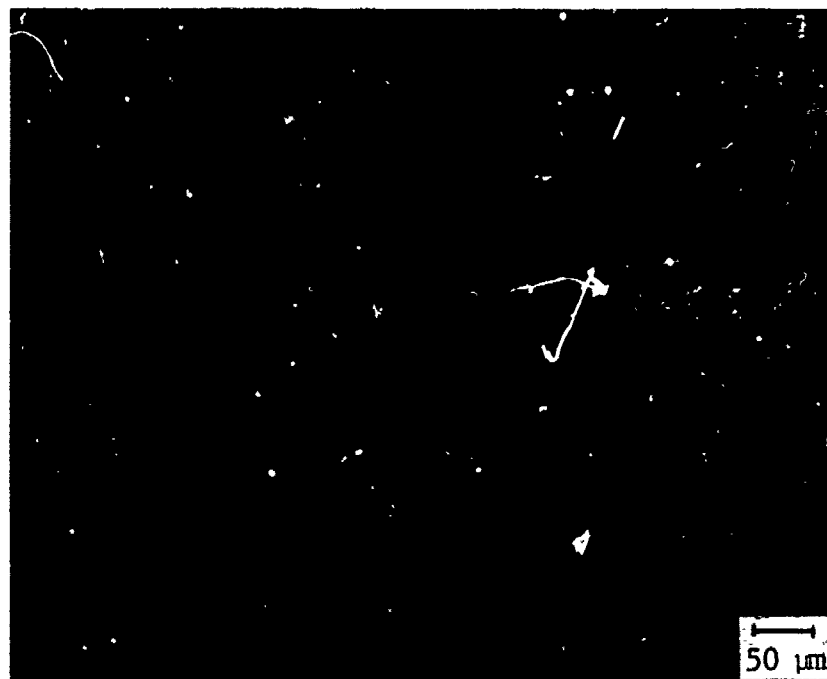
253

Figure 111.   Microstructure of zirconia A-1
polished and etched 50 sec.

(a)

(b)

Figure 112. Microstructure of zirconia A-2
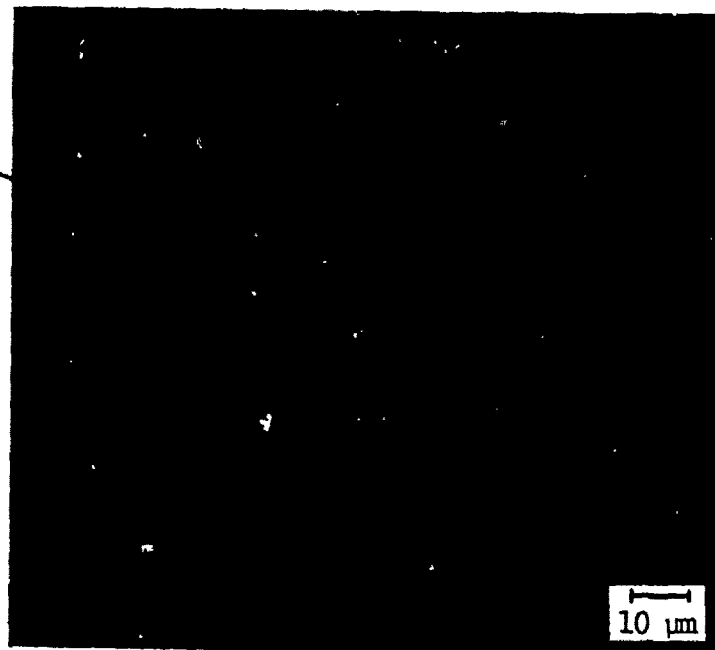polished and etched 30 sec.

Figure 113. Microstructure of zirconia G-1
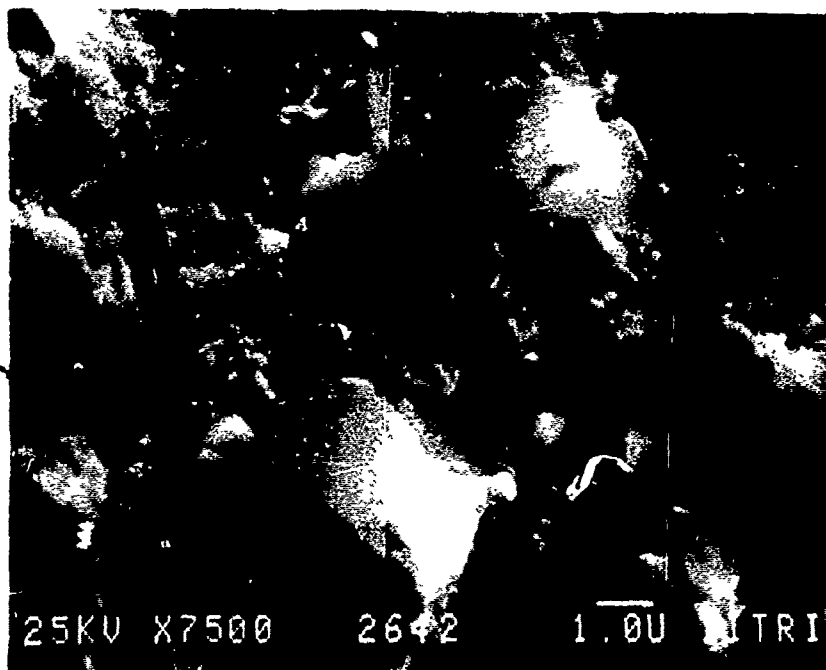polished and etched 50 sec.

Figure 114. Microstructure of zirconia U-4
polished and etched 55 sec.

Grain boundaries delineated in ink

10 μm

(a) Polished and etched 35 sec.

Large grains: cub. 1-5 μm

Submicron grains: presumably tetragonal

25KV X7500 26+2 1.0U TRI

(b) SEM micrograph of the fracture surface showing grain morphology.

Figure 115. Microstructure of zirconia J-1.
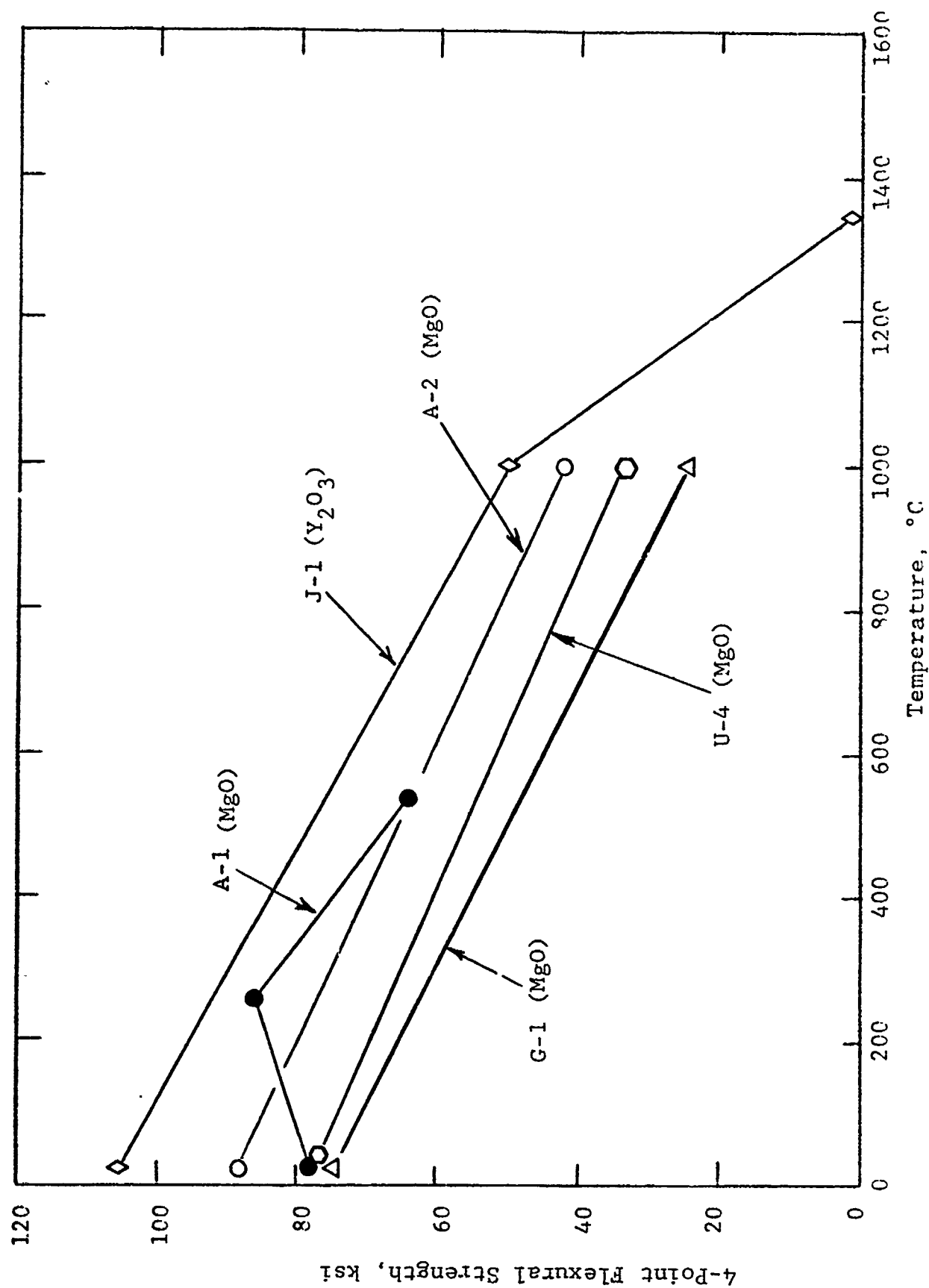
Figure 116. Flexural strength of various zirconia ceramics.
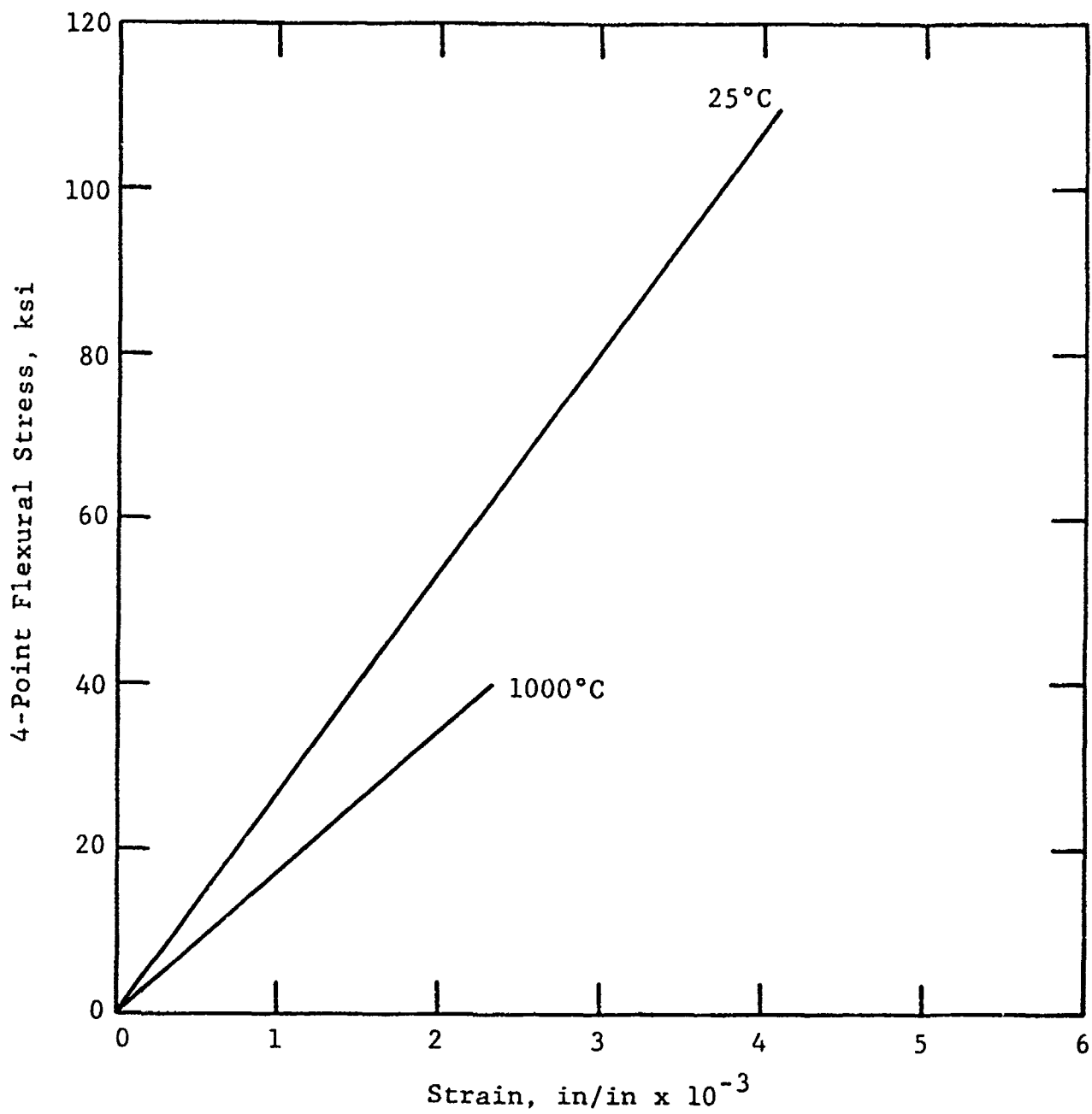
Figure 117.   Representative flexural stress-strain behavior of zirconia J-1

tend to rule out deformable grain boundary phases. However, Table 47 illustrates that strain-to-failure of the Y_2O_3-doped J-1 material is higher than that of the MgO-stabilized materials. Part of this effect, however, is due to the fact that the J-1 material was slightly stronger than the others (Figure 116).

TABLE 47. DEFORMATION OF TTZ AT 1000°C

Material	Failure Strain, 10^{-3}	Elastic Modulus, 10^6 psi
A-2	1.65	24.3
G-1	1.54	23.7
U-4	1.48	22.2
J-1	1.9, 3.0	17.1, 25.2

The two Australian materials are nominally 85 ksi materials. They are judged to be the most mature TTZ today. Much of the technology originated at CSIRO.

There are several domestic organizations developing TTZ, and it is encouraging to see a domestic ceramic supplier producing a high quality technical grade tough zirconia material. The strength of the U-4 material was 75-80 ksi.

The fracture mode appears mainly transgranular in these transformation-toughened ZrO_2 materials, as shown in Figures 118-125. A large inclusion or particle with larger thermal expansion than surrounding material is shown in Figure 118. Porosity is observed on the fracture surface of A-2 in Figure 119.

The fracture surface of G-1 shown in Figure 120 is especially interesting. Note the large grains, and intra- as well as intergranular porosity. The fracture mode in this material is entirely transgranular. This fracture surface is very similar to the TTZ fracture surface shown by Rice et al.,[99] where fracture origins were found to be predominantly single grain-boundary facets (i.e., the portion of a boundary between two grains, as opposed to grain junction triple points). Such intergranular
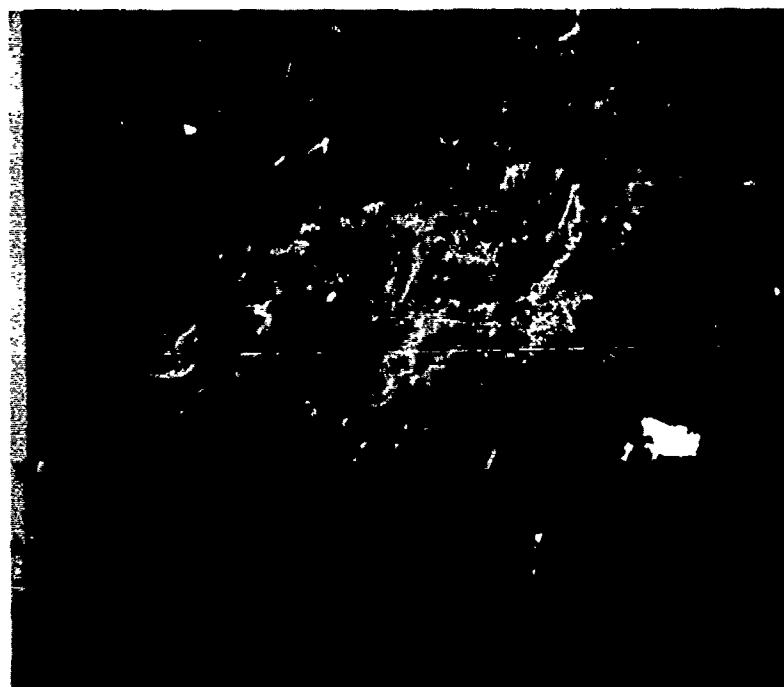
ZT2F1   130X

(a) Far from fracture origin on sample
      broken at 25°C (90.6 ksi)
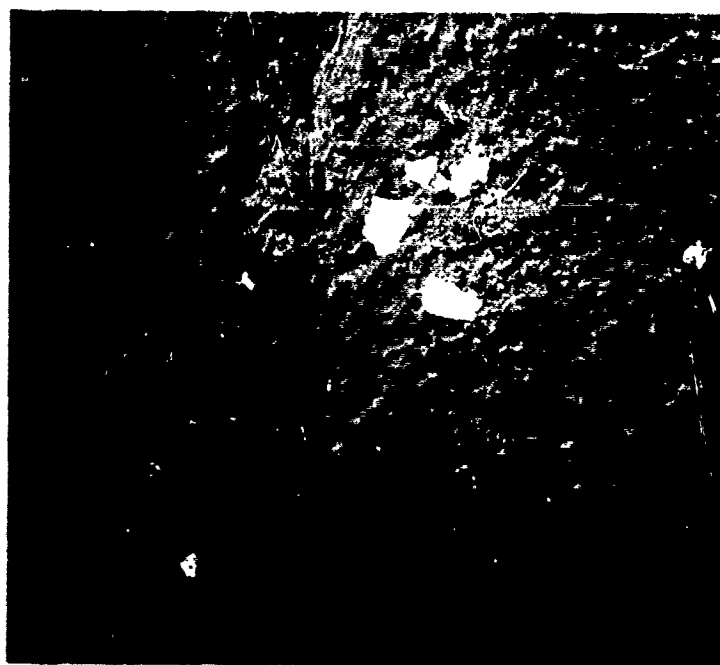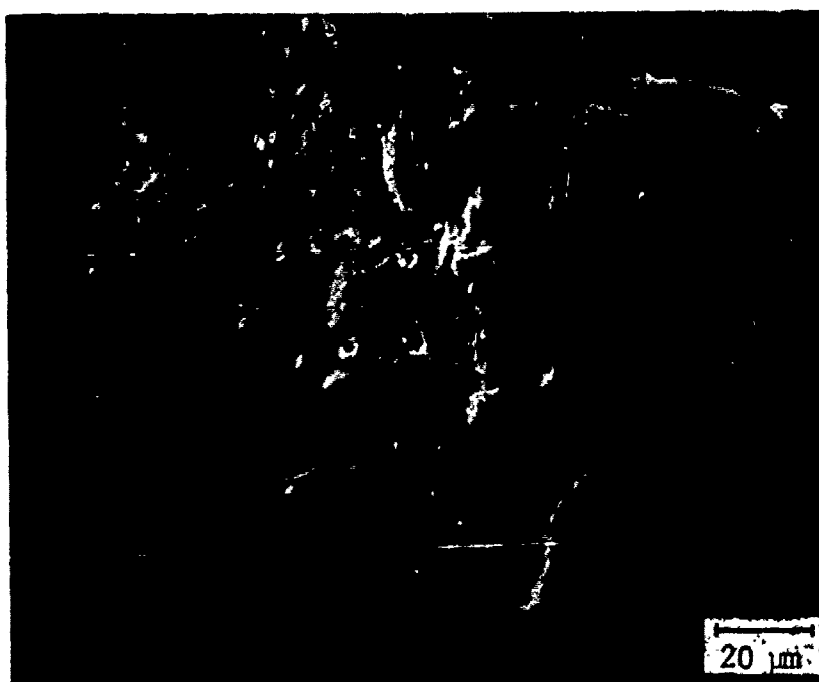

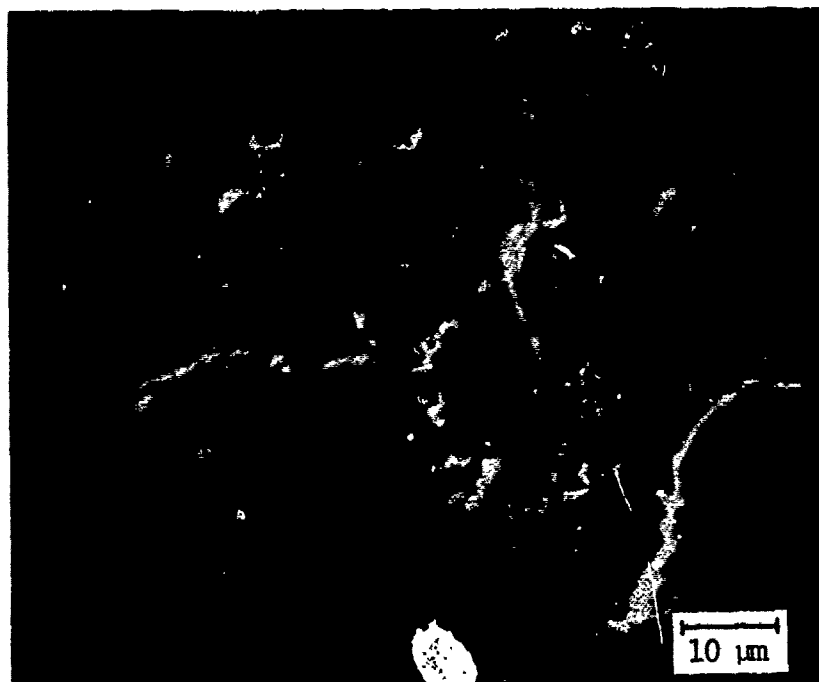ZT2F3   19.5X

(b) Fracture origin on sample broken at
      1000°C (tensile surfaces together,
                  38.5 ksi)
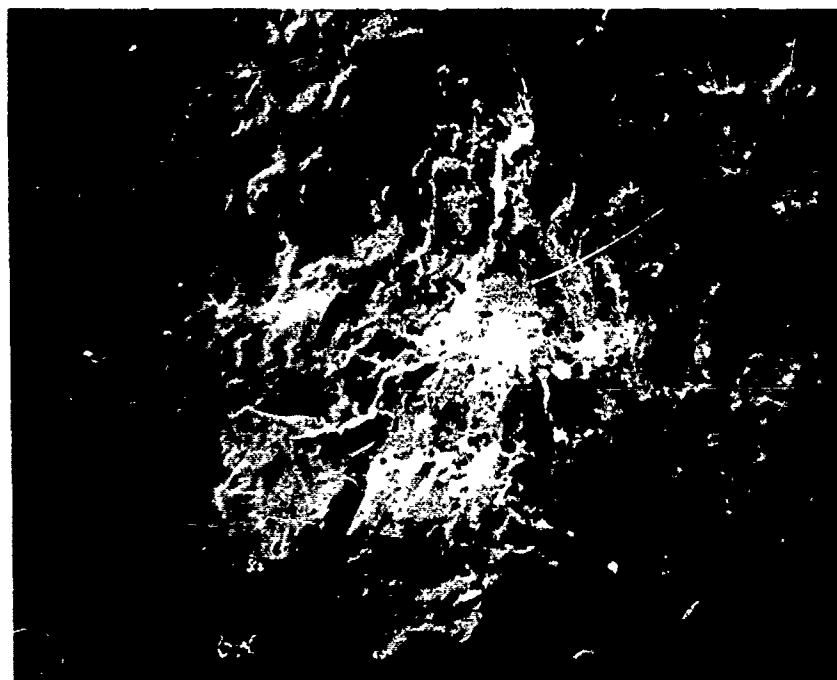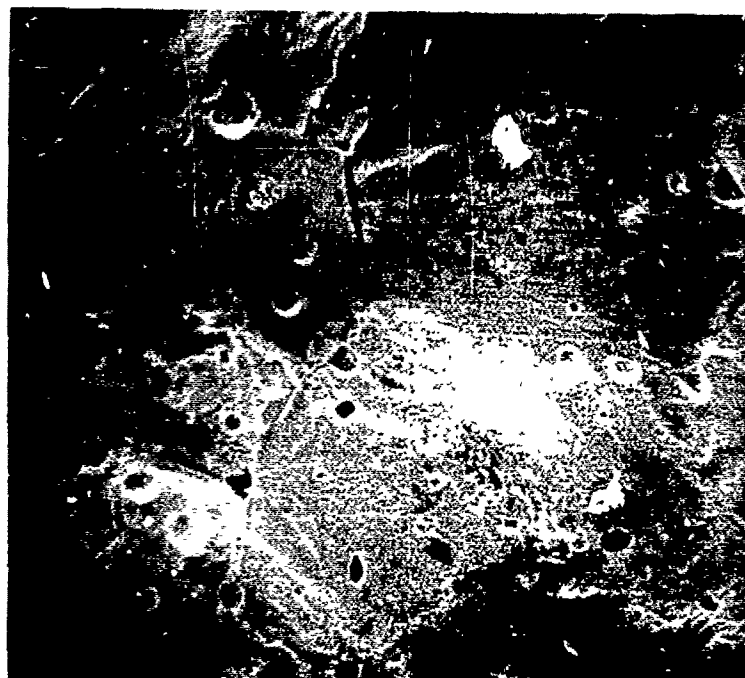
Figure 118.   SEM fracture surfaces of zirconia A-2.

261

(a)

(b)

Figure 119.   SEM micrographs of zirconia A-2
    broken at 25°C (far from the tensile
    surface).

262

:.'3F1   240X

(a) Far from origin on sample broken at 25°C
    (tensile surface is at bottom), 75.2 ksi

Zt3F4   490X

(b) Far from origin on samle broken at
    1000°C (note large grains). 37.6 ksi

Figure 120. SEM fracture surfaces of zirconia G-1.

263

fracture origins completely surrounded by transgranular failure also seem to be the case for the G-1 material. This fracture mode for the G-1 material is consistent with Lange's observations[113] that a cubic material produces a smooth, transgranular fracture (note in Table 46 that G-1 is predominantly cubic).

The fracture mode of the domestic U-4 material also appears transgranular, as shown in Figures 121-123. Intergranular porosity and large grain fracture origins are illustrated.

The J-1 material has a much finer grain size, and its fracture surfaces are shown in Figures 124 and 125. Note the high magnification of these photographs. The fracture mode appears to be irregular transgranular, which would correlate with Lange's observations[113] of the fracture mode in TTZ when substantial tetragonal phase was present. Note in Figure 125 a region of poor bonding and high local porosity in the J-1 material (subsurface, at the center of the specimen width).

12.4.4 Thermal Expansion, Long-Term Stability

Thermal expansion was evaluated using an automatic recording pushrod dilatometer. Measurements were made to 1500°C at a very slow rate, 1°C min^{-1}. It is recognized that these materials were not necessarily designed to be used at temperatures as high as 1500°C; however, testing to that temperature provides information that leads to a better understanding of microstructure, stability, role of impurities, etc., in PSZ.

The thermal expansion results are shown in Figures 126-129 and summarized in Table 48. It is observed that the A-2, G-1, and U-4 materials all exhibited stable behavior upon heating, but that a distinct indication of a phase transformation is apparent upon cooling. This phenomenon is similar to that described by Hannink et al.[98] when investigating isothermal aging of TTZ. If the tetragonal precipitate phase is within a certain small size range, then the matrix constrains the particles, the tetragonal phase is retained, and the transformation-toughening mechanism is

264

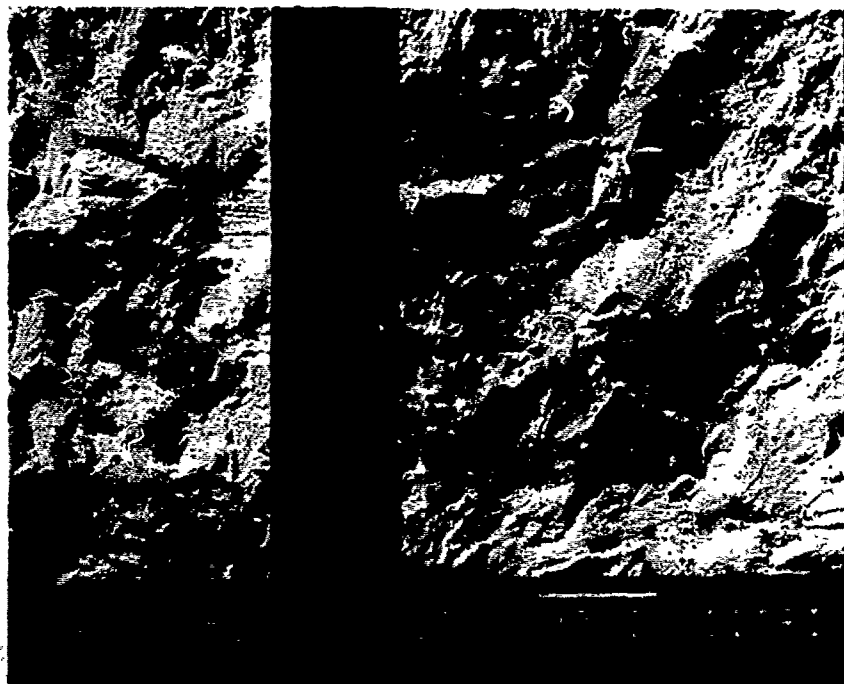(a) SEM micrograph of 25°C fracture surface

(b) SEM micrograph of sample broken at 25°C (far from the tensile surface).
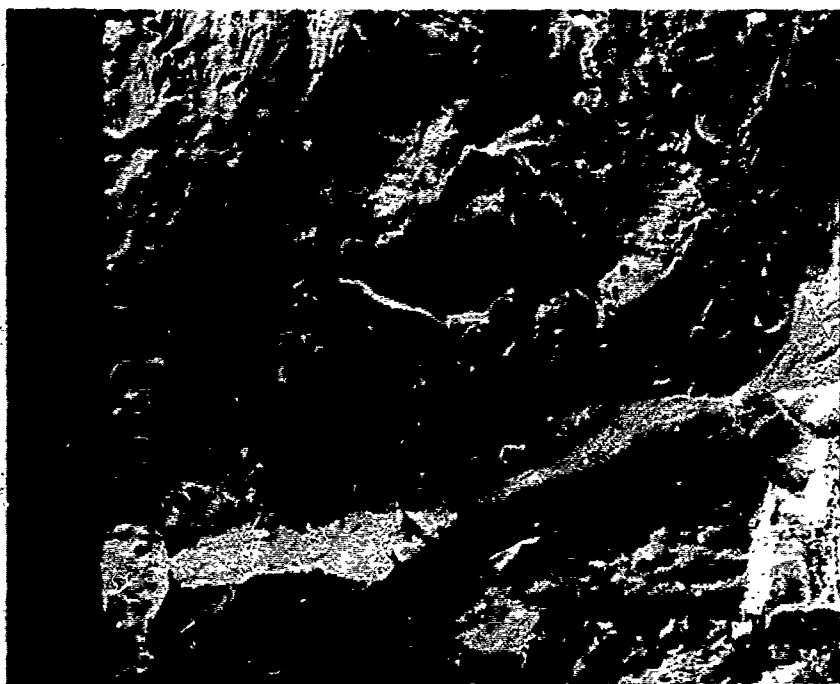
Figure 121. Fracture surfaces of zirconia U-4.

Figure 122. SEM fracture surface of zirconia U-4
at 1000°C, illustrating a large grain as the
fracture origin.

(a) SEM micrograph of fracture surfaces of
zirconia U-4 broken at 1000°C in flexure
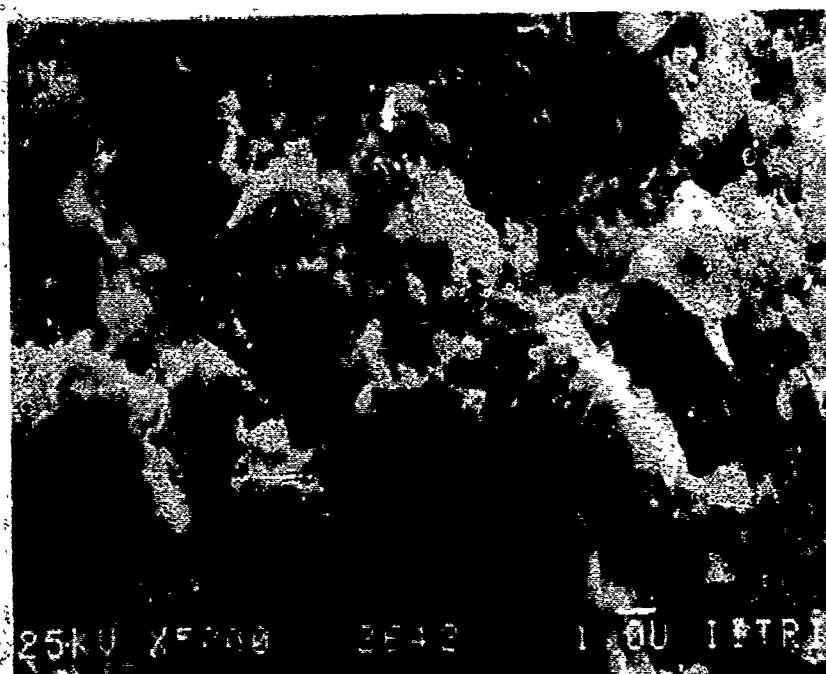(tensile surfaces mating).

(b) Higher magnification of fracture surface
illustrated in (a) above.

Figure 123.   Fracture surfaces of zirconia U-4.

(a)

(b)

Figure 124. SEM micrographs of zirconia J-1 broken at 25°C (far from the tensile surface.

475X

(a) Sample broken at 1000°C (tensile faces together) illustrating a region of poor bonding and high local porosity (51.6 ksi)

950X

(b) Higher magnification of (a) above.

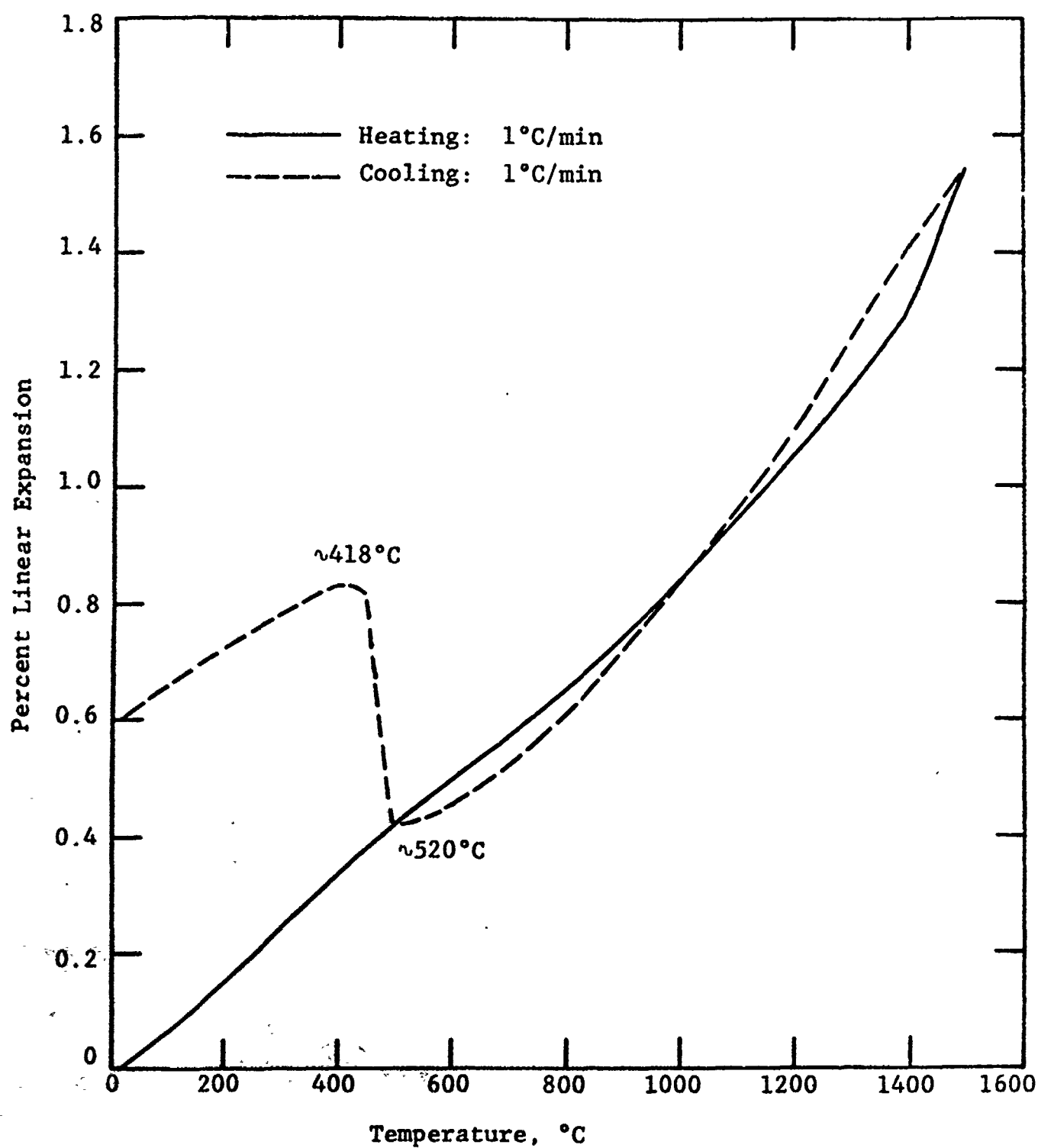Figure 125. SEM fracture surfaces of zirconia J-1.
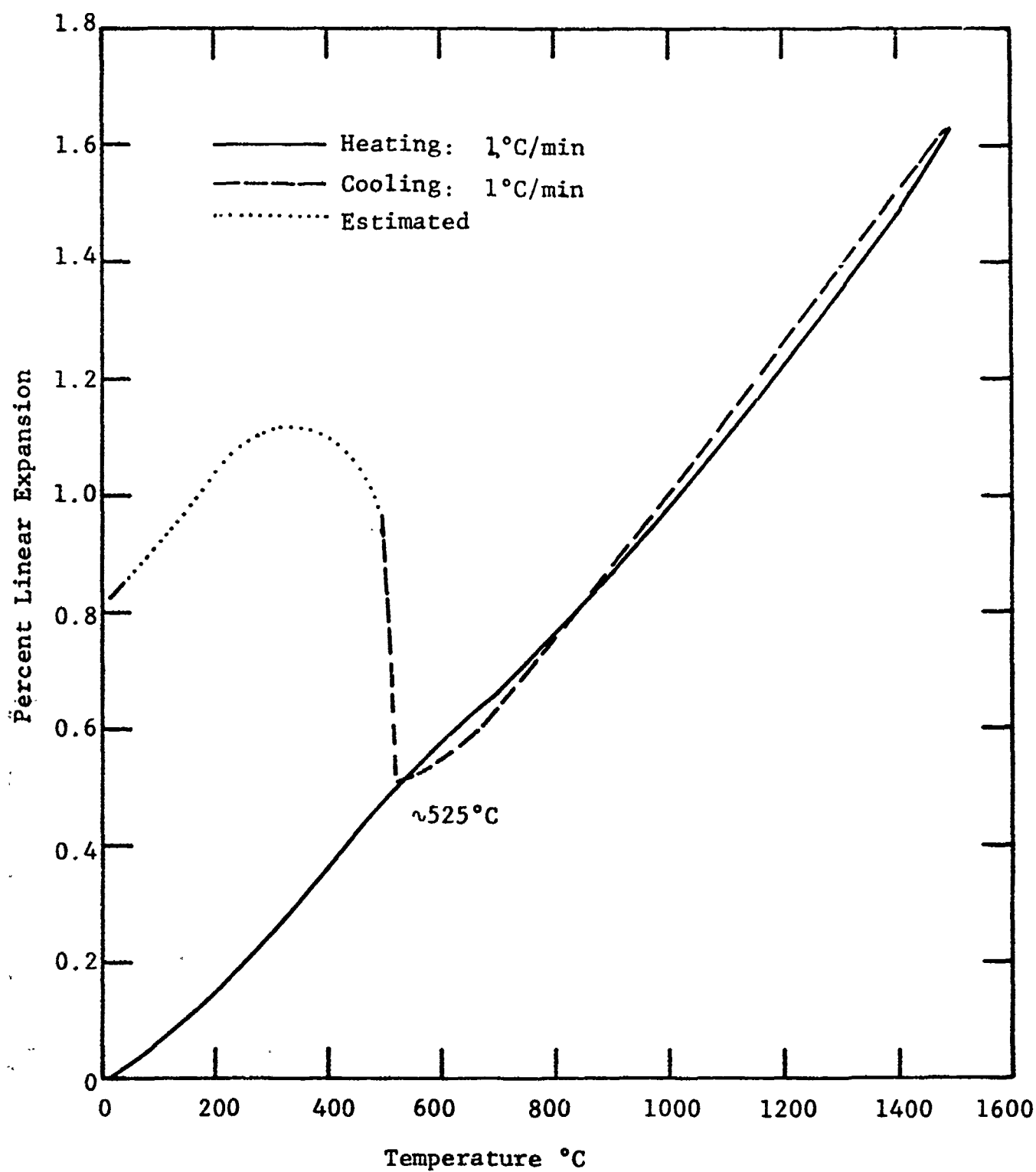
Figure 126. Thermal expansion of zirconia A-2.

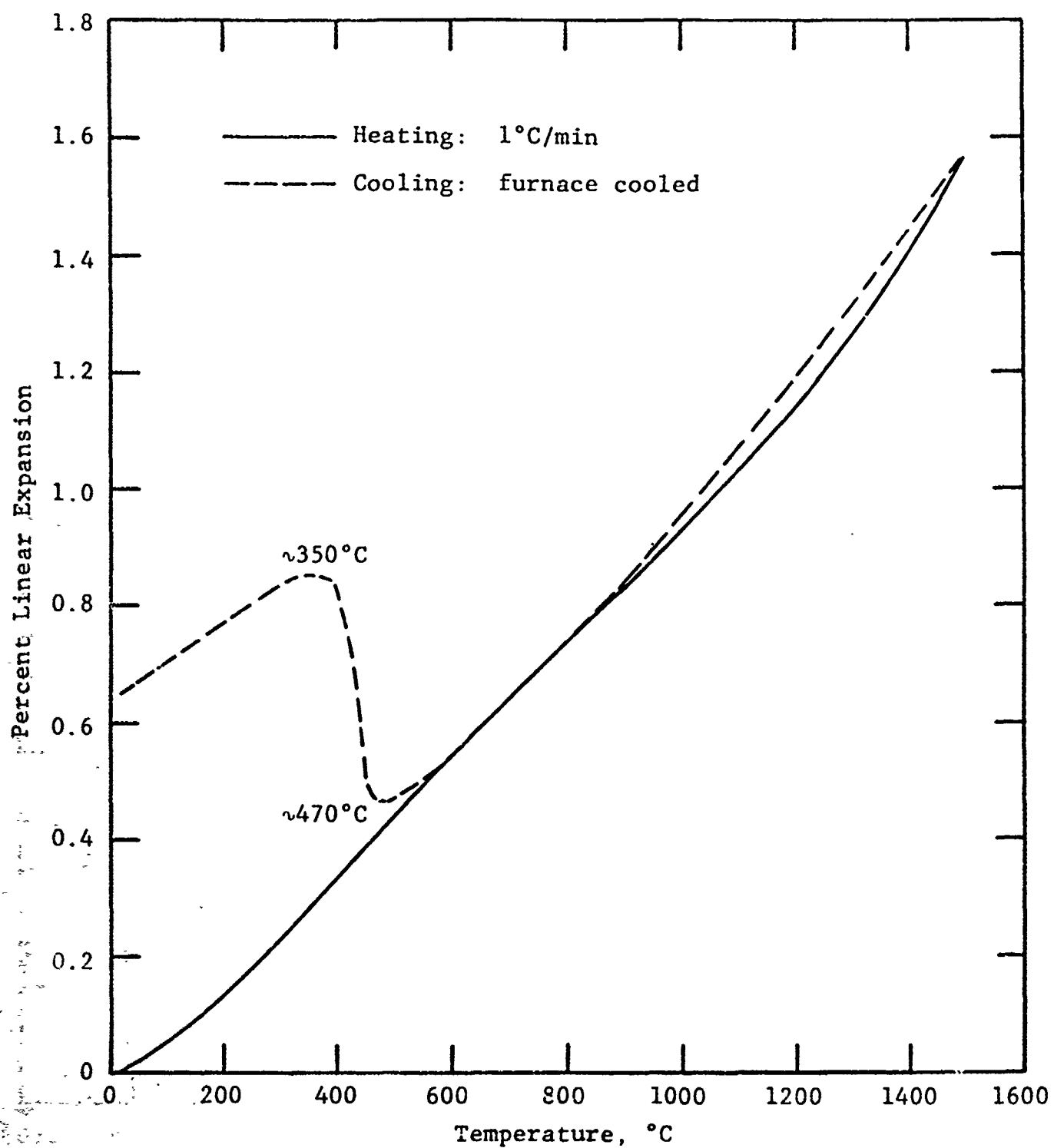Figure 127. Thermal expansion of zirconia G-1.

Figure 128. Thermal expansion of zirconia U-4.
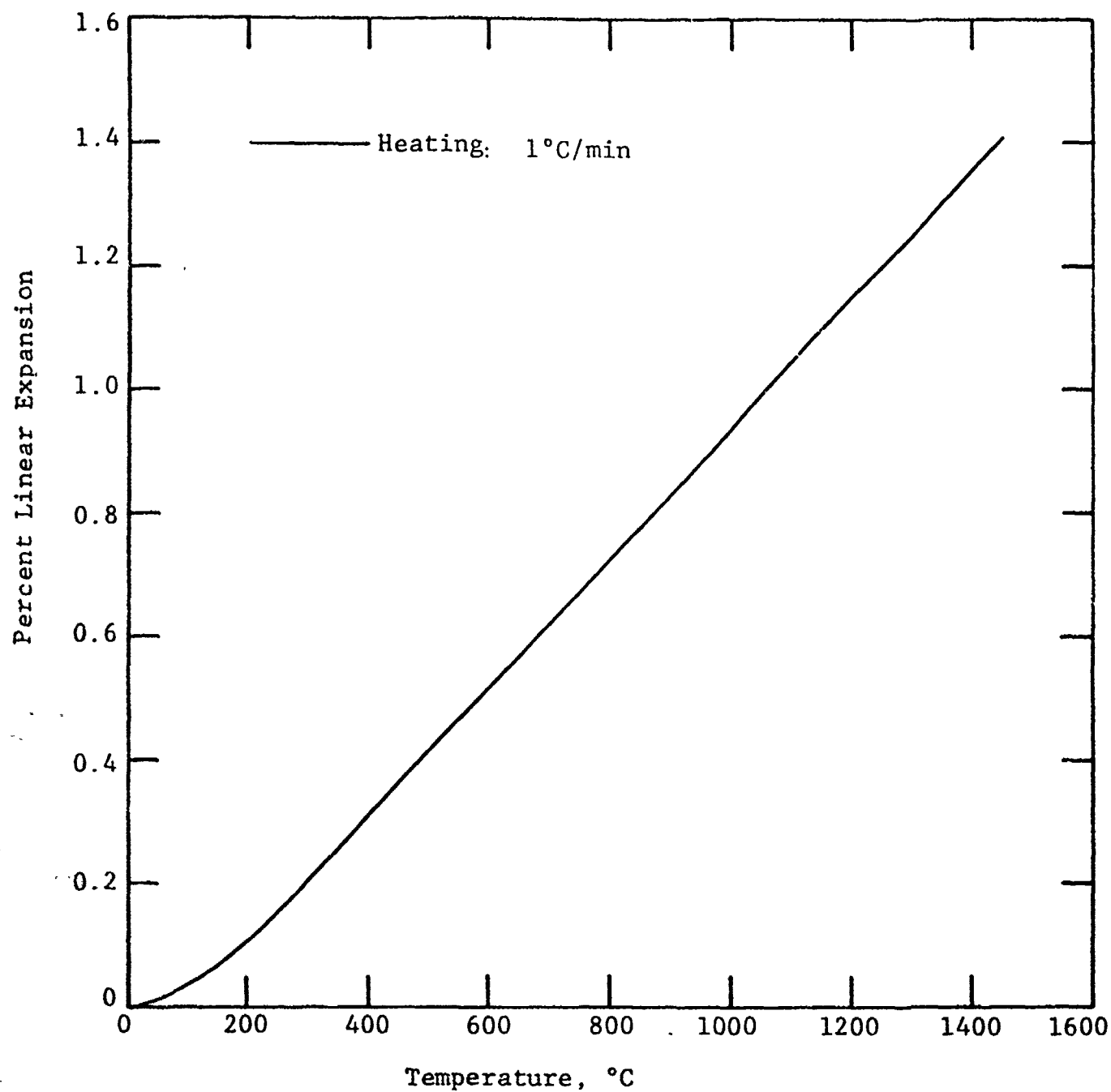
Figure 129.   Thermal expansion of zirconia J-1
(sample began to deform plasticially after
1200°C).

TABLE 48. THERMAL EXPANSION OF ZIRCONIA

Material	Percent Linear Expansion at 1000°C	
	Heating	Cooling
A-2	0.84	0.85
G-1	0.98	1.0
J-1	0.94	--
U-4	0.93	0.96

operative. Magnesia- and calcia-stabilized structures promote the coarsening of tetragonal precipitates during prolonged isothermal a. ing. Such large tetragonal particles will transform to the monoclinic symmetry upon subsequent cooling to room-temperature. X-ray analysis of these samples after thermal exposure confirms this. Table 49 illlustrates that after the one cycle expansion test to 1500°C, the exposed A-2, G-1, and U-4 magnesia-stabilized materials contained much transformed monoclinic phase. The metastable tetragonal phase was not retained. Note that the microcracking associated with this overaging phenomenon resulted in a greater than 60% strength decrease for these materials.

The fine grain Y_2O_3-stabilized J-1 material is particularly interesting. Figure 129 illustrates stable heating cycle thermal expansion behavior. However, this sample deformed badly (plastically) at T > 1200°C, and the cooling cycle expansion record could not be completed. However, Table 49 illustrates that the tetragonal phase was retained after the thermal exposure. Monoclinic zirconia was not detected in the exposed sample. Therefore, this demonstrates that the overaging phenomenon is much less pronounced in the Y_2O_3-stabilized material. Consistent with this observation, as shown in Table 49, is that the Y_2O_3-stabilized J-1 material exhibited only a 28% strength reduction after exposure. This is compared to the 60-70% strength loss for the MgO-stabilized materials.

TABLE 49. RESIDUAL STRENGTH AND PHASE ASSEMBLAGE IN ZIRCONIA MATERIALS AFTER THERMAL CYCLING

Material	Bulk Density, g cm^{-3}	Room Temperature 4-Point Flexure Strength, ksi		X-Ray Phase Identification[b]	
		As-Received	After One Thermal Cycle	As-Received	After One Thermal Cycle
G-1 (MgO)	5.776	75.0	29.0 (-61%)	cub c	mono., cubic (tet.?)
U-4 (MgO)	5.739	77.3	24.9 (-68%)	tet., cubic	mono., cubic (tet.?)
A-2 (MgO)	5.757	88.5	--	cubic, tet., mono.	mono., cubic
J-1 (Y$_2$O$_3$)	5.791	105.0	75.7 (-28%)	cubic, tet.	cubic, tet.

[a] Thermal cycle consisted of heating to 1500°C followed by cooling to 25°C, both at 1°C/min.

[b] Major phases only, conducted on a polished cross-section, believed to be representative of the bulk.

275

12.4.5 Conclusion

A domestic supplier is producing a transformation-toughened zirconia that is comparable in microstructure and properties to more mature foreign materials. Y_2O_3-stabilized materials have much finer grain size than MgO-stabilized materials. This results in superior (~30%) room temperature strength. However, creep may be a problem at elevated temperature with the Y_2O_3-stabilized materials. The fine grain Y_2O_3 systems appear to have less severe overaging problems associated with long-term high-temperature isothermal exposure when compared with the MgO-stabilized ZrO_2.

13. FUTURE WORK

Concurrent with the ending of the present program (F33615-79-C-5100), a new program has been initiated, AFWAL Contract F33615-82-C-5101, "Evaluation of Ceramics and Ceramic Composites for Turbine Engine Applications." Only a small portion of this new program involves monolithic silicon-base ceramics. The main thrust of the new program is ceramic fiber composites. These emerging materials offer the potential of high strength as well as high toughness. The scope of our work in this area will be mainly developing test methodology for obtaining tensile, flexure, compressive, and shear strength. The reports, however, will be restricted to a much more limited distribution than the present program.

14. CONCLUDING REMARKS

14.1 SILICON-BASE CERAMICS

A comparison of the major characteristics of the dense forms of SiC and Si_3N_4 is summarized in Table 50. SiC is intermediate in strength to Si_3N_4. However, SiC experiences much less strength degradation by subcritical crack growth, and thus SiC is superior at temperatures greater than 1400°C. Similarly, SiC is more stable and oxidation-resistant at extremely high temperatures. It is, in general, a purer material and not as affected by impurities or secondary phases as Si_3N_4 is. SiC has extremely good creep strength, which coupled with its good oxidation resistance and microstructural stability, make SiC a likely candidate for very long time, high temperature applications. SiC has much higher thermal conductivity and thermal diffusivity compared to Si_3N_4. This means that SiC would be a good candidate for a combustor in a gas turbine engine, but would not be a good candidate as a cast iron diesel engine cylinder liner.

The major disadvantages of SiC when directly compared to Si_3N_4 are its lower fracture toughness and lower thermal shock resistance. The low toughness of SiC is due to its low critical stress intensity factor and low fracture surface energy. Poor thermal shock resistance is often cited as the most critical difference between silicon carbide and silicon nitride. The low thermal shock resistance of SiC is due to the combination of its higher thermal expansion and higher elastic modulus in comparison to Si_3N_4. These properties are more or less inherent, and cannot be modified to any meaningful extent by varying composition or processing method. Thus SiC and Si_3N_4 are unique as engineering materials as are the various heat engine component designs for which they are being used.

During the time frame of this program, the structural ceramic technology can be characterized as a period when researchers

278

TABLE 50.   A COMPARISON OF MAJOR CHARACTERISTICS OF DENSE FORMS
OF SILICON CARBIDE AND SILICON NITRIDE

Silicon Carbide	Silicon Nitride
• Intermediate Strength	• High Strength
• High Thermal Expansion	• Low Thermal Expansion
• Poor Thermal Shock Resistance	• Good Thermal Shock Resistance
• Low Fracture Toughness	• Higher Fracture Toughness
• High Temperature Stability	• Strength Degradation by Slow-Crack Growth
• High Thermal Conductivity	• Low Thermal Conductivity
• Good Oxidation Resistance	• Oxidation Strong Function of Impurities
• High Creep Strength	• Low Creep Strength
• Low Influence of Impurities	• Second Phases Influence Behavior
• High Elastic Modulus	• Lower Elastic Modulus
• Transgranular Fracture	• Intergranular Fracture
• Little Subcritical Crack Growth	• Nonlinear Stress-Strain

realized the inadequacy of magnesia additives for $HP\text{-}Si_3N_4$, and the tendency of some Y_2O_3 compositions to form unstable phases. These problems have been solved. We have demonsterated that Y_2O_3- and ZrO_2-modified $HP\text{-}Si_3N_4$ materials are being produced that have excellent elevated temperature properties.

Also during the current reporting period, the technology was developed to produce sintered silicon carbide in a variety of complex component configurations. However, based on the sintered silicon carbide materials we have evaluated on this program and its predecessor, it appears that advances in SiC technology are not being made as rapidly as advances in Si_3N_4 technology. For Si_3N_4, the advances are being made by improvement of the performance-limiting aspect of that material--the intergranular phase, and its deformation at elevated temperature. For SiC the critical issues appear to be the elimination of isolated surface-connected porosity, and the inhibition of exaggerated α-phase grain growth. It may be that these performance-limiting aspects are more intrinsic for silicon carbide; perhaps SiC is nearer its inherent performance limit. The elimination of viscous intergranular regions in Si_3N_4 may be a more tractable problem.

14.2 TRANSFORMATION-TOUGHENED ZIRCONIA

Transformation-toughened zirconia is being considered for structural use in the hot sections of diesel engines. Its main attributes are low thermal conductivity and thermal expansion high enough to effectively used with cast iron engine components. It has a demonstrated high fracture toughness when compared with silicon-base ceramics. However, it must be recognized that TTZ is essentially a low-temperature material. Overaging phenomena, resulting in loss of toughness and strength, will occur during extended isothermal exposure above the martensitic transformation temperature ($\sim 900°C$). Those unfamiliar with the transformation toughening mechanism should use this material with caution. Partially stabilized zirconia has long been used in high-temperature refractory applications. The same high temperature stability does not exist for transformation-toughened zirconia, however.

REFERENCES

1. D. C. Larsen, "Property Screening and Evaluation of Ceramic Turbine Engine Materials," AFML-TR-79-4188, October, 1979.

2. D. C. Larsen and J. W. Adams, "Property Screening and Evaluation of Ceramic Turbine Materials," IITRI Semiannual Interim Report No. 8, AFWAL Contract F33615-79-C-5100, June 1980.

3. D. C. Larsen and J. W. Adams, "Property Screening and Evaluation of Ceramic Turbine Materials," IITRI Semiannual Interim Technical Report No. 9, AFWAL Contract F33615-79-C-5100, December 1980.

4. D. C. Larsen and J. W. Adams, "Property Screening and Evaluation of Ceramic Turbine Materials," IITRI Semiannual Interim Technical Report No. 10, AFWAL Contract No. F33615-79-C-5100, April 1981.

5. D. C. Larsen and J. W. Adams, "Property Screening and Evaluation of Ceramic Turbine Materials," IITRI Semiannual Interim Technical Report No. 11, AFWAL Contract F33615-79-C-5100, November 1981.

6. D. C. Larsen and J. W. Adams, "Property Screening and Evaluation of Ceramic Turbine Materials," IITRI Semiannual Interim Technical Report No. 12, AFWAL Contract F33615-79-C-5100, May 1982.

7. S. A. Bortz and D. C. Larsen, "Properties of Structural Ceramics," paper presented at 4th Annual Conference on Materials for Coal Conversion and Utilization, U.S. National Bureau of Standards, Gaithersburg, Maryland, October 9-11, 1979.

8. D. C. Larsen and R. Ruh, "Thermal Diffusivity of Silicon-Base Ceramics for Gas Turbine Applications," paper presented at the 16th International Thermal Conductivity Conference, IIT Research Institute, Chicago, Illinois, November 7-9, 1979.

9. D. C. Larsen, H. H. Nakamura, and R. Ruh, "Thermal Expansion of Silicon-Base Gas Turbine Ceramics," paper presented at the 7th International Thermal Expansion Symposium, IIT Research Institute, Chicago, Illinois, November 7-9, 1979.

10. M. G. Mendiratta, P. L. Land, R. Ruh, R. W. Rice, and D. C. Larsen, "Fractography of Reaction-Sintered Si_3N_4," Trans. ASME, J. Engr. Power, $\underline{102}$, pp. 244-248, 1980.

REFERENCES (cont.)

11. S. A. Bortz and D. C. Larsen, "Properties of Structural Ceramics," SAMPE Journal, January/February 1981.

12. D. C. Larsen, J. W. Adams, and R. Ruh, "Corrosion of Silicon-Ceramics and Oxide Ceramics in Coal Gas Environment," paper presented at the American Ceramic Society 83rd Annual Meeting, Washington, D.C., May 3-6, 1981.

13. D. C. Larsen, J. W. Adams, and R. Ruh, "Oxidation of Silicon Nitride and Silicon Carbide," paper presented at American Ceramic Society 83rd Annual Meeting, Washington, D.C., May 3-6, 1981.

14. D. C. Larsen, J. W. Adams, S. A. Bortz, and R. Ruh, "Evidence of Strength Degradation by Subcritical Crack Growth in Si_3N_4 and SiC," presented at the International Symposium on Fracture Mechanics of Ceramics, July 15-17, 1981, Pennsylvania State University, University Park, PA, in Fracture Mechanics of Ceramics, Vol. 5, R. C. Bradt, A. G. Evans, D. P. H. Hasselman, and F. F. Lange (eds.), pp. 571-586, Plenum Press, New York (1983).

15. D. C. Larsen, J. W. Adams, and R. Ruh, "The Nature of SiC for Use in Heat Engines Compared to Si_3N_4: An Overview of Property Differences," paper pesented at NATO Advanced Study Institute on Nitrogen Ceramics, University of Sussex, Brighton, U.K., 27 July-7 August 1981, in Progress in Nitrogen Ceramics, F. L. Riley (ed.), pp. 695-710, Martinus Nijhoff Publishers, Boston, Massachusetts (1983).

16. J. W. Adams, D. C. Larsen, and R. Ruh, "Strength-Microstructure Relations for Various SiC Ceramics," paper presented at American Ceramic Society Annual Meeting, Cincinnati, OH, May 1982.

17. D. C. Larsen, J. W. Adams, and R. Ruh, "Mechanical and Thermal Characterization of Foreign and Domestic Zirconia Ceramics for Diesel Engines," presented at the 85th Annual Meeting of the American Ceramic Society, Chicago, April 24-27, 1983.

18. J. W. Adams, D. C. Larsen, and R. Ruh, "Microstructural Study of Various Silicon Nitride Ceramics," presented at the 85th Annual Meeting of the American Ceramic Society, Chicago, April 24-27, 1983.

19. C. A. Johnson and S. Prochazka, "Microstructures of Sintered SiC," in Ceramic Microstructures '76, R. M. Fulrath and J. A. Pask (eds.), Westview Press, 1977.

20. G. W. Robinson and R. E. Gardner, "Ceramographic Preparation of Silicon Carbide," J. Amer. Ceram. Soc., 47 (4), p. 201, 1964.

21. K. S. Mazdiyasni and C. M. Cooke, "Synthesis, Characterization, and Consolidation of Si_3N_4 Obtained from Ammonolysis of $SiCl_4$," J. Amer. Ceram. Soc., 56, No. 12, p. 628, 1973.

22. G. Petzow, Metallographic Etching, Amer. Soc. for Metals, Metals Park, OH, p. 92.

23. K. S. Mazdiyasni and C. M. Cooke, "Consolidation, Microstructure, and Mechanical Properties of Si_3N_4-Doped with Rare-Earth Oxides," J. Amer. Ceram. Soc., 57, No. 12, p. 537, 1974.

24. D. Cheever, Coors Porcelain Co., Private communication, 1982.

25. F. B. Seely and J. O. Smith, Advanced Mechanics of Materials, John Wiley and Sons, Inc., New York, 1957.

26. S. Spinner and W. E. Tefft, "A Method for Determining Mechanical Resonance Frequencies and for Calculating Elastic Moduli from These Frequencies," ASTM Proceedings, 61, pp. 1221-1238, 1961.

27. G. Zener, Elasticity and Anelasticity of Metals, University of Chicago Press, 1948.

28. D. F. Moore, "Internal Friction," Principles and Applications of Tribology, Pergamon Press, New York, 1975.

29. N. F. Astbury and W. R. Davis, "Internal Friction in Ceramics," Trans. Brit. Ceram. Soc., 63, pp. 1-18, 1964.

30. H. Kolsky, Stress Waves in Solids, Oxford-Clarendon Press, 1953.

31. W. J. Parker, et al., J. Appl. Phys., 32, p. 1679, 1961.

32. J. A. Cape and G. W. Lehman, "Temperature and Finite Pulse Time Effects in the Flash Method for Measuring Thermal Diffusivity," J. Appl. Phys., 34, pp. 1909-1913, 1963.

33. R. E. Taylor and J. A. Cape, "Finite Pulse-Time Effects in the Flash Diffusivity Technique," Appl. Phys. Letters, 5, pp. 212-213, 1964.

REFERENCES (cont.)

34. R. E. Taylor, "Critical Review of Flash Method for Measuring Thermal Diffusivity," Report PRF-6764, by Thermophysical Properties Research Center, Purdue University, to National Science Foundation, October 15, 1973.

35. R. D. Cowan, "Pulse Method for Measuring Thermal Diffusivity at High Temperature," J. Appl. Phys., 34, pp. 926-927, 1963.

36. D. C. Larsen and J. W. Adams, "Property Screening and Evaluation of Ceramic Turbine Materials," IITRI Semiannual Interim Technical Report No. 14, AFWAL Contract F33615-79-C-5100, August, 1983.

37. A. G. Evans, "Structural Reliability—A Processing Dependent Phenomenon," J. Amer. Ceram. Soc., 65 (3), pp. 127-137, 1982.

38. R. W. Rice, "Microstructure Dependence of Mechanical Behavior of Ceramics," in Treatise on Materials Science and Technology, Vol. 11, Properties and Microstructure, R. K. MacCrone (ed.), Academic Press, 1977.

39. S. Prochazka and R. J. Charles, "Strength of Boron-Doped, Hot-Pressed Silicon Carbide," Bull. Amer. Ceram. Soc., 52 (12), pp. 885-891, 1973.

40. C. A. Johnson and S. Prochazka, "Microstructures of Sintered SiC" in Ceramic Microstructures '76, R. M. Fulrath and J. A. Pask (eds.), Westview Press, 1977.

41. P. Kennedy, J. V. Shennan, P. Braiden, J. McLaren, and R. Davidge, "An Assessment of the Performance of Refel Silicon Carbide under Conditions of Thermal Stress," Proc. Brit. Ceram. Soc. (22), pp. 67-87, June 1973.

42. D. C. Larsen and G. C. Walther, "Property Screening and Evaluation of Ceramic Turbine Engine Materials," IITRI Semiannual Interim Technical Report No. 6, AFML Contract No. F33165-75-C-5196, July 1978.

43. G. D. Quinn, "Review of Static Fatigue in Silicon Nitride and Silicon Carbide," presented at a Topical Meeting on Non-Oxide Ceramics, New England Section, American Ceramic Society, Cape Cod, MA, October 5-6, 1981.

44. D. C. Larsen and R. Ruh, "The Properties of SiC, Si_3N_4, and ZrO_2 for Engines, and the Potential of Ceramic Composites," 12th Automotive Materials Conference—Ceramics in Engines, University of Michigan, March 14-15, 1984.

REFERENCES (cont.)

45. R. R. Wills and M. C. Brockway, "Hot Isostatic Pressing of Silicon Base Ceramics, AFWL-TR-80-4193, January 1981.

46. A. G. Evans and S. M. Wiederhorn, "Crack Propagation and Failure Prediction in Silicon Nitride at Elevated Temperatures," J. Mater. Sci., 9 (2), pp. 270-278, 1974.

47. T. Vasilos, R. M. Cannon, Jr., and B. J. Wuensch, "Improving the Stress Rupture and Creep of Silicon Nitride," NASA-CR-159585, 1979.

48. G. G. Trantina and C. A. Johnson, "Subcritical Crack Growth in Boron-Doped SiC," J. Amer. Ceram. Soc., 58 (7-8), pp. 344-345, 1975.

49. A. G. Evans and S. M. Wiederhorn, "Crack Propagation and Failure Prediction in Silicon Nitride at Elevated Temperatures," J. Mater. Sci., 9 (2), pp. 270-278, 1974.

50. M. Srinivasan, R. H. Smoak, and J. A. Coppola, "Static Fatigue Resistance of Sintered Alpha SiC," Paper 10-C-79C presented at the American Ceramic Society 34d Annual Conference on Composites and Advanced Materials, Merritt Island, Florida, January 21-24, 1979.

51. K. D. McHenry and R. E. Tressler, "Subcritical Crack Growth in Silicon Carbide," J. Mater. Sci., 12, pp. 1272-1278, 1977.

52. M. S. Seltzer, "High Temperature Creep of Ceramics," AFML-TR-76-97, June 1976.

53. M. S. Seltzer, "High Temperature Creep of Silicon-Base Compounds," Bull. Amer. Ceram. Soc., 56 (4), pp. 418-423, 1977.

54. R. J. Charles, "High-Temperature Stress Rupture of Polycrystalline Ceramics," General Electric Report 77-CRD-036, May 1977.

55. R. W. Rice and W. J. McDonough, "Hot-Pressed Si_3N_4 with Zr-Based Additions," J. Amer. Ceram. Soc., 58 (5-6), p. 264, 1975.

56. W. J. McDonough, S. W. Freiman, P. F. Becher, and R. W. Rice, "Fabrication and Evaluation of Si_3N_4 Hot-Pressed with ZrO_2," ARPA/NAVSEA-Garrett/AiResearch Ceramic Gas Turbine Engine Program Review, Maine Maritime Academy, Castine, Maine, August 1-4, 1977.

REFERENCES (cont.)

57. S. W. Freiman, C. Wu, K. R. McKinney, and W. J. McDonough, "Effect of Oxidation on the Room Temperature Strength of Si_3N_4 Hot-Pressed with MgO or ZrO_2," ARPA/NAVSEA-Garrett/AiResearch Ceramic Gas Turbine Engine Program Review, Maine Maritime Academy, Castine, Maine, August 1-4, 1977.

58. D. C. Larsen and G. C. Walther, "Property Screening and Evaluation of Ceramic Turbine Engine Materials," IITRI Semiannual Interim Report No. 5, AFML Contract F33615-75-C-5196, January 1978.

59. S. Ud Din and P. S. Nicholson, "Creep Deformation of Reaction Sintered Silicon Nitrides," J. Amer. Ceram. Soc., 58 (11-12), pp. 500-502, 1975.

60. S. Grathwohl and F. Thummler, "Creep of Reaction-Bonded Silicon Nitride," J. Mater. Sci., 13, pp. 1177-1186, 1978.

61. J. M. Birch and B. Wilshire, "The Compression Creep Behavior of Silicon Nitride Ceramics," J. Mater. Sci., 13, pp. 2627-2636, 1978.

62. J. M. Birch et al., "The Influence of Stress Distribution on the Deformation and Fracture Behavior of Ceramic Materials Under Compression Creep Conditions," J. Mater. Sci., 11, pp. 1817-1825, 1976.

63. F. F. Lange, "Non-Elastic Deformation of Polycrystals with a Liquid Boundary Phase," in Deformation of Ceramic Materials, R. C. Bradt and R. E. Tressler (eds.), Plenum Press, New York, 1975.

64. T. L. Francis and R. L. Coble, "Creep of Polycrystalline Silicon Carbide," J. Amer. Ceram. Soc., 51 (2), pp. 115-116, 1968.

65. P. L. Farnsworth and R. L. Coble, "Deformation Behavior of Dense Polycrystalline SiC," J. Amer. Ceram. Soc., 49 (5), pp. 264-268, 1966.

66. D. P. H. Hasselman, "Thermal Stress Resistance Parameters for Brittle Refractory Ceramics: A Compendium," Bull. Amer. Ceram. Soc., 49, pp. 1033-1037, 1970.

67. D. C. Larsen and G. C. Walther, "Property Screening and Evaluation of Ceramic Vane Materials," IITRI Semiannual Interim Technical Report No. 4, AFML Contract F33615-75-C-5196, October 1977.

REFERENCES (cont.)

68. D. P. H. Hasselman, "Unified Theory of Thermal Shock Fracture Initiation and Crack Propagation in Brittle Ceramics," J. Amer. Ceram. Soc., 52, pp. 600-604, 1969.

69. S. C. Singhal, "Oxidation of Silicon-Based Structural Ceramics," in Properties of High Temperature Alloys (with Emphasis on Environmental Effects), Z. A. Foroulis and F. S. Pettit (eds.), Electrochemical Society, Inc., Princeton, NJ, pp. 697-712, 1977.

70. S. C. Singhal, "Oxidation of Silicon Nitride and Related Materials," in Nitrogen Ceramics, F. L. Riley (ed.), NATO Advanced Study Institute Series, Noordhoff International Publishing, pp. 607-626, 1977.

71. S. C. Singhal, "Oxidation and Corrosion-Erosion Behavior of Si_3N_4 and SiC," Ceramics for High-Performance Applications, J. J. Burke, A. E. Gorum, and R. N. Katz (eds.), Brook Hill Publishing Co., Chestnut Hill, MA pp. 533-548, 1974.

72. C. L. Quackenbush, J. T. Smith, J. Neil, "Oxidation in the $Si_3N_4-Y_2O_3-SiO_2$ System," Proceedings of DOE Automotive Technology Development Contractor Coordination Meeting, Dearborn, MI, November 11-14, 1980.

73. C. L. Quackenbush, "A Review of GTE Sintered Si_3N_4 Structural Ceramics," Proceedings of 5th International Symposium on Automotive Propulsion Systems, DOE CONF-800419, Vol. 1, Dearborn, MI, pp. 482-499, October 1980.

74. W. C. Tripp and H. C. Graham, "Oxidation of Si_3N_4 in the Range 1300° to 1500°C," J. Amer. Ceram. Soc., 59 (9-10), pp. 399-304, 1976.

75. S. C. Singhal, "Thermodynamics and Kinetics of Oxidation of Hot-Pressed Silicon Nitride," J. Mater. Sci., 11, pp. 500-509, 1976.

76. S. C. Singhal and F. F. Lange, "Effect of Alumina Content on the Oxidation of Hot-Pressed Silicon Carbide," J. Amer. Ceram. Soc., 58 (9-10), 1975.

77. J. W. Hinze, W. C. Tripp, and H. C. Graham, "The High Temperature Oxidation of Hot-Pressed Silicon Carbide," in Mass Transport Phenomena in Ceramics, A. R. Cooper and A. H. Heuer (eds.), Plenum Press, 1975.

78. S. C. Singhal, "Oxidation Kinetics of Hot-Pressed Silicon Carbide," J. Mater. Sci., 11, pp. 1246-1253, 1976.

REFERENCES (cont.)

79. S. C. Singhal, "Thermodynamic Analysis of the High-Temperature Stability of Silicon Nitride and Silicon Carbide," Ceramurgia Intl., $\underline{2}$ (3), pp. 123-130, 1976.

80. A. J. Kiehle et al., "Oxidation Behavior of Hot-Pressed Si_3N_4," J. Amer. Ceram. Soc., $\underline{58}$ (1-2), pp. 17-20, 1975.

81. F. F. Lange, "$Si_3N_4-Ce_2O_3-SiO_2$ Materials: Phase Relations and Strength," Ceram. Bull., $\underline{59}$ (2), p. 239, 1980.

82. C. L. Quackenbush and J. T. Smith, "Phase Effects of Si_3N_4 Containing Y_2O_3 or $CeO_2 \cdot$ II, Oxidation," Ceram. Bull., $\underline{59}$ (5), p. 533, 1980.

83. J. P. Guha, P. Goursat, and M. Billy, "Hot-Pressing and Oxidation Behavior of Silicon Nitride with Ceria Additive," J. Amer. Ceram. Soc., $\underline{63}$ (1-2), p. 119, 1980.

84. F. F. Lange and B. I. Davis, "Development of Surface Stresses During the Oxidation of Several Si_3N_4/CeO_2 Materials," J. Amer. Ceram. Soc., $\underline{62}$ (11-12), p. 629, 1979.

85. H. Knoch and G. E. Gazza, "Carbon Impurity Effect on the Thermal Degradation of a $Si_3N_4-Y_2O_3$ Ceramic," AMMRC TR-79-27, May 1979.

86. S. Schuon, "Effect of W and WC on the Oxidation Resistance of Yttria-Doped Silicon Nitride," NASA Technical Memorandum 81528, 1980.

87. A. G. Evans and R. W. Davidge, "The Strength and Oxidation of Reaction-Sintered Silicon Nitride," J. Mater. Sci., $\underline{5}$, pp. 314-325, 1970.

88. R. W. Davidge, A. G. Evans, D. Gilling, and P. R. Wilyman, "Oxidation of Reaction-Sintered Silicon Nitride and Effects on Strength," Special Ceramics 5, P. Popper (ed.), British Ceramic Research Association, pp. 329-342, 1970.

89. S. C. Singhal and F. F. Lange, "Oxidation Behavior of Sialons," J. Amer. Ceram. Soc., $\underline{60}$ (3-4), p. 190, 1977.

90. M. H. Lewis and P. Barnard, "Oxidation Mechanisms in Si-Al-O-N Ceramics," J. Mater. Sci., $\underline{15}$, pp. 443-448, 1980.

91. N. J. Tighe, "Microstructural Aspects of Deformation and Oxidation of Magnesia-Doped Silicon Nitride," U.S. National Bureau of Standards Report NSBIR 76-1153, September 1976.

92. W. Bryzik, "Adiabatic Diesel Engine," Research Development, January 1978.

93. R. Kamo and W. Bryzik, "Adiabatic Turbocompound Engine Performance Prediction," SAE Technical Paper 780068, presented at SAE Congress and Exposition, February 1978.

94. R. Kamo, "Cycles and Performance Studies for Advanced Diesel Engines," in Ceramics for High Performance Applications - II, pp. 907-922, J. J. Burke, E. N. Lenoe, and R. N. Katz (eds.), Brook Hill Publishing Company, Chestnut Hill, MA, 1978.

95. R. Kamo and W. Bryzik, "Cummins-TARADCOM Adiabatic Turbocompound Engine Program," SAE Paper 810070, SAE International Congress and Exposition, February 1981.

96. R. N. Katz and E. M. Lenoe, "Ceramics for Diesel Engines: Preliminary Results of a Technology Assessment," AMMRC SP 81-1, October 1981.

97. M. E. Woods and I. Oda, "PSZ Ceramics for Adiabatic Engine Components," SAE Technical Paper 820429, presented at SAE International Congress and Exposition, Detroit, MI, February 1982.

98. R. H. J. Hannink, K. A. Johnston, R. T. Pascoe, and R. C. Garvie, "Microstructural Changes during Isothermal Aging of Calcia Partially Stabilized Zirconia Alloy," in Advances in Ceramics, Volume 3, Science and Technology of Zirconia, pp. 116-136, A. H. Heuer and L. W. Hobbs (eds.), Amer. Ceram. Soc., Columbus, OH, 1981.

99. R. W. Rice et al., "Grain Boundaries, Fracture, and Heat Treatment of Commercial Partially Stabilized Zirconia," Com. Amer. Ceram. Soc., C-175, December 1981.

100. P. G. Valentine et al., "Microstructure and Mechanical Properties of Bulk Yttria-Partially-Stabilized Zirconia," NASA Contractor Report CR-165402, August 1981.

101. A. G. Evans and A. H. Heuer, "Review: Transformation-Toughening in Ceramics: Martensitic Transformation in Crack-Tip Stress Fields," J. Amer. Ceram. Soc., 63 (5-6), pp. 241-248, 1980.

102. R. T. Pascoe and R. C. Garvie, "Surface Strengthing of Transformation-Toughened Zirconia," in Ceramic Microstructure '76, R. M. Fulrath and J. A. Pask (eds.), Westview Press, Boulder, CO, 1977.

103.   T. K. Gupta, F. F. Lange, and J. H. Bechtold, "Effect of
       Stress-Induced Phase Transformation on the Properties of
       Polycrystalline Zirconia Containing Metastable Tetragonal
       Phase," J. Mater. Sci., 13, pp. 1464-1470, 1978.

104.   R. C. Garvie, R. H. Hannink, and R. T. Pascoe, "Ceramic
       Steel?" Nature, 258, pp. 703-704, 1975.

105.   R. C. Garvie, "Stabilization of the Tetragonal Structure
       in Zirconia Microcrystals," J. Phys. Chem., 82 (2), pp.
       218-224, 1978.

106.   A. H. Heuer, "Alloy Design in Partially Stabilized Zir-
       conia," in Advances in Ceramics, Volume 3, Science and
       Technology of Zirconia, A. H. Heuer and L. W. Hobbs
       (eds.), pp. 98-115, Amer. Ceram. Soc., Columbus, OH, 1981.

107.   N. Claussen and M. Ruhle, "Design of Transformation-
       Toughened Ceramics," in Advances in Ceramics, Volume 3,
       Science and Technology of Zirconia, A. H. Heuer and L. W.
       Hobbs (eds.), pp. 137-163, Amer. Ceram. Soc., Columbus,
       OH, 1981.

108.   H. P. Kirchner et al., "Crack Branching in Transformation-
       Toughened Zirconia," J. Amer. Ceram. Soc., 64 (9), pp.
       529-533, 1981.

109.   T. K. Gupta, "Role of Stress-Induced Phase Transformation
       in Enhancing Strength and Toughness of Zirconia Ceramics,"
       in Fracture Mechanics of Ceramics, Volume 4, Crack Growth
       and Microstructure, R. C. Bradt, D. P. H. Hasselman, and
       F. F. Lange (eds.), pp. 877-889, Plenum Press, NY, 1978.

110.   N. Claussen and D. P. H. Hasselman, "Improvement of Ther-
       mal Shock Resistance of Brittle Structural Ceramics by a
       Dispersed Phase of Zirconia," in Thermal Stresses in
       Severe Environments, D. P. H. Hasselman and R. A. Heller
       (eds.), pp. 381-395, 1980.

111.   R. W. Rice, "Further Discussion of 'Precipitation in Par-
       tially Stabilized Zirconia,'", J. Amer. Ceram. Soc., 60
       (5-6), p. 280, 1977.

112.   D. L. Porter and A. H. Heuer, Reply to "Further Discussion
       of 'Precipitation in Partially Stabilized Zirconia,'" J.
       Amer. Ceram. Soc., 60 (5-6), p. 280, 1977.

113.   F. F. Lange, "Transformation Toughening. Part 3: Experi-
       mental Observations in the $ZrO_2-Y_2O_3$ System," J. Mater.
       Sci., 17, pp. 240-246, 1982.

APPENDIX A

REFLECTED LIGHT AND SEM MICROGRAPHS OF POLISHED
REACTION-SINTERED SILICON NITRIDE MATERIALS
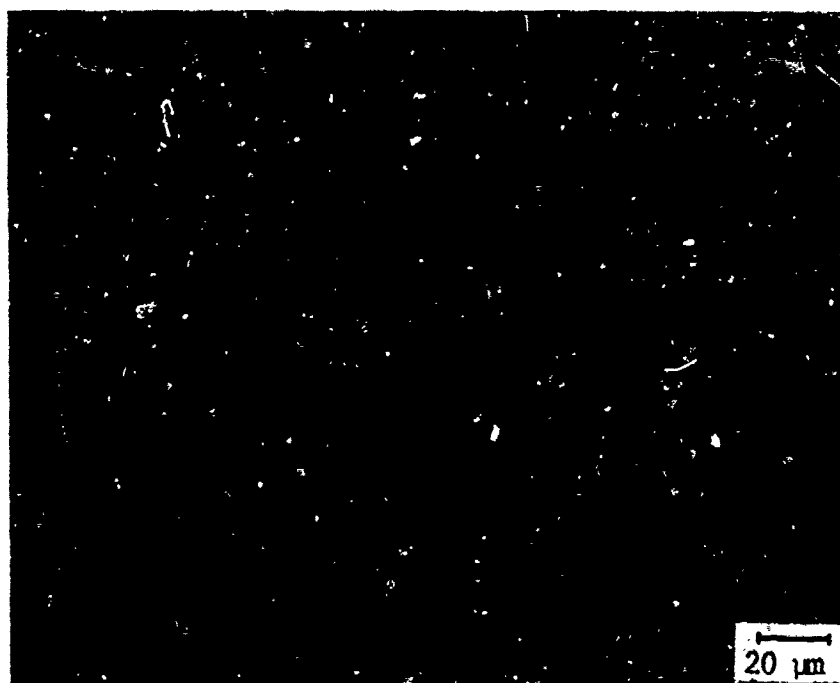
(a) Optical micrograph of polished section

(b) SEM view of polished section

Figure A1. Micrographs of 1976 Norton NC-350 RS-Si$_3$N$_4$.
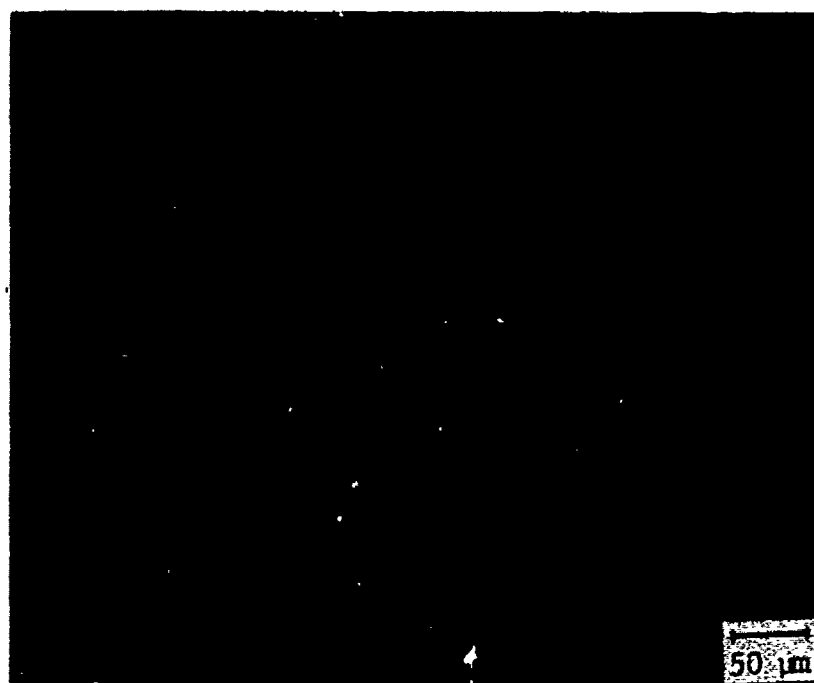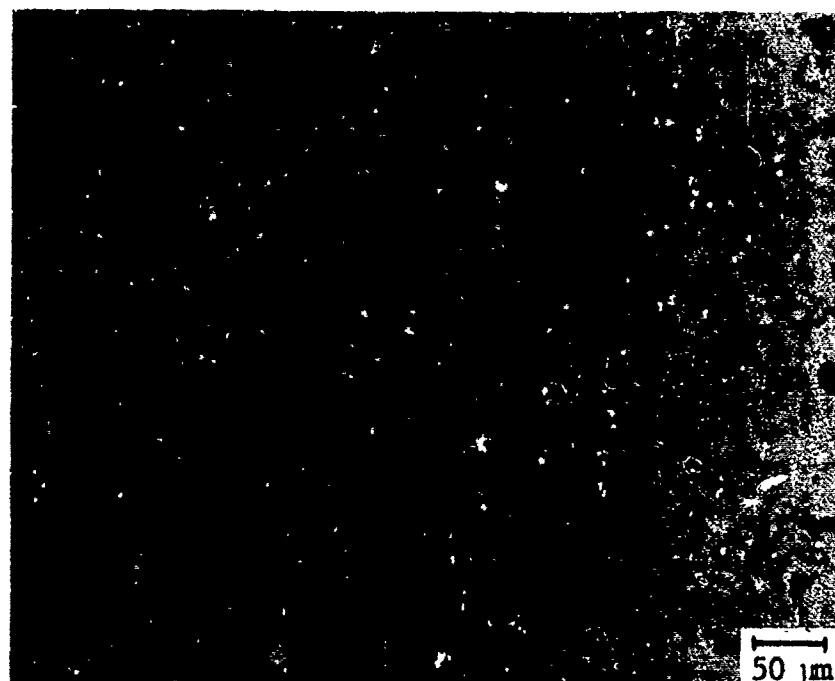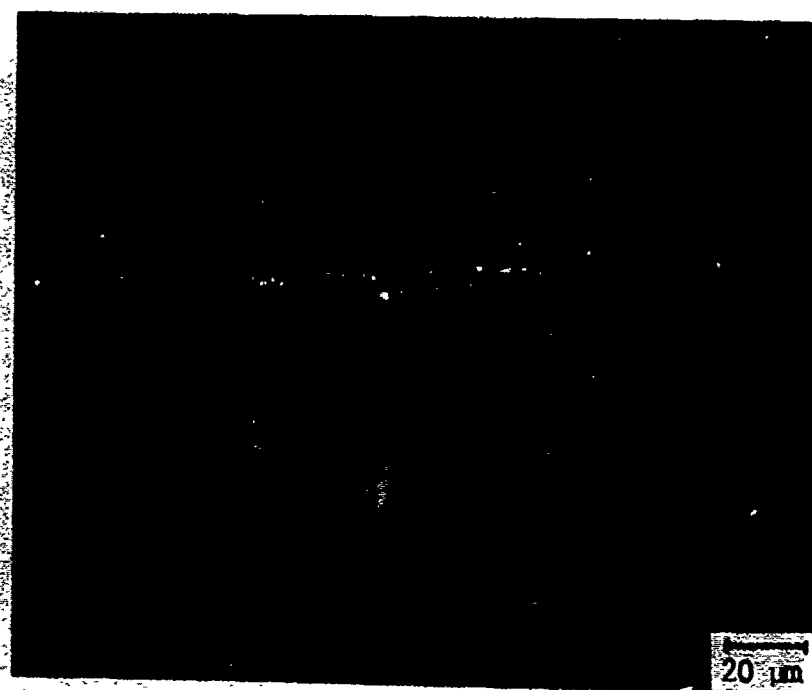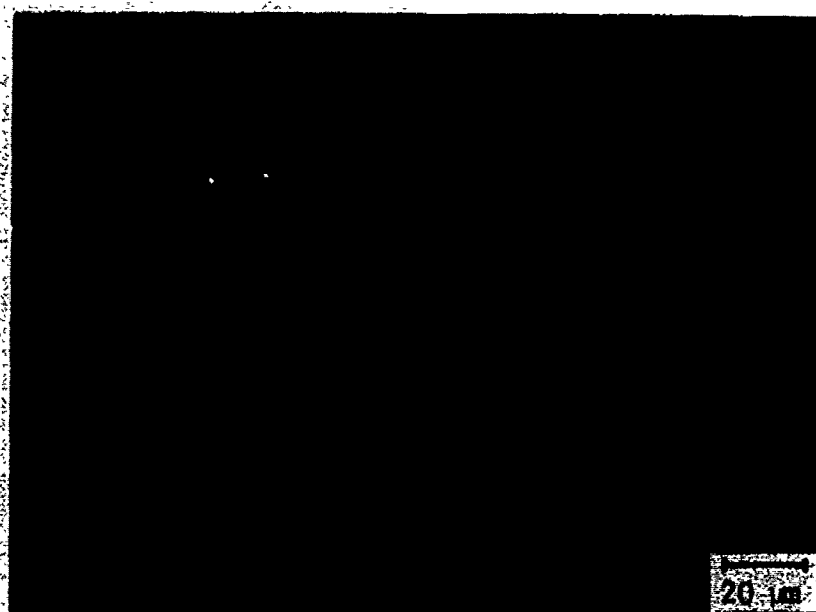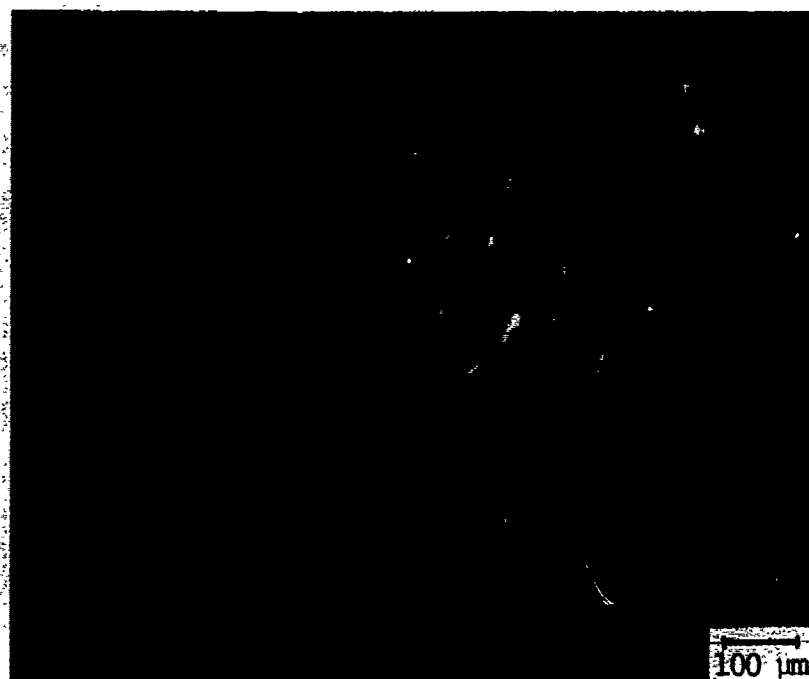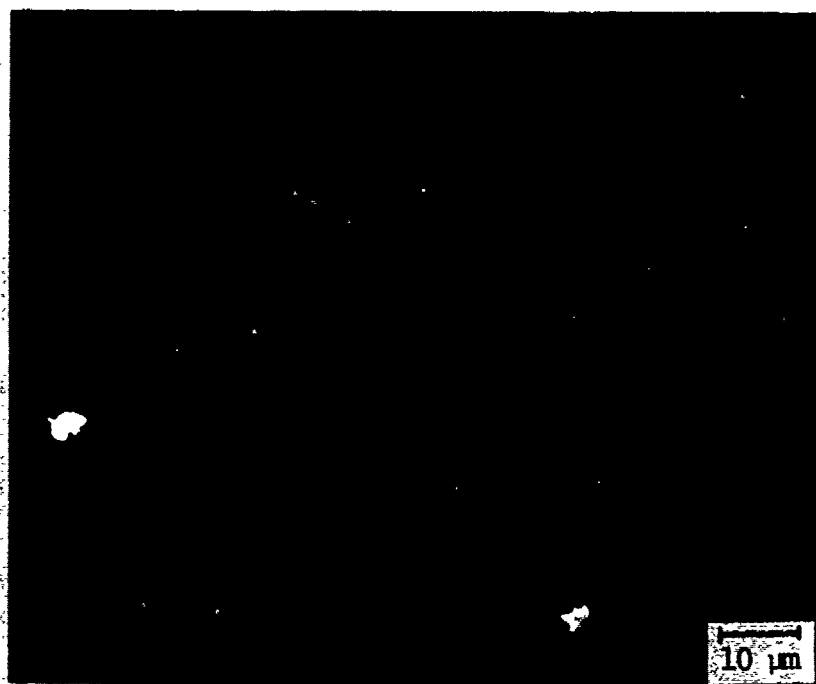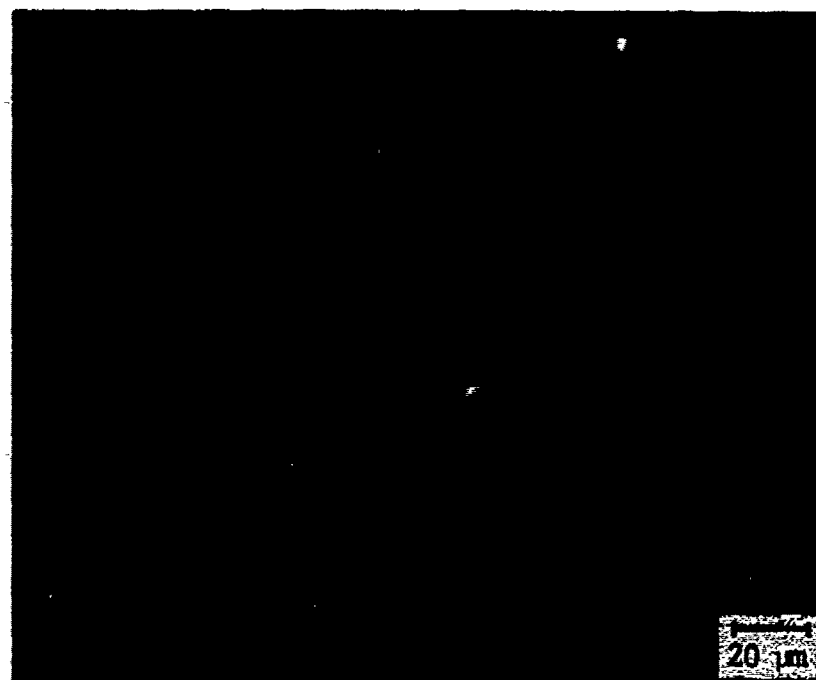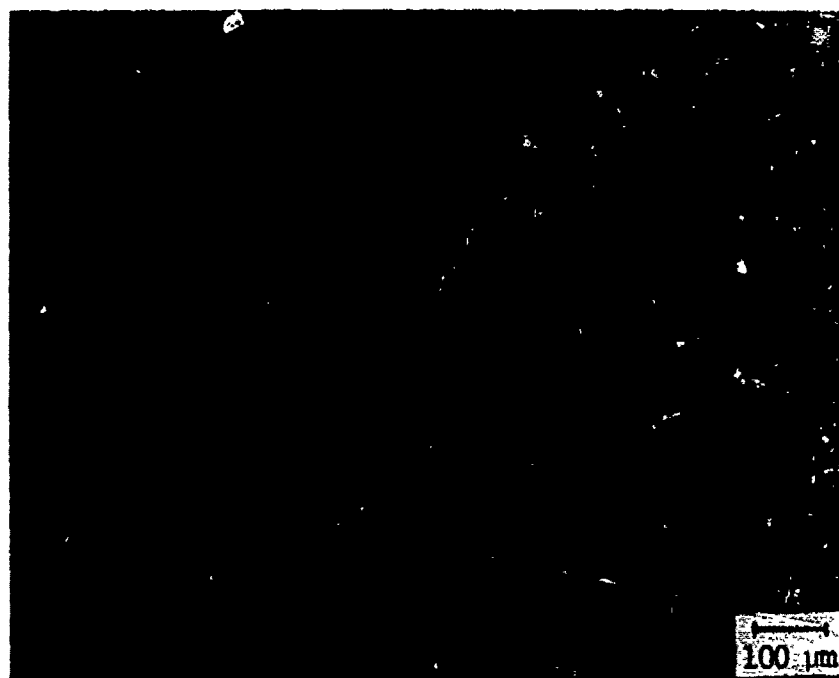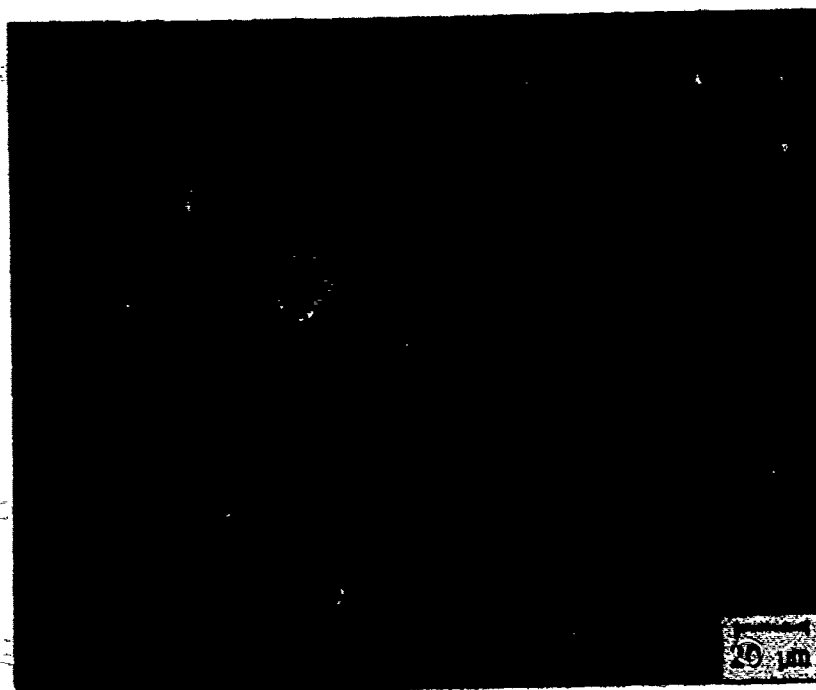
(a) Optical micrograph of polished section

(b) SEM view of polished section

Figure A2. Micrographs of 1977 Norton NC-350 RS-Si$_3$N$_4$.

293

(a) Optical micrograph of polished section

(b) SEM view of polished section

Figure A3. Micrographs of Kawecki-Berylco
(batch 2) RS-Si_3N_4.

(a) Optical micrograph of polished section

(b) SEM view of polished section

Figure A4. Micrographs of Kawecki-Berylco
(batch 3) RS-Si$_3$N$_4$.
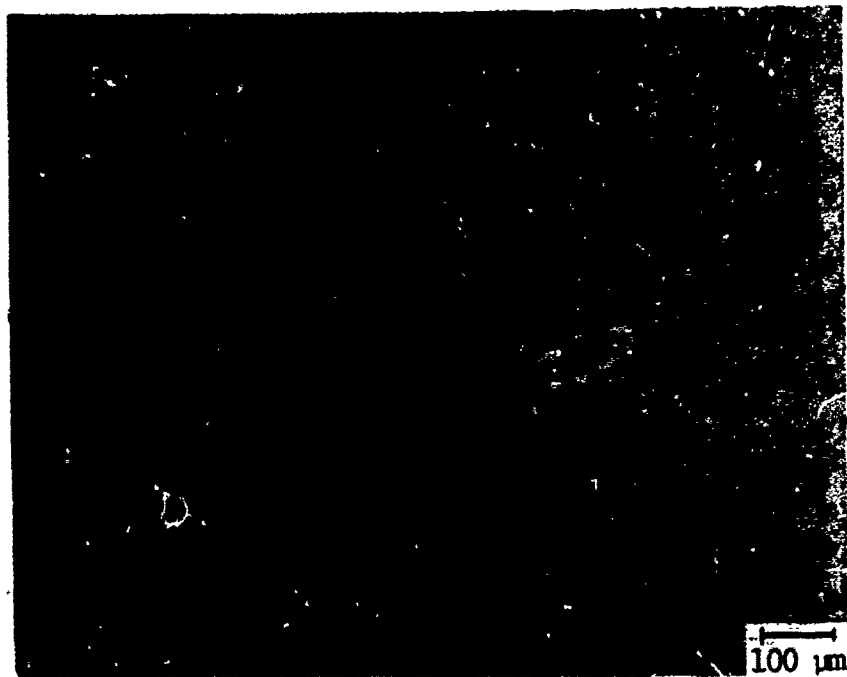
(a) Optical micrograph of polished section
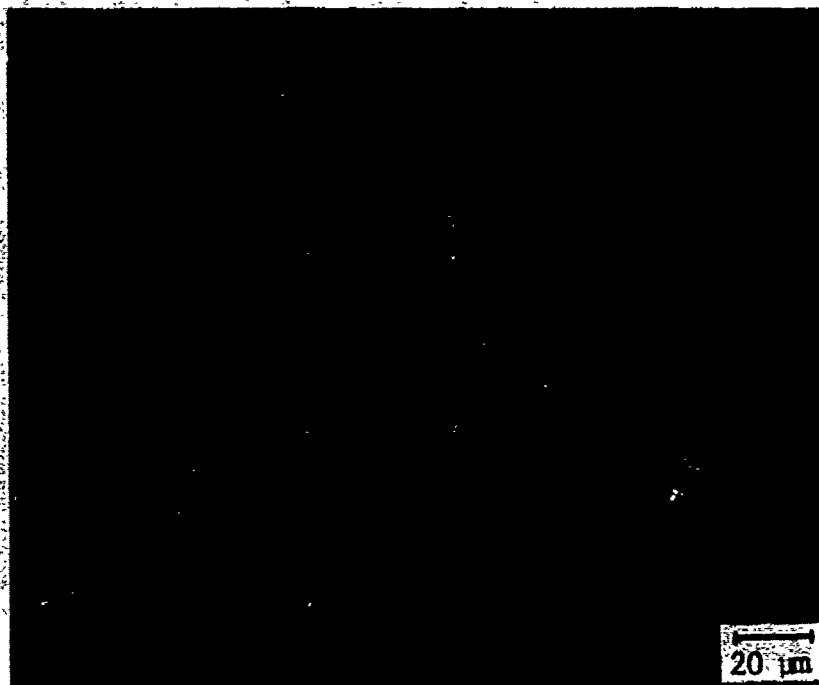
(b) SEM view of polished section

Figure A5.   Micrographs of Ford injection
molded RS-Si_3N_4.

296

(a) Optical micrograph of polished section

(b) SEM view of polished section

Figure A6. Micrographs of AiResearch slip cast
(Airceram RBN-101) RS-Si$_3$N$_4$.

(a) Optical micrograph of polished section

(b) SEM view of polished section

Figure A7.   Micrographs of Raytheon
isopressed RS-Si$_3$N$_4$.

298

(a) Optical micrograph of polished section

(b) SEM view of polished section

Figure A8.   Micrographs of Indussa/Nippon
Denko RS-Si_3N_4.

299

(a) Optical micrograph of polished section

(b) SEM view of polished section

Figure A9. Micrographs of AiResearch injection
molded (Airceram RBN-122) RS-Si$_3$N$_4$.

300

(a) Optical micrograph of polished section

(b) SEM view of polished section

Figure A10. Micrographs of 1979 Norton
NC-350 RS-Si$_3$N$_4$.

301

(a) Optical micrograph of polished section

(b) SEM view of polished section

Figure A11. Micrographs of Annawerk Ceranox
NR-115H RS-Si$_3$N$_4$.

302

(a) Optical micrograph of polished section

(b) SEM view of polished section

Figure A12.   Micrographs of Associated Engineering
Developments, Ltd., Nitrasil (batch 1) 1978 RS-
Si_3N_4.

(a) Optical micrograph of polished section
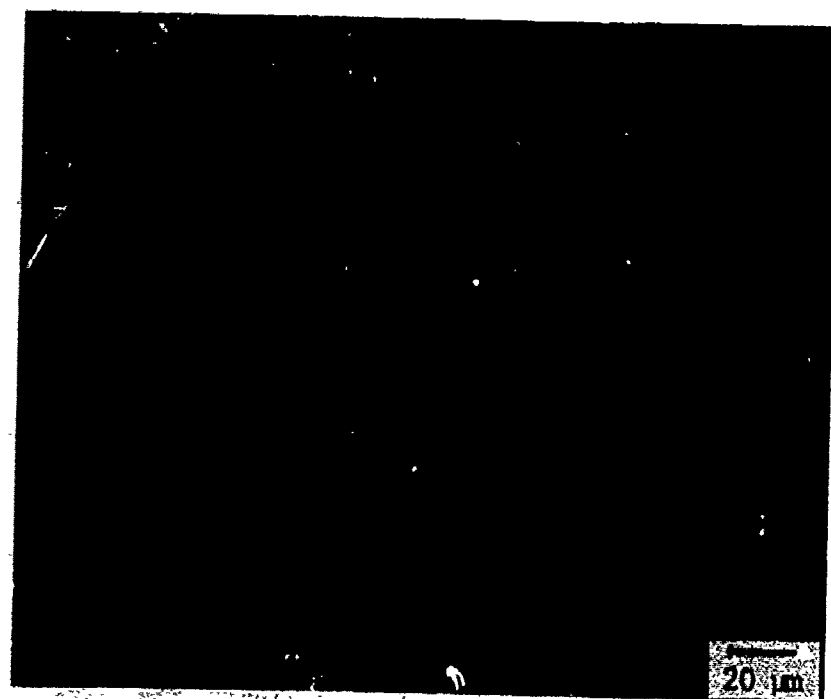
(b) SEM view of polished section

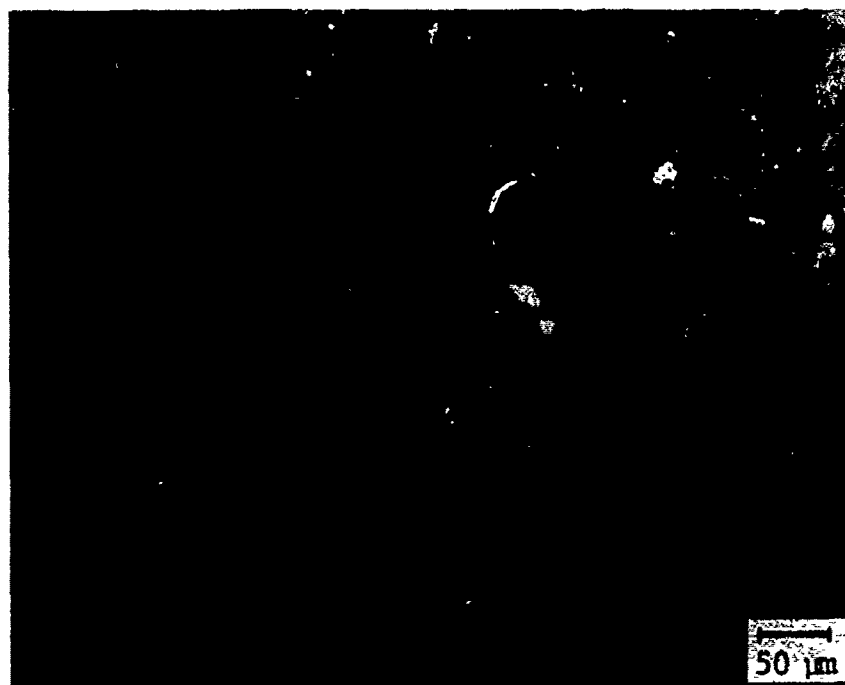Figure A13.   Micrographs of AED, Ltd., Nitrasil
(batch 2) 1978 RS-Si_3N_4.

304

(a) Optical micrograph of polished section
(gold shadowed)
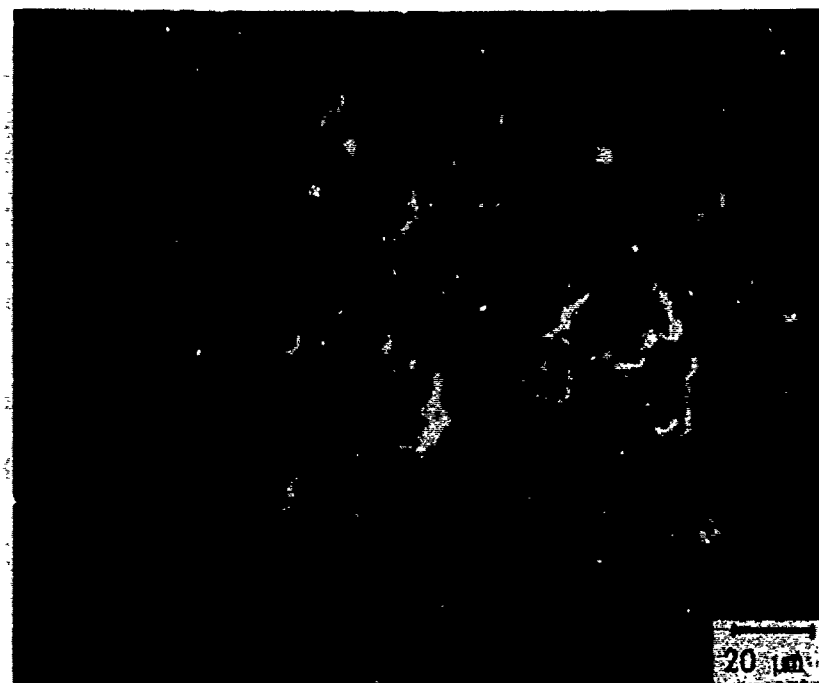
(b) SEM view of polished section

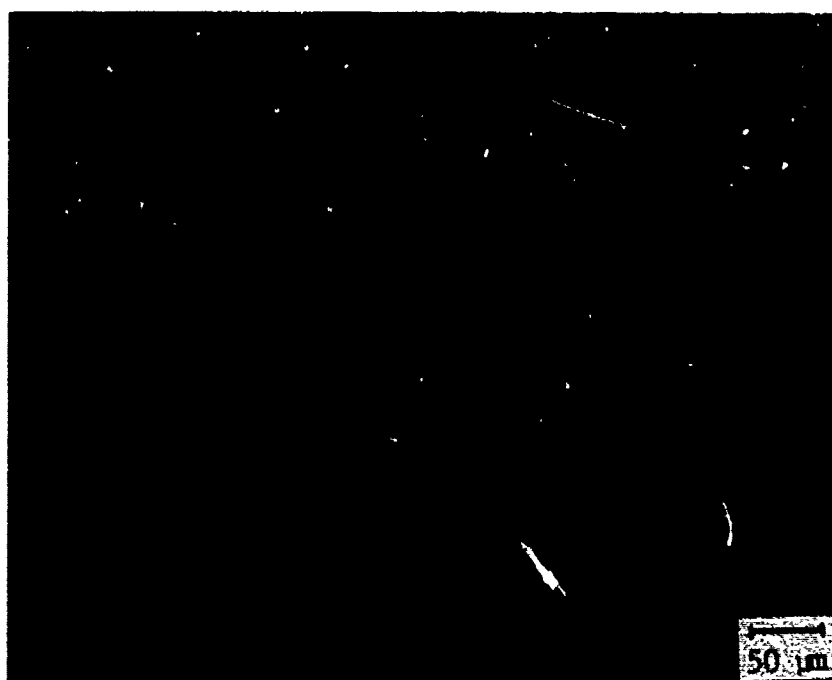Figure A14. Micrographs of AED, Ltd., Nitrasil
(batch 4) 1978 RS-Si$_3$N$_4$.

305

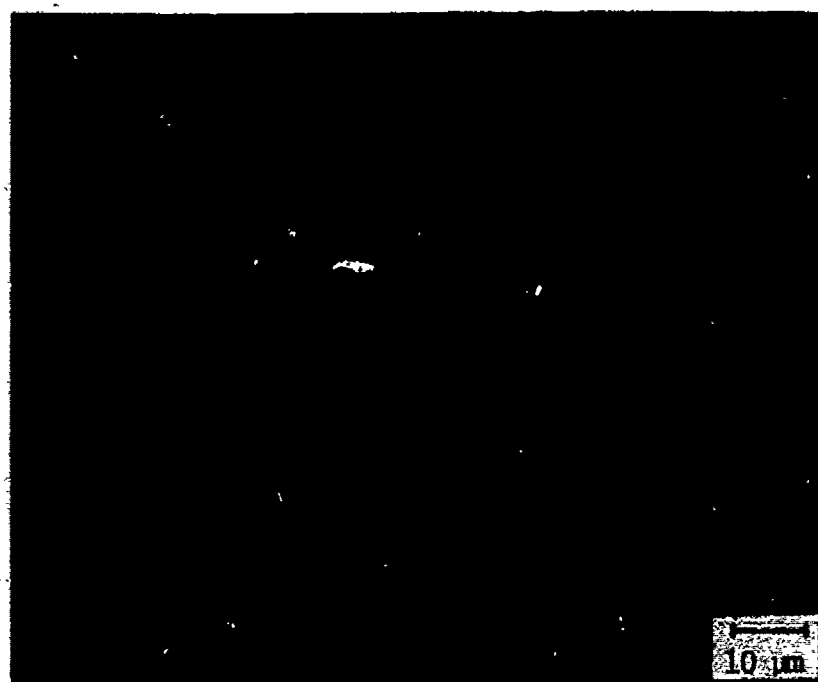(a) Optical micrograph of polished section

(b) SEM view of polished secti n

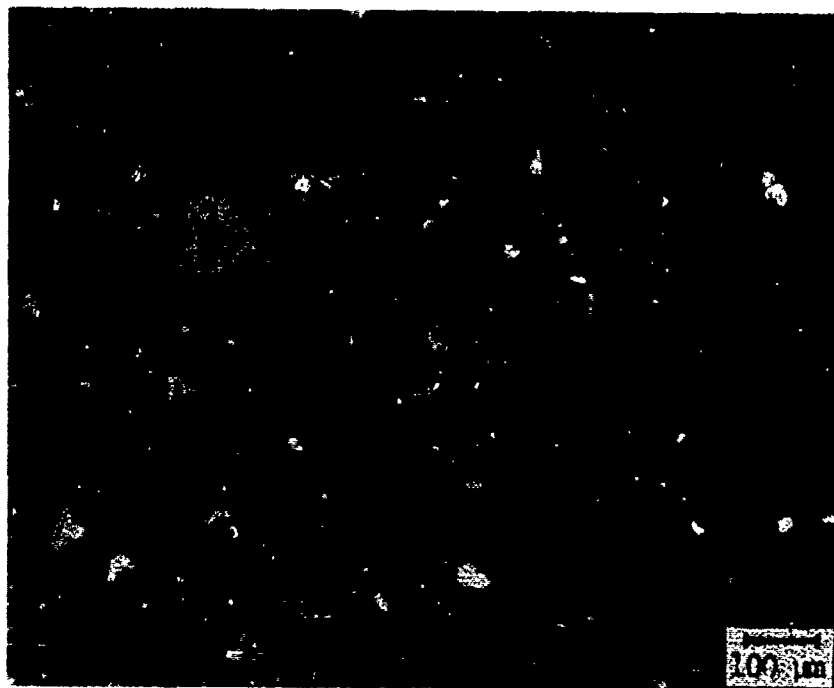Figure A15. Micrographs of AED, Ltd., Nitrasil
(batch 5) 1980 RS-Si$_3$N$_4$.

306

(a) Optical micrograph of polished section

(b) SEM view of polished section

Figure A16.   Micrographs of Georgia Tech RS-Si$_3$N$_4$.

(a) Optical micrograph of polished section

(b) Optical micrograph of polished section

Figure A17. Micrographs of AME RS-Si_3N_4.

308

(a) Optical micrograph of polished section

(b) SEM view of polished section

Figure A18.   Micrographs of AiResearch
RBN-104 RS-Si$_3$N$_4$.

309